*Mo*délisati*o*n at*o*mistique de la transf*o*rmati*o*n de phase austénite-ferrite dans les aciers

Yuri Borges Gomes Lima

▶ **To cite this version:**

Yuri Borges Gomes Lima. *Mo*délisati*o*n at*o*mistique de la transf*o*rmati*o*n de phase austénite-ferrite dans les aciers. Materials Science [cond-mat.mtrl-sci]. Normandie Université, 2024. English. NNT : 2024NORMR086 . tel-04916139

HAL Id: tel-04916139

https://theses.hal.science/tel-04916139v1

Submitted on 28 Jan 2025

HAL is a multi-disciplinary open access archive for the deposit and dissemination of scientific research documents, whether they are published or not. The documents may come from teaching and research institutions in France or abroad, or from public or private research centers.

L'archive ouverte pluridisciplinaire **HAL**, est destinée au dépôt et à la diffusion de documents scientifiques de niveau recherche, publiés ou non, émanant des établissements d'enseignement et de recherche français ou étrangers, des laboratoires publics ou privés.

Normandie Université

UNIVERSITÉ DE ROUEN NORMANDIE

THÈSE

Pour obtenir le diplôme de doctorat

Spécialité **PHYSIQUE**

Préparée au sein de l'**Université de Rouen Normandie**

Modélisation atomistique de la transformation de phase austénite-ferrite dans les aciers

Présentée et soutenue par

BORGES GOMES LIMA YURI

Thèse soutenue le 19/12/2024

devant le jury composé de :

M. LEDUE DENIS	Professeur des Universités - Université de Rouen Normandie (URN)	Directeur de thèse
M. POLITANO OLIVIER	Professeur des Universités - Universite de Bourgogne	Président du jury
MME ZAPOLSKY HELENA	Professeur des Universités - Université de Rouen Normandie (URN)	Co-directeur de thèse
M. DEMANGE GILLES	Maître de Conférences - Université de Rouen Normandie (URN)	Membre du jury
MME MOTTET CHRISTINE	Directeur de Recherche - Aix-Marseille université	Membre du jury
MME VARVENNE CELINE	Chargé de Recherche - Institut National des Sciences Appliquees de Lyon	Membre du jury
M. THUINET LUDOVIC	Maître de Conférences HDR - Universite de Lille	Rapporteur du jury

Thèse dirigée par **LEDUE DENIS** (GROUPE DE PHYSIQUE DES MATERIAUX) et **ZAPOLSKY HELENA** (GROUPE DE PHYSIQUE DES MATERIAUX)

ED 591 PSIME

GPM Groupe de Physique des Matériaux

Remerciements

Je tiens en premier lieu à exprimer ma profonde reconnaissance envers mes directeurs de thèse, les professeurs Denis Ledue et Helena Zapolsky, et mon encadrant de thèse, Gilles Demange. Leurs conseils, leur patience, leur disponibilité et la qualité de leur encadrement scientifique m'ont été d'une aide inestimable tout au long de mon doctorat et de la rédaction de ce manuscrit. J'aimerais aussi grandement remercier Renaud Patte, à la fois pour son aide précieuse en informatique mais aussi pour sa bienveillance et son attention.

De même, je souhaite adresser ma gratitude au professeur Olivier Politano et au docteur Ludovic Thuinet, pour avoir accepté de m'accorder leur expertise en qualité de rapporteur.

Je voudrais également exprimer mes sincères remerciements aux docteures Christine Mottet et Céline Varvenne pour avoir accepté de participer au jury en tant qu'examinatrices.

J'exprime toute ma gratitude envers le Groupe de Physique des Matériaux, dirigé par Xavier Sauvage, qui m'a accueilli en stage de licence et de master et qui m'a permis de réaliser mon doctorat dans les meilleures conditions possibles.

Je remercie le CRIANN (Centre Régional Informatique et d'Applications Numériques de Normandie) pour les ressources de calcul durant ces trois années, ainsi que l'Université de Rouen pour le financement de mon doctorat.

Merci à tous les autres doctorants et membres du laboratoire, en particulier Jules, Kylian, Jean-Baptiste, Arnaud, Yanis, Alexandre, Mehdi, Omar, Mohammed, Richel et Christian pour les bons moments passés ensemble.

Enfin, j'aimerais remercier Marina pour m'avoir accompagné et soutenu tout au long de ce doctorat.

Contents

List of Figures

List of Tables

Abreviations

ADF	**A**tomic **D**ensity **F**unction
BB/OC	**B**ogers **B**urgers **O**lson **C**ohen
BCC	**B**ody-**C**entered **C**ubic
BCT	**B**ody-**C**entered **T**etragonal
CNA	**C**ommon **N**eighbor **A**nalysis
CRSS	**C**ritical **R**esolved **S**hear **S**tress
EAM	**E**mbedded **A**tom **M**ethod
CADF	**C**ontinuous **A**tomic **D**ensity **F**unction
FCC	**F**ace-**C**entered **C**ubic
GT	**G**reninger-**T**roiano
HRTEM	**H**igh-**R**esolution **T**ransmission **E**lectron **M**icroscopy
HCP	**H**exagonal **C**lose **P**acked
HP	**H**abit **P**lane
KS	**K**urdjumov-**S**achs
KSN	**K**urdjumov-**S**achs-**N**ishiyama
LE	**L**ocal **E**quilibrium
LID	**L**attice **I**nvariant **D**islocation
ML	**M**achine **L**earning
MEAM	**M**odified **E**mbedded **A**tom **M**ethod
MD	**M**olecular **D**ynamics
NW	**N**ishiyama-**W**asserman
OR	**O**rientation **R**elationship
PFC	**P**hase **F**ield **C**rystal
PTMC	**P**Phenomenological **T**heory of **M**artensite **C**rystallography
QA	**Q**uasiparticles **A**pproach
RSS	**R**esolved **S**hear **S**tress
SVA	**S**lip **V**ector **A**nalysis
TM	**T**opological **M**odel

Introduction

Steel is employed across nearly all industries as a crucial structural material. This versatility stems from the broad range of mechanical properties of the materials, achieved through the incorporation of alloying elements and specific thermomechanical treatments, which produce microstructures. Indeed, the allotropic transformations of iron at atomospheric pressure lead to a rich microstructures arising from various phase transformations. Among all solid-state transformations in steels, the transformation from austenite γ (face-centered cubic phase, FCC) to ferrite α (body-centered cubic phase, BCC) is a key process in the production of most contemporary steels. This transformation results in numerous microstructures [1], such as allotrimorphic ferrite, perlite, bainite or martensite (considered here as a deformed, carbon-supersaturated BCC phase). Furthermore, in dual-phase steels, the FCC to BCC transformation controls subsequent bainitic or martensitic transformations. This phase transformation directly influences the final microstructure of steel, thereby impacting its mechanical properties. Additionally, the migration of the FCC-BCC interface is significantly affected by the segregation of solutes already present in steel.

The advances made in physical metallurgy over the past century have highlighted the close link between the macroscopic properties of steels and their atomic-scale organization. This understanding is particularly crucial for elucidating interface migration during the FCC to BCC transformation, which ultimately determines the final volume fraction of these two phases and predicts the segregation of alloying elements at this interface. These considerations have driven researchers to develop new experimental and modeling tools to investigate materials at increasingly finer scales. From an experimental perspective, this involves the use of high-resolution electron microscopy techniques [2–6] and atomic probe analyses [7–9] to investigate the structure of the interface and the atomic concentration across it. From a computational perspective, advancements include the development of various atomic-scale modeling methods, such as Molecular Dynamics (MD) [10–16], Monte Carlo simulation [17–20], and more recently, the Phase Field Crystal (PFC) method [21–25]. The objective is to achieve an optimal balance between 'computation time' and the accuracy of physical phenomena representation. Significant progress has been made in understanding the atomic structure of the FCC-BCC interface via MD simulations. However, this approach is limited in terms of the size of the modeled system (typically on the order of few nanometers) and especially by the short timescales simulated (on the order of nanoseconds). Monte Carlo simulations have also advanced our understanding of solute atom interactions with static interfaces [19,

26]. However, incorporating the cooperative movement of atoms that occurs during the FCC to BCC transformation remains challenging in the Monte Carlo models, which limits the application of this method for studying interface migration.

In this context, Elder et al. [21] in 2002, proposed a new simulation method known as the Phase Field Crystal method. This approach allows the simulation of phase transformation kinetics over physical timescales several orders of magnitude longer than those achievable with MD. Recently, the PFC method has been successfully applied to model grain boundary structure [27, 28], plasticity and creep in one-component and binary systems [29–32], dendrite growth [33], stress-induced grain boundary motion [34] and solute drag [35]. However, the PFC model does not account for variations in atomic radii of components in binary systems, limiting its accuracy in representing internal elastic fields associated with atomic size effects. This limitation can lead to the emergence of artificial strip structures in the solid phase. To overcome these issues, the Quasiparticle Approach (QA) was developed from the Continuous Atomic Density Function (CADF) framework [36]. This method introduces two key novelties: the concept of quasiparticles, called fratons, to describe dynamic degrees of freedom, and a model Hamiltonian that coonsiders the directionality, length, and strength of interatomic bonds as well as atomic size. Using this approach, the FCC to BCC phase transformation was successfully reproduced in the binary Cu-Fe system [37].

In the context of this work, the Quasiparticle Approach (QA) is applied to investigate the mechanisms driving the displacive FCC to BCC transformation in pure iron, considering different orientation relationships (ORs) between the two phases. Then, the QA is extended to the binary Fe-C system to model the interaction of interstitial carbon atoms with the migrating interface. In this context, the manuscript is organized in five chapters as follows.

The first chapter provides an overview of the literature on the FCC to BCC transformation. This includes a presentation of theoretical models for the transformation mechanism and interface morphology, atomistic modeling of the phase transformation in pure iron, a review of experimental results. This chapter concludes with a brief discussion of the thermodynamic models of carbon segregation at austenite-ferrite interface. The second chapter presents a detail description of the Quasiparticle Approach (QA). It begins with the theoretical foundations of this method, covering the formulation of the Hamiltonian and the Helmholtz free energy. Additionally, the chapter provides detailed descriptions of kinetic equations and interaction potentials for the FCC to BCC phase transformation, covering both one-component systems (pure iron) and two-component systems (Fe-C). In the third chapter, the Quasiparticle Approach is applied to simulate and analyze the FCC to BCC phase transformation in pure iron. The structural properties at the interface, including the nature of dislocation characteristics and strain field distribution, are analyzed across different orientation relationships. Additionally, the nucleation and propagation of the BCC phase in FCC matrix are discussed in connection with this structural analysis of interface. The fourth

chapter explores the mechanism of the FCC to BCC phase transformation across different orientation relationships, based on results from QA simulations. Finally, the fifth chapter investigates the interaction of carbon atoms with the moving FCC-BCC interface and examines its propagation mode within an Fe-C system. In the end, the impact of ORs on the carbon concentration at the FCC-BCC interface is analyzed.

The manuscript concludes with a general discussion on the mechanisms that drive the displacive FCC to BCC phase transformation in pure iron, along with some details on the interaction of carbon atoms with this migrated interface. Finally, some perspectives are provided for this work.

Chapter 1

FCC to BCC phase transformation

The FCC to BCC phase transformation occurs trough a diffusionless, cooperative movement of atoms, which transforms the parent FCC austenite crystal structure into the product BCC ferrite structure without any change in composition. However, diffusion of allowing elements, such as carbon, may occur alongside the FCC to BCC displacive transformation. Rapid quenching of austenite to room temperature often leads to the formation of the martensite BCT phase. In this phase, carbon atoms are distributed on one of the octahedral sublattices of the BCC structure, inducing tetragonal deformation.

Numerous theoretical models have been developed to understand the mechanism of the FCC to BCC phase transformation. Several theoretical models explain the atomic mechanisms of this phase transformation. Among them, the Bain model of FCC to BCC transformation [38], the Kurdjumov-Sachs mechanism (KS) [39], or the Boger-Burgers / Olson-Cohen (BB/OC) mechanism [40, 41]. The phenomenological theory of martensite crystallography [42], dislocation-based models [14], and topological models [43] gave an insight on the macroscopic shape of the FCC-BCC interface observed in experiments. Several atomistic simulations and experimental analyses have also been conducted to elucidate the nature of this phase transformation. The multi-scale nature of the FCC to BCC transformation makes it difficult, for a single approach, to reproduce all aspects of the process, including both the macroscopic shape of the interface and the atomic mechanisms of the transformation. Moreover, displacive phase transformation is a very rapid process which also makes it challenging to investigate this transformation in experiments.

This chapter aims at providing an overview of the literature on the FCC to BCC transformation. It is organized as follows. First, theoretical models and transformation mechanisms will be presented. Second, atomistic modeling of the austenite to ferrite phase transformation in pure iron will be addressed. Third, key experimental analyses will be reviewed. Finally, the role of carbon segregation at mobile interfaces will be assessed, as it plays a significant role in the phase transformation of Fe-C alloys.

1.1 Bain transformation

The austenite to ferrite phase transformation involves the rearrangement of the crystal structure from the FCC phase to the BCC phase, as illustrated in Figures 1.1a and 1.1b, respectively. Several modes of transformation are described in the literature. Among them, the earliest and still the most widely accepted model is the Bain path [38], which is the basis of the Phenomenological Theory of Martensite Crystallography (PTMC) [42].

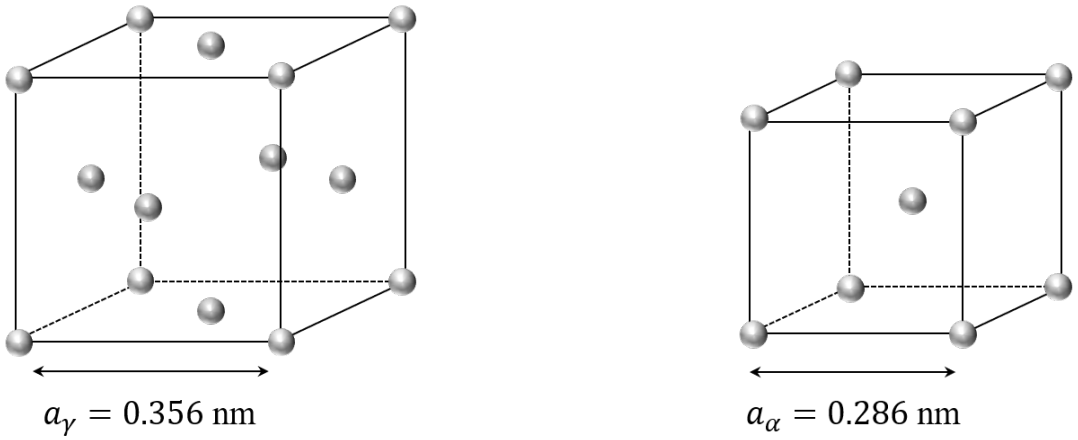

(a) (b)

Figure 1.1: **(a)** FCC unit cell **(b)** BCC unit cell.

The Bain path represents the smallest distortion that allows an FCC lattice to transform into a BCC, pathing though a body-centered tetragonal (BCT) lattice [38, 44, 45]. This path is illustrated in Figure 1.2. The BCC lattice is constructed from the FCC austenite by a homogeneous deformation with contraction along the c-axis and extension along the a-axis of a BCT cell. In the case of pure iron, a 20% compression along c-axis and a 12% expansion along the a-axis of the BCT cell completes the transformation. The resulting Bain strain matrix B, where $\eta_1 = \eta_2 = \frac{a_\alpha\sqrt{2}}{a_\gamma}$ and $\eta_3 = \frac{a_\alpha}{a_\gamma}$ is given by:

$$\mathrm{B} = \begin{pmatrix} \eta_1 & 0 & 0 \\ 0 & \eta_2 & 0 \\ 0 & 0 & \eta_3 \end{pmatrix}, \tag{1.1.1}$$

This deformation corresponds to the formation of a perfect BCC unit cell. However, in steels, the resulting structure often retains some degree of tetragonality. The Honda and Nishiyama model [46], derived from experimental results for steels containing more than 0.6 wt% carbon, provides the tetragonality ratio c_α/a_α as a function of carbon content:

$$\frac{c_\alpha}{a_\alpha} = 1 + 0,045\mathrm{wt\%C}. \tag{1.1.2}$$

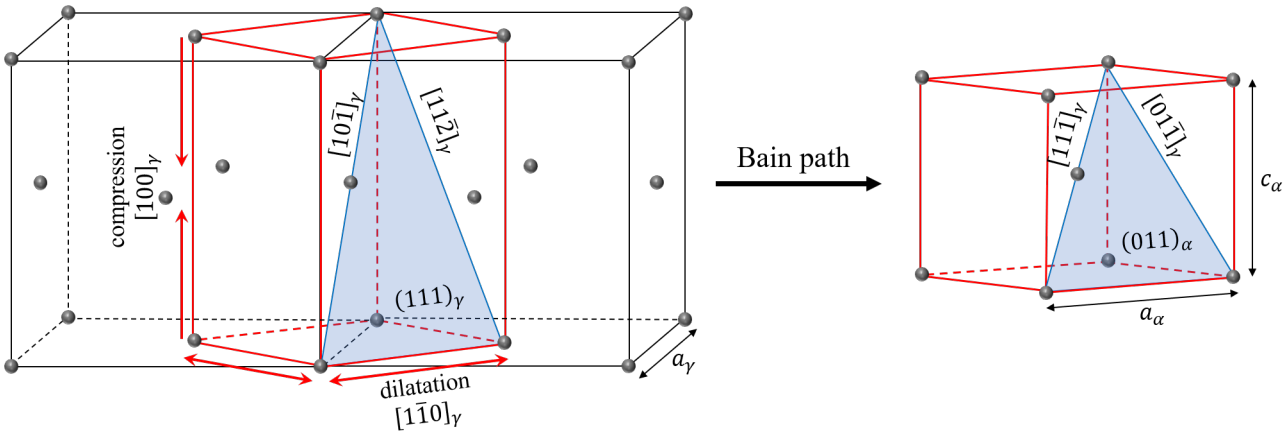

Figure 1.2: Bain transformation: FCC→ BCT→ BCC.

While the Bain mode of transformation is often primarily considered, even in recent studies [47, 48], it is relatively uncommon and observed only in specific cases, such as in ultrathin Fe films [49]. To minimize the energy of the system during the FCC to BCC transformation, the interface between the two phases should have minimal interfacial energy. This can be achieved if the interface aligns with a crystallographic plane that do not undergo distortion or rotation during the phase transformation. This plane is called invariant plane. However, while the Bain strain preserves an undistorted direction [42, 44, 50], it does not maintain an unrotated direction. The Bain strain is schematized in Figure 1.3a, where the black circle is deformed to obtain the blue ellipse. As illustrated in this figure, this deformation does not maintain an invariant line, as the directions $a'b'$ and $c'd'$ in the blue ellipse are rotated from their original positions in the black circle. An additional rigid body rotation is required to keep the direction unrotated. This is schematized in Figure 1.3b.

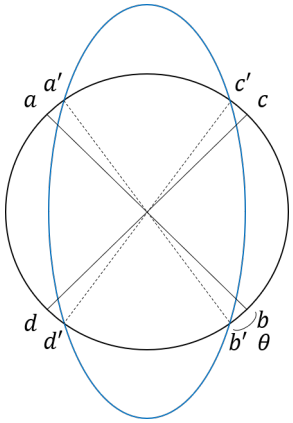

(a) Bain strain

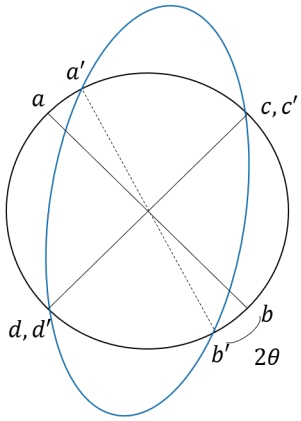

(b) Bain strain and rigid body rotation

Figure 1.3: Schematic representation of the **(a)** Bain strain that keeps the direction cc' undistored **(b)** Bain strain and rigid body rotation that keeps the direction cc' undistored and unrotated.

This total strain determines the final orientation relationship between two phases, while the Bain strain achieves the complete FCC to BCC lattice change [42, 44, 50, 51]. The Bain strain and the associated rotation are not physically distinct: the separation of the total transformation strain into these components is a matter of mathematical convenience [44]. The Bain strain and rigid body rotation result in specific ORs. The choice of OR is not arbitrary [44]: a specific OR allows the best fit at the interface between the two crystals for a defined misfit, thus minimizing the interface energy. However, as shown in Figure 1.4, the change in crystal structure during the FCC to BCC transformation induces a change in the macroscopic crystal structure, which generates significant internal stress. Therefore, an additional lattice invariant transformation is required to alleviate this internal stress, as first proposed by Greninger and Troiano [52].

1.2 Phenomenological Theory of Martensite Cristallography

The Phenomenological Theory of Martensite Crystallography (PTMC) introduces the concepts of invariant plane, schematized in Figure 1.4 and invariant plane strain as discussed previously[42, 45, 53]. The general form of the invariant plane strain starts with the general equation of a plane [45], where $\boldsymbol{n}$ is the unit vector normal to the plane, $\boldsymbol{r}$ the position vector of points in the plane and d represents the distance of the plane from the origin:

$$\boldsymbol{r}\boldsymbol{n} = d = constant, \tag{1.2.1}$$

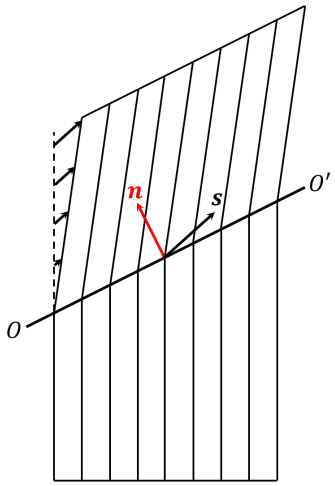

Figure 1.4: Schematic representation of the invariant plane OO', its normal $\boldsymbol{n}$ and the displacement direction $\boldsymbol{s}$ caused by the lattice invariant deformation, inspired from [45].

In the PTMC, the habit plane (HP), which is the mean interface plane between the FCC and BCC structures, must coincide with the invariant plane [42, 45, 53]. The normal to this plane can be calculated using equations provided in [45], where it is incorporated into the definition of the invariant plane strain matrix, denoted as $\mathrm{A_{inv}}$. Introducing the direction $\boldsymbol{s}$ of displacements caused

by the lattice invariant deformation, and the dimensionless constant ϵ representing the amount of strain, and I as the identity matrix, the invariant plane strain is expressed as follows:

$$\mathrm{A}^{-1} = \mathrm{I} + \varepsilon \boldsymbol{s} \otimes \boldsymbol{n}. \tag{1.2.2}$$

Then, the habit plane normal is expressed by Khachaturyan in [45], by means of eigenvalues $\lambda_{1,3}$ and eigenvectors $\boldsymbol{e}_{1,3}$ of this invariant plain strain matrix , where $\lambda_1 < 1$, $\lambda_3 > 1$ and $\lambda_2 = 1$:

$$\boldsymbol{n} = \sqrt{\frac{\lambda_3^2 - 1}{\lambda_3^2 - \lambda_1^2}}\boldsymbol{e}_3 + \sqrt{\frac{1 - \lambda_1^2}{\lambda_3^2 - \lambda_1^2}}\boldsymbol{e}_1. \tag{1.2.3}$$

Two mechanisms of lattice invariant transformation that maintain the invariant plane unrotated and undistorted have been considered to obtain equation 1.2.3: slip and twinning [42, 44, 45, 53]. First, slip mechanism results from periodic shear atomic displacements in the close packed slip planes, along close-packed directions. This mechanism is illustrated in Figure 1.7a, where volume conservation is achieved by the periodic slip. In contrast, the twinning mechanism involves a shear on the twinning plane, reorienting part of the crystallographic structure into a mirror image, as depicted in Figure 1.7b. Both slip or twinning deformations need to be addressed to evaluate the invariant plane strain matrices. These matrices for slip and twinning can be defined using the PTMC framework introduced by Welsher et al. [42]. In the following equation, g defines the shear magnitude, and x represents the relative proportion of the second twin formation in a twinning system:

$$\mathrm{A}_{\mathrm{slip}} = \begin{pmatrix} \eta_1\left(1 - \dfrac{\eta_1\eta_2}{\eta_1^2+\eta_2^2}g\right) & -\eta_1\dfrac{\eta_1^2}{\eta_1^2+\eta_2^2}g & 0 \\ \eta_2\dfrac{\eta_2}{\eta_1^2+\eta_2^2}g & \eta_2\left(1 + \dfrac{\eta_1\eta_2}{\eta_1^2+\eta_2^2}\right) & 0 \\ 0 & 0 & \eta_1 \end{pmatrix}, \tag{1.2.4}$$

$$\mathrm{A}_{\mathrm{twin}} = \begin{pmatrix} \eta_2\left(1 + x\dfrac{\eta_1^2+\eta_2^2}{\eta_1^2+\eta_2^2}\right) & -x\eta_2\dfrac{\eta_1^2-\eta_2^2}{\eta_1^2+\eta_2^2} & 0 \\ x\eta_1\dfrac{\eta_1^2-\eta_2^2}{\eta_1^2+\eta_2^2} & \eta_1\left(1 - x\dfrac{\eta_1^2-\eta_2^2}{\eta_1^2+\eta_2^2}\right) & 0 \\ 0 & 0 & \eta_1 \end{pmatrix}. \tag{1.2.5}$$

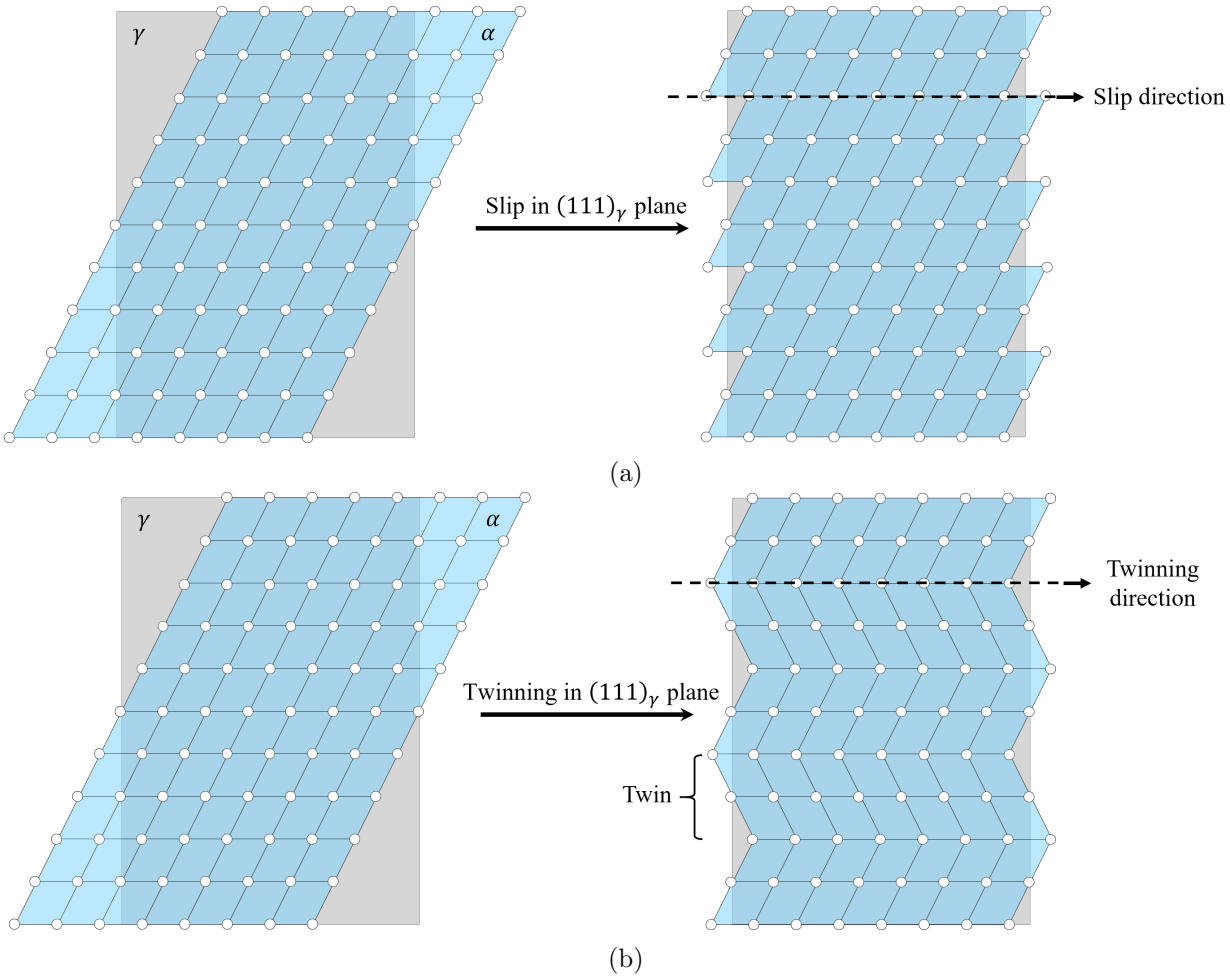

Figure 1.5: Schematic representation of the **(a)** slip mechanism and **(b)** twinning mechanism, allowing the α-phase to fit in the macroscopic shape of its crystal parent γ-phase.

A key conclusion of the PTMC is that these matrices are analogous to each other. Specifically, the shear magnitude g in the slip invariant plane strain matrix $\mathrm{A}_{\mathrm{slip}}$ can be replaced by a parameter $f = \dfrac{\eta_1\eta_2}{\eta_1^2 - \eta_2^2} g$, in the twin deformation matrix $\mathrm{A}_{\mathrm{twin}}$:

$$\mathrm{A}_{\mathrm{slip}} = \begin{pmatrix} \eta_2\left(1 + f\dfrac{\eta_1^2+\eta_2^2}{\eta_1^2+\eta_2^2}\right) & -f\eta_2\dfrac{\eta_1^2-\eta_2^2}{\eta_1^2+\eta_2^2} & 0 \\ f\eta_1\dfrac{\eta_1^2-\eta_2^2}{\eta_1^2+\eta_2^2} & \eta_1\left(1 - f\dfrac{\eta_1^2-\eta_2^2}{\eta_1^2+\eta_2^2}\right) & 0 \\ 0 & 0 & \eta_1 \end{pmatrix}. \tag{1.2.6}$$

Therefore, since both matrices are equivalent, they yield the same expression for the invariant plane of transformation, which is also the HP. Various expressions for the habit plane exist in the literature, based on the application of the PTMC with chosen crystallographic reference frame. While these expressions do not always align perfectly with experimental results [14, 42], they provide valuable insights about the possible HPs at the FCC-BCC interface. Based on Welsher et

al. [42], the HP is $(h\,k\,l)_\alpha$ in the BCC reference frame, where:

$$h = \frac{1}{2\eta_1}\left(\sqrt{\frac{\eta_1^2+\eta_2^2-2\eta_1^2\eta_2^2}{1-\eta_1^2}} - \sqrt{\frac{2-\eta_1^2-\eta_2^2}{1-\eta_2^2}}\right), \tag{1.2.7}$$

$$k = \frac{1}{2\eta_1}\left(\sqrt{\frac{\eta_1^2+\eta_2^2-2\eta_1^2\eta_2^2}{1-\eta_1^2}} + \sqrt{\frac{2-\eta_1^2-\eta_2^2}{1-\eta_2^2}}\right), \tag{1.2.8}$$

$$l = \frac{1}{\eta_1}\frac{\eta_1^2-1}{1-\eta_2^2}. \tag{1.2.9}$$

Using the lattice parameters of pure iron $a_\alpha = 0.286$ nm and $a_\gamma = 0.356$ nm the Equations 1.2.10-1.2.12 yields the HP normal $\boldsymbol{n} = [0.571, 0.197, 0.797]_\alpha$, which is close to $\{1\,2\,1\}_\gamma$ HPs in FCC. However, a more recent PTMC model gives a different expression and results for the HP orientation. Using the expression 1.2.3 proposed by Khachaturyan [45], the HP is $(h\,k\,l)_\gamma$ in the FCC reference frame, where:

$$h = \frac{1}{\sqrt{2}}\sqrt{d\frac{\left(\eta_1^2-1\right)\eta_1^2}{\eta_1^4-\eta_3^2\left(2\eta_1-1\right)^2}}, \tag{1.2.10}$$

$$k = \frac{1}{\sqrt{2}}\sqrt{d\frac{\left(\eta_1^2-1\right)\eta_1^2}{\eta_1^4-\eta_3^2\left(2\eta_1-1\right)^2}}, \tag{1.2.11}$$

$$l = \sqrt{\frac{\eta_1^2-\eta_3^2\left(2\eta_1-1\right)^2}{\eta_1^4-\eta_3^2\left(2\eta_1-1\right)^2}}. \tag{1.2.12}$$

Keeping the same lattice parameters, the habit plane normal calculated in Equations 1.2.10-1.2.12 is $\boldsymbol{n} = [0.5494, 0.5494, 0.6295]_\gamma$, which is at 3.7° form the $(1\,1\,1)_\gamma$ plane. In contrast to the expression given by Welscher et al. in Equations 1.2.10-1.2.12, this formulation consistently produces habit planes of the type $(a\,b\,a)_\gamma$, which are the most commonly found in the literature. Various theoretical models [14, 43, 46, 54], as well as experimental observations [2, 4, 5, 55, 56], support this type of habit plane. However various theoretical PTMC-based models provide different expression for the habit plane [14], as no consensus has been reached. These considerations will be applied to the QA simulation in Chapter 4.

The PTMC models not only predict the habit plane but also determine the orientation relationship (OR) between the FCC and BCC phases. In steels, the most frequently described ORs are Kurdjumov-Sachs (KS) [39], Nishiyama-Wasserman (NW) [46], and Greninger-Troiano (GT) [52]. Each of the ORs involves specific parallel planes and directions, as listed in Table 1.1. Other ORs such a Pitch OR and inverse GT are described for FCC to BCC phase transformation. However they are observed in very specific cases, such as Widmanstätten ferrite for inverse GT OR [57]. For KS and GT ORs, for each of 4 $(1\,1\,1)_\gamma$ plane, there are 6 different orientation of the $(0\,1\,1)_\alpha$, resulting in a total of 24 variants. In the case of NW ORs, the same BCC direction is chosen for each variant, resulting in only 12 variants for this type of OR. The complete list of all variants for

these three ORs is provided in Appendix A. The KS OR variants that share the same FCC plane are illustrated in Figure 1.6.

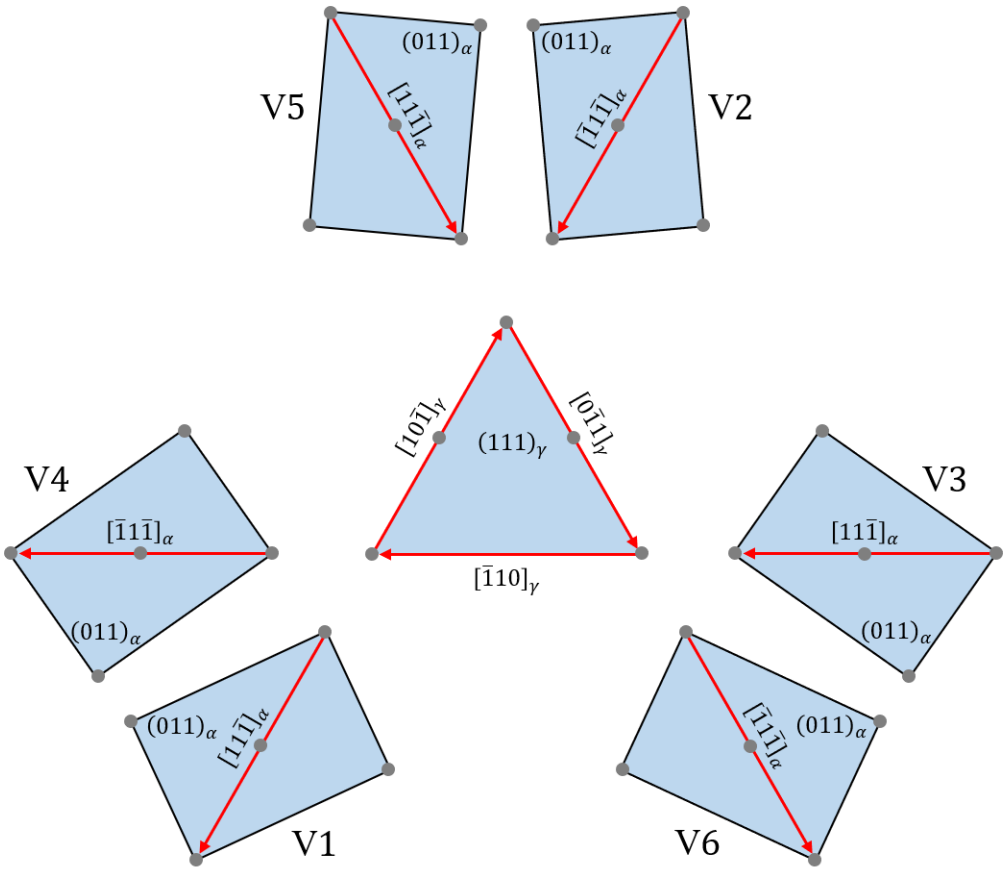

Figure 1.6: KS ORs variants $1-6$.

Orientation Relationship (OR)	FCC plane	BCC plane	FCC direction	BCC direction	Variants n°
Kurdjumov-Sachs (KS)	$\{1\,1\,1\}_\gamma$	$\{0\,1\,1\}_\alpha$	$\langle 1\,0\,\bar{1}\rangle_\gamma$	$\langle 1\,1\,\bar{1}\rangle_\alpha$	24
Nishiyama-Wasserman (NW)	$\{1\,1\,1\}_\gamma$	$\{0\,1\,1\}_\alpha$	$\langle 1\,0\,\bar{1}\rangle_\gamma$	$\langle 1\,0\,0\rangle_\alpha$	12
Greninger-Troiano (GT)	$\{1\,1\,1\}_\gamma$	$\{0\,1\,1\}_\alpha$	$\langle 12\,5\,\bar{17}\rangle_\gamma$	$\langle 7\,17\,\bar{17}\rangle_\alpha$	24

Table 1.1: KS, NW and GT parallels planes, parallels directions and number of variants.

An equivalent way to define NW and GT ORs is by their rotation relative to KS ORs. The Table 1.2 provides the deviation angles between KS, GT, and NW ORs for variants sharing the same parallel plane and Bain strain (KS v1, GT v1, and NW v2).

	FCC	BCC	Deviation angle		
			KS v1	GT v1	NW v2
dense || plane	$(1\,1\,1)_\gamma$	$(0\,1\,1)_\alpha$	$0°$	$0°$	$0°$
dense dir. 1	$[1\,0\,\bar{1}]_\gamma$	$[1\,1\,\bar{1}]_\alpha$	$0°$	$2.4°$	$5.26°$
dense dir. 2	$[0\,\bar{1}\,1]_\gamma$	$[1\,\bar{1}\,1]_\alpha$	$-10.52°$	$-8.12°$	$-5.26°$
secondary dir.	$[1\,1\,\bar{2}]_\gamma$	$[0\,1\,\bar{1}]_\alpha$	$5.26°$	$2.86°$	$0°$

Table 1.2: Main crystallographic plane/directions and their correspondences in FCC and BCC crystals with KS v1, GT v1 and NW v2 ORs.

In conclusion, the PTMC provides a foundational understanding of the FCC to BCC phase transformation by defining the orientation relationship (OR), habit plane (HP), and two invariant transformation modes: slip and twinning. To better understand the twinning and slip mechanisms, as well as the atomic displacements that occur at the interface, further investigation of the interface morphology and the nature of its defects is required.

1.3 Interface morphology and dislocations

The PTMC alone does not describe the shape and morphology of the FCC-BCC interface. In particular, the nature of dislocations which are usually presented at this interface is not considered, despite the fact that it strongly impact the mechanical properties of steel. Then, first an overview of dislocation properties is provided before discussing the FCC-BCC interface morphology as described in the literature.

1.3.1 Dislocations properties

A dislocation is a crystalline linear defect characterized by two vectors: the line direction $\boldsymbol{l}$ and the Burgers vector $\boldsymbol{b}$. The Burgers vector represents the magnitude and direction of the lattice distortion caused by the dislocation, while the dislocation line direction is a vector that indicates the path along which the dislocation extends through the crystal lattice. If $\boldsymbol{l}$ and $\boldsymbol{b}$ are parallel, the dislocation is classified as a 'screw' dislocation and if they are perpendicular, it is referred to as an 'edge' dislocation. When the dislocation has both edge and screw components, it is classified as a 'mixed-type' dislocation. Schematic representations of edge and screw dislocations are shown in Figure 1.7. In general, a Burgers vector can be calculated as the closer failure of the Burgers circuit around the dislocation line direction. This Burgers circuit is highlighted in blue in Figure 1.7, with the Burgers vector in red and line direction in green.

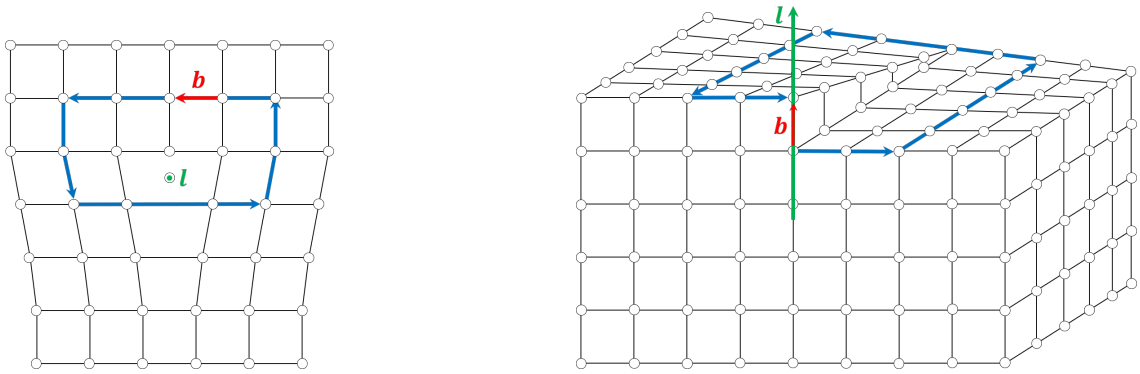

(a) Edge dislocation (b) Screw dislocations

Figure 1.7: Schematic representation of **(a)** an edge dislocation, **(b)** a screw dislocations. Red: Burgers vector $\boldsymbol{b}$, green: line direction of dislocation $\boldsymbol{l}$, blue: Burgers circuit.

Plastic deformation and displacive transformation result from the motion of dislocations. In a single crystal, plastic deformation occurs through the translation of one atomic plane over another, with this plane referred to as the slip plane. The glide of dislocations within a slip plane takes place along specific crystallographic directions, known as slip directions. Thus, a slip system is defined by a slip direction and a slip plane.

For a dislocation to move within a slip system, a shear stress must act in the slip direction along the slip plane. This stress is generated by an externally applied stress [58]. The resolved shear stress (RSS), related to the applied stress, is given by Schmid's law. In the following equation σ is the applied stress, ϕ is the angle between the normal of the slip plane and the applied stress, λ is the angle between the applied stress and the slip direction and m is the Schmid factor:

$$\tau_{\text{rss}} = \sigma m = \sigma \cos\phi \cos\lambda. \tag{1.3.1}$$

A slip will occur in a system when the resolved shear stress becomes superior or equal to the critical resolved shear stress (CRSS) τ_{crss}:

$$\tau_{\text{crss}} = \sigma m_{\text{max}}. \tag{1.3.2}$$

Furthermore, the maximum Schmid factor m_{max}, is specific to each crystallographic structure, resulting in different slip planes for each structure. As a result, each structure has a distinct CRSS. Slip systems consist of dense planes and directions. The primary slip planes and directions for FCC and BCC structures are given in Table 1.3.

Crystal structure	**Slip plane**	**Slip direction**
FCC	$\{1\,1\,1\}_\gamma$	$\langle 0\,1\,1\rangle_\gamma$
BCC	$\{0\,1\,1\}_\alpha$ $\{1\,1\,2\}_\alpha$ $\{1\,2\,3\}_\alpha$	$\langle 1\,1\,1\rangle_\alpha$

Table 1.3: Common slip plane and slip direction for FCC and BCC structures.

While only one slip system is possible for the FCC structure, three competing slip systems exist for the BCC structure. In the FCC structure, close packed $(1\,1\,1)_\gamma$ plane is slip plane. In contrast, BCC is less dense than FCC structure, and the atomic density of its close-packed plane $(0\,1\,1)_\alpha$ is comparable to that of the $\{1\,1\,2\}_\alpha$ and $\{1\,2\,3\}_\alpha$ planes. Therefore, under specific amplitudes and angles of the shear stress and/or thermal activation, additional slip planes can become activated in BCC crystals [59].

Slip systems in FCC and BCC crystals are of particular importance for describing the interface propagation during FCC to BCC transformation. Therefore, for dislocations to move with the interface, they need to be in both an FCC and a BCC slip system. This results in specific geometries, where dislocations lie on parallel FCC and BCC planes at the interface.

Dislocations in slip systems are full dislocations. A full dislocation occurs when the Burgers vector of a dislocation aligns with a close-packed direction in a given crystalline structure. For example, $\langle 1\,1\,1\rangle_\alpha$ dislocations in the BCC structure and $\langle 0\,1\,1\rangle_\gamma$ dislocations in the FCC structure are full dislocations. These types of dislocations are responsible for the slip mechanism in the PTMC.

However, another type of dislocation is possible when its Burgers vector does not point toward to a specific close-packed direction, such as $\langle 1\,1\,2\rangle_\gamma$ dislocations in FCC. These dislocations are referred to as partial dislocations and create stacking faults in the material, as they do not restore the lattice periodicity. This type of dislocation step in in the twinning mechanism (see Figure 1.2). The case of the twinning invariant shear of the FCC structure, depicted in Figure 1.7b, is also shown in Figure 1.8. In this Figure, the partial dislocation indicated by red vector as well as the location of stacking fault delimited by the red atoms between the twin boundaries. Furthermore, the presence of this partial dislocation changes the ABCABC stacking of close-packed planes in FCC crystal into the ABAB stacking of close-packed planes of the hexagonal close-packed (HCP) structure, represented by the red atoms in Figure 1.8.

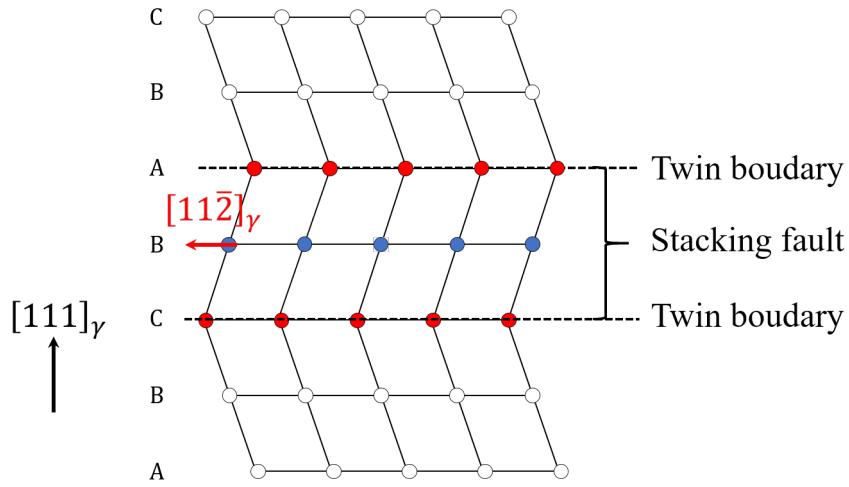

Figure 1.8: Schematic representation of a twinning mechanism with a $(1\,1\,1)_\gamma$ stacking fault created by a partial disloction with a Burgers vector along the direction $[1\,1\,\bar{2}]_\gamma$. Blue vector: partial dislocation Burgers vector, red atoms: HCP stacking due to the stacking fault.

The presence of a dislocation increases the free energy of a system, compared to a defect-free structure. This is primarily due to the elastic stress field generated by the dislocation. The energy of a dislocation line can be estimated as the elastic energy of the region surrounding the dislocation core, where interactions can be treated using continuum elastic theory [59]. With b is the norm of the Burgers vector of the dislocation, and μ the shear modulus, this elastic energy U_e is expressed as follows:

$$U_e = \frac{1}{2}\mu b^2. \tag{1.3.3}$$

This expression of elastic energy alone can explain dislocation recombination and dissociation. Two dislocations, $\boldsymbol{b}_1$ and $\boldsymbol{b}_2$, can combine into another dislocation $\boldsymbol{b}_3$ if $b_3^2 < b_1^2 + b_2^2$. In contrast, a dislocation $\boldsymbol{b}_1$ will split into two dislocations, $\boldsymbol{b}_2$ and $\boldsymbol{b}_3$, if $b_1^2 > b_2^2 + b_3^2$.

Partial dislocations occur when it is more energetically favorable for a full dislocation to dissociate into two partials. This dissociation of a full dislocation into two Shockley partials occurs primarily in crystalline structures with the highest atomic density, such as FCC or HCP structures, while it is not observed for BCC structure which is less dense. For example, in FCC, a dislocation with the Burgers vector $\boldsymbol{b}_1 = a_\gamma/2\,[1\,0\,\bar{1}]_\gamma$ can split into two Shockley partials with Burgers vectors $\boldsymbol{b}_2 = a_\gamma/6\,[2\,\bar{1}\,\bar{1}]_\gamma$ and $\boldsymbol{b}_3 = a_\gamma/6\,[1\,1\,\bar{2}]_\gamma$, where $b_1^2 = \frac{a_\gamma^2}{2}$ and $b_2^2 = b_3^2 = \frac{a_\gamma^2}{6}$, gives $b_1^2 > b_2^2 + b_3^2$.

The Thomson tetrahedron, in Figure 1.9, can be used to visualize the possible dissociation of a full dislocation into two Shockley partial dislocations.

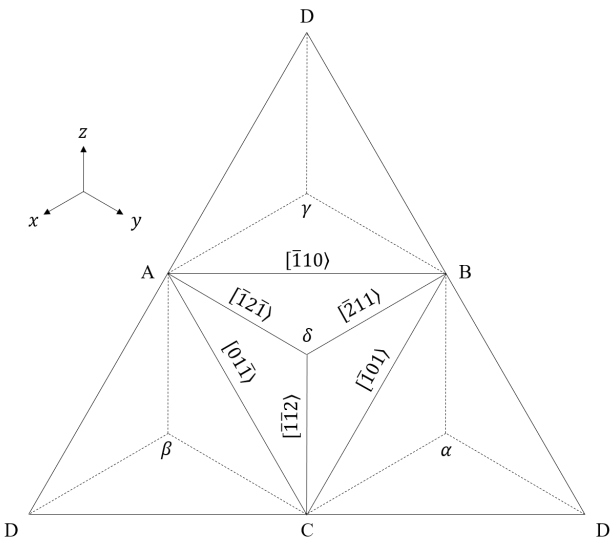

Figure 1.9: Thomson tetrahedron for an FCC structure.

1.3.2 Topological model

Some theoretical models, such as the Topological Model (TM) [43, 60–63], use dislocations to determine the FCC-BCC orientation relationship, habit plane, and various other interface characteristics. Therefore, in this section, we will examine the morphology of the semi-coherent interface between the FCC and BCC phases using the TM. The interface shape described in most theoretical models, and depicted in Figure 1.10, consists of periodically spaced steps and misfit dislocations [4, 14, 43, 44, 55, 56, 64, 65]. Furthermore, it has been demonstrated that the appearance of the steps is a result of the misfit between the two coexisting phases [45] and that the presence of steps induces a dislocation along the terrace ledge [56]. In Figure 1.10, the interface shape consists of coherent terraces with parallel $(1\,1\,1)_\gamma$ and $(0\,1\,1)_\alpha$ planes between the FCC and BCC structures. The terraces are delineated by the line direction $\boldsymbol{\xi}_1$ of the dislocations along the terrace ledges, shown in blue, and the line direction $\boldsymbol{\xi}_2$ of the misfit dislocation, shown in red. The habit plane normal $\boldsymbol{n}_{\mathrm{HP}}$ is defined as the normal of the plane containing these two line directions. Moreover, the step height h and the spacings d_1 and d_2 between each dislocation line $\boldsymbol{\xi}_1$ and $\boldsymbol{\xi}_2$ are also depicted in this figure.

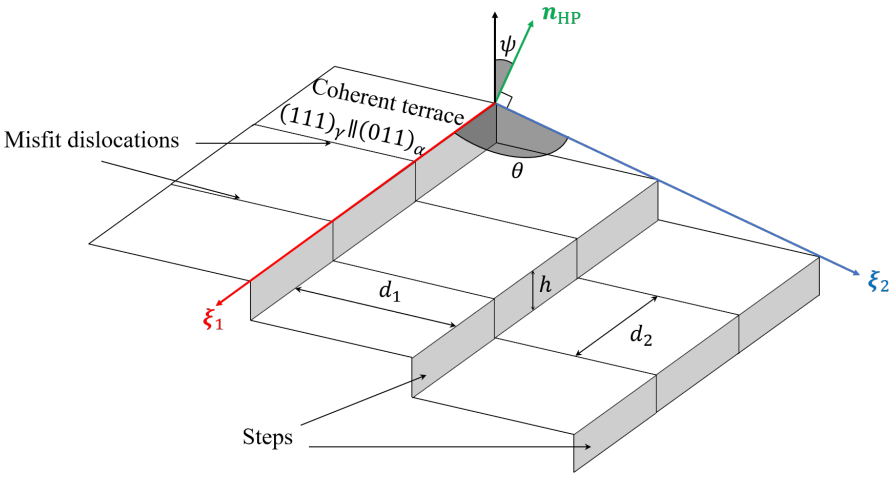

Figure 1.10: Scheme of the FCC-BCC semi-coherent interface relief: showing coherent terraces between FCC and BCC structures on $(1\,1\,1)_\gamma$ planes, with the mean direction $\boldsymbol{\xi}_1$ of disconnections (red arrow) and the mean direction $\boldsymbol{\xi}_2$ of misfit dislocations (blue arrows). The angle θ indicates the angle between the $\boldsymbol{\xi}_1$ and $\boldsymbol{\xi}_2$ directions, while the step height h and the interface habit plane normal vector $\boldsymbol{n}_{\mathrm{HP}}$ deviate from the normal vector of the terrace by an angle ψ, which can be up to 20 degrees.

This model also introduces the concept of a disconnection. The disconnection is identified by the $\boldsymbol{\xi}_1$ line direction shown in Figure 1.10. It can be described by a set of topological parameters $(\boldsymbol{b}, h)$, where $\boldsymbol{b}$ is the Burgers vector of the dislocation and h is the step height. Three categories of disconnections can be defined. First, transformation disconnections are characterized by a non-zero step height [60]. It is postulated in [43, 62] that the movement of these disconnections along the interface drives the phase transformation and facilitates the migration of the interface. The second category is a simple dislocation, where the step height is zero, with topological parameters $(\boldsymbol{b}, 0)$. These are referred to as lattice invariant dislocations (LID) in the TM. They accommodate the crystalline lattices at the interface but do not directly contribute to the phase transformation. The final category is a pure step, with topological parameters $(\boldsymbol{0}, h)$, which is not considered in the current TM [43].

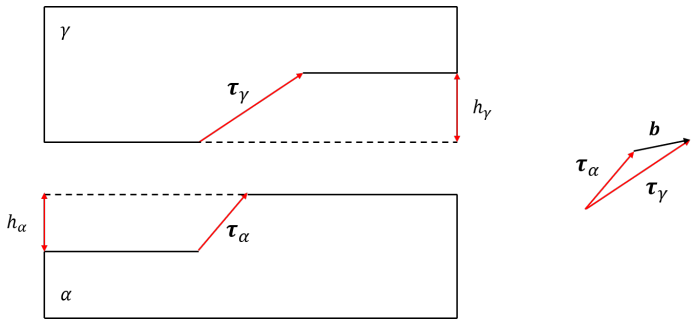

Figure 1.11: Schematic representation of a disconnection, with translation vectors $\boldsymbol{\tau_\alpha}$ and $\boldsymbol{\tau_\gamma}$ with yield the Burgers vector $\boldsymbol{b}$ of the disconnection. The smallest step height of the two crystals, here h_α, is equal to the step height h of the disconnection.

The structure of a disconnection is illustrated in Figure (1.11). Each surface contains a step characterized by translation vectors $\boldsymbol{\tau}_\alpha$ and $\boldsymbol{\tau}_\gamma$. The step height of each crystal, denoted as h_α and h_γ, is defined as the orthogonal component of each translation vector. The bicrystal is distorted in the vicinity of the interface step due to the overlapping of these translation vectors, creating a line defect. The interface step height is determined by the overlap of the step heights of the two crystals and is equal to the smaller of the two defined step heights. The Burgers vector of the disconnection is given by:

$$\boldsymbol{b} = \boldsymbol{\tau}_\gamma - \boldsymbol{\tau}_\alpha. \tag{1.3.4}$$

The other fundamental concept introduced in the TM is the presence of coherent terraces between arrays of dislocations and disconnections. Coherent interfaces between distinct phases generally require the adjacent crystals to be strained [62]. Such elastic strains are reduced through a network of line defects, including disconnections and dislocations. To calculate this theoretical elastic strain, 'natural' and 'coherent' reference states are defined for the system [43]. In the natural state, each crystal retains its free lattice parameters. The crystals are then oriented with a specific OR, and then a deformation is applied so that the common planes between the two crystals align with matching atomic sites. This process is illustrated in Figure (1.12).

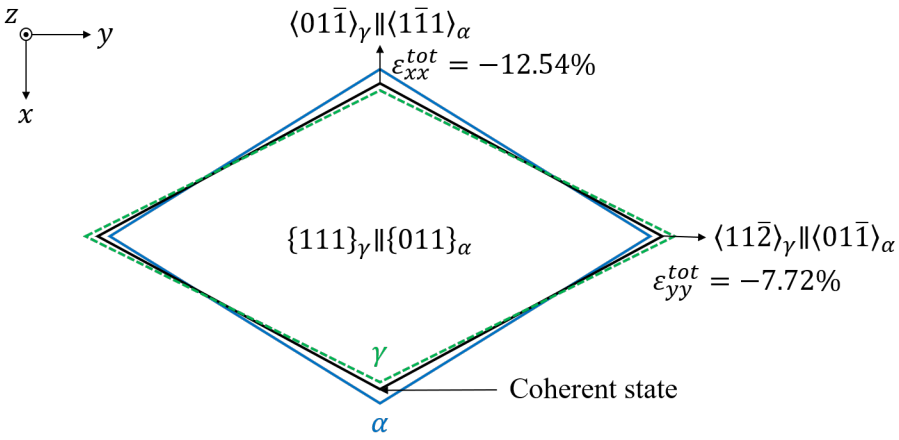

Figure 1.12: Elastic strain in the $\{1\,1\,1\}_\gamma \,||\, \{0\,1\,1\}_\alpha$ terrace plane gives rise to the coherent state. The values of the elastic strain are calculated with $a_\alpha = 0.2870$ nm and $a_\gamma = 0.3580$ nm, such as in [43].

Defining the 'coherent' and 'natural' states is the first of three steps in the TM method. Next, it is necessary to determine the possible interfacial defects that will arrange into a network to create the interface structure. The total elastic strain from the natural to the coherent state, denoted ${}_n\boldsymbol{E}_c^{-1}$ (subscript n signifying 'natural') iis determined by the deformation of the parent FCC crystal from the natural to the coherent state, denoted ${}_c\boldsymbol{P}_n^{-1}$ (subscript n signifying 'coherent') and by the deformation of the martensite (BCC) crystal, denoted ${}_c\boldsymbol{M}_n^{-1}$ [43]. This strain is expressed as follows:

$$ {}_n\boldsymbol{E}_c^{-1} = \left({}_c\boldsymbol{P}_n^{-1} -_c \boldsymbol{M}_n^{-1}\right). \tag{1.3.5} $$

In the case depicted in Figure 1.12, the deformation along the x and y axes can be approximated by the difference in interatomic distances between the FCC and BCC structures, denoted $d_{xx}^{\alpha,\gamma}$ and $d_{yy}^{\alpha,\gamma}$, relative to the average interaction distance in each of these directions. Therefore, an estimation of the deformation along the directions $\langle 0\,1\,\bar{1}\rangle_\gamma \,||\, \langle 1\,\bar{1}\,1\rangle_\alpha$ can be expressed as:

$$ \varepsilon_{xx}^{tot} = 2\left(d_{xx}^{\gamma} - d_{xx}^{\alpha}\right) / \left(d_{xx}^{\gamma} + d_{xx}^{\alpha}\right), \tag{1.3.6} $$

and the deformation along directions $\langle 1\,1\,\bar{2}\rangle_\gamma \,||\, \langle 0\,1\,\bar{1}\rangle_\alpha$ is:

$$ \varepsilon_{yy}^{tot} = 2\left(d_{yy}^{\gamma} - d_{yy}^{\alpha}\right) / \left(d_{yy}^{\gamma} + d_{yy}^{\alpha}\right). \tag{1.3.7} $$

A compression of the FCC structure along the direction $\langle 0\,1\,\bar{1}\rangle_\gamma$ and a dilatation along the direction $\langle 1\,1\,\bar{2}\rangle$ should both be observed at coherent terraces. Using the same lattice parameters for pure iron as for the PTMC model, i.e, $a_\alpha = 0.286$nm and $a_\gamma = 0.356$nm, yields $\varepsilon_{xx}^{tot} = -12.7\%$ and $\varepsilon_{yy}^{tot} = 7.50\%$, which means a compression of the FCC structure along $\boldsymbol{x}$ and a dilatation along $\boldsymbol{y}$.

The second step in the TM is the identification of the disconnections and lattice invariant dislo-

cations (LID) that can form, depending on the coherent state. This is achieved using the topological theory of interfacial defects [43, 66]. The fundamental requirements are that each set of disconnections and dislocations must be glissile within the terrace plane, and the intersection between the disconnection and the LID should be glissile as well. The topological parameters of dislocations and disconnections applied to the FCC to BCC phase transformation [43] are presented in Table 1.4. In this table, misfit dislocations are denoted as $\boldsymbol{b}_1$ and $\boldsymbol{b}_2$, while disconnections are denoted as $\boldsymbol{b}_{-1/-1}$, $\boldsymbol{b}_{-2/-2}$, and $\boldsymbol{b}_{+1/+1}$, with the subscript indicating the step height in the FCC and BCC phases, as in [43].

Defect	$\boldsymbol{b}_\gamma$	$\boldsymbol{b}_\alpha$	h
$\boldsymbol{b}_1$	$\frac{1}{2}[1\,0\,1]_\gamma$	$\frac{1}{2}[1\,\bar{1}\,1]_\alpha$	0
$\boldsymbol{b}_2$	$\frac{1}{2}[\bar{1}\,0\,1]_\gamma$	$\frac{1}{2}[\bar{1}\,\bar{1}\,1]_\alpha$	0
$\boldsymbol{b}_{-1/-1}$	$\frac{1}{2}[\bar{1}\,\bar{1}\,0]_\gamma$	$\frac{1}{2}[1\,\bar{1}\,\bar{1}]_\alpha$	-1
$\boldsymbol{b}_{-2/-2}$	$\frac{1}{2}[\bar{2}\,\bar{1}\,\bar{1}]_\gamma$	$[0\,1\,1]_\alpha$	-2
$\boldsymbol{b}_{+1/+1}$	$\frac{1}{2}[0\,1\,1]_\gamma$	$\frac{1}{2}[\bar{1}\,1\,1]_\alpha$	$+1$

Table 1.4: Dislocations and disconnections proposed by the TM at FCC-BCC interface [43].

The final step of the TM is related to the determination of line directions and spacings of the arrays of disconnections and LIDs that accommodate the coherency elastic strain. This is achieved using the Frank-Bilby equation [67], which provides the theoretical total Burgers vector $\boldsymbol{b}_{\text{tot}}$ of all interfacial defects whose line directions intersect a 'probe' vector $\boldsymbol{v}$ lying in the interface. This probe vector is defined as a vector in the plane of the interface, which helps determining the displacement field cause by dislocations. The Frank-Bilby equation is expressed as follows :

$$\boldsymbol{b}_{\text{tot}} = \mathrm{F}\boldsymbol{v}, \tag{1.3.8}$$

with F representing the closure failure of the Burgers circuit. In the case where no additional rotation was applied after the coherency strain was defined, it is expressed as $\mathrm{F} = -{}_{\mathrm{n}}\mathrm{E}_{\mathrm{c}}$ [43]. The Topological Model considers the NW OR when defining the coherent and natural states. To obtain the others ORs, such as KS or GT, a supplementary rotation is applied. The Frank-Bilby equation is then applied to each predetermined disconnection, allowing the determination of their line directions and the spacing between arrays. Moreover, the TM can calculate a theoretical habit plane for each chosen array of defects. The solution to the Frank-Bilby equation is not unique, which allows the unique description of different cases associated with various solutions to this equation. Therefore iterative refinements of solutions must be made to achieve accurate results.

The TM has been specifically applied to describe the FCC to BCC martensitic transformation [43]. In this study, a set of LID and disconnections leading to a semi-coherent interface, where migration occurs through the lateral motion of disconnections. By selecting one set of LID and one set

of disconnections, such as the $\boldsymbol{b}_1$ LID with the $\boldsymbol{b_{-1/-1}}$ disconnection, specific habit planes, mostly of the form (a, b, a), were computed. Notably, solutions consistent with the $\{2\,9\,5\}_\gamma$, $\{1\,2\,1\}_\gamma$, and $\{5\,7\,5\}_\gamma$ habit planes in various ferrous alloys were obtained [4, 5, 14, 43, 55, 68].

While the stepped interface model with two sets of defects proposed by the TM qualitatively describes the FCC to BCC transformation interface, it requires strong assumptions about the nature of dislocations and disconnections at the interfaces.

1.4 FCC to BCC transformation mechanism

Since the 1950s, several theories have sought to explain the mechanism of displacive FCC to BCC transformation, with one of the earliest being the Bain path [42], as discussed in Section 1.2. While the Bain path give some basic ideas to understand the FCC to BCC phase transformation, it does not fully describes the atomic displacement involved in this transformation. Nowadays, two major models describing the transformation path are used: the Kurdjumov-Sachs (KS) [39, 46, 69] and the Bogers-Burgers-Olson-Cohen (BB/OC) transformation mechanisms [40, 41].

1.4.1 Kurdjumov-Sachs (KS)

The KS mechanism posits that the FCC to BCC transformation results from the action of two shear displacements. While the directions of these shears depend on the specific KS OR variant, the underlying mechanism remains consistent across all variants. In this section, the shear directions will be described for the first KS variant (KS v1) only.

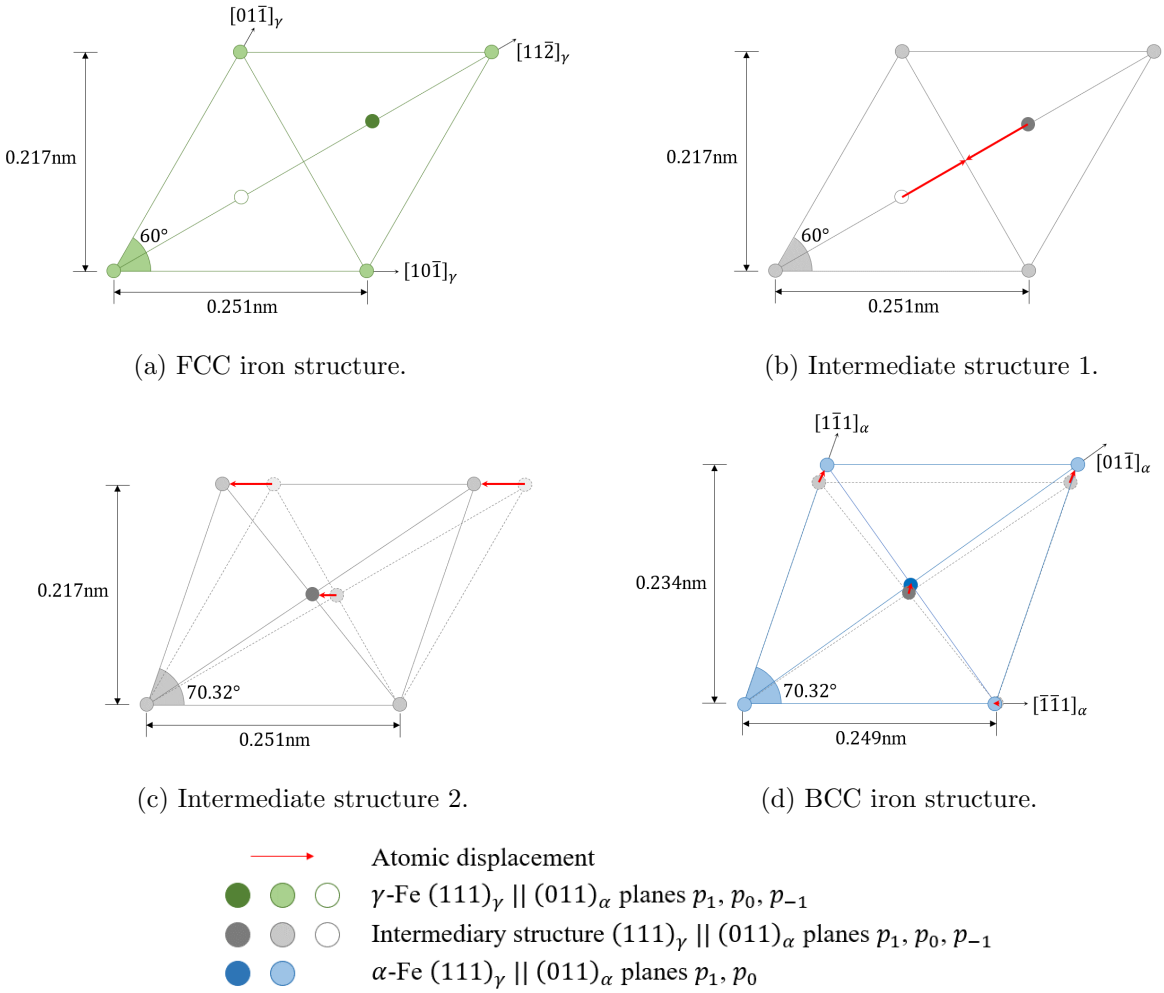

(a) FCC iron structure.

(b) Intermediate structure 1.

(c) Intermediate structure 2.

(d) BCC iron structure.

Figure 1.13: Schematic representation of the KS transformation mechanism from the FCC lattice (green) to the BCC lattice (blue), through intermediate lattices (gray). Color coding also indicates the sequence of three $(1\,1\,1)_\gamma$ planes along the $\boldsymbol{z}$ direction: p_1 plane is dark, p_0 plane is light and p_-1 plane is empty. Dashes are used when two structures are superimposed to indicate the initial lattice. The chosen lattice parameter for the FCC phase is $a_\gamma = 0.365$nm.

The complete KS transformation mechanism for the KS v1 OR is illustrated in Figure 1.13, where p_1, p_0 and p_{-1} corresponds to the sequence of three $(1\,1\,1)_\gamma$ planes along the $\boldsymbol{z}$ direction. The first shear occurs along the direction $[1\,1\,\bar{2}]_\gamma$ in $(1\,1\,1)_\gamma$ planes p_1 and p_{-1}, as shown in Figure 1.13a. This induces the transformation from an ABCABC sequence of close-packed $(1\,1\,1)_\gamma$ FCC planes in planes p_1 and p_-1 to an ABAB sequence corresponding to the HCP structure. The second shear occurs along the direction $[1\,0\,\bar{1}]_\gamma$ within $(1\,1\,1)_\gamma$ planes, as illustrated in Figure 1.13c. This shear results in the transformation of the FCC rhombic cell in the $(1\,1\,1)_\gamma \,||\, (0\,1\,1)_\alpha$ plane into the corresponding BCC cell. The FCC to BCC transformation is completed by an expansion along the $[1\,\bar{1}\,1]_\alpha$ and $[0\,1\,1]_\alpha$ directions, as depicted in Figure 1.13d, accompanied by a minor compression

along the $[\bar{1}\,\bar{1}\,1]_\alpha$ direction. While these shears are presented as sequential steps in Figure 1.13, in reality, they occur simultaneously, resulting in the displacement pattern of the KS mechanism illustrated in Figure 1.14a.

The KS transformation mechanism was reinterpreted by Nishiyama as the KSN mechanism [46, 69] to explain the FCC to BCC phase transformation with the Nishiyama-Wasserman orientation relationship (NW OR). The KSN mechanism (see Figure 1.14c) involves the same first shear along the direction $[1\,1\,\bar{2}]_\gamma$ in the p_1 and p_{-1} $(1\,1\,1)_\gamma$ as the KS. However, the second shear displacement of the KS mechanism is replaced by a so-called stretch displacement which can be seen as the summation of the second shear displacements of the first and the sixth variants of the KS mechanism. More generally, the KSN mechanism can be seen as the addition of the first and sixth variant KS v1 and KS v6, depicted on Figure 1.14b, of the KS mechanism.

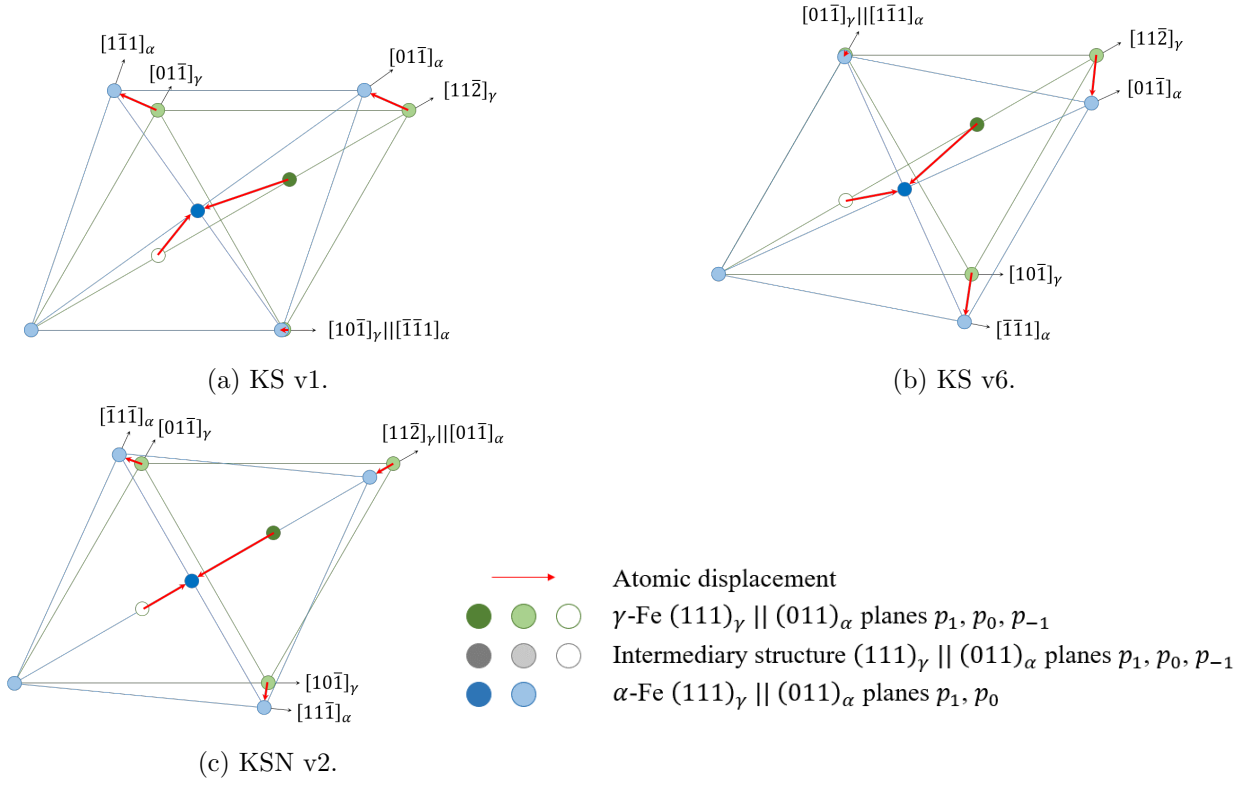

(a) KS v1.

(b) KS v6.

(c) KSN v2.

Figure 1.14: Schematic representation of **(a)** the total KS v1 of the KS transformation mechanism, **(b)** the total KS v6 of the KS transformation mechanism, **(c)** The total KSN v2 of the KSN transformation mechanism.

The KS and KSN mechanisms were proposed before the introduction of partial dislocation theories. However, they are not incompatible with the presence of partial dislocations [70]. The glide of $\frac{a_\gamma}{6}[1\,1\,\bar{2}]_\gamma$ Shockley partials is consistent with the $[1\,1\,\bar{2}]_\gamma$ shearing illustrated in Figure 1.14. In the case of the shear displacement along $[1\,0\,\bar{1}]_\gamma$, it can be achieved by the glide of screw

dislocations $[1\,0\,\bar{1}]_\gamma$ in $(1\,1\,1)_\gamma$ plane. This observation will be further explored in the context of experimental findings and atomistic simulations related to the FCC to BCC phase transformation.

1.4.2 Bogers-Bugers-Olson-Cohen

According to the BB/OC model [40, 41], the shear required to transform an FCC lattice into a BCC one require the presence of two different Shockley partials, corresponding to two shear systems (Figure 1.15a). The first shear displacement is $a_\gamma/18\,[\bar{1}\,2\,\bar{1}]_\gamma$. This shear can be achieved by an array of $a_\gamma/6\,[\bar{1}\,2\,\bar{1}]$ Shockley partial dislocations in every third $(1\,1\,1)_\gamma$ plane, shown by the orange plane in Figure 1.15a. The second shear is $a_\gamma/12\,[1\,\bar{2}\,\bar{1}]_\gamma$. It can be achieved by an array of $a_\gamma/6\,[1\,\bar{2}\,\bar{1}]_\gamma$ Shockley partials in every second $(1\,1\,\bar{1})_\gamma$ plane, shown by the blue plane in Figure 1.15a.

The presence of the two Shockley partials dislocations alters the stacking of the system, as described in Section 1.3.1. In the BB/OC model, the overall phase transformation involves the formation of an intermediate HCP phase, during the FCC→HCP→BCC [41, 71] transition. As shown in Figure 1.15b, the BB/OC transformation mechanism can be described as the creation of two HCP lattices, ε_1 and ε_2, in blue, which form the BCC phase at their intersection, in orange.

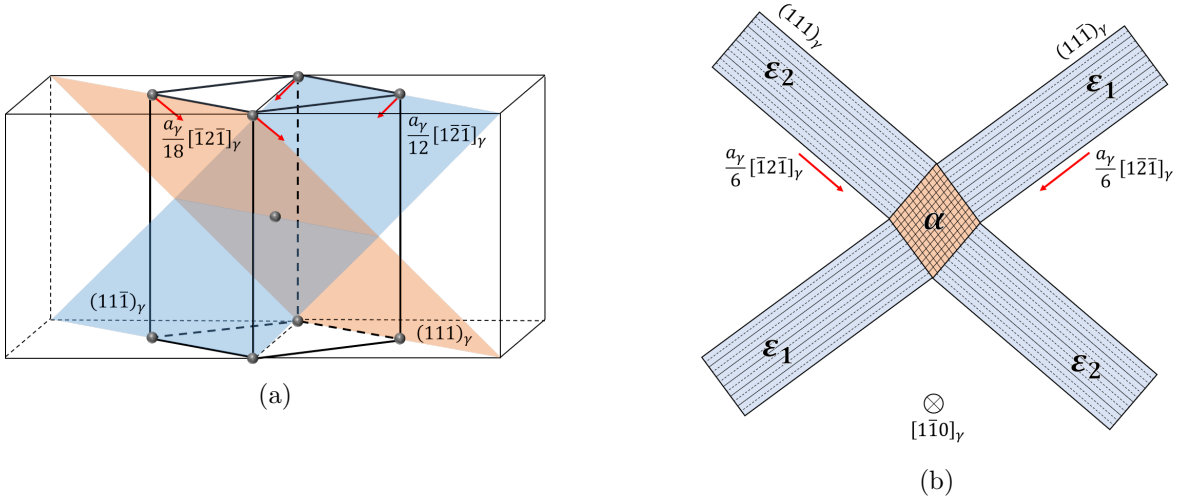

Figure 1.15: Schematic of the FCC→HCP→BCC BB/OC transformation mechanism. (**a**) Shear system in the austenite lattice. (**b**) Transformation mechanism viewed in the $(1\,\bar{1}\,0)_\gamma$ plane. The BCC phase is formed at the intersection of two HCP plates.

It is noteworthy that the KS transformation path also involves the formation of an intermediate HCP phase. The difference between KS and BB/OC models lies in the appearance of two HCP plates with different orientations generated by two distinct sets of Shockley partial dislocations. While the BB/OC mechanism does not involve shear along the directions $[1\,0\,\bar{1}]_\gamma||[1\,1\,\bar{1}]_\alpha$, dislocations with Burgers vectors $\frac{a_\alpha}{2} = [1\,1\,\bar{1}]_\alpha$ in the BCC phase can be observed, as these dislocations can dissociate into Shockley partials in FCC to facilitate the BB/OC phase transformation. A careful

assessment of the atomic displacements at the interface will therefore be necessary to distinguish between the KS and BB/OC mechanisms, as both involve similar dislocations.

1.5 Atomistic modeling of the FCC to BCC phase transformation

Modeling and simulation tools proved useful to confirm, refine or even inspire theoretical predictions, as well as interpret or even surrogate experiments on martensitic transformations. Computer modeling of FCC-BCC interface structures began as early as 1979 with the work of Rigsbee et al. [72]. Using geometrical models based on the Moiré pattern such as O-lattice theory [73], it was demonstrated that the misfit stress induced by the lattice mismatch between the FCC and the BCC structures at the interface could be relieved by the incorporation of structural ledges (dislocation+step) and arrays of misfit dislocations at the interface. Although it provides a first numerical modeling of the FCC-BCC interface, the predicted misfit dislocations were shown to be unable to glide with the interface, making the athermal propagation of the FCC-BCC interface impossible, in contradiction with the theory of martensitic transformation.

Although manifold numerical models were developed since then to simulate the FCC to BCC transformation, both at the mesoscale with the phase-field model (PFM) [74–76], and at the atomic scale with the Monte Carlo (MC) and Kinetic Monte Carlo (KMC) approaches [17, 18], molecular dynamics (MD) is now the baseline numerical tool to study displacive/martensitic structural transformations. In this approach, the trajectories of particles (atoms, molecules etc.) are determined by numerically solving Newton's equations of motion. For that purpose, the forces between particles are calculated from an interaction potential, which replaces the true interatomic interactions with a simplified parametric model. Several classes of interaction potentials with different functional forms have been developed, including Pair-wise potentials such as Lennard-Jones and Morse potentials [77], and many-body potentials such as the Embedded Atom Method (EAM) [78] and an empirical extension of the EAM called the Modified Embedded Atom Method (MEAM) [79]. In the EAM/MEAM potentials, the energy of the atom is given by the energy associated with the electron density of the atom plus a constant background density which represents the energy needed to 'embed' an atom into the electron density contributed by all the surrounding atoms. EAM/MEAM potentials are particularly suitable for metals, as they accurately replicate the vibrational properties of the material [80–83]. MD models equipped with this class of potentials was specifically applied to the austenite-ferrite and austenite-martensite transformations in pure Iron, low carbon steels and ferrous alloys [10–16].

A complete description of the FCC to BCC phase transformation includes the structure of the interface, the propagation mode and mobility of the interface, and the FCC to BCC transformation path. The present section thus provides an thematic overview of the numerical treatment of these three salient features of the FCC to BCC phase transformation, using MD.

1.5.1 Interface structure

First, Maresca et al. [14] confirmed the standard model of a one-stepped FCC-BCC interface reticulated by arrays of misfit dislocations depicted in Figure 1.10. In this work, different lattice misfit ratios $\frac{a_\gamma}{a_\alpha}$ ranging from 1.25 to 1.27, which is typical in low alloy steels and ferrous alloys, as well as various ORs such as KS and NW and various HPs such as $(1\,2\,1)_\gamma$ and $(5\,7\,5)_\gamma$ were considered. As a result, terrace steps in the $[\bar{1}\,0\,1]_\gamma$ with step heights of one or several $(1\,1\,1)_\gamma$ interplanar spacings could be observed in every case.

Alternatively, Tateyama et al. [10], Ou et al. [12, 13], and Tripathi et al. [16] focused on the FCC to BCC phase transformation in pure Iron for the NW and KS ORs. Although the formation of steps at the FCC-BCC interface was not directly assessed in these studies, the atomic potential energy map at the matching area of the FCC-BCC interface (see Figure 1.16) provided a first insight on the underlying structural symmetry of the interface. As can be seen in Figure 1.16b, a characteristic diamond-shaped pattern could be observed for the NW OR. In details, the matching areas between FCC and BCC regions are highlighted by red circles. They correspond to regions of low potential energy. On the contrary, higher potential energy (light blue and green), is observed in low coherency regions. This diamond-shaped pattern could lead to two arrays of disconnections in the $[\bar{1}01]_\gamma$ and $[0\bar{1}1]_\gamma$ directions. For the KS OR (Figure 1.16a), the potential energy pattern at the interface differs significantly. Elongated regions of high coherency, marked by red ellipses and relatively low interfacial energy, suggest the formation of extended terraces along this direction, with a single step defining their boundary. This observation aligns with the single-step interface model presented in the previous section. While a double-stepped interface was not directly confirmed in their studies, it appears to be a possibility for orientations close to the NW OR. On the contrary, the usual one stepped profile could be recovered for the KS OR.

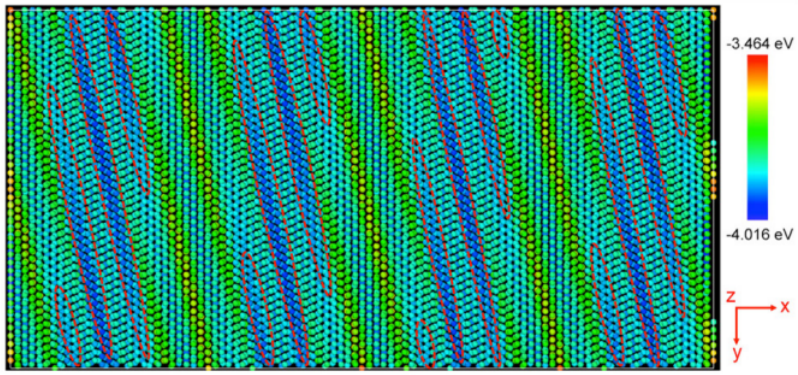

(a) KS OR

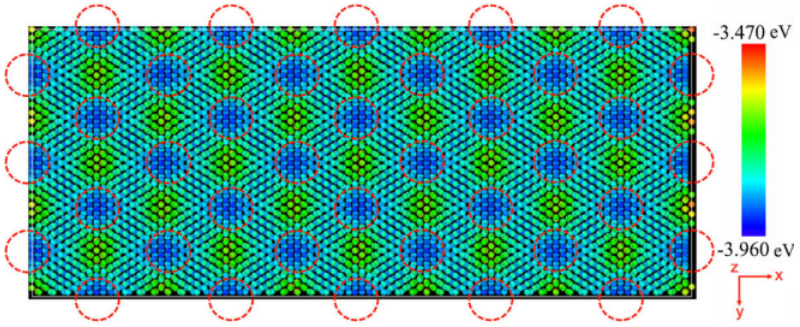

(b) NW OR

Figure 1.16: Superposed view of NW and KS ORs showing the $(1\,1\,1)_\gamma$ and $(0\,1\,1)_\alpha$ planes at the matching area of the interface from Ou et al. [12]. Atoms are colored according to their potential energy.

1.5.2 Interface dislocations

Different sets of screw dislocations with Burgers vectors of the type $\frac{a_\gamma}{2}\langle 1\,0\,1\rangle_\gamma$ have been observed in numerous MD simulations [10–14, 16]. In these studies, a first set of screw dislocations with $\frac{a_\gamma}{2}[\bar{1}\,0\,1]_\gamma$ Burgers vector was consensually detected alongside terrace steps. It should also be noted that a deviation from the prefect $\langle 1\,0\,1\rangle_\gamma$ was observed in [14] due to the presence of dislocation kinks. Finally, this first dislocation was located in the FCC phase in [14], but not in [16]. The spacing between arrays of this first set of disconnections was systematically determined, depending on the lattice parameter misfit ratio between the FCC and BCC phases, and the OR. In [14], a distance of 1.45 nm between two successive steps was found for a 1.254 misfit ratio and an OR close to NW, in good agreement with previous high-resolution electron microscopy (HRTEM) measurements (1.33 nm) [56].

A second set of dislocations was also identified in the aforementioned MD studies, except for the KS OR. In [14], this second set of dislocations was found to be bcc kinked screw dislocations with $\frac{a_\alpha}{2}[1\,\bar{1}\,1]_\alpha$ Burgers vector, which accommodate the misorientation between the $[\bar{1}\,0\,1]_\gamma$ and $[\bar{1}\,\bar{1}\,1]_\alpha$ directions when the OR is different from KS. The same second set of screw dislocations

was observed in [16] for the NW OR, but not necessarily in the BCC phase. In addition, they were not treated as misfit compensating dislocations, but rather transformation dislocations that contribute to the propagation of the FCC-BCC interface in the same way as the first set of screw dislocations. The spacing between these defects was measured [14], where it varies from 1.2 nm to 4 nm, depending on the OR (except KS) and the lattice misfit ratio. For the KS OR, it was found in [14] that the second set of dislocations disappears due to the perfect alignment between $[\bar{1}\,0\,1]_\gamma$ and $[\bar{1}\,\bar{1}\,1]_\alpha$ dense directions. It was then suggested that this second set of screw dislocations are actually replaced by BCC edge dislocations with $\frac{a_\alpha}{2}[1\,\bar{1}\,1]_\alpha$ Burgers vector in this case. However, only few experimental studies support this conclusion [4], while these BCC edge dislocations were not detected elsewhere [5].

The presence of partial dislocations at the FCC-BCC interface has also been observed in several molecular dynamics simulations [12, 13, 16, 84]. In [16], it was suggested that the presence of stacking faults bordering ribbons of HCP phase, result from the action of partial dislocations with Burgers vectors in the $\langle 1\,1\,2\rangle_\gamma$ direction in FCC. The presence at the FCC-BCC interface of Shockley partials with a $\frac{a_\gamma}{6}\langle 1\,1\,\bar{2}\rangle_\gamma$ Burgers vector was also observed in [13].

1.5.3 Interface mobility

In [10–14, 16], it was consensually concluded that the glide of the two sets of screw dislocations carries the propagation of the FCC-BCC interface. However significant differences can be found between these studies. First, it was found in [16] that both the first and second set of screw dislocations glide in the same $(1\,1\,1)_\gamma \parallel (0\,1\,1)_\alpha$ slip plane, while the second set of dislocations was found to glide in the $(\bar{1}\,0\,1)_\alpha$ plane in [14].

Moreover, edge-character kinks lying in the glide plane of both the first and second set of screw dislocations were observed in [14], whereas it was not mentioned in [12, 13, 16]. In [14], it was argued that edge-character kinks lying in the glide plane of the screw dislocation can move at very low stress levels, which facilitate the glide of screw dislocations through side-wise kink motion. On the contrary, they showed that the absence of kinks at the interface can impede the propagation of the FCC-BCC interface. This is the case of the KS OR, where only the first set of screw dislocations with $[1\,0\,\bar{1}]_\gamma$ Burgers vector remained, but effectively collapsed to a straight (not kinked) bcc screw dislocation, which has high Peierls stress, and is thus sessile. It should be noted that the presence of kinks was detected in other MD studies on pure iron. For instance, Tateyama et al. [10] observed kinks forming as part of the disconnections at the interface, and concluded that these kinks contribute to the propagation of screw dislocations along these ledges. Similar kinks at terrace ledges were also envisioned in [11].

Finally, dislocation glide is not the only possible mode of dislocation propagation, dislocation climb can also occur. Dislocation climb is a purely diffusive mode of propagation, where the

dislocation moves due to vacancy diffusion within the material. Although it is not compatible with a purely displacive transformation, it still needs to be considered in the FCC to BCC phase transformation, as a temperature dependence of interface mobility has been observed by Bos et al. using molecular dynamics simulations [85]. Additionally, they showed that differences in interface velocities also depend on the OR, with velocities ranging from 200 to 700 m/s.

1.5.4 FCC to BCC transformation mechanism

In [16], two different FCC to BCC transformation paths were observed for the NW OR and $(1\,1\,1)_\gamma$ flat interface. First, the KS transformation mechanism was identified in the areas of maximum slip for the first and second sets of screw dislocations, through characteristic shear displacements alongside $\frac{a_\gamma}{2}\langle 1\,0\,1\rangle_\gamma$ dense directions. These displacements are highlighted by the red ellipses on the segments of the diamond-shaped unit shown in Figure 1.17.

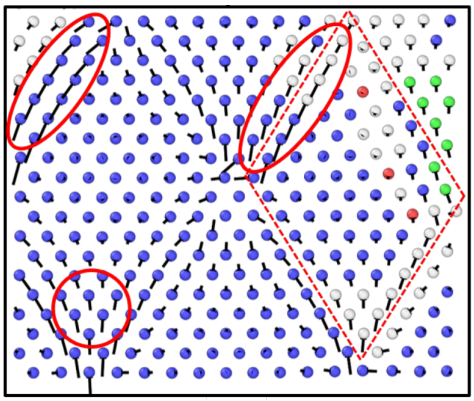

Figure 1.17: Atomic displacements observed during the FCC to BCC transformation using molecular dynamics simulation in Tripathi et al. [16]. Major regions of atomic displacement are circled in red and the diamond unit pattern is showcased by dotted lines. Blue: BCC, green: FCC, red: HCP, white: perturbed structure.

Large amplitude displacements in the $\langle 1\,1\,\bar{2}\rangle_\gamma$ direction were also observed at the intersections of the two screw dislocations (red circle in Figure 1.17). Because these displacements match the second $a_\gamma/12\,[1\,\bar{2}\,\bar{1}]_\gamma$ shear displacements induced by the $a_\gamma/6\,[1\,\bar{2}\,\bar{1}]_\gamma$ Shockley partial in the BB/OC transformation mechanism, it was concluded in [16] that the BB/OC is the second transformation path involved in the FCC to BCC transformation for the NW OR. In [12, 13] and [84], only the BB/OC mechanism was explicitly mentioned, but the exact same displacements patterns as in [16] were envisioned, thereby consistently supporting the paradigm of the concurrent action of the KS and the BB/OC mechanism for the FCC to BCC transformation. It should finally be mentioned, that no transformation path was proposed in [14].

1.6 Experimental observations of the FCC to BCC phase transformation

The experimental data on the FCC to BCC phase transformation provides valuable insights on the interface structures, defects, and mobility. It should be noted that most experimental observations of the FCC to BCC phase transformation have been conducted on iron alloys, while molecular dynamics simulations results primarily focus on pure iron. This section will follow a structure similar to that of the atomistic modeling section.

1.6.1 Interface structure

In experimental observations of the FCC to BCC transformation, consistent features emerge across studies on iron alloys. Sandvik and Wayman [55, 56, 86, 87] conducted an in-depth study of the crystallography and substructural features of low-carbon steels and Fe-Ni-Mn alloys using transmission electron microscopy (TEM). In Fe-20Ni-5.5Mn steels [87], they observed an irrational habit plane close to $(5\,7\,5)_\gamma$ for an orientation relationship that was deviated by 3.9° from the KS OR, thus positioned between the NW and GT ORs. The observed interface was stepped, with planar $(1\,1\,1)_\gamma||(0\,1\,1)_\alpha$ terraces. Also, the presence of misfit dislocations was confirmed. In [56], the step spacing was measured at approximately 1.3 nm.

Similar interface morphologies were detected by Moritani et al. [4] in Fe-0.6C-2Si-1Mn wt% and lath martensite Fe-20Ni-5.5Mn wt% using HRTEM. Despite differences in composition and thermal treatment, both alloys presented habit planes around $(1\,2\,1)_\gamma$ plane. The orientation relationships scattered around the KS, NW, and GT ORs. In each case, monoatomic steps with $(1\,1\,1)_\gamma||(0\,1\,1)_\alpha$ were observed, as shown in Figure 1.18. Although the terrace spacing was not quantitatively measured, using Figure 1.18, is can be estimated to be less than 1 nm. These narrow terraces are observed in the case of a 19.47° angle between the habit plane normal and the $[1\,1\,1]_\gamma$ direction. By comparison, wider steps observed in molecular dynamics simulations [14] occur for smaller angles (11.42°) between the habit plane and the $[1,1,1]_\gamma$ direction.

Ogawa and Kajiwara in [5, 6] investigated several iron alloys using HRTEM. In [5], they studied an Fe-23.0Ni-3.8Mn wt%, an Fe-30.5Ni-10Co-3Ti wt% and an Fe-8.8Cr-1.1C wt% alloys with OR ranging from KS to NW and a $(1\,2\,1)_\gamma$ HP for all alloys. In [6], they focused on Fe-23Ni-3.8Mn wt% and an Fe-9Cr-1.1C wt% alloy, both having a KS OR and $\{1\,1\,2\}_\gamma$ HP. Across all these different alloys, the interface structure remained consistent, exhibiting $(1\,1\,1)_\gamma||(0\,1\,1)_\alpha$ terraces and arrays of dislocations. However, contrary to Mortani et al. HRTEM observation [4], they measured steps that are several $(1\,1\,1)_\gamma||(0\,1\,1)_\alpha$ plane. This is consistent with the topological model [43], where disconnection exhibiting step character of several $(1\,1\,1)_\gamma||(0\,1\,1)_\alpha$ plane were considered.

As reported in the literature, most FCC to BCC transformation interfaces in iron alloys, have

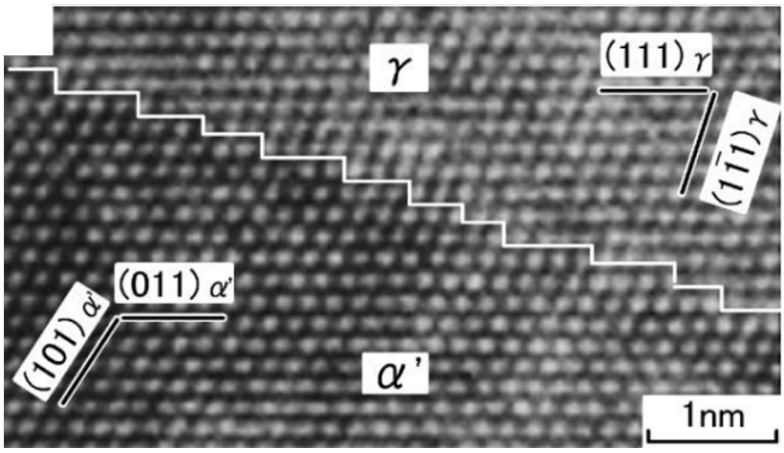

Figure 1.18: HREM micrograph of Fe-20Ni-5.5Mn steel, showing the broad face of lath martensite viewed along $[\bar{1}\,0\,1]_\gamma \,||\, [\bar{1}\,\bar{1}\,1]_\alpha$ [4].

HPs ranging between $(5\,7\,5)_\gamma$ and $(1\,2\,1)_\gamma$ planes and ORs that range from KS to NW. However, in some alloys, different ORs such as GT are also observed. All these interfaces consistently exhibit a stepped nature with dislocations or disconnections [2, 4, 5, 55, 56, 86–90].

1.6.2 Interface dislocations

Interface dislocations were also prospected experimentally. Sandvik and Wayman [55, 56, 86, 87] identified the presence of screw dislocations with Burgers vectors in the direction $\langle\bar{1}\,\bar{1}\,1\rangle_\alpha$ in Fe-20Ni-5Mn steels. They observed a single set of parallel screw dislocations, using dark field imaging, with a Burgers vector of $\frac{a_\gamma}{2}[0\,\bar{1}\,1]_\gamma||\frac{a_\alpha}{2}[1\,\bar{1}\,1]_\alpha$. Notably, they found that the dislocation lines deviated by about 10° to 15° from the pure screw orientation, suggesting the presence of kinks along the dislocation line. At the atomic scale, the dislocations were pure screw, but they deviated from an exact screw orientation macroscopically due to the stepped structure of the interface. The spacing between dislocation arrays ranged from 2.6 nm to 6.3 nm. These observations were further confirmed by Ogawa and Kajiwara [5, 6], who detected dislocations with Burgers vectors of $\frac{a_\gamma}{2}\,[\bar{1}\,0\,1]_\gamma$ or $\frac{a_\alpha}{2}\,[\bar{1}\,\bar{1}\,1]_\alpha$ in Fe-23.0Ni-3.8Mn, Fe-30.5Ni-10Co-3Ti and Fe-8.8Cr-1.1C alloys.

Moritani et al. [4] observed similar kinked screw dislocations with a Burgers vector of $\frac{a_\alpha}{2}\langle\bar{1}\,\bar{1}\,1\rangle_\alpha$ in lath martensite Fe-20Ni-5.5Mn alloy using dark field imaging. From the HRTEM observations, they deduced two types of perfect screw dislocations: $\boldsymbol{b}_1 = \frac{a_\gamma}{2}[0\,\bar{1}\,1]_\gamma||\frac{a_\alpha}{2}[1\,\bar{1}\,1]_\alpha$ and $\boldsymbol{b_2} = \frac{a_\gamma}{2}[\bar{1}\,0\,1]_\gamma||\frac{a_\alpha}{2}[\bar{1}\,\bar{1}\,1]_\alpha$ that accommodate the shear strain. Notably, the $\boldsymbol{b}_1$ dislocation was observed along the step ledge described earlier. They concluded that the macroscopic habit plane consists of monoatomic steps, corresponding to the $\boldsymbol{b}_1$ and $\boldsymbol{b_2}$ transformation dislocations observed. However, they did not perform HRTEM imaging along the $[0\,\bar{1}\,1]_\gamma$ direction to observe potential steps associated with the $\boldsymbol{b_2}$ dislocation, making this conclusion incomplete. Moreover, Moritani et al. proposed a schematic representation of atomic matching in $(1\,1\,1)_\gamma$ plane. In Figure 1.19, the

diamond-shaped pattern due to atomic matching for NW ORs, which highlights dislocations $\boldsymbol{b}_1$ and $\boldsymbol{b_2}$ along the regions of atomic mismatch indicated by the black lines.

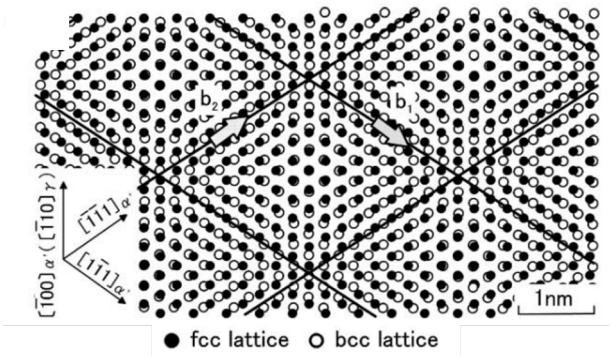

Figure 1.19: Atomic matching on the $(1\,1\,1)_\gamma||(0\,1\,1)_\alpha$ plane when NW OR is held [4].

These dislocations were also detected in alloys with KS OR. It was concluded that, while the $\boldsymbol{b_2} = \frac{a_\gamma}{2}[\bar{1}\,0\,1]_\gamma$ dislocations remained nearly perfect screw types, as observed in NW OR, the $\boldsymbol{b}_1 = \frac{a_\gamma}{2}[0\,\bar{1}\,1]_\gamma$ dislocations exhibited a mixed character, with their line direction close to $[\bar{1}\,0\,1]_\gamma$. Using O-lattice calculations, they demonstrated that the line direction $\boldsymbol{D_1}$ of $\boldsymbol{b}_1$ dislocations gradually deviates as the θ angle between $[\bar{1}\,0\,1]_\gamma$ and $[\bar{1}\,\bar{1}\,1]_\alpha$ directions decreases from 5.26° for NW OR to 0° for KS OR (see Figure 1.20).

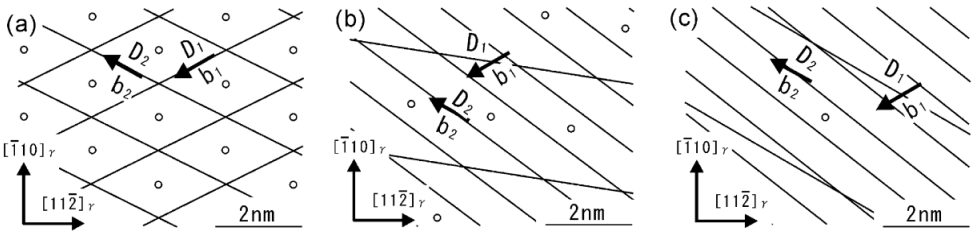

Figure 1.20: O-lattice calculation from Mortani et al. [4] for $(1\,1\,1)_\gamma||(0\,1\,1)_\alpha$ interface with a misorientation θ between $[\bar{1}\,0\,1]_\gamma$ and $[\bar{1}\,\bar{1}\,1]_\alpha$. **(a)** $\theta = 5.26°$ (NW OR), **(b)** $\theta = 1°$, **(c)** $\theta = 0°$ (KS OR). The Burgers vectors are $\boldsymbol{b}_1 = \frac{a_\gamma}{2}[0\,\bar{1}\,1]_\gamma$ and $\boldsymbol{b_2} = \frac{a_\gamma}{2}[\bar{1}\,0\,1]_\gamma$.

The observations and conclusions from Moritani et al. [4] align well with the molecular dynamics simulations conducted by Tripathi et al. [16]. Both studies reveal a similar diamond-shaped dislocation pattern in the $(1\,1\,1)_\gamma$ plane for the NW OR at the interface. In particular, Tripathi et al. highlighted major atomic displacements occurring along the $\boldsymbol{b}_1$ and $\boldsymbol{b_2}$ dislocations, highlighting their crucial role in the transformation process.

Partial dislocations were also observed in some experiences, notably in [2] in an Fe-8Cr-1C wt % alloy. Using HRTEM imaging, they visualized Shockley partial dislocations with a Burgers vector

of $\frac{a_\gamma}{6}\langle 1\,1\,2\rangle_\gamma$. Additionally, they observed two structural ledges associated with these dislocations, which had Burgers vectors of $\frac{a_\gamma}{12}[1\,1\,2]_\gamma$ or $\frac{a_\gamma}{12}[2\,\bar{1}\,1]_\gamma$. They concluded that the interface movement was achieved by the glide of these dislocations on each close-packed plane.

In summary, both experimental observations and simulation results consistently observed perfect dislocations $\frac{a_\gamma}{2}[1\,0\,\bar{1}]_\gamma$ and $\frac{a_\gamma}{2}[0\,1\,\bar{1}]_\gamma$ The first set of dislocations aligns with the terrace step direction. However, the nature of the second set of dislocations remains unclear. Additionally, partial dislocations with Burgers vector $\frac{a_\gamma}{6}[1\,1\,\bar{2}]_\gamma$ have been detected, playing a role in the transition from the FCC stacking of $(1\,1\,1)_\gamma$ dense planes to the BCC stacking of $(0\,1\,1)_\gamma$ dense planes.

1.6.3 Interface mobility

The interface mobility during FCC to BCC phase transformations has also been investigated using various experimental techniques. In studies of the transformation dynamics at the austenite-ferrite interface in Fe-C-Mo alloys [91], two types of interfaces were identified: a featureless, highly mobile interface and a less mobile, faceted interface associated with the KS OR. In addition to the transformation mechanisms described mostly for pure iron in this chapter, other processes might take place due to the presence of alloying elements and their interactions, which could influence the phase transformation kinetics, defect formation, and interface mobility. A more recent study on dual-phase steels revealed similar findings: a highly mobile interface far from KS OR and a less mobile interface close to KS OR [7]. Understanding the causes of these observations in these alloys is challenging, as both the structure of the interface and the diffusion of alloying elements play significant roles in the austenite to ferrite phase transformation. This particular aspect of the transformation will be explored in greater detail in Section 1.7.

1.6.4 FCC to BCC transformation mechanism

In spite of the extremely high velocity associated with displacive phase transformations, experimental techniques have been applied to study the FCC to BCC transformation mechanism. Some experimental results appear to support a KS mechanism. The HRTEM has been applied by Kajiwara et al. [3] to investigate the austenite to ferrite phase transformation in an Fe-23.0Ni-3.8Mn alloy. In this study, it was suggested that the phase transformation in this alloy can be described by the KS mechanism. They found that the shear amplitude along $[\bar{1}\,2\,\,1]_\gamma$ direction on $(1\,1\,\bar{1})_\gamma$ plane was greater than that proposed by the BB/OC model, matching more closely the shear described in the KS model. Additionally, they did not observed any disturbance in the high-resolution images of the atomic rows along the $[1\,0\,1]_\gamma$ and $[1\,1\,1]_\alpha$ directions, as would have been expected if a BB/OC mechanism were active. Therefore, they concluded that the KS mechanism is the only plausible deformation mechanism in the FCC to BCC displacive transformation. A later study by Ogawa and Kajiwara [6], which examined the FCC to BCC phase transformation for Fe-23Ni-3.8Mn and Fe-9Ni-1.1C alloys and focused on interface structure and dislocations, further confirmed these observations.

A recent study by He et al. (2022) [92] on strain-induced martensitic transformation using HRTEM yet aligns with the BB/OC model. However it was not observed experimentally for martensitic transformation with no external stress. Their atomic-scale observations revealed a $\gamma \rightarrow \epsilon \rightarrow \alpha$ transformation sequence, consistent with the path proposed by the BB/OC mechanism. Moreover, the transformation from FCC to HCP was attributed to the gliding of Shockley partials with Burgers vectors $a_\gamma/6\,\langle 1\,1\,2\rangle_\gamma$ on $(1\,1\,1)_\gamma$ plane. Earlier studies by Weina et al. [93] and Yang et al. [94], also on strain-induced martensitic transformation, for Fe-20Mn-3Si-3Al alloys also supported the BB/OC mechanism, observing the expected FCC to HCP to BCC transformation path. However, although FCC to HCP to BCC transformation paths are often linked with the BB/OC mechanism, the shear along the $[1\,1\,\bar{2}]_\gamma$ direction in the KS transformation path also induces a stacking change, potentially forming an intermediary HCP phase. Careful examination of the transformation path is crucial, insofar as the sole observation of the FCC to HCP to BCC transition does not conclusively point to a BB/OC mechanism.

1.7 Carbon segregation at mobile interfaces in Fe-C alloys

Carbon segregation at phase boundaries, especially during the FCC to BCC transformation, plays a critical role in determining the mechanical properties and stability of iron-based alloys [95–97]. The segregation of carbon at the interface affects transformation kinetics by altering the propagation rate of the interface, often through pinning and unpinning mechanisms [19, 98–100]. This phenomenon is particularly pronounced in Fe-C alloys, where carbon atoms segregate at dislocations. This carbon segregation can simultaneously promote the FCC to BCC phase transformation [96] and hinder the transformation by pinning dislocations at the boundary [75].

Different solute elements presented in steels also interact with carbon, inducing additional effects such as co-segregation. For example, carbon co-segregates with manganese in Fe-C-Mn alloys, as shown in [7], and with heavy elements like niobium and molybdenum in [101]. Although ternary and quaternary alloy systems are more common in experimental studies, analyzing the iron-carbon interaction with a moving interface remains important due to the rapid migration of carbon atoms to the transformation interface.

Numerous ab initio calculations [95–97, 101–103] and molecular dynamics simulations [100, 104–106] have been conducted to describe the interaction of carbon atoms with crystal defects and FCC-BCC interface. Despite the intersting and important results obtained using these methods, these approaches can not capture the diffusion time sacle, which is crucial to this phenomenon.

This section is organized as follows. A review on the literature on the interactions between carbon and moving dislocations will be presented first, following the consideration of recently

proposed models of interface prolongations.

1.7.1 Carbon interaction with moving dislocations

In the pioneering work of Cottrell and Bilby [98, 99], it was demonstrated that carbon atoms interact with the elastic field created by dislocations and segregate around them, leading to the formation of so-called 'Cottrel atmospheres'. This segregation creates a 'pinning' effect, which reduces the mobility of the dislocation, and strengthen the material [59, 98, 100, 107]. A segregation of carbon atoms around a BCC screw dislocation, has been simulated in [19], is shown in Figure 1.21 using Monte-carlo. The result of this simulation, highlighting the formation of Cottrell atmosphere around the dislocation, is shown in Figure 1.21.

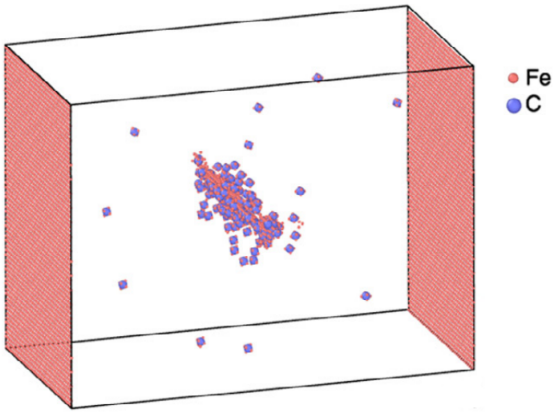

Figure 1.21: Monte-Carlo equilibrated carbon Cottrel [19] atmosphere at $T = 300$ K for 500 ppm of carbon. Only non-BCC iron atoms (red) and carbon atoms (blue) are shown.

As mentioned before, the FCC-BCC interface is reticulated by two sets of screw dislocations. Cottrell atmospheres around these dislocations have been observed experimentally using atom probe tomography (APT) in Fe-0.45 at%C BCC ferrite [108]. Moreover, simulation methods, including ab initio/DFT [95–97, 101–103] and Monte Carlo [19, 26], have been applied to study the segregation of carbon atoms around dislocations in iron alloys. It was shown that ab initio and Monte Carlo methods have successfully reproduced Cottrell atmosphere interactions around screw dislocations. Also, it was demonstrated using molecular dynamics simulations, that carbon atoms strongly interact with dislocations in iron [100, 104].

Moreover, the pinning-unpinning effect of Cottrell atmosphere around a moving dislocation was observed using Monte-Carlo simulations in [19]. The critical velocity of dislocation motion determines whether solute atoms will follow the dislocation. If the dislocation moves faster than this critical velocity, it may escape the Cottrell atmosphere, leading to unpinning. The following

expression for this critical dislocation velocity v_{dc} has been provided in [59]:

$$v_{dc} = \frac{4DkT}{\beta}. \tag{1.7.1}$$

Here, D is the diffusion coefficient of the solute atoms, k the Boltzmann constant, T the temperature and β a proportionality factor related to the dislocation-solute interaction strength. This equation demonstrates a strong dependence of critical velocity with the temperature, with temperature appearing both directly in the equation and indirectly through the solute diffusion coefficient. Consequently, at high temperatures, dislocation unpinning becomes unlikely due to increased solute mobility. In contrast, for lower temperatures favor dislocation unpinning is likely to occur, as solute mobility is reduced. While the Cottrell effect is well-understood, the interaction of carbon solutes with the fast-moving FCC to BCC phase transformation interface remains an area of active research. Recent ab initio calculations in [102] suggest that carbon solute pinning at interface dislocations enhances phase stability, impacting the kinetics of the FCC to BCC transformation.

1.7.2 Interface propagation models

In general, interface propagation models for the FCC to BCC transformation in Fe-C systems fall into three main categories: diffusion-controlled models [109–111], interface-controlled models [111, 112], and mixed-mode models [111, 113–116]. Each model represents a distinct approach to understanding the interplay between diffusion, thermodynamics, and the dynamics of the moving interface, and each is governed by specific assumptions and boundary conditions.

Diffusion controlled model

When the austenite-ferrite phase transformation is treated as a purely diffusion-controlled (DC) model [109–111], the dissipation of the energy at the interface due to displacive transformation occurring at the interface is neglected. As a result, the local equilibrium conditions are determined by minimizing the Gibbs free energy function under conditions of constant temperature and pressure. Under these conditions, the chemical potentials of carbon and iron must be equal across the migrating interface in both the austenite and ferrite phases:

$$\begin{cases} \mu_C^\alpha = \mu_C^\gamma, \\ \mu_{Fe}^\alpha = \mu_{Fe}^\gamma. \end{cases} \tag{1.7.2}$$

For a binary alloy, the boundary conditions for the diffusion problem can be directly evaluated from the phase diagram. At a given temperature $T = T_1$, the equilibrium compositions at the interface corresponding to the minimum Gibbs free energy can be obtained by a common tangent construction, depicted in Figure 1.22. The equilibrium concentration in α and γ phase are denoted as C_c^α and C_c^γ, respectively. The mean concentration in the alloy is C_c^0.

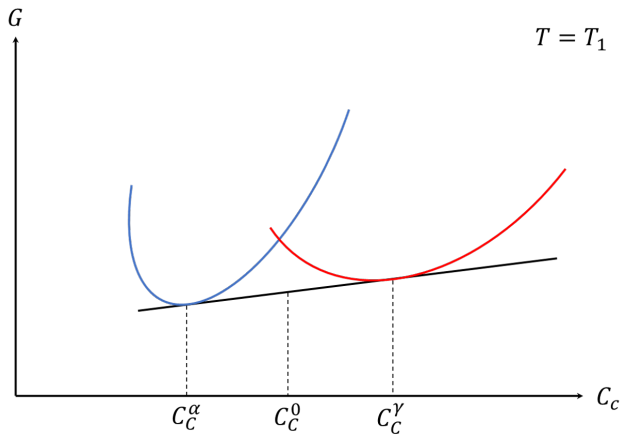

Figure 1.22: Schematic Gibbs energy diagram of carbon concentration in an austenite-ferrite at $T = T_1$. C_c^α and C_c^γ are the equilibrium carbon concentration in the ferrite and austenite, respectively, while C_c^0 is the mean concentration in the material.

The carbon composition profile at the interface illustrating the local equilibrium condition is depicted in Figure 1.23. The difference in solubility between the austenite and ferrite phases leads to a partitioning at the interface, where carbon rejected from the ferrite phase diffuse into the austenite. It gradually increase the concentration in the austenite with a maximum carbon concentration at the austenite-ferrite interface.

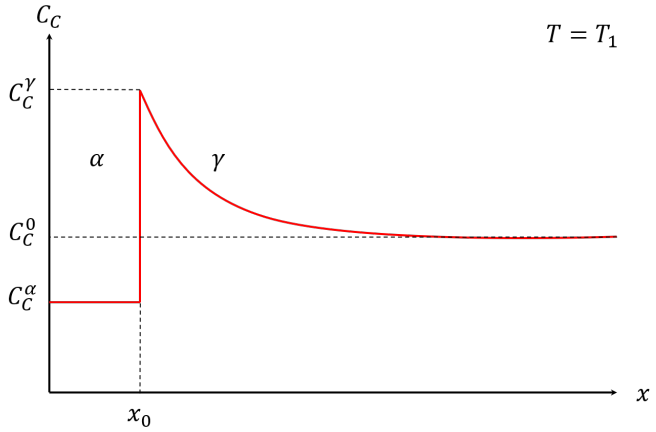

Figure 1.23: Schematic carbon composition profile illustrating local equilibrium conditions at the austenite-ferrite migrating inteface at T_1.

According to the Zener model [109, 110], the interface velocity is controlled by the diffusion of carbon in austenite. This is because the carbon concentration reaches its saturation point, C_c^γ, at the austenite-ferrite interface. For the ferrite to propagate, the carbon needs to diffuse away from the interface further into the austenite. Therefore, using Fick's first law, the velocity v of the interface is proportional to the diffusion coefficient D of carbon in the austenite, the interface velocity v can be expressed in the following expression, where ΔC_c is the difference in carbon

concentration between the two phases at the interface:

$$v = D\frac{\Delta C_c}{C_c^{\alpha} - C_c^{\gamma}}. \tag{1.7.3}$$

The interface moves at a rate that balances the diffusion of carbon, which means that the speed of interface migration is limited by how quickly carbon can diffuse away from the growing phase.

The local equilibrium assumption is a significant simplification as it is purely thermodynamic [111]. However, many experimental and numerical analysis of proeutectoid ferrite formation in an Fe-C system use the local equilibrium condition to describe the austenite-ferrite interface [117–120]. The simplest diffusion-controlled model is known as the sharp interface model (SI), as it assumes an interface with no width, where properties such as crystalline structure and composition change abruptly from one side of the austenite-ferrite interface to the other.

Interface controlled model

In contrast to the diffusion-controlled model, an interface-controlled (IC) model has been developed in [111, 112]. This model suggests that the transformation rate is controlled by the energy required to move the interface rather than by the diffusion of carbon. This model can be applied when an infinitely fast diffusion rate of carbon is considered, or when the interface can move faster than carbon can diffuse. In the first case, this leads to a sharp transition at the interface with no buildup of carbon. In the second case, as the interface moves faster than carbon can diffuse, this could lead to non-equilibrium carbon concentrations at the interface. Both scenarios are shown in Figure 1.24.

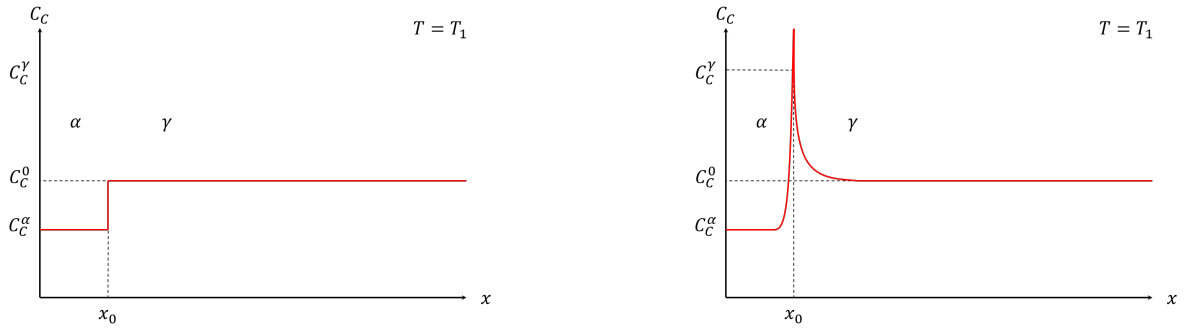

Figure 1.24: Schematic carbon composition profile at the austenite-ferrite migrating interface in the IC model with (a) infinitely fast carbon diffusion into the austenite and (**b**) the interface moving faster than the carbon can diffuse.

Mixed mode model

The diffusion-controlled and interface-controlled approaches can both be seen as extreme cases of the actual kinetics of the austenite to ferrite phase transformation in Fe-C systems. Models

that include both diffusion and interfacial mobility in Fe-C steels have been developed and are referred to as mixed-mode models [111, 113–116]. A mixed-mode model was developed in [113, 114], where the nature of the transformation is governed by a single dimensionless parameter Z. This parameter is proportional to the diffusivity D of the partitioning elements and the area-to-volume ratio A_α/V_α of the phase. It is inversely proportional to the interface mobility and a thermodynamic proportionality factor related to the driving force χ is:

$$Z = \frac{D}{M\chi}.\frac{A_\alpha}{V_\alpha}. \tag{1.7.4}$$

The interface mobility M is an effective mobility, as assessed in [121], and can account for solute drag and transformation strain effects. Solute drag occurs when solute atoms segregate at the interface, creating a drag force that impedes the motion of the interface. The solute drag effect is particularly significant in cases where the solute atoms have a strong interaction with the interface. This could be the case for carbon at FCC-BCC interface in specific condition, like in co-segregation mechanism with another alloying element, such as manganese [7]. Although carbon segregation during the phase transformation is considered, its interaction with other alloying elements leaves the exact interaction with the interface undetermined.

When $Z = 0$, it implies that the phase transformation is purely diffusion-controlled, while when $Z \to \infty$, it implies that the transformation is interface-controlled. An S parameter is introduced to quantify the character of the transformation. The S parameter is related to the Z parameter, with $S = 1$ indicating an interface-controlled transformation and $S = 0$ indicating a diffusion-controlled transformation. The concentration at the interface and the resulting interface velocity are directly influenced by the Z or equivalently the S parameter. In [116], the interface velocity was defined using the S parameter:

$$v = M\chi S\left(C^{\beta\alpha} - C^0\right), \tag{1.7.5}$$

where $C^{\beta\alpha}$ is the equilibrium concentration of carbon at the interface and C^0 is the average concentration of the partitioning element in the system.

Moreover, the mixed-mode model, when specifically applied to austenite-ferrite phase transformation in Fe-C [113, 114] and Fe-C-Mn systems [116], has shown that the Z parameter decreases as the growth of the new phase progresses. This means that the transformation initially starts as interface-controlled and gradually shifts toward being diffusion-controlled. This shift is accompanied by a gradual decrease in interface velocity, as described by equation (1.7.5), with the S parameter decreasing accordingly. This gradual decrease in interface velocity could be due to the carbon segregation at the interface, creating a solute drag effect slowing down the transformation rate. However, incorporating all of the interface characteristics, such as interface width, transformation dislocations, stacking faults, and intermediary phases, into mixed-mode models is not an

easy task. Modeling the austenite to ferrite phase transformation may offer new perspectives for understanding the transformation mechanism from austenite to ferrite, both in pure iron and in Fe-C alloys.

1.8 Conclusions

This chapter provides a review of the austenite to ferrite phase transformation in pure iron and Fe-based alloys. Theoretical models, along with experimental and simulation results that explain the FCC to BCC displacive transformation, were thoroughly assessed, covering both atomic rearrangement and mobility of the transformation interface. It was emphasized that current experimental and theoretical data do not provide a clear consensus regarding the FCC to BCC transformation mechanism.

In Fe-C systems, mixed-mode models provide valuable insights into the dual nature of the transformation, which is both displacive and diffusive. However, since interface defects, such as transformation dislocations, can serve as preferential sites for carbon diffusion, significant further work is required to accurately assess these phenomena.

Chapter 2

Quasiparticle approach

At the atomic scale, Molecular Dynamics (MD) and Monte Carlo (MC) methods are commonly used to study phase transformations. MD, which enables tracking of individual atoms, is especially effective for studying phase transformations from FCC to BCC. However, its effectiveness is limited by the number of variables, which restricts the length and time scale of simulated systems. This makes it less suitable for studying diffusive phase transformations. Conversely, kinetic MC can simulate diffusive processes at the atomic scale, but it does not account for elasticity.

The Atomic Density Function (ADF), introduced by A.G.Khachaturyan in the 1970s [45, 122], is a method employed to investigate the long-term evolution of systems at the atomic scale. Within the ADF framework, the atomic configuration of the system is described by a set of occupation probability $\rho_\alpha(r,t)$, which represents the probability of a lattice site r to be occupied by an atom of type α at a given time t. The temporal evolution of atomic configuration follows Onsager-type diffusion equations [45]. The probability function is specified at each site of the underlying Ising lattice which coincides with the simulation grid. This confides the models application to isostructural phase transformation such as ordering or decomposition.

The phase-field crystal model (PFC)[21, 123] describes the temporal evolution of materials at the atomic scale. In this model, the phase field is interpreted as an atomic density function in the continuum space. Y.Jin and A.G.Khachaturyan [36] demonstrated that the PFC is a specific case of the ADF and developed a more generalized approach by introducing the Continuous Atomic Density Function (CADF). This models aims to remove constraints linked with a fixed lattice while considering the elastic properties of the system.

The Quasi-particle approach, introduced in 2014 by A.G. Khachaturyan, H. Zaplosky and M. Larvskyi [124] further extends the CADF framework. In this approach, the simulation grid spacing Δx is several times smaller than the lattice parameter a. Then, atoms are no longer treated as points but as spheres containing some simulation grid nodes. These grids are called fratons, from the contraction of "fraction of atoms" and possess the same properties as fermions, including the

Pauli principle: two fratons cannot occupy the same simulation grid. The displacement of atoms is thus due to the creation and annihilation of fratons. Fraton positions at a time t are described by the configuration number $c(\boldsymbol{r}, t)$:

$$c(\boldsymbol{r}, t) = \begin{cases} 1 \text{ if site } \boldsymbol{r} \in \text{atom}, \\ 0 \text{ if site } \boldsymbol{r} \notin \text{atom}. \end{cases} \tag{2.0.1}$$

In the case of the two-component system, each component has its own configuration number at each site $\boldsymbol{r}$. The distinction between ADF and Quasi-Particle grids is illustrated in Figure 2.1.

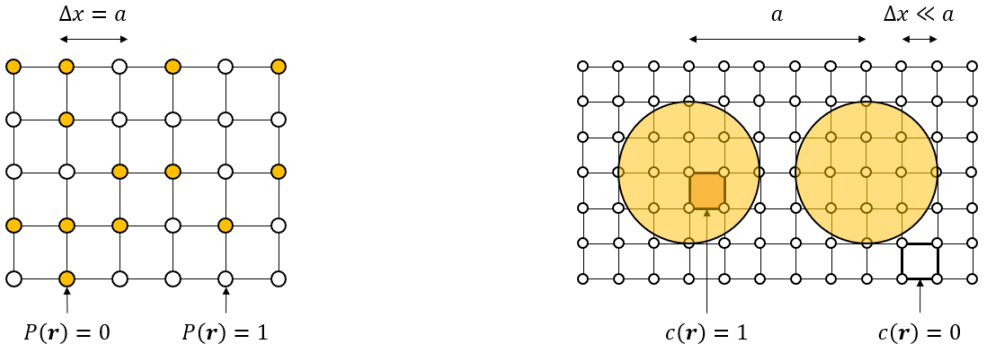

(a) (b)

Figure 2.1: Schematic representation of atomic configurations on the rigid lattice for the ADF model (**a**) and in the case of QA (**b**).

2.1 Hamiltonian and free energy

The Hamiltonian, which is based on the Ising model, can be formulated for both one-component and two-component systems. This formulation assumes pair interactions and uses the mean-field approximation. In this approximation, the interaction of all other particles with a pair of fratons, located at positions $\boldsymbol{r}$ and $\boldsymbol{r'}$ is taken into account and averaged to form a mean-field. For a one-component system, the Hamiltonian is expressed as follows:

$$\mathcal{H} = \frac{1}{2} \sum_{\boldsymbol{r}, \boldsymbol{r'}} V\left(\boldsymbol{r} - \boldsymbol{r'}\right) c(\boldsymbol{r}, t) c(\boldsymbol{r'}, t), \tag{2.1.1}$$

where $V\left(\boldsymbol{r} - \boldsymbol{r'}\right)$ represents the interaction between fratons at a distance $|\boldsymbol{r} - \boldsymbol{r'}|$. For a system with m components, the system description in terms of fratons can be realized with m configuration numbers. In this case, component α with $\alpha \in \{1, .., m\}$ is described by the configuration number $c_\alpha(\boldsymbol{r}, t)$. The Hamiltonian for the m-components system with components α and β is written:

$$\mathcal{H} = \frac{1}{2} \sum_{\alpha, \beta} \sum_{\boldsymbol{r}, \boldsymbol{r'}} V_{\alpha,\beta}\left(\boldsymbol{r} - \boldsymbol{r'}\right) c_{\alpha,\beta}(\boldsymbol{r}, t) c_{\alpha,\beta}(\boldsymbol{r'}, t). \tag{2.1.2}$$

For the m-component system $V_{\alpha,\beta}\left(\boldsymbol{r}-\boldsymbol{r'}\right)$ is the interaction between the fratons of component α at the position $\boldsymbol{r}$ and of the component β at the position $\boldsymbol{r'}$ with $(\alpha,\beta)=\{1,...,m\}^2$. To express the free energy of the system, the internal energy is defined as the average value of the Hamiltonian $\mathcal{H}$:

$$U=\langle H\rangle=\frac{1}{2}\sum_{\alpha,\beta}\sum_{\boldsymbol{r},\boldsymbol{r'}}V_{\alpha,\beta}\left(\boldsymbol{r}-\boldsymbol{r'}\right)\left\langle c_{\alpha,\beta}\left(\boldsymbol{r},t\right)c_{\alpha,\beta}\left(\boldsymbol{r'},t\right)\right\rangle, \tag{2.1.3}$$

where the $\langle . \rangle$ symbol denotes the Gibbs ensemble average at temperature T and time t. In the QA approach or in the phase field crystal model, atoms occupy a space proportional to their vibration around their equilibrium position. The time average is thus calculated under the ergodic hypothesis at a time scale that is greater than the vibrating period of the atoms. In this system, the number of fratons, the volume of the simulation box, and the temperature are all constants. The equilibrium state of the system is obtained by minimizing the Helmholtz free energy. Under the mean-field approximation, the average ensemble segment of Equation 2.1.3 is reformulated as follows:

$$\left\langle c_{\alpha}\left(\boldsymbol{r},t\right)c_{\beta}\left(\boldsymbol{r'},t\right)\right\rangle=\left\langle c_{\alpha}\left(\boldsymbol{r},t\right)\right\rangle\left\langle c_{\beta}\left(\boldsymbol{r'},t\right)\right\rangle. \tag{2.1.4}$$

Configuration numbers $c_{\alpha}\left(\boldsymbol{r},t\right)$ are averaged over the time-dependent Gibbs ensemble to yield the occupation probability function $\rho_{\alpha}\left(\boldsymbol{r},t\right)=c_{\alpha}\left(\boldsymbol{r},t\right)$. This definition renders $\rho_{\alpha}\left(\boldsymbol{r},t\right)$ the probability of finding a fraton at the site $\boldsymbol{r}$ and time t. For m-components systems, $\rho_{\alpha}(\boldsymbol{r},t)$ must be defined for each component. The schematic spatial evolution of the fratons density, in the case of atomic spheres formation, is illustrated in a two dimensions case in Figure 2.2.

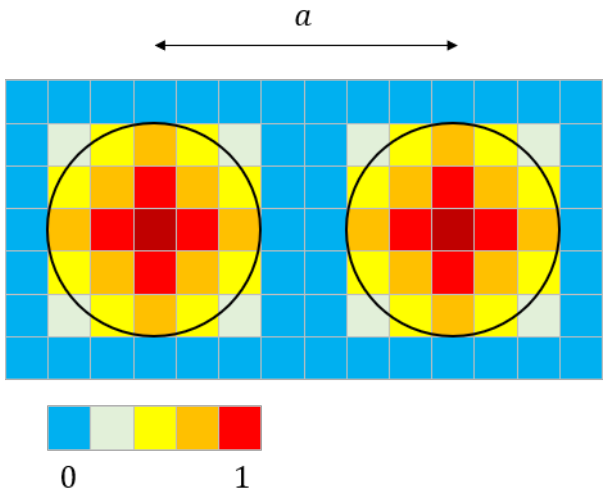

Figure 2.2: Schematic representation of fratons condensation in two dimension. '0' represents the minima of the normalized occupation probability function and '1' the maxima.

To determine fratons density, the mean concentration of fratons of type α in the simulation

box, denoted $\bar{\rho_\alpha}$, is directly proportional to the atomic density of component α, denoted as ρ_α^{at}:

$$\bar{\rho_\alpha} = \rho_\alpha^{at} \frac{4}{3} \pi R_\alpha^3, \tag{2.1.5}$$

where R_α is the atomic radius of the atoms. The internal energy is reformulated from Equations 2.1.3 and 2.1.4 as follows:

$$U = \frac{1}{2} \sum_{\alpha,\beta} \sum_{\boldsymbol{r},\boldsymbol{r'}} V_{\alpha,\beta} \left(\boldsymbol{r} - \boldsymbol{r'} \right) \rho_\alpha \left(\boldsymbol{r}, t \right) \rho_\beta \left(\boldsymbol{r'}, t \right). \tag{2.1.6}$$

The entropy of the energy is then defined as:

$$S = -k_B \sum_{\alpha} \sum_{\boldsymbol{r}} \rho_\alpha \left(\boldsymbol{r}, t \right) \ln \rho_\alpha \left(\boldsymbol{r}, t \right), \tag{2.1.7}$$

where k_B is the Boltzmann constant.Therefore, the expression of the Hermoltz free energy in a one-component system is given by:

$$F = U - TS = \frac{1}{2} \sum_{\alpha,\beta} \sum_{\boldsymbol{r},\boldsymbol{r'}} V_{\alpha,\beta} \left(\boldsymbol{r} - \boldsymbol{r'} \right) \rho_\alpha \left(\boldsymbol{r}, t \right) \rho_\beta \left(\boldsymbol{r'}, t \right) + k_B T \sum_{\alpha} \sum_{\boldsymbol{r}} \rho_\alpha \left(\boldsymbol{r}, t \right) \ln \rho_\alpha \left(\boldsymbol{r}, t \right), \tag{2.1.8}$$

where T is the temperature.

2.2 Stability of homogeneous state with respect to infinitesimal fluctuations and response function

In the Quasi-particle approach, the response function is used to describe the stability of the system in response of the fluctuations of the occupation probabilities. Near the phase transition temperature,T_c, the occupation probability can be expressed as follows:

$$\rho_\alpha \left(\boldsymbol{r} \right) = \bar{\rho}_\alpha \left(\boldsymbol{r} \right) + \Delta\rho_\alpha \left(\boldsymbol{r} \right), \tag{2.2.1}$$

where $\bar{\rho}_\alpha$ is the average occupation probabilities and $\Delta\rho_\alpha$ the fluctuations of the occupation probabilities. The variation of Hermoltz free energy $\Delta F = F\left[\rho_\alpha(\boldsymbol{r})\right] - F\left[\bar{\rho}_\alpha\right]$ can then be expended in a Taylor series around $\bar{\rho}_\alpha$ with respect to the these fluctuations [36]:

$$\begin{aligned} \Delta F = & \sum_{\boldsymbol{r}} \sum_{\alpha} A_\alpha \left(\boldsymbol{r} \right) \Delta\rho_\alpha(\boldsymbol{r}) + \frac{1}{2} \sum_{\boldsymbol{r},\boldsymbol{r'}} \sum_{\alpha,\beta} B_{\alpha\beta} \left(\boldsymbol{r}, \boldsymbol{r'} \right) \Delta\rho_\alpha(\boldsymbol{r}) \Delta\rho_\beta(\boldsymbol{r'}) \\ & + \frac{1}{3!} \sum_{\boldsymbol{r},\boldsymbol{r'},\boldsymbol{r''}} \sum_{\alpha,\beta,\gamma} C_{\alpha\beta\gamma} \left(\boldsymbol{r}, \boldsymbol{r'}, \boldsymbol{r''} \right) \Delta\rho_\alpha(\boldsymbol{r}) \Delta\rho_\beta(\boldsymbol{r'}) \Delta\rho_\gamma(\boldsymbol{r''}). \end{aligned} \tag{2.2.2}$$

where:

$$A_\alpha(\boldsymbol{r}) = \left.\frac{\delta F}{\delta\rho_\alpha(\boldsymbol{r})}\right|_{\bar{\rho}_\alpha},$$
$$B_{\alpha\beta}(\boldsymbol{r},\boldsymbol{r'}) = \left.\frac{\delta^2 F}{\delta\rho_\alpha(\boldsymbol{r})\delta\rho_\beta(\boldsymbol{r'})}\right|_{\bar{\rho}_\alpha\bar{\rho}_\beta},$$
$$C_{\alpha\beta\gamma}(\boldsymbol{r},\boldsymbol{r'},\boldsymbol{r''}) = \left.\frac{\delta^3 F}{\delta\rho_\alpha(\boldsymbol{r})\delta\rho_\beta(\boldsymbol{r'})\delta\rho_\gamma(\boldsymbol{r''})}\right|_{\bar{\rho}_\alpha\bar{\rho}_\beta\bar{\rho}_\gamma},$$

are the expansion coefficients calculated in the disordered homogeneous state. The variation of Hermoltz free energy presented in Equation 2.2.2 has the same characteristic as in PFC models, as demonstrated in [125]. In this state, all sites are equivalent, thus $A_\alpha(\boldsymbol{r}) = const$. Furthermore, the number of fratons is conservative, as such the sum of the fluctuation of occupation probabilities over all sites is:

$$\sum_{\boldsymbol{r}} \Delta\rho_\alpha(\boldsymbol{r}) = 0. \tag{2.2.3}$$

Therefore, the first term of the Taylor expansion is always zero:

$$\sum_{\boldsymbol{r}}\sum_{a} A_\alpha(\boldsymbol{r})\,\Delta\rho_\alpha(\boldsymbol{r}) = 0. \tag{2.2.4}$$

When the system is close to the phase transition temperature T_C, the fluctuations are small. As such, only the first non-vanishing term of the Taylor expansion is considered. Therefore, Equation 2.2.2 simplifies as follows:

$$\Delta F = \frac{1}{2}\sum_{\boldsymbol{r},\boldsymbol{r'}}\sum_{\alpha,\beta} \left.\frac{\delta^2 F}{\delta\rho_\alpha(\boldsymbol{r})\delta\rho_\beta(\boldsymbol{r'})}\right|_{\bar{\rho}_\alpha\bar{\rho}_\beta} \Delta\rho_\alpha(\boldsymbol{r})\Delta\rho_\beta(\boldsymbol{r'}), \tag{2.2.5}$$

where the second derivative of the free energy, in the Fourier space, is the response function $D_{\alpha\beta}(\boldsymbol{k},T)$ defined as follows:

$$D_{\alpha\beta}(\boldsymbol{k},T,\{\bar{\rho}_\alpha\}) = \frac{\delta^2 F}{\delta\rho_\alpha(\boldsymbol{k})\delta\rho_\beta(\boldsymbol{k})} = \widetilde{V}_{\alpha\beta}(\boldsymbol{k}) + \left.\frac{\partial^2 S}{\partial\rho_\alpha(\boldsymbol{k})\partial\rho_\beta(\boldsymbol{k})}\right|_{\bar{\rho_\alpha}\bar{\rho_\beta}} k_B T. \tag{2.2.6}$$

The response function, as defined in Equation 2.2.6, is an element of the $m \times m$ matrix $\hat{D}(\boldsymbol{k},T,\{\rho_\alpha\})$ where m is the number of independent components. This matrix is both Hermitian and symmetric, which is due to the possible inversion of indexes α and β and the fact that all

terms of Equation 2.2.6 are real values. The matrix can be written as:

$$\hat{D}\left(\boldsymbol{k}, T, \{\bar{\rho}_\alpha\}\right) = \begin{pmatrix} D_{11} & D_{12} & \cdots & D_{1m} \\ D_{12} & D_{22} & \cdots & D_{2m} \\ \vdots & \vdots & \ddots & \vdots \\ D_{1m} & D_{2m} & \cdots & D_{mm} \end{pmatrix} \left(\boldsymbol{k}, T, \{\bar{\rho}_\alpha\}\right). \tag{2.2.7}$$

With this definition of the response function, the Hermoltz free energy variation presented in Equation 2.2.5 can be rewritten in the Fourier space as follows:

$$\Delta F = \frac{1}{2} \sum_{\boldsymbol{k}} \sum_{\alpha\beta} D_{\alpha\beta}\left(\boldsymbol{k}, T, \{\rho_\alpha\}\right) \widetilde{\Delta\rho}_\alpha\left(\boldsymbol{k}\right) \widetilde{\Delta\rho}^*_\beta\left(\boldsymbol{k}\right). \tag{2.2.8}$$

Given that the variation of the Helmholtz free energy is a function of small perturbations and is close to equilibrium, the normal mode representation of static concentration waves can be used to reformulate Equation 2.2.8 [36]. In this representation, the system is decomposed in a superposition of normal modes. Consequently, the occupation probability fluctuation $\Delta\rho_\alpha\left(\boldsymbol{r}\right)$ can be expressed as a linear superposition of normal static concentration waves $\Psi_\alpha\left(s, \boldsymbol{k}\right)$:

$$\Delta\rho_\alpha\left(\boldsymbol{r}\right) = \sum_{\boldsymbol{k}} \sum_{s=1}^{m} Q\left(s, \boldsymbol{k}\right) \Psi_\alpha\left(s, \boldsymbol{k}\right), \tag{2.2.9}$$

where $Q\left(s, \boldsymbol{k}\right)$ is the amplitude of the normal mode concentration wave $\Psi_\alpha\left(s, \boldsymbol{k}\right)$ and $s = \{1, 2, \cdots, m\}$ corresponds to a normal mode. The function $\Psi_\alpha\left(s, \boldsymbol{k}\right)$ represents atomic vibrations of component α around their equilibrium position on different sub-lattices. This function can be expressed in the form of Bloch functions:

$$\Psi_\alpha\left(s, \boldsymbol{k}\right) = u_\alpha\left(s, \boldsymbol{k}\right) e^{i\boldsymbol{k}.\boldsymbol{r}}, \tag{2.2.10}$$

where $u_\alpha\left(s, \boldsymbol{k}\right)$ is the "polarization vector" [36], which is a normalized eigenvector of the matrix $\hat{D}\left(\boldsymbol{k}, T, \{\bar{\rho}_\alpha\}\right)$. This relation yields the following expression introducing the eigenvalues $\lambda\left(s, \boldsymbol{k}, T, \{\bar{\rho}_\alpha\}\right)$ of the matrix $\hat{D}\left(\boldsymbol{k}, T, \{\bar{\rho}_\alpha\}\right)$:

$$\hat{D}\left(\boldsymbol{k}, T, \{\bar{\rho}_\alpha\}\right) u_\alpha\left(s, \boldsymbol{k}\right) = \lambda\left(s, \boldsymbol{k}, T, \{\bar{\rho}_\alpha\}\right) u_\alpha\left(s, \boldsymbol{k}\right), \tag{2.2.11}$$

Therefore, by injecting the Equation 2.2.9 into Equation 2.2.10, the Fourier transformation of the occupation probabilities can be written as:

$$\widetilde{\Delta\rho}_\alpha\left(\boldsymbol{k}\right) = \sum_{s=1}^{m} Q\left(s, \boldsymbol{k}\right) u_\alpha\left(s, \boldsymbol{k}\right), \tag{2.2.12}$$

and as such the free energy variation expressed in Equation 2.2.8 can be simplified as follows:

$$\Delta F = \frac{1}{2} \sum_{\boldsymbol{k}} \sum_{s=1}^{m} \lambda \left(s, \boldsymbol{k}, T, \{\bar{\rho}_\alpha\} \right) \left| Q \left(s, \boldsymbol{k} \right) \right|^2 . \tag{2.2.13}$$

In the Equation 2.2.13, the sign of the energy variation ΔF depends solely on the sign of the eigenvalue $\lambda \left(s, \boldsymbol{k}, T, \{\bar{\rho}_\alpha\} \right)$. Therefore the stability of the system depends of the sign of the lowest eigenvalue denoted as $\lambda \left(\boldsymbol{k}, T, \{\bar{\rho}_\alpha\} \right)$. If the sign of the eigenvalues $\lambda \left(\boldsymbol{k}, T, \{\bar{\rho}_\alpha\} \right)$ is positively defined for all $\boldsymbol{k}$ vectors, any concentration fluctuations will increase the Helmholtz free energy. As such, the disordered homogeneous phase remains stable with respect to infinitesimal fluctuations. If the sign of the eigenvalue $\lambda_0 \left(\boldsymbol{k_0}, T, \{\bar{\rho}_\alpha\} \right)$ is negative for one $\boldsymbol{k_0}$ vector, then the corresponding infinitesimal fluctuation will decrease the energy and the phase transformation will happen. If various $\boldsymbol{k}$ vectors exist where the eigenvalue $\lambda \left(s, \boldsymbol{k}, T, \{\bar{\rho}_\alpha\} \right)$ is less than 0, he system is unstable with respect to all the corresponding fluctuations. However, the fluctuation corresponding to the lowest value of $\lambda \left(s, \boldsymbol{k}, T, \{\bar{\rho}_\alpha\} \right)$ will grow faster.

The critical temperature, denoted as T_C, is the temperature at which the system becomes unstable with respect to infinitesimal fluctuations. Above this temperature, the homogeneous solution remains stable. At $T = T_C$, the lowest value of $\lambda \left(s, \boldsymbol{k_0}, T, \{\bar{\rho}_\alpha\} \right)$ reaches 0 causing the system to lose its stability with respect to infinitesimal fluctuations. The eigenvalues of the response function, as a function of T, are presented in Figure 2.3.

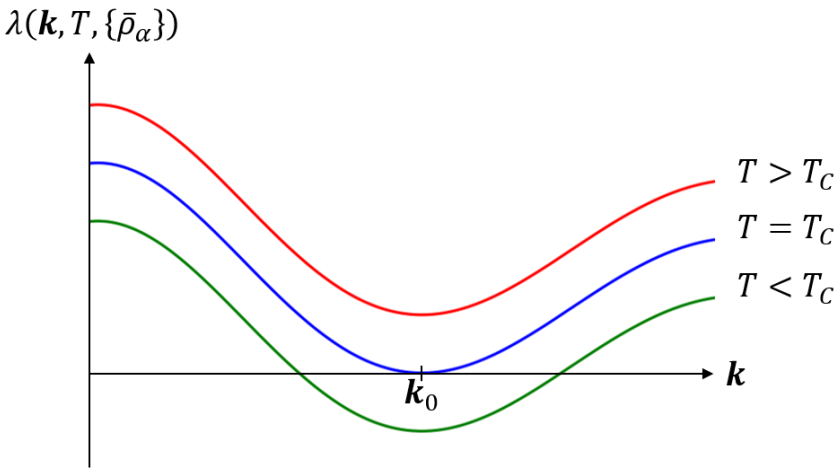

Figure 2.3: Schematic representation of the eigenvalue $\lambda \left(\boldsymbol{k}, T, \{\bar{\rho}_\alpha\} \right)$ at different temperatures. All functions reach their minimum at $\boldsymbol{k} = \boldsymbol{k_0}$ where $\boldsymbol{k}$ is a one-dimensional vector. At $T \leq T_C$ the system becomes unstable and the phase transformation occurs.

The response function and eigenvalues can be expressed more in details for one- and two-components systems. For a one-component system, the matrix $\hat{D}$ consist of only one element, thus

it can be expressed from Equation 2.2.6 as:

$$\lambda\left(\boldsymbol{k}, T, \{\bar{\rho_\alpha}\}\right) = D\left(\boldsymbol{k}, T, \{\bar{\rho_\alpha}\}\right) = \widetilde{V}\left(\boldsymbol{k}\right) + \frac{\partial^2 S}{\partial \rho\left(\boldsymbol{k}\right)} k_B T. \tag{2.2.14}$$

The Equation 2.2.14 can then be simplified by taking into consideration the definition of entropy in the QA approach, as given in Equation 2.1.7:

$$\lambda\left(\boldsymbol{k}, T, \{\bar{\rho_\alpha}\}\right) = \widetilde{V}\left(\boldsymbol{k}\right) + \frac{k_B T}{\bar{\rho}\left(1-\bar{\rho}\right)}. \tag{2.2.15}$$

The first term in Equation 2.2.15, which is the interaction potential, will define the minima $\boldsymbol{k}_0$ and the second defines the temperature at which the system becomes unstable with respect to infinitesimal fluctuations.

For two-component systems, in order to obtain the expression of the eigenvalues, the matrix $\hat{D}\left(\boldsymbol{k}, T\left\{\bar{\rho}\right\}\right)$ of the response function and its components need to be defined:

$$\hat{D}\left(\boldsymbol{k}, T\left\{\bar{\rho}\right\}\right) = \begin{pmatrix} D_{11} & D_{12} \\ D_{12} & D_{22} \end{pmatrix}, \tag{2.2.16}$$

where the components of the matrix are obtained from Equations 2.2.6 and 2.1.7:

$$D_{11}\left(\boldsymbol{k}, T, \{\bar{\rho}_\alpha\}\right) = \widetilde{V}_{11} + k_B T\left(1-\bar{\rho}_2\right) / \left(\bar{\rho}_1\left(1-\bar{\rho_1}-\bar{\rho}_2\right)\right), \tag{2.2.17}$$

$$D_{12}\left(\boldsymbol{k}, T, \{\bar{\rho}_\alpha\}\right) = \widetilde{V}_{12} + k_B T\left(1-\bar{\rho}_1-\bar{\rho}_2\right), \tag{2.2.18}$$

$$D_{22}\left(\boldsymbol{k}, T, \{\bar{\rho}_\alpha\}\right) = \widetilde{V}_{22} + k_B T\left(1-\bar{\rho}_1\right) / \left(\bar{\rho}_2\left(1-\bar{\rho_1}-\bar{\rho}_2\right)\right). \tag{2.2.19}$$

The eigenvalues can then be determined with the following characteristic equations for eigenvalues of a matrix:

$$\begin{vmatrix} D_{11}-\lambda & D_{12} \\ D_{12} & D_{22}-\lambda \end{vmatrix} = 0. \tag{2.2.20}$$

As such, the eigenvalues for two component system has two solutions:

$$\lambda_{1,2}\left(\boldsymbol{k}, T, \{\bar{\rho_\alpha}\}\right) = \frac{D_{11}+D_{22} \pm \sqrt{\left(D_{11}-D_{22}\right)^2 + 4D_{12}^2}}{2}. \tag{2.2.21}$$

In consequence of the third term of the Equation 2.2.21 always being greater or equal to zero, the lowest branch of the equation is:

$$\lambda_2\left(\boldsymbol{k}, T, \{\bar{\rho_\alpha}\}\right) = \frac{D_{11}+D_{22} - \sqrt{\left(D_{11}-D_{22}\right)^2 + 4D_{12}^2}}{2}. \tag{2.2.22}$$

The temperature T_C of the order-disorder transition can then be found with $\min\left(\lambda_2\left(\boldsymbol{k}, T, \{\bar{\rho_\alpha}\}\right)\right) = 0$.

2.3 Kinetic equation

The temporal evolution of the occupation probability function $\rho_\alpha\left(\boldsymbol{r}, t\right)$ follows an Onsager microscopic diffusion equation, which has already been used in the CADF theory [36]. For the α component, where $(\alpha, \beta) = \{1, ..., m\}^2$, this function is expressed as follows:

$$\frac{\partial \rho_\alpha\left(\boldsymbol{r}, t\right)}{\partial t} = \sum_{\beta=1}^{m} \sum_{\boldsymbol{r'}} \frac{L_{\alpha\beta}\left(\boldsymbol{r} - \boldsymbol{r'}\right)}{k_B T} \frac{\delta F}{\delta \rho_\beta\left(\boldsymbol{r'}, t\right)}, \tag{2.3.1}$$

where $L_{\alpha\beta}$ is the matrix of kinetic coefficients between fratons of the kind α and β. Summation is carried out over all points r' of the computational grid approximating the continuum space. The sum of occupation probabilities for the α-component over all the sites is a constant equal to the total number of fratons of type α, denoted N_α, over the entire system:

$$\sum_{\boldsymbol{r}} \rho_\alpha\left(\boldsymbol{r}, t\right) = N_\alpha. \tag{2.3.2}$$

Hence, for all $\alpha \in \{1, ..., m\}$, the summation of Equation 2.3.1 over all the sites equal zero:

$$\sum_{\boldsymbol{r}} \frac{\partial \rho_\alpha}{\partial t} = \sum_{\boldsymbol{r}} \left(\sum_{\beta=1}^{m} \sum_{\boldsymbol{r'}} \frac{L_{\alpha\beta}\left(\boldsymbol{r} - \boldsymbol{r'}\right)}{k_B T} \frac{\delta F}{\delta \rho_\beta\left(\boldsymbol{r'}, t\right)} \right) = 0. \tag{2.3.3}$$

As the driving force term in Equation 2.3.3 is independent of $\boldsymbol{r}$, but not r', this equation can be reformulated as follows:

$$\sum_{\boldsymbol{r}} \frac{\partial \rho_\alpha}{\partial t} = \frac{1}{k_B T} \sum_{\beta=1}^{m} \sum_{\boldsymbol{r'}} \frac{\delta F}{\delta \rho_\beta\left(\boldsymbol{r'}, t\right)} \sum_{\boldsymbol{r}} L_{\alpha\beta}\left(\boldsymbol{r} - \boldsymbol{r'}\right) = 0. \tag{2.3.4}$$

In the general case, the sum of the driving force over all sites and components is different than zero:

$$\sum_{\beta=1}^{m} \sum_{r'} \frac{\delta F}{\delta \rho_\beta\left(\boldsymbol{r'}, t\right)} \neq 0. \tag{2.3.5}$$

Consequently, in order to satisfy the Equation 2.3.4, the sum of the Onsager kinetics coefficient matrix over all sites must be equal to zero:

$$\sum_{\boldsymbol{r}} L_{\alpha\beta}\left(\boldsymbol{r} - \boldsymbol{r'}\right) = 0. \tag{2.3.6}$$

The conservation condition of the total number of fratons of each kind is satisfied by Equation 2.3.6. This condition translate in the reciprocal space as $\widetilde{L}_{\alpha\beta}(\boldsymbol{k}) = 0$. The Fourier transformation of the coefficients can be expressed as follows:

$$\widetilde{L}_{\alpha\beta}(\boldsymbol{k}) = \sum_{\boldsymbol{r}} L_{\alpha\beta}(\boldsymbol{r})\, e^{-i\boldsymbol{k}\boldsymbol{r}}. \tag{2.3.7}$$

The function $\widetilde{L}_{\alpha\beta}(\boldsymbol{k})$ is symmetrical, and due to Equation 2.3.6, for large distance $\boldsymbol{r} - \boldsymbol{r'}$, which correspond to small $\boldsymbol{k}$, the first non-vanishing term of the Taylor expansion is:

$$\widetilde{L}_{\alpha\beta}(\boldsymbol{k}) = \left.\frac{\partial^2 \widetilde{L}_{\alpha\beta}(\boldsymbol{k})}{\partial k^2}\right|_{\boldsymbol{k}=0} k^2, \tag{2.3.8}$$

where $\left.\frac{\partial^2 \widetilde{L}_{\alpha\beta}(\boldsymbol{k})}{\partial k^2}\right|_{\boldsymbol{k}=0}$ is the mobility coefficient matrix. This term is proportional to the jump probability between a pair of fratons of type α and β at nearest-neighbor sites per time unit. Therefore, in the reciprocal space, by means of Fourier transformation, the temporal evolution of the occupation probability function is written:

$$\frac{\partial \tilde{\rho}_\alpha(\boldsymbol{k},t)}{\partial t} = -\sum_{\beta=1}^{m} \widetilde{L}_{\alpha\beta}(\boldsymbol{k}) \left(\widetilde{V}_{\alpha\beta} \tilde{\rho}_\beta(\boldsymbol{k},t) + \left\{ \ln \frac{\rho_\beta(\boldsymbol{r},t)}{\rho_m(\boldsymbol{r},t)} \right\}_{\boldsymbol{FT}} \right), \tag{2.3.9}$$

where $\{.\}_{FT}$ denotes the Fourier transformation. Equation 2.3.9 is the one implemented in the QA, with calculations being done in the reciprocal space.

2.4 One component systems

2.4.1 Free energy and kinetic equation

A simulation grid in the system can be described by the presence or absence of a fraton. The probability of such a grid to be occupied by a fraton is denoted $\rho_f(\boldsymbol{r},t)$ and the probability of the absence of fraton, i.e a vacancy, is denoted as $\rho_v(\boldsymbol{r},t)$. Due to the conservation condition, these two variables are inter-dependent, with $\rho_v(\boldsymbol{r},t) = 1 - \rho_f(\boldsymbol{r},t)$. Therefore, the system can be described solely by the occupancy probability of the fraton, denoted as $\rho(\boldsymbol{r},t) = \rho_f(\boldsymbol{r},t)$. Vacancy-vacancy and vacancy-fratons interactions are not considered in this study. Therefore, the free energy function given by Equation 2.1.8 is expressed as follows:

$$\begin{aligned} F = & \frac{1}{2} \sum_{\boldsymbol{r},\boldsymbol{r'}} V\left(\boldsymbol{r} - \boldsymbol{r'}\right) \rho(\boldsymbol{r},t)\, \rho\left(\boldsymbol{r'},t\right) \\ & + k_B T \sum_{\boldsymbol{r}} \left[\rho(\boldsymbol{r},t) \ln \rho(\boldsymbol{r},t) + (1 - \rho(\boldsymbol{r},t)) \ln (1 - \rho(\boldsymbol{r},t)) \right]. \end{aligned} \tag{2.4.1}$$

And the response function is written:

$$D\left(\boldsymbol{k}, T, \{\bar{\rho}\}\right) = \widetilde{V}\left(\boldsymbol{k}\right) + \frac{k_B T}{\bar{\rho}\left(1-\bar{\rho}\right)}. \tag{2.4.2}$$

In this case, the temperature T_C of order-disorder transition is only linked to the minimal value of $\widetilde{V}\left(\boldsymbol{k}\right)$ and the mean concentration of fratons $\bar{\rho}$. As demonstrated in Section 2.3.1 and in Equation 2.4.2, increasing the temperature will increase the minimal value of $D\left(\boldsymbol{k}, T, \{\bar{\rho}\}\right)$, while increasing the mean concentration of fratons $\bar{\rho}$ will decrease the minimal value of $D\left(\boldsymbol{k}, T, \{\bar{\rho}\}\right)$. Therefore, the driving force of transformation will follow the same rules.

The kinetics equation, in the Fourier space, as presented in Equation 2.3.9, is also simplified as follows:

$$\frac{\partial \tilde{\rho}\left(\boldsymbol{k}, t\right)}{\partial t} = \widetilde{L}_{\alpha\beta}\left(\boldsymbol{k}\right)\left[\tilde{V}\left(\boldsymbol{k}\right)\tilde{\rho}\left(\boldsymbol{k}, t\right) + k_B T\left\{\ln\frac{\rho\left(\boldsymbol{r}, t\right)}{1-\rho\left(\boldsymbol{r}, t\right)}\right\}_{FT}\right]. \tag{2.4.3}$$

2.4.2 Interaction potentials

The choice of the interaction potential of the Hamiltonian in Equation 2.1.1 is crucial for accurately simulating the solid phases and phase transformation. The Hamiltonian should ensure the condensation of randomly distributed fratons into atomic spheres that reproduce the spatial periodicity of the selected complex structure. To meet these criteria, the interaction potential is divided into two parts [25, 124, 126]: a short-range potential which fixes the atomic radius and the long-range potential that determine the crystallographic structure.

$$V_{1-1}\left(\boldsymbol{r}-\boldsymbol{r'}\right) = \lambda_1^{sr} V_1^{sr}\left(\boldsymbol{r}-\boldsymbol{r'}\right) + \lambda_{1-1}^{lr} V_{1-1}^{lr}\left(\boldsymbol{r}-\boldsymbol{r'}\right), \tag{2.4.4}$$

where $V_1^{sr}\left(\boldsymbol{r}-\boldsymbol{r'}\right)$ and $V_{1-1}^{lr}\left(\boldsymbol{r}-\boldsymbol{r'}\right)$ represent the short- and long-range potentials, respectively, each equipped with their amplitudes λ_1^{sr} and λ_{1-1}^{lr}. Setting these amplitudes ensures that atoms have a specific and finite size while maintaining the long-range interaction strong enough to reproduce the desired crystallographic structure. In Quasi-Particle approach, this expression is implemented in reciprocal space through its Fourier transformation and normalized:

$$\begin{aligned}\widetilde{V}_{1-1}\left(\boldsymbol{k}\right) =& \lambda_1^{sr}\frac{\widetilde{V}_1^{sr}\left(\boldsymbol{k}\right)}{\max\left(\hat{V}_1^{sr}\left(\boldsymbol{k}\right)\right) - \min\left(\hat{V}_1^{sr}\left(\boldsymbol{k}\right)\right)} \\ &+ \lambda_{1-1}^{sr}\frac{\hat{V}_{1-1}^{lr}\left(\boldsymbol{k}\right)}{\max\left(\widetilde{V}_{1-1}^{lr}\left(\boldsymbol{k}\right)\right) - \min\left(\hat{V}_{1-1}^{lr}\left(\boldsymbol{k}\right)\right)},\end{aligned} \tag{2.4.5}$$

where $\widetilde{V}_1^{sr}$ and $\hat{V}_{1-1}^{lr}$ are the Fourier transformations of short- and long-range potential. The expressions of these potentials are normalized, and their respective strengths in the total potential are determined by their amplitudes λ_1^{sr} and λ_{1-1}^{lr}.

Short range potential

In the one-component simulation of austenite (FCC) to ferrite (BCC) transformation, one short-range potential and three long-range potentials were used: one for the BCC structure, another for the FCC structure, and a third to ensure a controlled phase transformation from FCC to BCC.

The short-range potential $V_{Fe}^{sr}(\boldsymbol{r}-\boldsymbol{r'})$ is a hard sphere potential chosen as a single step function in the real space. In the following, $\boldsymbol{r}-\boldsymbol{r'}$, which represented the separation distance between two fratons will be denoted as $\boldsymbol{r}$. Therefore the iron short-range potential will now be denoted $V_{Fe}^{sr}(\boldsymbol{r})$ instead of $V_{Fe}^{sr}(\boldsymbol{r}-\boldsymbol{r'})$. Its expression is given by Equation 2.4.6, and the shape of the potential is shown in Figure 2.4.

$$V_{Fe}^{sr}(\boldsymbol{r}) = \begin{cases} -1 & \text{, if } 0 < r < R_{Fe}, \\ \xi & \text{, if } R_{Fe} \leq r \leq R_{Fe} + \Delta R_{Fe}, \\ 0 & \text{, else.} \end{cases} \tag{2.4.6}$$

In this equation, R_{Fe} sets the width of the attractive part of the short-range potential, enabling the condensation of fratons into atomic spheres of radius R_{Fe}. ΔR_{Fe} and ξ are represent respectively the width and the height of the potential barrier. The repulsive contribution in the short-range potential prevents the overlapping of atomic spheres. Their impact on the elastic properties of the system will be discussed in Section 2.7.

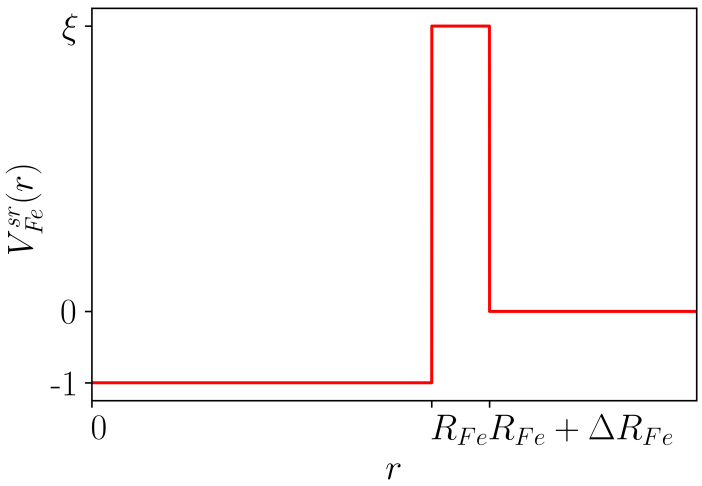

Figure 2.4: Schematic iron short-range interaction potential $V_{Fe}^{sr}(r)$. ξ =4, $R_{Fe} = 2.81$ and $\Delta R_{Fe} = 0.17 R_{Fe}$.

The Fourier transformation of this potentiel is written:

$$\widetilde{V}_{Fe}^{sr}(\boldsymbol{k}) = \sum_{\boldsymbol{r}} V_{Fe}^{sr}(\boldsymbol{r}) e^{-i\boldsymbol{k}.\boldsymbol{r}}. \tag{2.4.7}$$

The Equation 2.4.7 yields:

$$\begin{aligned}\widetilde{V}_{Fe}^{sr}(\boldsymbol{k}) = \frac{4\pi}{k^3}\Big[\, & kR_{Fe}\cos\left(kR_{Fe}\right) - \sin\left(kR_{Fe}\right) \\ & + \xi\left(-kR_{Fe}^{*}\cos\left(k\tilde{R}_{Fe}\right) + \sin\left(kR_{Fe}^{*}\right)\right. \\ & + \left.\ kR_{Fe}\cos\left(kR_{Fe}\right) - \sin\left(kR_{Fe}\right)\right)\Big]\,,\end{aligned} \tag{2.4.8}$$

where $R_{Fe}^{*} = R_{Fe} + \Delta R_{Fe}$. The Fourier transformation of the short range potential is depicted in Figure 2.5.

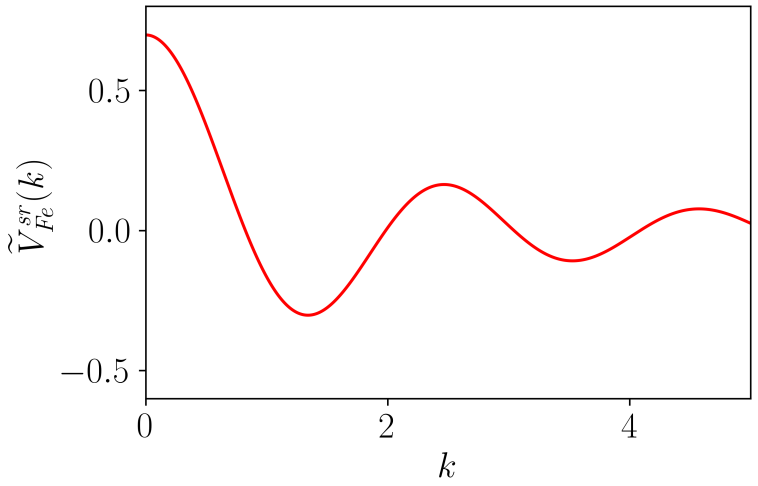

Figure 2.5: Schematic Fourier transformation of the normalized iron short-range interaction potential $\tilde{V}_{Fe}^{sr}(k)$. ξ =4, $R_{Fe} = 2.81$ and $\Delta R_{Fe} = 0.17 R_{Fe}$.

Long range potentials

The long range potential defines the specific crystal structure for each component. The challenge faced with the FCC to BCC transformation is the presence of two phases with different crystallographic structures for only one component. As such, the potential driving the transformation must allow the growth of the BCC phase at the interface with the FCC structure while keeping the FCC phase metastable to reproduce the displasive FCC to BCC structural transformation. The choice to use only one potential to describe both FCC and BCC phases is a good compromise between computational cost and a yield between the lattice parameters of both phase being close to $\sqrt{(3/2)}$ with correspond to the conservation of volume between FCC and BCC phases. The misfit used in QA is of $a_{FCC}/a_{BCC} = 1.23$ which is underestimated compared to experimental observations where it is between 1.25 and 1.27. This may result in different elastic strain and shape of FCC to BCC interface. However, it is assumed, based on MD simulations [45], that this version of QA should be able to reproduce the mechanism of the FCC to BCC phase transformation.

Furthermore, the FCC to BCC simulation with the QA requires pre-relaxed FCC and BCC structures in two independent single-phase simulations. With this context, three different long-range potentials were used: one for FCC, one for BCC, and one to perform the FCC to BCC phase transformation. All three potentials are expressed in the reciprocal space:

$$\widetilde{V}^{lr}_{Fe-Fe}(\boldsymbol{k}) = \sum_{\boldsymbol{r}} V^{lr}_{Fe-Fe}(\boldsymbol{r})\, e^{-i\boldsymbol{k}.\boldsymbol{r}}, \tag{2.4.9}$$

where $\boldsymbol{k}$ belongs to the first Brillouin zone. In the following, the long range potentials for homogeneous FCC, BCC and FCC to BCC phase transformation, will respectively be denoted V^{lr}_{γ}, V^{lr}_{α} and $V^{lr}_{\gamma-\alpha}$. These potentials are defined as linear combinations of Gaussian functions [126]. In the general case, the number of minima present in the long-range potential should be equal to the number of non-equivalent structural reflections in the first Brillouin zone of a given crystallographic structure. The first Brillouin zone for FCC and BCC structure are depicted in Figure 2.6.

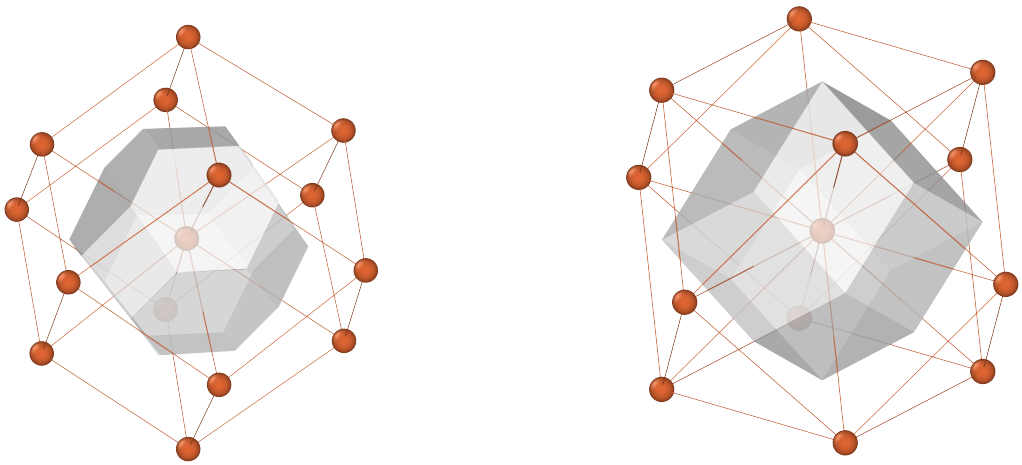

(a) (b)

Figure 2.6: First Brillouin zone for FCC (**a**) and BCC crystal lattice(**b**) where high symmetry points are represented.

When examining the diffraction pattern of the FCC structure, two non-equivalent structural reflections are found in the first Brillouin zone, each with the same number of spots. These spots are located at $k^{\gamma}_1 = 2\pi\sqrt{3}/a_{\gamma}$ and $k^{\gamma}_2 = 4\pi/a_{\gamma}$, resulting in the long-range FCC interaction potential $\hat{V}^{lr}_{\gamma}$ having two wells of equal depth. For the BCC structure, the long-range potential features with a single well located at $k^{\alpha} = 2\pi\sqrt{2}/a_{\alpha}$, as it is sufficient to reproduce the crystallographic structure [25, 124].

The FCC and BCC long range potentials are then expressed by Equations 2.4.10:

$$\begin{cases} \widetilde{V}_{\gamma}^{lr}(k) = -\exp\left(-\frac{\left(k-k_1^{\gamma}\right)^2}{2\left(\sigma_1^{\gamma}\right)^2}\right) - \exp\left(-\frac{\left(k-k_2^{\gamma}\right)^2}{2\left(\sigma_2^{\gamma}\right)^2}\right), \\ \widetilde{V}_{\alpha}^{lr}(k) = -\exp\left(-\frac{(k-k^{\alpha})^2}{2(\sigma^{\alpha})^2}\right), \end{cases} \tag{2.4.10}$$

where σ_1^{α}, σ_2^{α} and σ^{γ} are the standard deviation of Gaussian wells. Their impact on the elastic properties of the system will be discussed later.

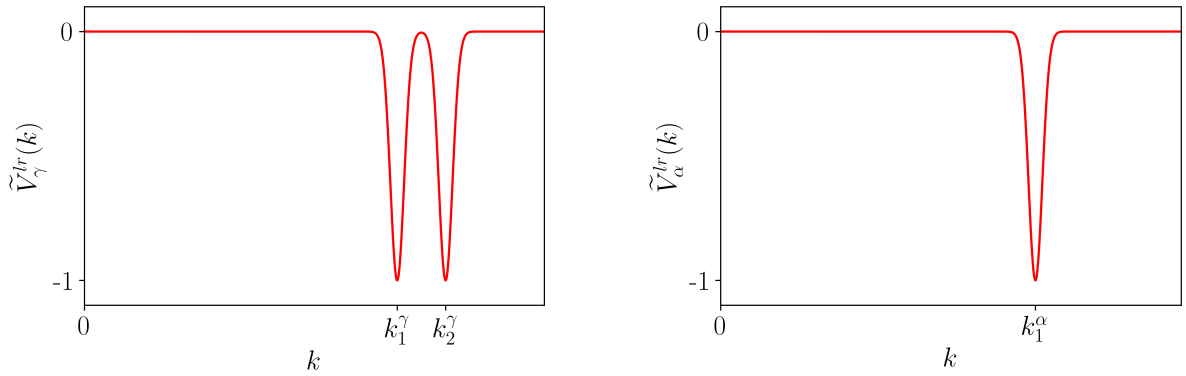

(a) (b)

Figure 2.7: Schematic representation of long-range interaction for FCC (**a**) and BCC structures (**b**).

Those two long range potentials, depicted in Figure 2.7, are used to simulate pure FCC or BCC structure but are unable to simulate the displacive transformation from FCC to BCC. In fact, if the BCC long-range potential is used to simulate the FCC to BCC transformation, the initial FCC structure becomes strongly unstable: the transformation will thus occur throughout the entire FCC bulk instead of propagating from the interface. In order to maintain the driving force of transformation in favor of the BCC structure while rendering the FCC structure metastable, the second well of $\hat{V}_{\gamma}^{lr}(k)$ was added to $\hat{V}_{\alpha}^{lr}(k)$ with a smaller depth. The amplitude of this second well is controlled by a multiplicative factor ϵ with $0 < \epsilon < 1$ to ensure that the BCC strucure still has a lower value of chemical potential than the FCC phase. The obtained potential is given by Equation 2.4.11 and depicted schematically in Figure 2.8.

$$\widetilde{V}_{\gamma-\alpha}^{lr} = -\exp\left(\frac{(k-k_1^{\alpha})^2}{(2\sigma^{\alpha})^2}\right) - \epsilon\exp\left(\frac{(k-k_2^{\gamma})^2}{(2\sigma_2^{\gamma})^2}\right). \tag{2.4.11}$$

The total interaction potentials, for each long-range potentials described by Equations 2.4.10 and 2.4.11, is depicted in Figure 2.9.

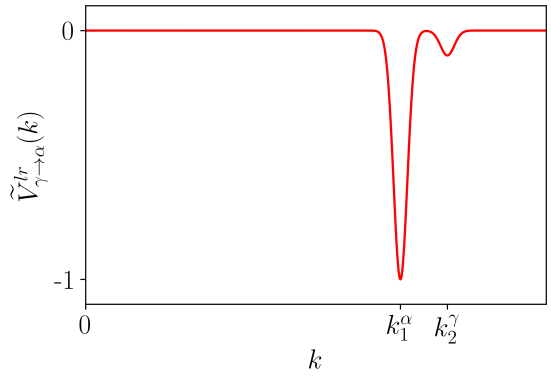

Figure 2.8: Schematic interaction potential used to simulate FCC to BCC phase transformation.

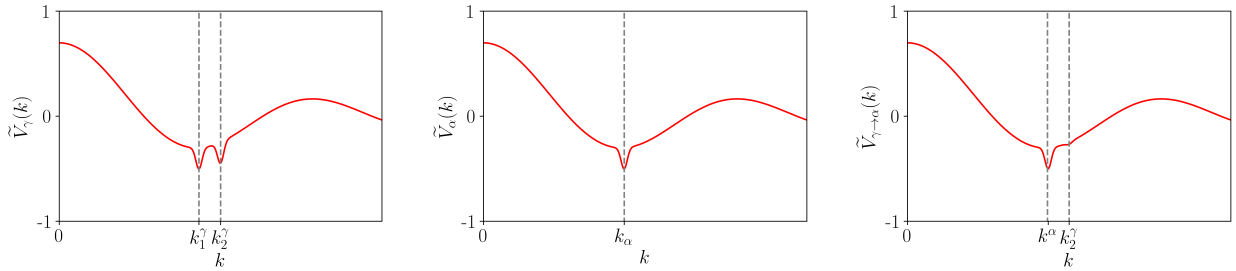

(a) (b) (c)

Figure 2.9: Normalized interaction potentials $V_\gamma(k)$ (**a**), $V_\alpha(k)$ (**b**) and $V^{lr}_{\gamma\to\alpha}(k)$ (**c**). $\sigma^\alpha = \sigma_1^\gamma = \sigma_2^\gamma = 0.03$, $a_\alpha = 6.5\Delta x$ and $a_\gamma = 8.0\Delta x$.

2.5 Two components systems

2.5.1 Free energy and kinetic equation

For two-components systems, every grid can be occupied by either a vacancy or two possible type of fratons. The probability of a grid to be occupied by a 'vacancy,' as for one-component systems, depends on the probability of the grid to be occupied by a fraton. The difference is that two different types of fratons coexist. Therefore, the occupation probability of a grid not containing a fraton is $\rho_v(\boldsymbol{r},t) + \rho_1(\boldsymbol{r},t) + \rho_2(\boldsymbol{r},t) = 1$. In this case, the system is completely described by two occupation probabilities: $\rho_1(\boldsymbol{r},t)$ for first type of fratons and $\rho_2(\boldsymbol{r},t)$ for second type of fratons. Similar to the one-component system, vacancy interactions were neglected, and likewise, for two-component systems, only interactions between fratons of iron and carbon will be considered. Thus,

the free energy function for two-component systems can be written as:

$$\begin{aligned} F =& \frac{1}{2}\sum_{\boldsymbol{r},\boldsymbol{r'}}\left[V_{1-1}\left(\boldsymbol{r}-\boldsymbol{r'}\right)\rho_1\left(\boldsymbol{r},t\right)\rho_1\left(\boldsymbol{r},t\right)+2V_{1-2}\left(\boldsymbol{r}-\boldsymbol{r'}\right)\rho_1\left(\boldsymbol{r},t\right)\rho_2\left(\boldsymbol{r},t\right)\right. \\ &\left.+\ V_{2-2}\left(\boldsymbol{r}-\boldsymbol{r'}\right)\rho_2\left(\boldsymbol{r},t\right)\rho_2\left(\boldsymbol{r},t\right)\right]+k_BT\sum_{\boldsymbol{r}}\left[\rho_1\left(\boldsymbol{r},t\right)\ln\rho_1\left(\boldsymbol{r},t\right)\right. \\ &\left.+\rho_2\left(\boldsymbol{r},t\right)\ln\rho_2\left(\boldsymbol{r},t\right)+\left(1-\rho_1\left(\boldsymbol{r},t\right)-\rho_2\left(\boldsymbol{r},t\right)\right)\ln\left(1-\rho_1\left(\boldsymbol{r},t\right)-\rho_2\left(\boldsymbol{r},t\right)\right)\right], \end{aligned} \tag{2.5.1}$$

As demonstrated in section.(2.2), the response function is a two-by-two matrix:

$$D\left(\boldsymbol{k},T,\bar{\rho}_1,\bar{\rho}_2\right)=\begin{pmatrix} D_{1-1}\left(\boldsymbol{k},T,\bar{\rho}_1,\bar{\rho}_2\right) & D_{1-2}\left(\boldsymbol{k},T,\bar{\rho}_1,\bar{\rho}_2\right) \\ D_{1-2}\left(\boldsymbol{k},T,\bar{\rho}_1,\bar{\rho}_2\right) & D_{2-2}\left(\boldsymbol{k},T,\bar{\rho}_1,\bar{\rho}_2\right)\end{pmatrix}, \tag{2.5.2}$$

where:

$$D_{1-1}\left(\boldsymbol{k},T,\bar{\rho}_1,\bar{\rho}_2\right)=\hat{V}_{1-1}\left(\boldsymbol{k}\right)+k_BT\frac{1-\bar{\rho}_2}{\bar{\rho}_1\left(1-\bar{\rho}_1-\bar{\rho}_2\right)}, \tag{2.5.3}$$

$$D_{1-2}\left(\boldsymbol{k},T,\bar{\rho}_1,\bar{\rho}_2\right)=\hat{V}_{1-1}\left(\boldsymbol{k}\right)+k_BT\frac{1}{1-\bar{\rho}_1-\bar{\rho}_2}, \tag{2.5.4}$$

$$D_{2-2}\left(\boldsymbol{k},T,\bar{\rho}_1,\bar{\rho}_2\right)=\hat{V}_{1-1}\left(\boldsymbol{k}\right)+k_BT\frac{1-\bar{\rho}_1}{\bar{\rho}_2\left(1-\bar{\rho}_1-\bar{\rho}_2\right)}. \tag{2.5.5}$$

For a two-components system two kinetics equation should be solved, one for each component. They are expressed and solved in the reciprocal space by mean of Fourier transformation:

$$\begin{aligned} \frac{\partial\rho_1\left(\boldsymbol{k},t\right)}{\partial t} =& L_{1-1}k^2\Bigg[V_{1-1}\left(\boldsymbol{k}\right)\rho_1\left(\boldsymbol{k},t\right)+V_{1-2}\left(\boldsymbol{k}\right)\rho_2\left(\boldsymbol{k},t\right) \\ &+k_BT\left\{\ln\frac{\rho_1\left(\boldsymbol{r},t\right)}{1-\rho_1\left(\boldsymbol{r},t\right)-\rho_2\left(\boldsymbol{r},t\right)}\right\}_{FT}\Bigg] \\ &+L_{1-2}k^2\Bigg[V_{1-2}\left(\boldsymbol{k}\right)\rho_1\left(\boldsymbol{k},t\right)+V_{2-2}\left(\boldsymbol{k}\right)\rho_2\left(\boldsymbol{k},t\right) \\ &+k_BT\left\{\ln\frac{\rho_2\left(\boldsymbol{r},t\right)}{1-\rho_1\left(\boldsymbol{r},t\right)-\rho_2\left(\boldsymbol{r},t\right)}\right\}_{FT}\Bigg], \end{aligned} \tag{2.5.6}$$

$$\begin{aligned} \frac{\partial\rho_2\left(\boldsymbol{k},t\right)}{\partial t} =& L_{1-2}k^2\Bigg[V_{1-1}\left(\boldsymbol{k}\right)\rho_1\left(\boldsymbol{k},t\right)+V_{1-2}\left(\boldsymbol{k}\right)\rho_2\left(\boldsymbol{k},t\right) \\ &+k_BT\left\{\ln\frac{\rho_1\left(\boldsymbol{r},t\right)}{1-\rho_1\left(\boldsymbol{r},t\right)-\rho_2\left(\boldsymbol{r},t\right)}\right\}_{FT}\Bigg] \\ &+L_{2-2}k^2\Bigg[V_{1-2}\left(\boldsymbol{k}\right)\rho_1\left(\boldsymbol{k},t\right)+V_{2-2}\left(\boldsymbol{k}\right)\rho_C\left(\boldsymbol{k},t\right) \\ &+k_BT\left\{\ln\frac{\rho_2\left(\boldsymbol{r},t\right)}{1-\rho_1\left(\boldsymbol{r},t\right)-\rho_2\left(\boldsymbol{r},t\right)}\right\}_{FT}\Bigg]. \end{aligned} \tag{2.5.7}$$

Equations 2.5.6 and 2.5.7 are then applied to the specific case of Fe-C two-components system,

which allows further simplifications.

2.5.2 Diffusion coefficients in an iron-carbon system

As shown in Section 2.3.1, the Onsager kinetics coefficient matrix is a two by two matrix. In the case of an Fe-C system it is wrote:

$$L = \begin{pmatrix} L_{Fe-Fe} & L_{Fe-C} \\ L_{Fe-C} & L_{C-C} \end{pmatrix}, \tag{2.5.8}$$

where the matrix is symmetric and positive definite. Carbon atoms are small (approximately 70pm of radius) compared to iron atoms (approximately 140pm of radius), therefore they diffuse through lattice interstices in the octahedral sites. As such, it can be assumed that there is no substitution mechanism. Consequently, L_{Fe-C} is equal to zero, which simplifies Equations 2.5.6 and 2.5.7:

$$\begin{aligned} \frac{\partial \rho_{Fe}(\boldsymbol{k},t)}{\partial t} =& L_{Fe-Fe}k^2\Big[V_{Fe-Fe}(\boldsymbol{k})\,\rho_{Fe}(\boldsymbol{k},t) + V_{Fe-C}(\boldsymbol{k})\,\rho_C(\boldsymbol{k},t) \\ &+ k_BT\left\{\ln\frac{\rho_{Fe}(\boldsymbol{r},t)}{1-\rho_{Fe}(\boldsymbol{r},t)-\rho_C(\boldsymbol{r},t)}\right\}_{FT}\Big], \end{aligned} \tag{2.5.9}$$

$$\begin{aligned} \frac{\partial \rho_{C}(\boldsymbol{k},t)}{\partial t} =& L_{C-C}k^2\Big[V_{Fe-C}(\boldsymbol{k})\,\rho_{Fe}(\boldsymbol{k},t) + V_{C-C}(\boldsymbol{k})\,\rho_C(\boldsymbol{k},t) \\ &+ k_BT\left\{\ln\frac{\rho_{C}(\boldsymbol{r},t)}{1-\rho_{Fe}(\boldsymbol{r},t)-\rho_C(\boldsymbol{r},t)}\right\}_{FT}\Big]. \end{aligned} \tag{2.5.10}$$

The kinetic diffusion coefficient L_{C-C} must be higher than L_{Fe-Fe}. However it has been found in [127] that the system is quite insensitive to the exact values chosen for these coefficients, as long as the matrix is positive definite.

2.5.3 Interaction potentials

In the Fe-C two-component system, three potentials must be defined: the Fe-Fe $V_{Fe-Fe}(\boldsymbol{r}-\boldsymbol{r'})$, the Fe-C $V_{Fe-C}(\boldsymbol{r}-\boldsymbol{r'})$ and the C-C $V_{C-C}(\boldsymbol{r}-\boldsymbol{r'})$ interaction potentials.

Carbon-carbon interaction potential

The C-C interaction potential $V_{C-C}(\boldsymbol{r}-\boldsymbol{r'})$ like the Fe-Fe interaction potential, is divided into two parts: a short-range potential that assembles carbon fratons into atomic spheres of radius R_C and a long range interaction potential. The shape of the short-range potential is identical to the one used for the Fe-Fe interaction potential in Equation 2.4.6. However, the long-range potential should be defined differently. For the C-C interaction, this potential must take into account the strong repulsion between carbon atoms situated in the octahedral sites of the iron lattice [128]. This repulsion decays rapidly with distance; hence, it is called a "short-range" repulsion, even though it is modeled by a long-range interaction potential. This interaction mimic chemical and

elastic interaction between carbon at octahedral position which is highly repulsive at close range [128]. It can be evaluated using ab-initio methods, as demonstrated in [128, 129]. In this work, this potential was chosen as a decay exponential function:

$$V_{C-C}^{lr}(\boldsymbol{r}) = \begin{cases} 0 & \text{, if } r < R_C + \Delta R_C, \\ e^{-\alpha t} & \text{, if } r \geq R_C + \Delta R_C, \end{cases} \tag{2.5.11}$$

where ΔR_C is the width of the potential barrier of the short range potential and α determines the strength of the repulsive force. Then the Fourier transformation of the potential V_{C-C}^{lr} can be written as:

$$\begin{aligned} \widetilde{V}_{C-C}^{LR}(\boldsymbol{k}) =& \frac{4\pi}{k} e^{-\alpha R^*} \left[\frac{R^* k \cos(kR^*) + R^* \alpha \sin(kR^*)}{\alpha^2 + k^2} \right. \\ & \left. + \frac{\left(\alpha^2 - k^2\right) \sin(kR^*) + 2\alpha k \cos(kR^*)}{\left(\alpha^2 + k^2\right)^2} \right], \end{aligned} \tag{2.5.12}$$

where $R^* = R_C + \Delta R_C$. The C-C long-range interaction potential, its Fourier transformation and the Fourier transformation of the total C-C interaction potential are all schematically depicted in Figure 2.10.

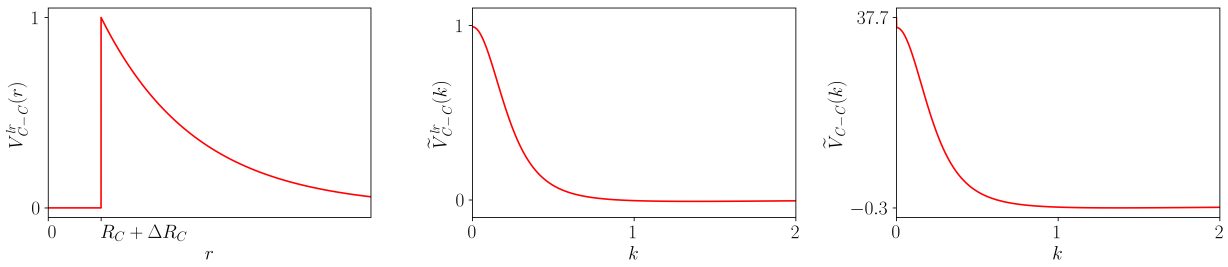

(a) (b) (c)

Figure 2.10: Schematic illustration of long-range C-C interaction potential (**a**), its Fourier transformation (**b**) and the Fourier transformation of the total C-C interaction potential.

Like the Fe-Fe interaction potential in Equation 2.4.5, the C-C interaction potential is normalized and the strengths of short- and long-range potentials are determined by their respective amplitudes λ_C^{sr} and λ_{C-C}^{lr}:

$$\begin{aligned} \widetilde{V}_{C-C}(\boldsymbol{k}) =& \lambda_C^{sr} \frac{\widetilde{V}_C^{sr}(\boldsymbol{k})}{\max\left(\widetilde{V}_C^{sr}(\boldsymbol{k})\right) - \min\left(\widetilde{V}_C^{sr}(\boldsymbol{k})\right)} \\ & + \lambda_{C-C}^{sr} \frac{\widetilde{V}_{C-C}^{lr}(\boldsymbol{k})}{\max\left(\widetilde{V}_{C-C}^{lr}(\boldsymbol{k})\right) - \min\left(\widetilde{V}_{C-C}^{lr}(\boldsymbol{k})\right)}. \end{aligned} \tag{2.5.13}$$

This normalization allows a better control of the simulation and keeps a simple parametrization of the systems

Iron-carbon interaction potential

In the case of the Fe-C interaction potential $V_{Fe-C}\left(\boldsymbol{r}-\boldsymbol{r'}\right)$, there is no requirement for an atomic sphere formation. As such this potential is entirely expressed by its long-range part $V^{lr}_{Fe-C}\left(\boldsymbol{r}-\boldsymbol{r'}\right)$. In this work, the Fe-C potential used was proposed by A.G.Khachaturyan in [130] as a pairwise repulsive potential under the form of a screened Coulomb potential:

$$V^{lr}_{Fe-C}\left(\boldsymbol{r}\right)=\frac{e^2}{r}\exp\left(-\frac{r}{r_d}\right), \tag{2.5.14}$$

where $r_d=0.2036a_\gamma$ is the Debye radius which set the screening distance and e the effective charge of interstitial atoms. This charge is set to one in the simulations since electromagnetic effects are not considered. The Fourier transformation of this potential is given by the following equation:

$$\hat{V}^{lr}_{Fe-C}\left(\boldsymbol{k}\right)=\frac{1}{\left(\frac{1}{r_d}\right)^2+k^2}. \tag{2.5.15}$$

Then, the long-range potential in Equation 2.5.15, schematized in Figure 2.11 is normalized and controlled by an amplitude λ^{lr}_{Fe-C}:

$$\widetilde{V}_{Fe-C}\left(\boldsymbol{k}\right)=\lambda^{lr}_{Fe-C}\frac{\widetilde{V}^{lr}_{Fe-C}\left(\boldsymbol{k}\right)}{\max\left(\widetilde{V}^{lr}_{Fe-C}\left(\boldsymbol{k}\right)\right)-\min\left(\widetilde{V}^{lr}_{Fe-C}\left(\boldsymbol{k}\right)\right)}. \tag{2.5.16}$$

All the potential for the Fe-C system are thus defined and their normalization and given amplitude allow a fine tuning of the simulation.

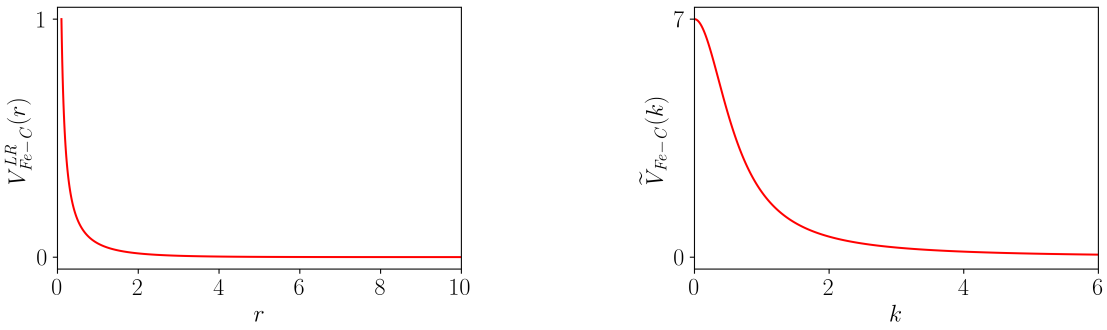

(a) (b)

Figure 2.11: Schematic illustration of the Fe-C long-range (**a**) and total (**b**) interaction potentials.

2.6 Numerical schemes

For a one-component system, the numerical resolution of the kinetic equation is done with a the combination of the Fourier-spectral treatment of space and the time integration of Eyre [131, 132]. It is written under a discretized form in [132]:

$$\frac{\partial \widetilde{\rho}(\boldsymbol{k},t)}{\partial t} = a\left(\widetilde{\rho}(\boldsymbol{k},t)\right) + b(\boldsymbol{k})\,\widetilde{\rho}(\boldsymbol{k},t+\Delta t)\,, \tag{2.6.1}$$

where:

$$a\left(\widetilde{\rho}(\boldsymbol{k},t)\right) = |\boldsymbol{k}|^2\left[\left(A_c + \widetilde{V}_{1-1}^{LR}(\boldsymbol{k})\right)\widetilde{\rho}(\boldsymbol{k},t) - \left\{\ln\frac{\rho(\boldsymbol{r}),t}{1-\rho(\boldsymbol{r},t)}\right\}_{FT}\right], \tag{2.6.2}$$

$$b = |\boldsymbol{k}|^2\left(A_c + \widetilde{V}_1^{SR}(\boldsymbol{k})\right). \tag{2.6.3}$$

The parameter A_c in Equations 2.6.2 and 2.6.3 is a "weight" defined in [132]. This numerical scheme allows the use of high time steps, several orders of magnitude higher than in semi-implicit Fourier, while guaranteeing the gradient-stability of the numerical solutions with a small trade-off in precision.

For the two-component system, a third order semi-implicit scheme is used [133]:

$$\frac{\partial \widetilde{\rho}(\boldsymbol{k},t)}{\partial t} = \frac{11\partial\widetilde{\rho}(\boldsymbol{k},t+\Delta t) - 18\partial\widetilde{\rho}(\boldsymbol{k},t) + 9\partial\widetilde{\rho}(\boldsymbol{k},t-\Delta t) - 2\partial\widetilde{\rho}(\boldsymbol{k},t-2\Delta t)}{6\Delta t}. \tag{2.6.4}$$

At the first time step this equation is replaced by a first order derivative and at the second time step by a second order derivative.

2.7 Elastic properties

In the Quasi-particles approach, the elastic properties of the system can be adjusted with some specific parameters. The values of standard Gaussian deviation of the Fe-Fe long-range interaction potentials $(\sigma_1^\alpha, \sigma_2^\gamma, \sigma_2^\gamma)$ considered in Equation 2.4.10 and 2.4.11 serve to adjust these properties. However, other parameters such as the height ξ and width ΔR_{Fe} of the potential barrier, considered for the short range potential in Equation 2.4.6. These two parameters were set to minimize their impact on the elastic properties [25] and as such only $(\sigma_1^\alpha, \sigma_2^\gamma, \sigma_2^\gamma)$ are set to adjust elastic properties.

Both FCC and BCC are cubic crystals and in this case, only three independent elastic constants are considered: C_{11}, C_{12}, C_{44}. The free energy in the QA is dependent of the deformation tensor $\hat{\varepsilon}$, for small deformations it can be written in the form of Taylor series in relation with ε_k variables

in Voigt notation:

$$F\left(\varepsilon_k\right) = F_0 + \frac{V_0}{2} \sum_{m,n=1}^{6} C_{mn} \epsilon_m \varepsilon_n, \tag{2.7.1}$$

where F_0 is the free energy of the system defined in Equation 2.1.8 and V_0 the volume of the system before the deformation.

In order to determine the elastic constants of the system, three type of deformations are applied: cubic ($\widehat{D}_c$), orthorhombic ($\widehat{D}_o$) and monoclinic ($\widehat{D}_m$). Their deformation matrices are:

$$\widehat{D}_c = \begin{pmatrix} 1+\varepsilon & 0 & 0 \\ 0 & 1+\varepsilon & 0 \\ 0 & 0 & 1+\varepsilon \end{pmatrix}, \widehat{D}_o = \begin{pmatrix} 1+\varepsilon & 0 & 0 \\ 0 & 1-\varepsilon & 0 \\ 0 & 0 & 0 \end{pmatrix}, \widehat{D}_m = \begin{pmatrix} 1 & \varepsilon & 0 \\ 0 & 1 & 0 \\ 0 & 0 & 0 \end{pmatrix}. \tag{2.7.2}$$

The free energy is then expressed for each type of deformation:

$$F_c(\varepsilon) = F_0 + \frac{3}{2} V_0 \left(C_{11} + 2C_{12}\right) \varepsilon^2 \tag{2.7.3}$$

$$F_o(\varepsilon) = F_0 + V_0 \left(C_{11} - C_{12}\right) \varepsilon^2 \tag{2.7.4}$$

$$F_m(\varepsilon) = F_0 + V_0 \frac{C_{44}}{2} \varepsilon^2 \tag{2.7.5}$$

The definition of the Hermoltz free energy with respect to the three type of deformation of Equation 2.7.2 allow the calculation of elastic constants. In particular, the yield between the bulk modulus $B = \left(C_{11} + 2C_{12}\right)/3$ of each phase and the Zener anisotropy parameter $A = 2C_{44}/\left(C_{11} - C_{12}\right)$ are computed. The comparison between QA simulation for each phase and the literature is done in the following chapter.

Chapter 3

QA modeling of FCC to BCC phase transformation

In this chapter, the Quasi-Particles approach (QA) is applied to investigate the FCC to BCC phase tranformation. The objective is to gain a deeper understanding of the structure and propagation mode of the FCC-BCC interface and identify the transformation pathway.

In addition, in order to extract the relevant information from the simulation results, several analysis tools were adapted from atomistic simulation methods or experimental techniques to fit the QA framework. The results from QA simulations were analyzed using Slip Vector Analysis (SVA) [134] and Common Neighbor Analysis (CNA). The austenite to ferrite phase transformation was visualized with Paraview [135] and Ovito [136], after extracting atomic positions from the fluctuations of the occupation probability field provided by QA simulations, using the *fraton2atom* package [137].

The wide range of possible geometries for the austenite-ferrite interface requires to define a specific set of simulated interfaces. As detailed in Chapter 1, the principal geometric properties, i.e, the orientation relationship (OR) and the habit plane (HP), determine the characteristics of the FCC-BCC interface. Furthermore, theoretical models such as the PTMC [42] suggest a dependence between the misfit and orientation of the HP. Most ORs observed in experience lie between the Kurdjumov-Sachs (KS) [39] OR and the Nishiyama-Wasserman (NW) [46] OR, conserving the parallel alignment between $\{1\,1\,1\}_\gamma$ and $\{0\,1\,1\}_\alpha$ planes.

In this study, three ORs are considered: KS, NW, and an intermediate OR, known as the Greninger-Troiano (GT) OR [52]. The GT OR has an angle of approximately 2.40° between the $\langle 1\,1\,1\rangle_\gamma$ and $\langle 1\,1\,\bar{1}\rangle_\alpha$.directions. A table with all variants for these three ORs is provided in **Appendix A**. To ensure that QA simulations results remains consistent across different OR variants, two variants with distinct Bain directions were simulated for each OR. The list of simulated ORs

is presented in Table 3.1.

OR	FCC plane	BCC plane	FCC direction	BCC direction	Bain variant
KS v1	$\mathbf{(1\,1\,1)_\gamma}$	$\mathbf{(0\,1\,1)_\alpha}$	$\mathbf{[1\,0\,\bar{1}]_\gamma}$	$\mathbf{[1\,1\,\bar{1}]_\alpha}$	$\boldsymbol{B_3}$
KS v2	$(1\,1\,1)_\gamma$	$(0\,1\,1)_\alpha$	$[1\,0\,\bar{1}]_\gamma$	$[\bar{1}\,1\,\bar{1}]_\alpha$	B_1
NW v2	$\mathbf{(1\,1\,1)_\gamma}$	$\mathbf{(0\,1\,1)_\alpha}$	$\mathbf{[\bar{1}\,1\,0]_\gamma}$	$\mathbf{[1\,0\,0]_\alpha}$	$\boldsymbol{B_3}$
NW v3	$(1\,1\,1)_\gamma$	$(0\,1\,1)_\alpha$	$[0\,\bar{1}\,1]_\gamma$	$[1\,0\,0]_\alpha$	B_1
GT v1	$\mathbf{(1\,1\,1)_\gamma}$	$\mathbf{(0\,1\,1)_\alpha}$	$\mathbf{[12\,5\,\bar{17}]_\gamma}$	$\mathbf{[7\,17\,\bar{17}]_\alpha}$	$\boldsymbol{B_3}$
GT v2	$(1\,1\,1)_\gamma$	$(0\,1\,1)_\alpha$	$[\bar{17}\,5\,12]_\gamma$	$[7\,\bar{17}\,17]_\alpha$	B_1

Table 3.1: KS, NW and GT simulated ORs with the Quasi-particles approach. ORs presented in this chapter are in bold.

No meaningful differences were found between different variants for a given OR. Therefore, the results presented in this chapter will primarily focus on one variant for each OR (in bold characters in Table 3.1. However, as discussed in Chapter 1, the OR alone does not fully describe the morphology of the interface, as the habit plane must also be taken into account. In low-alloy steel and pure iron, this plane can differ from the close-packed plane $\{1\,1\,1\}_\gamma$ and is often found between $\{1\,1\,1\}_\gamma$ and $\{1\,2\,1\}_\gamma$ [14, 45]. Therefore, it can deviate by up to 20° from the close-packed plane.

Both the HP and OR depend on lattice misfit between the FCC and BCC phases and the concentration of alloying elements. For low-alloy steels and pure iron, the expected OR is typically Kurdjumov-Sachs (KS) [138]. The habit plane for a misfit of 1.23, calculated using Khachaturyan's formula [45] Equation 1.2.9 in the Chapter 1, is predicted to deviate by less than 1° from the $(1\,1\,1)_\gamma$ plane. However, using the habit plane expression determined by Wechsler et al. [42], the habit plane is at 21° from $(1\,1\,1)_\gamma$, close to $(1\,2\,1)_\gamma$ HP. Moreover, experimental analyses show that the austenite-ferrite interface is not perfectly consistent with these predictions and can exhibit multiple HPs even when the composition and lattice parameters are fixed [7]. Similarly, the OR can deviate by a few degrees from KS and NW [7].

Therefore, to represent a wide range of interfaces, several different ORs and HPs were selected in QA simulations. For all ORs, the $(1\,1\,1)_\gamma$ habit plane was simulated, along with at least one additional HP close to the habit plane reported in the literature for a specific OR [14]. Additionally, the habit planes $(5\,7\,5)_\gamma$ and $(1\,2\,1)_\gamma$ were simulated to explore HPs with significant deviation from $(1\,1\,1)_\gamma$. The complete list of HPs simulated for each OR is provided in Table 3.2, where HPs presented in the manuscripts are in bold characters.

However, as is common in many atomistic simulations [13, 14, 16, 64, 85, 139], the simulations in this study are conducted on pure iron with fixed lattice parameters. The interface characteristics, including its shape, a careful assessment of interfacial defects, and its motion, must then be defined.

	KS OR	NW OR	GT OR
HP	$[1\,1\,1]_\gamma$ $\mathbf{[5\,7\,5]_\gamma}$ $\mathbf{[1\,2\,1]_\gamma}$	$\mathbf{[1\,1\,1]_\gamma}$ $[5\,7\,5]_\gamma$ $\mathbf{[2\,3\,2]_\gamma}$ $[1\,2\,1]_\gamma$	$\mathbf{[1\,1\,1]_\gamma}$ $[5\,7\,5]_\gamma$ $\mathbf{[1\,2\,1]_\gamma}$

Table 3.2: HP simulated for each OR variant. HPs presented in this chapter are in bold.

This chapter is organized as follows. First, the numerical implementation of the QA simulation for the FCC to BCC phase transformation in pure iron is presented. Then, the interface structure and its motion for each OR will be examined.

3.1 Numerical implementation

3.1.1 Numerical parameters

In order to apply our simulation model to the FCC to BCC phase transformation in iron, we need to estimate the values of various input parameters. The lattice parameters of austenite and ferrite were set to achieve a misfit of 1.23 between the FCC and BCC structures. In our simulations, with the length scale set to $\Delta x = 0.0445$ nm, this corresponds to $a_\gamma = 8.0\Delta x = 0.356$ nm and $a_\alpha = 6.5\Delta x = 0.289$ nm. As discussed in Chapter 2, while this misfit is underestimated compared to experimental observations for different steels and may result in slightly different elastic strains across the FCC-BCC interface, we suggest that it might reproduce the FCC to BCC phase transformation and its characteristics. Indeed, with the selected parameters, the Zener anisotropy parameter for the interaction potential was calculated for both the FCC and BCC phases: $A_\gamma = 3.1$ for the FCC phase and $A_\alpha = 1.3$ for the BCC phase. Because $A > 1$ for both phases, the elastic 'soft' directions, which minimize the elastic energy, are $\langle 1\,0\,0\rangle_\gamma$. Furthermore, the ratio between the bulk modulus of BCC and FCC gives $B_\alpha/B_\gamma = 1.4$, ensuring that the BCC structure is harder than the FCC. This is qualitatively consistent with the experiential anisotropy parameter for BCC iron [140, 141]. Moreover, the yield between the bulk modulus of the BCC and FCC structures in the QA (1.4) is close to the experimental values for BCC Fe/FCC Fe (1.27)[140, 141].

Two different reduced time scales were used in this work. In the preliminary simulations of homogeneous FCC and BCC structures, a first time step of $\Delta t = 0.05$ was used to relax both structures within a reasonable time frame. However, higher accuracy was required for the FCC to BCC phase transformation simulations, so the time step was reduced to $\Delta t = 0.01$. For clarity, a time unit of $t^* = N_{it} \cdot \Delta t$ will be used throughout this work, where N_{it} is the number of iterations.

All parameters used to set up the FCC to BCC simulations are provided in Table 3.3. The average fraton density, $\bar{\rho}$ was defined as $4\pi R^3 N/(3V)$, where V is the total volume of the sys-

a_α	a_γ	R	ΔR	ξ	λ^{lr}	λ^{sr}	ϵ	σ^α	$\sigma^\gamma_{1,2}$	k_BT	$\bar{\rho}$
8.0	6.5	2.81	0.48	4.0	1.0	0.2	0.1	0.03	0.03	0.05	0.17

Table 3.3: Parameters used in QA simulations.

tem ($V = (\Delta x N)^3$). In this work, simulations were conducted with an average fraton density of $\bar{\rho} = 0.17$, consistently with [124]. Moreover, k_BT and ξ were expressed in units of k_BT_m, where T_m is the melting temperature of the system.

3.1.2 Simulation initial conditions

In order to observe and analyze the phase transformation at a sufficient spatial scale, the size of the simulation box was set to $(512\Delta x)^3$, which is equivalent to $(22.8\,\text{nm})^3$, with $\Delta x = 0.0445$ nm. In some cases, the size of the simulation box was slightly adjusted in the $\boldsymbol{x}$ and $\boldsymbol{y}$ directions on the box to further minimize elastic strains for specific OR-HP combinations. In the case of of the KS v1 OR with a $(1\,2\,1)_\gamma$ HP, the simulation box size was $(502\Delta x)^2 \times (512\Delta x)$. Additionally, the simulation boxes were equipped with periodic boundary conditions (PBC).

All rotation matrices for the FCC and BCC phases were configured so that the habit plane is parallel to the $\boldsymbol{z}$ axis of the simulation box. This alignment ensures that the BCC phase grows along the same axis in all simulations of the FCC to BCC phase transformation. However, the $\boldsymbol{x}$ and $\boldsymbol{y}$ axes of the simulation box were not aligned with specific Miller indices, meaning no particular direction is favored in the FCC or BCC structures.

Relaxed FCC and BCC structures oriented along specific HP-OR combination were first prepared based on preliminary QA simulations. Then, the initial configuration for the FCC to BCC transformation was prepared, upon embedding a slice of the relaxed BCC structure, with $40\Delta x = 1.8nm$, into the relaxed FCC structure. QA simulations of the FCC to BCC simulations were then conducted, starting from this initial configuration, using he FCC to BCC transformation potential applied throughout the entire box. The initial configuration is depicted in Figure 5.1, using CNA method from Ovito [136], for the NW v2 OR with the $(2\,3\,2)_\gamma$ HP. Blue atoms belong to the BCC phase, green atoms to the FCC phase, while the white atoms at the interface indicate an unknown or perturbed structure.

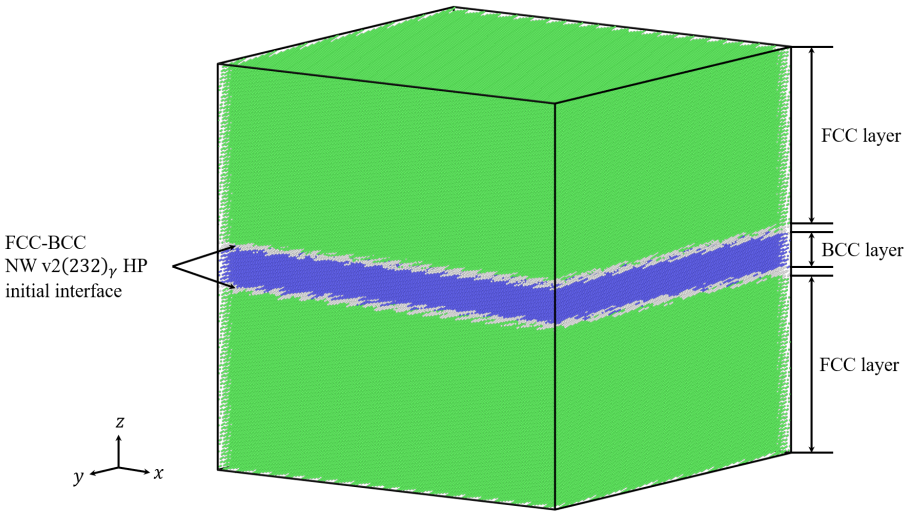

Figure 3.1: Initial configuration in QA simulation of the FCC to BCC phase transformation for the NW v2 OR with the $(2\,3\,2)_\gamma$ HP. Visualization using the CNA method in Ovito [136]: green represents FCC, blue represents BCC, and grey indicates unknown or perturbed structures.

3.1.3 Interface propagation

For the majority of QA simulations of the FCC to BCC phase transformation in iron, the complete transformation is achieved in 15 000 steps at $t^* = 150$. These simulations all begin with a short relaxation of the interface ($t^* < 30$), during which its structure forms. Therefore, most of the interfacial structure and shape characterization was done at $t^* = 70$, when the interface is fully relaxed and there is no self-interaction between the upper and lower interfaces due to the PBC ($t^* > 140$). The QA simulation for the NW v2 OR with the $(2\,3\,2)_\gamma$ HP is shown at $t^* = 70$ and at $t^* = 150$ in Figure 3.2. At $t^* = 150$, self-interaction between interfaces due to PBC is observed at the edges of the simulation box.

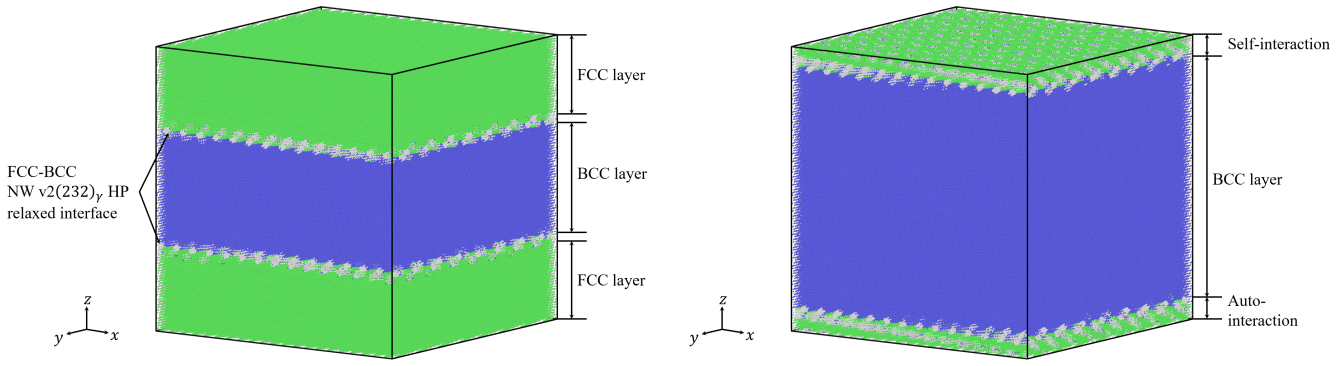

(a) $t^* = 70$. (b) $t^* = 150$.

Figure 3.2: Atomic configurations during FCC to BCC phase transformation for the NW v2 OR with $(2\,3\,2)_\gamma$ HP. Extracted from Qa simulations at $t^* = 70$ and $t^* = 150$. Visualization using the CNA method in Ovito [136]: green represents FCC, blue represents BCC, and grey indicates unknown or perturbed structures.

3.2 Interface characteristics

A common conclusion drawn from theoretical models such as the Topological model [43], experimental observations [3–5, 55, 56, 86, 87], and atomistic simulations [13, 14, 16], is that interface characteristics, such as the nature of the dislocations, their spacing, and the step height, are dependent on the interface geometry, starting with OR and the HP. Therefore, this section will be divided into three parts: NW, GT, and KS ORs, each of them associated with different HPs, as listed in Table 3.2. The ORs will be presented starting with NW OR, which has the highest angle (5.26°) between the $[1\,0\,\bar{1}]_\gamma$ and $[1\,1\,\bar{1}]_\alpha$ directions, followed by the intermediary GT OR with an angle of 2.40° between those directions, and concluding with the KS OR, where the $[1\,0\,\bar{1}]_\gamma$ and $[1\,1\,\bar{1}]_\alpha$ directions are parallel.

3.2.1 Nishiyama-Wasserman orientation relationship

The interface structure and motion with an NW OR between the FCC and BCC phases is investigated in this subsection. The second (NW v2) and third (NW v3) variants were simulated for multiple habit planes. As no meaningful differences were found between the OR variants, the results and figures provided in this subsection will focus only on the NW v2 OR. In the case of NW v2 OR, FCC and BCC structures have $(1\,1\,1)_\gamma$ and $(0\,1\,1)_\alpha$ parallel close-packed planes with $[\bar{1}\,1\,0]_\gamma$ and $[1\,0\,0]_\alpha$ parallel directions. The FCC to BCC phase transformation with NW ORs was simulated with four different HPs:$(1\,1\,1)_\gamma$, $(5\,7\,5)_\gamma$, $(2\,3\,2)_\gamma$ and $(1\,2\,1)_\gamma$, but only the $(1\,1\,1)_\gamma$ and $(2\,3\,2)_\gamma$ HPs are presented in the manuscript. One the one hand, the $(1\,1\,1)_\gamma$ HP represents a limit case where the HP is parallel to the close-packed planes of the FCC and BCC phases. This type of HP is sometimes treated independently as "flat interfaces" in the literature, such as in [16].

Furthermore, using Kachaturyan's expression of habit plane in Chapter 1, with the QA lattice parameters $a_\gamma = 8\Delta x$ and $a_\alpha = 6.5\Delta x$, the deviation of HP by 0.5° from $(1\,1\,1)_\gamma$ was calculated. On the other hand, the $(2\,3\,2)_\gamma$ HP was not directly predicted by the theoretical calculations using our lattice parameters. However, this type of plane is obtained with typical iron misfit for NW OR in [14]. Morevoer, habit planes of form $(a\,b\,a)_\gamma$ are typically expected at FCC-BCC interfaces in [45].

For the NW v2 OR, the dense directions $[1\,0\,\bar{1}]_\gamma$ and $[0\,1\,\bar{1}]_\gamma$ are close to $[1\,1\,\bar{1}]_\alpha$ and $[1\,\bar{1}\,1]_\alpha$ by an angle of 5.26°, respectively. In this section, directions close to $[1\,0\,\bar{1}]_\gamma \sim [1\,1\,\bar{1}]_\alpha$ and $[0\,1\,\bar{1}]_\gamma \sim [1\,\bar{1}\,\bar{1}]_\alpha$ will be denoted as $[1\,0\,\bar{1}]^*_\gamma$ and $[0\,1\,\bar{1}]^*_\gamma$.

This section is organized into two subsections. First, the characteristics of the interface structure and its defects, such as the dislocation properties, will be discussed. Then, the interface motion will be prospected, it depends on the interface dislocations.

3.2.1.1 Interface structure

The structure of the interface at $t^* = 70$ is shown in Figure 3.3a for the $(1\,1\,1)_\gamma$ HP and in Figures 3.3b and 3.3c for the $(2\,3\,2)_\gamma$ HP . In these figures, only atoms belonging to the BCC structure were retained. NW OR interfaces consist of a periodic distribution of $(0\,1\,1)_\alpha||(1\,1\,1)_\gamma$ flat terraces for all simulated HPs. They are indicated by the black circles in Figure 3.3. Additionally, two arrays of periodically spaced perturbed regions are observed across the interface. It can be concluded that the morphology of the interface is stepped, as highlighted in Figure 3.3c for the $(2\,3\,2)_\gamma$ HP interface, where the steps are aligned along the $[1\,0\,\bar{1}]^*_\gamma$ and $[0\,1\,\bar{1}]^*_\gamma$ directions. These steps will be referred to as step (1) and step (2), with their directions indicated by blue and red arrows, respectively.

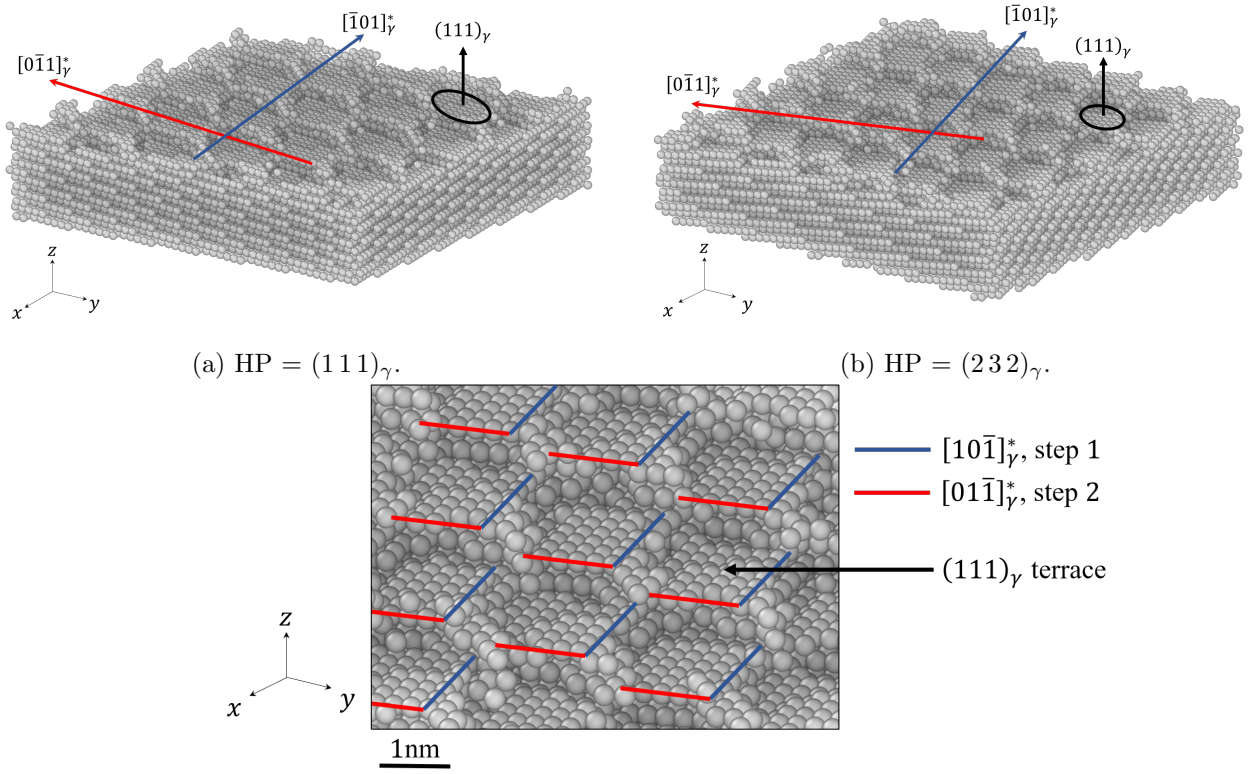

(a) HP = $(1\,1\,1)_\gamma$.

(b) HP = $(2\,3\,2)_\gamma$.

(c) Zoomed HP = $(2\,3\,2)_\gamma$.

Figure 3.3: FCC-BCC semi-coherent interface relief for NW OR, extracted from the QA simulation at $t^* = 70$. Surface relief was obtained using 'ambient occlusion' rendering in Ovito [136], displaying only BCC atoms. Blue and red arrows indicate the $[1\,0\,\bar{1}]^*_\gamma$ and $[0\,1\,\bar{1}]^*_\gamma$ directions, respectively. Terraces are parallel to $(1\,1\,1)_\gamma$ as indicated by the black circle and arrow.

Terrace coherency is evaluated by computing the elastic strain at the interface. The volumetric strain $\Delta V/V$ in the BCC phase is visualized using Ovito, for the $(1\,1\,1)_\gamma$ HP in Figure 3.4a and the $(2\,3\,2)_\gamma$ HP in Figure 3.4b. A color scale accompanies these figures, with the highest volumetric strain measured for both the $(1\,1\,1)_\gamma$ and for the $(2\,3\,2)_\gamma$ HPs being 3.5%. The large positive or large negative values of $\Delta V/V$ are observed at the terrace ledges and their intersections, while $\Delta V/V$ is nearly zero for atoms on the terraces. In particular, the higher volumetric strain amplitudes for each HP are located at the intersections of the terrace ledges. The presence of high elastic strain values at the terrace ledges indicates the presence of transformation dislocations (see paragraph 'dislocations') at the interface, primarily along the step directions. As no elastic strain was detected on the terraces, these measurements confirm the semi-coherency of the interface, where atomic sites of the FCC and BCC structures match along the terrace. The same interface region depicted in Figure 3.3c is shown in Figure 3.4c, where low elastic strain at the terrace is particularly visible, further confirming that the interface is semi-coherent.

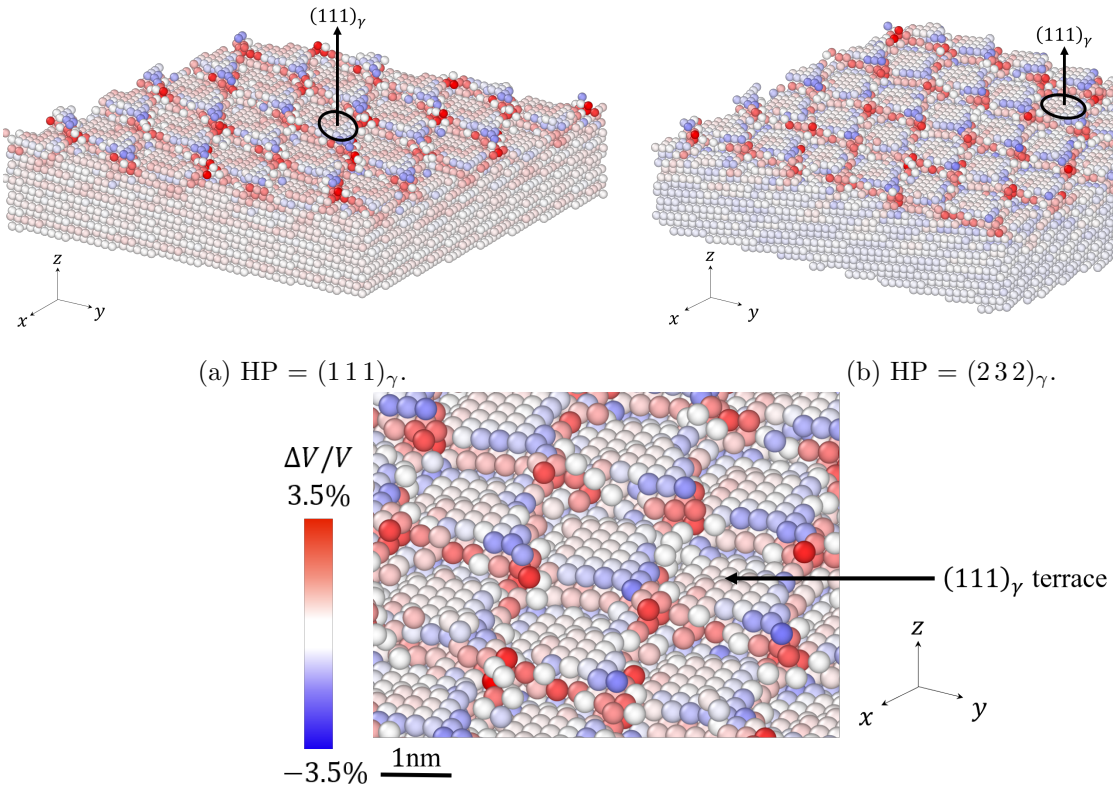

(a) HP = $(1\,1\,1)_\gamma$.

(b) HP = $(2\,3\,2)_\gamma$.

(c) Zoomed HP = $(2\,3\,2)_\gamma$.

Figure 3.4: Volumetric strain for FCC-BCC semi-coherent interface relief for NW OR, extracted from the QA simulation at $t^* = 70$. Rendering done in Ovito [136], displaying only BCC atoms. Atom coloration is based on elastic strain calculations, displaying volumetric strain $\Delta V/V$. Red indicates the maximum $\Delta V/V$, and blue the minimum.

The observed volumetric strain can be compared to the potential energy map from molecular dynamics simulations of the FCC to BCC phase transformation with NW OR in the $(1\,1\,1)_\gamma$ plane, conducted by Ou et al. [12] and depicted in Figure 1.16 in Chapter 1. Indeed, the higher the elastic strain, the more stretched or compressed the atomic bonds. In their figure, a diamond-shaped pattern is produced by the intersection of two high-potential energy regions, with even higher potential energy at their intersection. This pattern is similar to the volumetric strain observations in Figure 3.4 for the QA simulation of NW OR. Indeed, the highest volumetric strain regions are observed at the intersections of the two steps.

In order to further characterize the interface steps, slices of the simulation box around the interface were extracted parallel to each step direction in the FCC reference frame, along the $[\bar{1}\,0\,1]_\gamma$ direction for step (1) and the $[0\,1\,\bar{1}]_\gamma$ direction for step (2). These slices are shown for the $(1\,1\,1)_\gamma$ HP in Figure 3.5a and 3.5b and for the $(2\,3\,2)_\gamma$ HP in Figures 3.5c and 3.5d. The black lines represent a guide for the eyes of the interface location, indicating the overall shape of the interface between the BCC phase (blue atoms) and the FCC phase (green atoms). The red line indicates

the intersection between the HP and the cutting plane. Due to the precision of the CNA and the manner in which the BCC phase propagates and nucleates, the steps may not be perfectly flat locally. This point will be discussed later in 3.2.1.2.

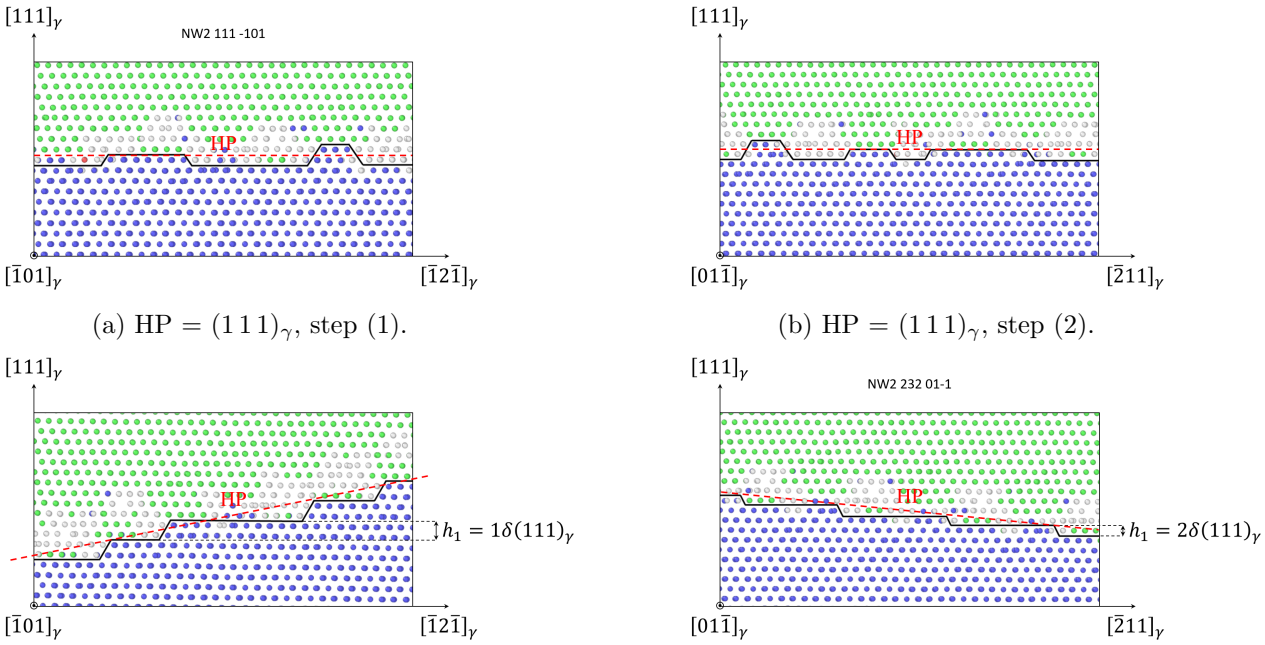

(a) HP = $(1\,1\,1)_\gamma$, step (1).

(b) HP = $(1\,1\,1)_\gamma$, step (2).

(c) HP = $(2\,3\,2)_\gamma$, step (1).

(d) HP = $(2\,3\,2)_\gamma$, step (2).

Figure 3.5: Two dimensional views of the area around the FCC-BCC interface for NW OR, extracted from the QA simulation at $t^* = 70$. Green: FCC, blue: BCC, white: unknown. The dark lines are qualitative guides, indicating the overall shape of the interface

For all HPs other than $(1\,1\,1)_\gamma$ (including the $(2\,3\,2)_\gamma$ HP shown and $(5\,7\,5)_\gamma$ and $(1\,2\,1)_\gamma$ HPs shown in the figures) the stepped nature of both arrays of defects is clearly visible. The step height varies depending on the habit plane orientation. This is evident in Figures 3.5c and 3.5d, where the differences in step height and length allow the macroscopic interface shape to be aligned with the HP. When the HP deviates from the terrace plane, steps accommodate the tilt angle between the two planes. For the $(1\,1\,1)_\gamma$ HP, while terrace still form, steps do not participate in the tilt of the interface as it is already aligned with the HP.

For the $(5\,7\,5)_\gamma$ (not shown) and $(2\,3\,2)_\gamma$ HPs, the normal vectors are deviated of 9.4° and 11.4°, respectively, from the $[1\,1\,1]_\gamma$ direction. For both HPs, the height of step (1) is $2\delta(1\,1\,1)_\gamma$, while the height of step (2) is $1\delta(1\,1\,1)_\gamma$. For the $(1\,2\,1)_\gamma$ HP (not shown), which has its normal at an angle of 19.5° from the $[1\,1\,1]_\gamma$ direction, the height of step (1) is a mix of $2\delta(1\,1\,1)_\gamma$ and $3\delta(1\,1\,1)_\gamma$, while the height of step (2) is a mix of $1\delta(1\,1\,1)_\gamma$ and $2\delta(1\,1\,1)_\gamma$. Therefore, a larger angle between the terrace plane $(0\,1\,1)_\alpha||(1\,1\,1)_\gamma$ and the HP seems to favor higher step heights in both directions.

Moreover, the step heights observed in Figure 3.5 are compatible with the Topological Model (TM), as disconnections with step heights of 1 or $2\delta(1\,1\,1)_\gamma$ are expected. Furthermore, for the $(5\,7\,5)_\gamma$ HP, multiple step heights can coexist in the same step direction, which was observed in HRTEM experimental studies [4, 5] and described by Maresca et al. [14] in his version of the PTMC model. It should be emphasized that the presence of a second step at the interface is uncommon, as a single-step interface was postulated in the literature review in Chapter 1. However, dislocation analysis will give insights about the nature of this second step.

As stated in [4], steps directions should be aligned with the transformation dislocations at the interface. Therefore, the Slip Vector Analysis (SVA) [134, 142], was applied to analyze the presence of dislocations and their Burgers vectors in all NW OR simulations. As detailed in the Appendix B, the slip vector represents an accurate representation of the Burgers vector for each atoms. In the following results and Figures, this vector will be therefore directly referred as Burgers vector.

The Burgers vectors of dislocations obtained by the SVA at the FCC-BCC interface in the HP are shown in Figure 3.6a for the $(1\,1\,1)_\gamma$ HP. For the $(2\,3\,2)_\gamma$ HP, Burgers vectors are depicted both in the HP, in Figure 3.6b, and in the $(1\,1\,1)_\gamma$ terrace plane, in Figure 3.6c. Blue Burgers vectors points in the $[1\,0\,\bar{1}]_\gamma$ direction, while red Burgers vectors points in the $[0\,1\,\bar{1}]_\gamma$ direction. In these figures, mean dislocation lines $\boldsymbol{\xi}_1$ and $\boldsymbol{\xi}_2$, the angle θ between them, and their respective angles $\phi_{1,2}$ with Burgers vectors $\boldsymbol{b}_1$ and $\boldsymbol{b}_2$ are indicated. In Figure 3.6c, mean line directions $\boldsymbol{\xi}_1$ and $\boldsymbol{\xi}_2$ are projected onto the terrace $(1\,1\,1)_\gamma$ plane and denoted as $\boldsymbol{\xi}_1^{(1\,1\,1)_\gamma}$ and $\boldsymbol{\xi}_2^{(1\,1\,1)_\gamma}$.

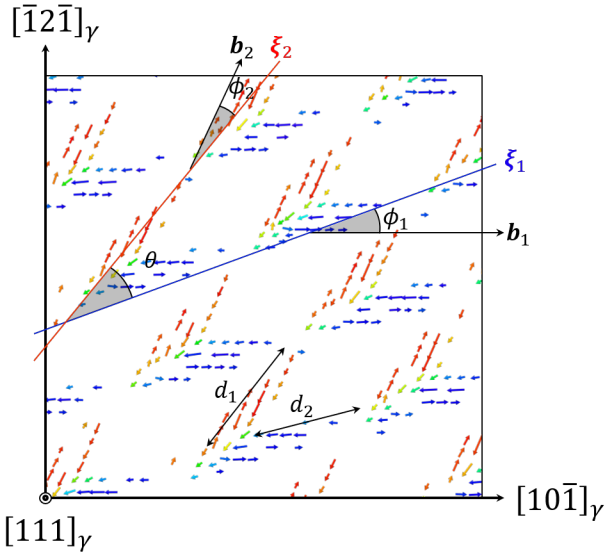

(a) HP = $(1\,1\,1)_\gamma$.

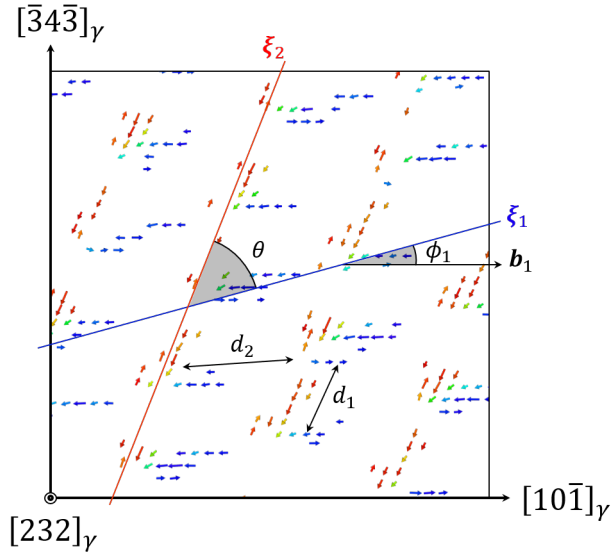

(b) HP = $(2\,3\,2)_\gamma$, shown in $(2\,3\,2)_\gamma$ plane.

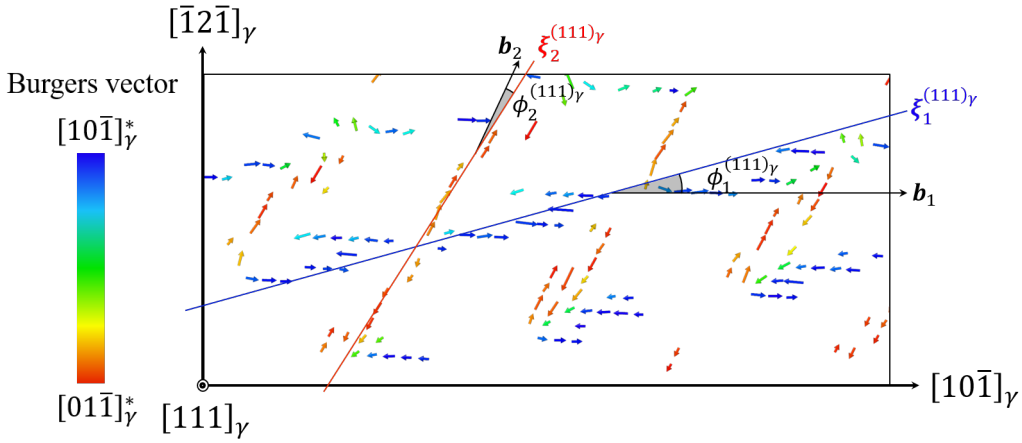

(c) HP = $(2\,3\,2)_\gamma$, shown in $(1\,1\,1)_\gamma$ plane.

Figure 3.6: Slip vector analysis of the dislocation networks at the FCC-BCC interface in the $(1\,1\,1)_\gamma$ plane for NW OR, extracted from the QA simulation at $t^* = 70$. Only slip vectors with an amplitude of $> 0.5\|\boldsymbol{b_{1,2}}\|$ are displayed. Blue: $[1\,0\,\bar{1}]^*_\gamma$ direction, red: $[0\,1\,\bar{1}]^*_\gamma$ direction. Mean line directions $\boldsymbol{\xi}_1$ and $\boldsymbol{\xi}_2$, steps spacing d_1 and d_2, and Burgers vectors $\boldsymbol{b}_1$, $\boldsymbol{b}_2$ are represented. Vectors are scaled 6 times.

In these figures, two arrays of dislocations are observed, with Burgers vectors $\boldsymbol{b}_1 = \frac{a_\gamma}{2}[1\,0\,\bar{1}]^*_\gamma$ and $\boldsymbol{b}_2 = \frac{a_\gamma}{2}[0\,1\,\bar{1}]^*_\gamma$. These two sets of dislocations border terrace steps, thereby confirming that the elastic strain observed at terrace ledges arises from the presence of transformation dislocations, as postulated by Moritani et al. [4]. Morevoer, $\boldsymbol{b}_1$ and $\boldsymbol{b}_2$ dislocations are locally oriented along the $[\bar{1}\,0\,1]^*_\gamma$ and $[0\,1\,\bar{1}]^*_\gamma$ directions. Thus, both dislocation sets have parallel Burgers vector and local dislocation line, which makes them screw dislocation.

However, the mean dislocation directions $\boldsymbol{\xi}_1$ and $\boldsymbol{\xi}_2$ of $\boldsymbol{b}_1$ and $\boldsymbol{b}_2$ dislocations are deviated

with respect to the $[1\,0\,\bar{1}]_\gamma$ and $[0\,1\,\bar{1}]_\gamma$ local dislocation lines, respectively. For instance, $\boldsymbol{\xi}_1 = [0.59, 0.19, -0.78]_\gamma$ and $\boldsymbol{\xi}_2 = [0.19, 0.59, -0.78]_\gamma$ for the $(1\,1\,1)_\gamma$ HP, while for the $(2\,3\,2)_\gamma$ HP, $\boldsymbol{\xi}_1 = [0.61, 0.11, -0.78]_\gamma$ and $\boldsymbol{\xi_2} = [-0.16, 0.62, -0.77]_\gamma$. For all HPs but $(1\,1\,1)_\gamma$, including the $(2\,3\,2)_\gamma$ HP, the deviations between mean line directions and Burgers vectors have two origins. First, $\boldsymbol{\xi}_1$ and $\boldsymbol{\xi}_2$ lie in the terrace plane but not in the $(1\,1\,1)_\gamma$ plane, therefore $\boldsymbol{\xi}_1$ and $\boldsymbol{\xi}_2$ deviate from $[1\,0\,\bar{1}]^*_\gamma$ and $[0\,1\,\bar{1}]^*_\gamma$ directions due to the inclination of the HP. Second, portion of $\boldsymbol{b}_1$ and $\boldsymbol{b}_2$ dislocations lying in the $(1\,1\,1)_\gamma$ also deviate from $[1\,0\,\bar{1}]^*_\gamma$ and $[0\,1\,\bar{1}]^*_\gamma$ directions in the terrace plane by the angles $\phi^{(}_{1,2}1\,1\,1)_\gamma$.

The two contributions to the mean line direction deviations are enabled in two different ways. At each dislocation intersection, a cross-slip (CS) mechanism occurs . This CS mechanism generates out of terrace plane kinks and contributes to $\boldsymbol{\xi}_2$ deviation from $\boldsymbol{b}_2$ due to the HP orientation. The role of CS in interface propagation will be examined in Section 3.2.1.2. The second contribution to this deviation comes from edge character of kinks in $(1\,1\,1)_\gamma$ plane. These kinks and the deviation from the pure screw direction are predicted by Maresca et al. [14]. Additionally, several experimental studies [4, 5] have observed this deviation from the pure screw direction due to these kinks of edge character. The role and nature of these kinks in interface propagation and dislocation glide will also be addressed with the interface motion in Section 3.2.1.2.

Figure 3.6 also provides points of comparison with the literature, including the deviation angle ϕ_1 between $[1\,0\,\bar{1}]_\gamma$ and $\boldsymbol{\xi}_1$ directions in the HP, the angle θ between $\boldsymbol{\xi}_1$ and $\boldsymbol{\xi}_2$ in the same plane, and the distances d_1 and d_2 between two successive $\boldsymbol{b}_1$ and $\boldsymbol{b}_2$ dislocations. Based on the deviation angle values $\phi_{1,2}$, presented in Table 3.5, it can be concluded that all line directions deviate from their pure screw direction by an angle between 8.2° and 24.6° for all HPs and line direction types. The deviation angle ϕ_1 is significantly larger than in Maresca et al. [14] and in the topological model [43]. Based on the topological model, the deviation angle ϕ_1, for the 1.23 misfit used in QA simulations should be around 1.6°.

The steps spacing can be calculated as the shortest distance between two line direction intersections for a given step. This is depicted in Figures 3.6a and 3.6c for the $(1\,1\,1)_\gamma$ and $(2\,3\,2)_\gamma$ HPs by the distance d_1 for step (1) and d_2 for step (2). Mean line directions $\boldsymbol{\xi}_{1,2}$ and steps spacing $d_{1,2}$ were calculated for the whole simulation box. The values of the mean line directions $\boldsymbol{\xi}_{1,2}$ and the angle θ are given in Table 3.4, while steps spacing $d_{1,2}$ and angles $\phi_{1,2}$ are listed in Table 3.5. The average step (1) spacing, d_1, measured for NW ORs ranges between 1.4 nm and 3.4 nm. In comparison, Sandvik et al. [56] reported an experimental value of $d_1 = 1.3$ nm, while molecular dynamics simulations by Maresca et al. [14] yielded $d_1 = 1.45$ nm for a NW OR, with $(2\,3\,2)_\gamma$ HP, and a lattice misfit of 1.25. For the same OR and HP, with a QA misfit of 1.23, the average step spacing is $d_1 = 1.7$ nm, which is close to the TM prediction of $d_1 = 1.67$ nm for NW OR [14]. Variations in the calculated step (1) spacing may partially arise from differences in misfit values

between our simulations and the molecular dynamics simulations in [14]. Moreover, the spacing between the $\boldsymbol{\xi}_2$ lines was measured to range from 2.6 nm to 6 nm in HRTEM experiments [56]. This spacing is expected to correspond closely to the step (2) spacing, denoted d_2. In each HP simulation, d_2 varies between 2.4 nm and 3.3 nm, which aligns with the range observed in HRTEM [56]. Additionally, for NW OR, the topological model [43] calculated a step (2) spacing of 2.32 nm, which is close to QA simulations results.

The presence of two sets of kinked screw dislocations $\boldsymbol{b}_1$ and $\boldsymbol{b}_2$ at the interface was attested by molecular dynamics simulations [12–14, 16] and experimental results [4]. These dislocations arise to accommodate the atomic mismatch between the BCC and FCC phase at the interface. The misfit between the two interfaces can be seen using the Moiré pattern, shown in Figure 3.7a. The Moiré pattern shows that lower coherency areas are along the $\boldsymbol{\xi}_1$ and $\boldsymbol{\xi}_2$ and can be accommodated by $\boldsymbol{b}_1$ and $\boldsymbol{b}_2$ dislocations. Moreover, theoretical O-lattice calculation from Hall et al. [54] and Moritani et al. [4], both predict the same interface structure with two arrays of kinked screw dislocations, as schematized in Figure 3.7b. In these figures, theoretical mean line directions $\boldsymbol{\xi}_1$ and $\boldsymbol{\xi}_2$ are indicated by the blue and red lines, respectively, with black arrows representing their Burgers vector.

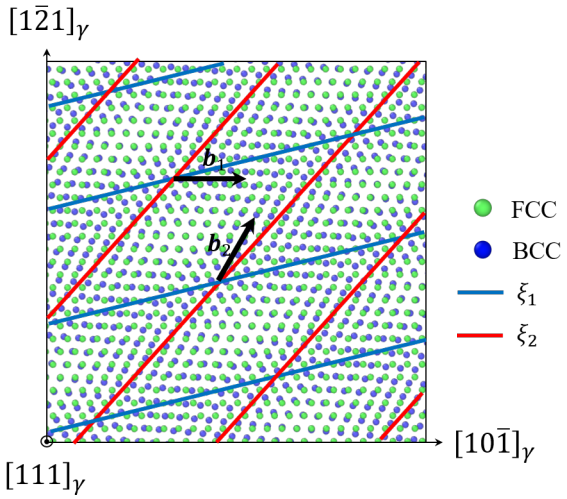

(a) Moiré pattern.

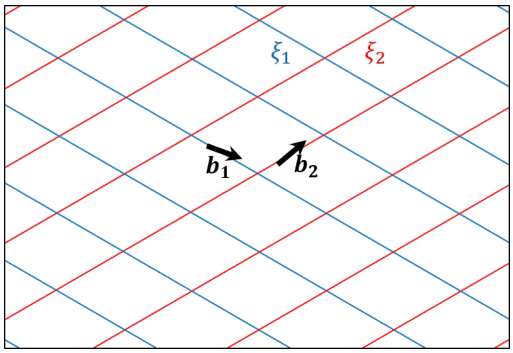

(b) O-lattice theory [4, 54]

Figure 3.7: **(a)** Moiré patterns for NW OR in $(1\,1\,1)_\gamma$ with QA simulation misfit of 1.23. Green atoms: FCC, Blue atoms: BCC. Blue and red lines highlight region of high atomic mismatch between FCC and BCC structure along $\boldsymbol{b}_1$ and $\boldsymbol{b}_2$ respectively.**(b)** O-lattice calculation for NW OR, schematized from [4, 54].

It should be underlined that it was stated by Moritani et al.[4] that transformation dislocations are situated on the steps. Although the presence of both $\boldsymbol{b}_1$ and $\boldsymbol{b}_2$ was previously discussed in literature for NW OR, this is the first time that a two-stepped interface is clearly observed with steps along both transformation dislocations. Further details regarding the two-stepped nature of

the interface will be given in the discussion.

Moreover, the energy of dislocations $\boldsymbol{b}_1$ and $\boldsymbol{b}_2$ can be computed. As presented in Chapter 1, the energy of a dislocation line can be estimated as the elastic energy of the region surrounding the dislocation core, where interactions are treated using continuum elastic theory [59]. With b the norm of the Burgers vector of the dislocation, μ the shear modulus, and l the length of the dislocation, the elastic energy U_e is expressed as follows:

$$U_e = \frac{1}{2}\mu b^2 \tag{3.2.1}$$

Using this approximation, where the length of $\boldsymbol{b}_1$ corresponds to the d_2 spacing and the length of $\boldsymbol{b}_2$ corresponds to the d_1 spacing, the elastic energy of each dislocation along each step is provided in Table 3.5. The smallest values for both dislocations has been found for $(1\,2\,1)_\gamma$ HP, while the highest were for $(1\,1\,1)_\gamma$ HP.

According to the simulation, conclusions about the relationship between the HP with the interface structure can be drawn. The angle $\theta_{1,2}$ between the two mean dislocation lines increases the further the HP deviates from$(1\,1\,1)_\gamma$. Both steps spacing $d_{1,2}$ decrease with increasing HP angle, though this effect is more pronounced for step 1. Regarding the angles $\phi_{1,2}$ between a Burgers vector and its line direction, while the HP orientation has an influence, a direct correlation is not apparent. However, it can be stated that the HP impacts the kinked nature of the dislocations. Moreover, it is noteworthy that the highest $\phi_{1,2}$ angles were found for habit planes further from the$(2\,3\,2)_\gamma$ HP predicted for NW OR in [14].

OR	HP	$\boldsymbol{\xi}_1$	$\boldsymbol{\xi}_2$	$\theta(^\circ)$
NW v2	$(1\,1\,1)_\gamma$	$[0.59, 0.19, -0.78]_\gamma$	$[0.19, 0.59, -0.78]_\gamma$	32.6
	$(5\,7\,5)_\gamma$	$[0.63, 0.11, -0.77]_\gamma$	$[-0.07, 0.61, -0.79]_\gamma$	50.6
	$(2\,3\,2)_\gamma$	$[0.61, 0.11, -0.78]_\gamma$	$[-0.16, 0.62, -0.77]_\gamma$	54.9
	$(1\,2\,1)_\gamma$	$[0.58, 0.12, -0.81]_\gamma$	$[-0.40, 0.56, -0.72]_\gamma$	65.3

Table 3.4: NW OR line directions $\boldsymbol{\xi}_1$, $\boldsymbol{\xi}_2$, and angle θ between the two lines directions.

OR	HP	$\boldsymbol{\phi_1}(^\circ)$	$\boldsymbol{\phi_2}(^\circ)$	d_1 (nm)	d_2 (nm)	$U_e^{\boldsymbol{b}_1}$ (eV)	$U_e^{\boldsymbol{b}_2}$ (eV)
NW v2	$(1\,1\,1)_\gamma$	13.7	13.7	3.3	3.3	50.6	50.6
	$(5\,7\,5)_\gamma$	8.8	8.2	2.0	2.9	44.5	30.7
	$(2\,3\,2)_\gamma$	9.3	10.3	1.7	2.9	44.5	26.1
	$(1\,2\,1)_\gamma$	11.5	24.6	1.4	2.4	36.8	21.5

Table 3.5: NW OR angle $\phi_{1,2}$ between line directions $\boldsymbol{\xi}_{1,2}$ and Burgers vector $\boldsymbol{b_{1,2}}$, steps spacing $d_{1,2}$ and estimated elastic energy of each dislocation straight line $U_e^{\boldsymbol{b_{1,2}}}$

3.2.1.2 Interface propagation

A displacement vector analysis was implemented in the QA simulation to quantify and observe atomic displacements. The displacement maps, for the $(1\,1\,1)_\gamma$ HP and for the $(2\,3\,2)_\gamma$ HP, are shown in Figure 3.8. In this figure, atomic displacement vector amplitudes are displayed for $t^* = 70$ and were calculated as the difference in atomic positions between $t^* = 60$ and $t^* = 70$. The color coding is in units of Δx, ranging from 0 in blue to $1.5\Delta x$ in red, with $\Delta x = 0.0445$ nm. the maximum displacement measured was of $5.6\Delta x$. However, extreme displacements, partly due to numerical artifacts generated during the fraton to atom conversion, can affect the interpretation of the results. Therefore, displacements greater than $1.5\Delta x$ are also displayed in red for better visualization. From Figure 3.8, it can be concluded that interface propagation is primarily driven by atomic displacement along the dislocations $\boldsymbol{b}_1$, $\boldsymbol{b}_2$ and their intersections.

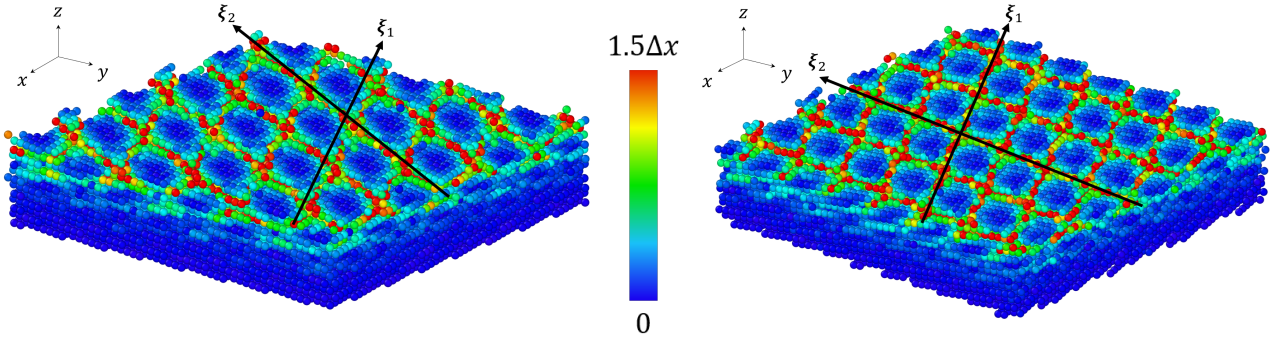

(a) HP = $(1\,1\,1)_\gamma$. (b) HP = $(2\,3\,2)_\gamma$.

Figure 3.8: Atomic displacement map at the FCC-BCC interface, with only BCC atoms remaining and NW OR. Extracted from QA simulation at $t^* = 70$, with atomic displacement vectors calculated between $t^* = 60$ and $t^* = 70$. Color coding based on atomic displacement amplitude.

In Figure 3.9, the FCC-BCC interface is presented at $t^* = 74$, where only the atoms belonging to the BCC structure are shown. In Figure 3.9a, a slice along the $[1\,\bar{2}\,1]_\gamma$ direction is depicted. This direction is normal to the step (1) direction and the terrace plane. In Figure 3.9b, a slice the $[\bar{2}\,1\,1]_\gamma$ direction is shown, with this direction normal to the step (2) direction and the terrace plane. Atoms that shifted to the BCC structure between time steps $t^* = 70$ and $t^* = 72$ are depicted in red, while those between $t^* = 72$ and $t^* = 74$ are shown in yellow. The outward propagation of terrace steps (1) and (2) in the $(0\,1\,1)_\alpha$ terrace is indicated by black arrows, and the nucleation of new $(0\,1\,1)_\alpha$ layers is indicated by blue arrows. Additionally, the growth for a single terrace is visualized in Figure 3.10 between time $t^* = 70$ and $t^* = 71.5$. In this figure, atoms that shifted into the BCC structure between time steps $t^* = 70$ and $t^* = 70.5$ are depicted in red, those between $t^* = 70.5$ and $t^* = 71$ in yellow, and those between $t^* = 71$ and $t^* = 71.5$ in green.

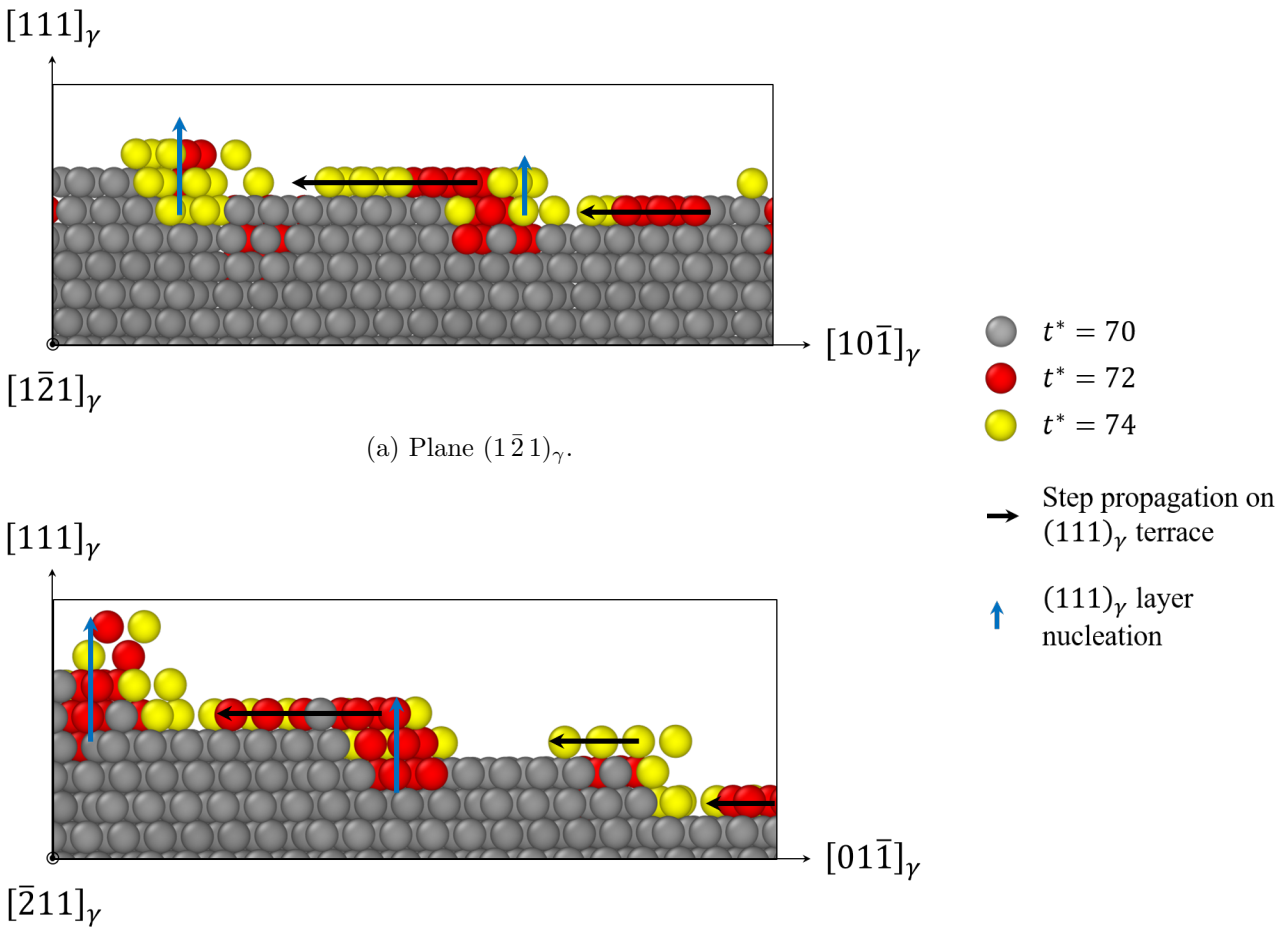

(a) Plane $(1\,\bar{2}\,1)_\gamma$.

(b) Plane $(\bar{2}\,1\,1)_\gamma$.

Figure 3.9: Step-flow propagation mode of the FCC-BCC interface surface, for NW OR, as extracted from QA simulations between $t^* = 70$ and $t^* = 74$. Only BCC atoms are retained. Grey: atomic configuration at t^*70, red: at $t^* = 72$ and yellow at $t^* = 74$. Blue arrow: $(0\,1\,1)_\alpha$ layer nucleation, black arrow: step propagation in $(0\,1\,1)_\alpha$. **(a)**plane $(1\,\bar{2}\,1)_\gamma$, **(b)** plane $(\bar{2}\,1\,1)_\gamma$.

The growth mode for the BCC phase corresponds to a step-flow growth mechanism, described in [143]. This propagation involves two processes occurring in parallel: the propagation of existing steps in the $(0\,1\,1)_\alpha$ plane and the nucleation of new BCC layers. As observed in Figures 3.9 and 3.10, the step propagation follows both step (1) and step (2) directions, with no observable difference in propagation rate. However, as shown in Figure 3.9, the nucleation of new BCC layers occurs only at the terrace ledges and is followed by the progression of the newly formed terrace.

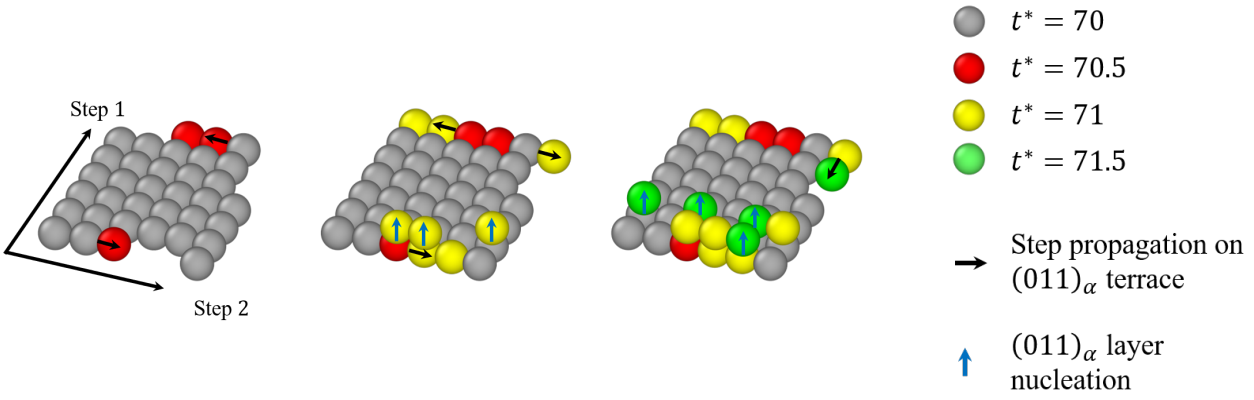

Figure 3.10: Step-flow propagation mode of the FCC-BCC interface for a single terrace, as extracted from QA simulations between $t^* = 70$ and $t^* = 71.5$. Only BCC atoms are retained. Only BCC atoms are retained. Grey: atomic configuration at t^*70, red: at $t^* = 72$ and yellow at $t^* = 74$. Blue arrow: $(0\,1\,1)_\alpha$ layer nucleation, black arrow: step propagation in $(0\,1\,1)_\alpha$.

As the propagation of terraces in $(1\,1\,1)_\gamma||(0\,1\,1)_\alpha$ planes is associated with the glide of $\boldsymbol{b}_1$ and $\boldsymbol{b}_2$ screw dislocations, the slip plane for these dislocations is therefore $(1\,1\,1)_\gamma$. This provides the $(1\,1\,1)_\gamma[1\,0\,\bar{1}]^*_\gamma$ and the $(1\,1\,1)_\gamma[0\,1\,\bar{1}]_\gamma$ slip systems for $\boldsymbol{b}_1$ and $\boldsymbol{b}_2$ screw dislocations, respectively. Propagation of these dislocations is facilitated by the side-wise kink motion along the dislocations line in the $(0\,1\,1)_\alpha||(1\,1\,1)_\gamma$ plane.

The given slip systems for each dislocation supports the cross-slip mechanism. This cross-clip mechanism is depicted in Figure 3.11a, where the slip vector detection cutoff was increased to highlight only atoms with a slip vector amplitude $> 0.7\|\boldsymbol{b_{1,2}}\|$. More precisely, in Figure 3.11b, CS glide planes and slip directions are depicted as extracted from the QA simulation results. BCC screw line directions cross-slip easily, as mentioned in Chapter 1. In Figure 3.11b, it can be seen that $\boldsymbol{b}_1$ dislocations, which have a $(0\,1\,1)_\alpha[1\,1\,\bar{1}]_\alpha$ slip system can cross-slip in the $(1\,0\,1)_\alpha$ plane, depicted in blue, while $\boldsymbol{b}_2$ dislocations, which have a $(0\,1\,1)_\alpha[1\,\bar{1}\,1]_\alpha$ slip system, can cross-slip in the $(\bar{1}\,0\,1)_\alpha$ plane, depicted in red.

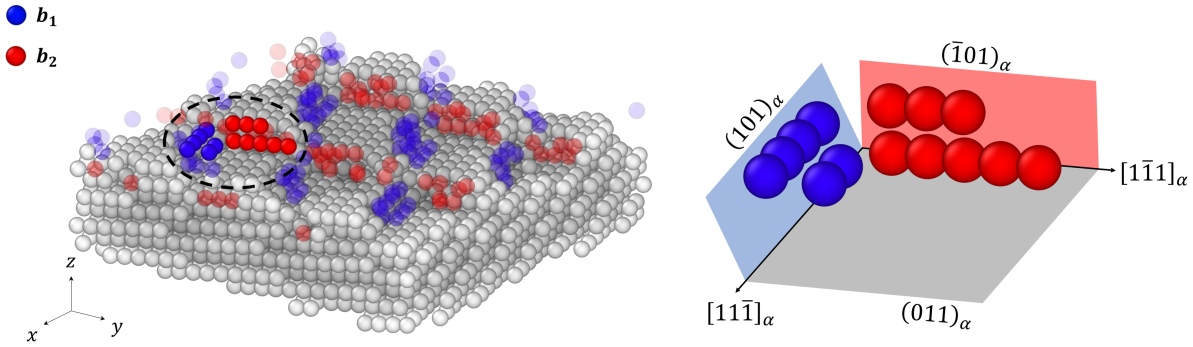

(a) Cross-slip mechanism at dislocations intersections.

(b) Cross-slip planes and slip directions.

Figure 3.11: Cross-slip mechanism at the FCC-BCC interface, with only BCC atoms remaining, for NW OR with the $(2\,3\,2)_\gamma$ HP. Extracted from the QA simulation at $t^* = 70$. Only atoms with slip vectors of amplitude $> 0.7\|\boldsymbol{b_{1,2}}\|$ are colored. Blue: atoms belonging to $\boldsymbol{b}_1$ dislocations, red: atoms belonging to $\boldsymbol{b}_2$ dislocations. **(a)** Interface relief, cross slip region is highlighted by the black circle. **(b)** Cross-slip mechanism as observed from the interface relief.

As this cross-slip process occurs at the dislocation intersections, it can be concluded that the nucleation of the new $(0\,1\,1)_\alpha$ layer is specifically driven by this mechanism. Moreover, the glide of the $\boldsymbol{b}_1$ and $\boldsymbol{b}_2$ screw dislocations, facilitated by the sidewise motion of edge-character kinks in the $(1\,1\,1)_\gamma||(0\,1\,1)_\alpha$ plane, is responsible for the in-plane propagation of the BCC phase.

3.2.2 Grenning-Troiano orientation relationship

The next OR simulated in this work is the Greninger-Troiano (GT) OR. Likewise NW OR, two variants were simulated, GT v1 and GT v2 OR, but only GT v1 will be showcased in this section. As stated in Table 3.1, this OR has parallel close-packed planes $(1\,1\,1)_\gamma$ and $(0\,1\,1)_\alpha$ between the FCC and BCC phases, with $[12\,5\,\bar{1}7]_\gamma$ and $[7\,17\,\bar{1}7]_\alpha$ as parallel directions. The GT v1 OR was simulated for three different HPs: $(1\,1\,1)_\gamma$, $(5\,7\,5)_\gamma$ and $(1\,2\,1)_\gamma$.

The angle between $[1\,0\,\bar{1}]_\gamma$ and $[1\,1\,\bar{1}]_\alpha$ directions is 2.40°, while the angle between $[0\,1\,\bar{1}]_\gamma$ and $[1\,\bar{1}\,1]_\alpha$ directions is 8.13°. Directions close to $[1\,0\,\bar{1}]_\gamma \sim [1\,1\,\bar{1}]_\alpha$ and $[0\,1\,\bar{1}]_\gamma \sim [1\,\bar{1}\,1]_\alpha$ will be denoted $[1\,0\,\bar{1}]^*_\gamma$ and $[0\,1\,\bar{1}]^*_\gamma$, respectively.

The same subsection organization as for NW OR is followed here. First, the interface structure characteristics and defects, such as the dislocation characteristics, will be discussed. Then, the interface propagation modes will be addressed.

3.2.2.1 Interface structure

In this section, only GT v1 simulations with the habit planes $(1\,1\,1)_\gamma$ and $(1\,2\,1)_\gamma$ HPs will be discussed. In the same manner as for NW OR, the interface is depicted for the $(1\,1\,1)_\gamma$ HP in Figure 3.12a and for the $(1\,2\,1)_\gamma$ HP in Figures 3.12b and 3.12c. In these figures, atoms belonging to the BCC structure were retained. The GT OR interface consists of a periodic distribution of $(0\,1\,1)_\alpha||(1\,1\,1)_\gamma$ flat terraces with steps, as depicted in Figure 3.12c. The steps are aligned along the $[1\,0\,\bar{1}]^*_\gamma$ (step (1), blue) and $[0\,1\,\bar{1}]^*_\gamma$ (step (2), red) directions. The GT OR interface structure is similar to that of the NW OR, with both displaying a double-stepped interface. However, Figure 3.12c shows a greater length difference between steps (1) and (2).

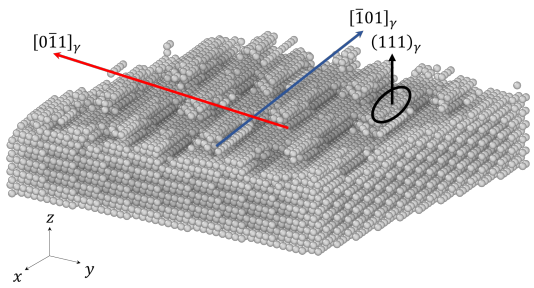

(a) HP = $(1\,1\,1)_\gamma$.

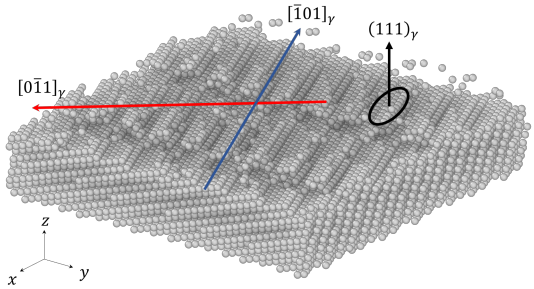

(b) HP = $(1\,2\,1)_\gamma$.

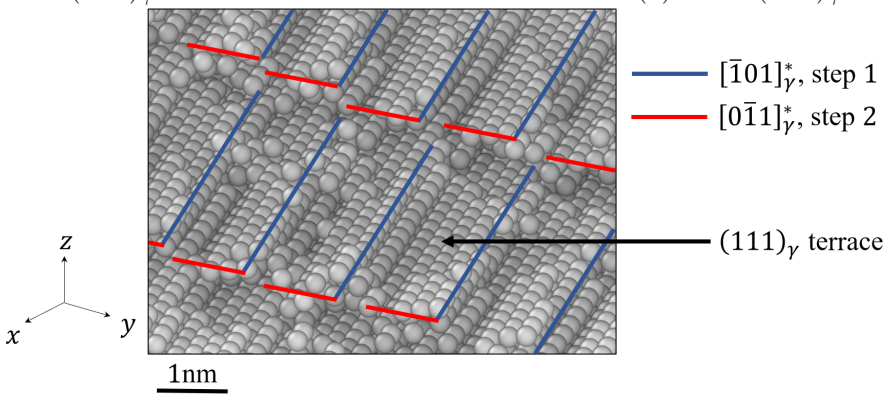

(c) Zoomed HP = $(1\,2\,1)_\gamma$.

Figure 3.12: FCC-BCC semi-coherent interface relief for GT OR, extracted from the QA simulation at $t^* = 70$. Surface relief was obtained using 'ambient occlusion' rendering in Ovito [136], displaying only BCC atoms. Blue and red arrows indicate the $[1\,0\,\bar{1}]^*_\gamma$ and $[0\,1\,\bar{1}]^*_\gamma$ directions, respectively. Terraces are parallel to $(1\,1\,1)_\gamma$ as indicated by the black circle and arrow.

Similarly to the NW OR, terrace coherency was evaluated by computing the elastic strain at the interface for all HPs. The interpretation was consistent with that for the NW OR: higher elastic strain values were measured along the steps, while lower values were observed on the terraces, confirming the semi-coherency of the interface with coherent terraces and arrays of transformation dislocations.

The assessment of step (1) and step (2) heights was also carried out for GT OR, with slices of the simulation box around the interface taken parallel to the step directions, as shown in Figure 3.13. The black lines are qualitative guides indicating the overall shape of the interface between the BCC phase (blue atoms) and the FCC phase (green atoms) and the red line indicates the HP.

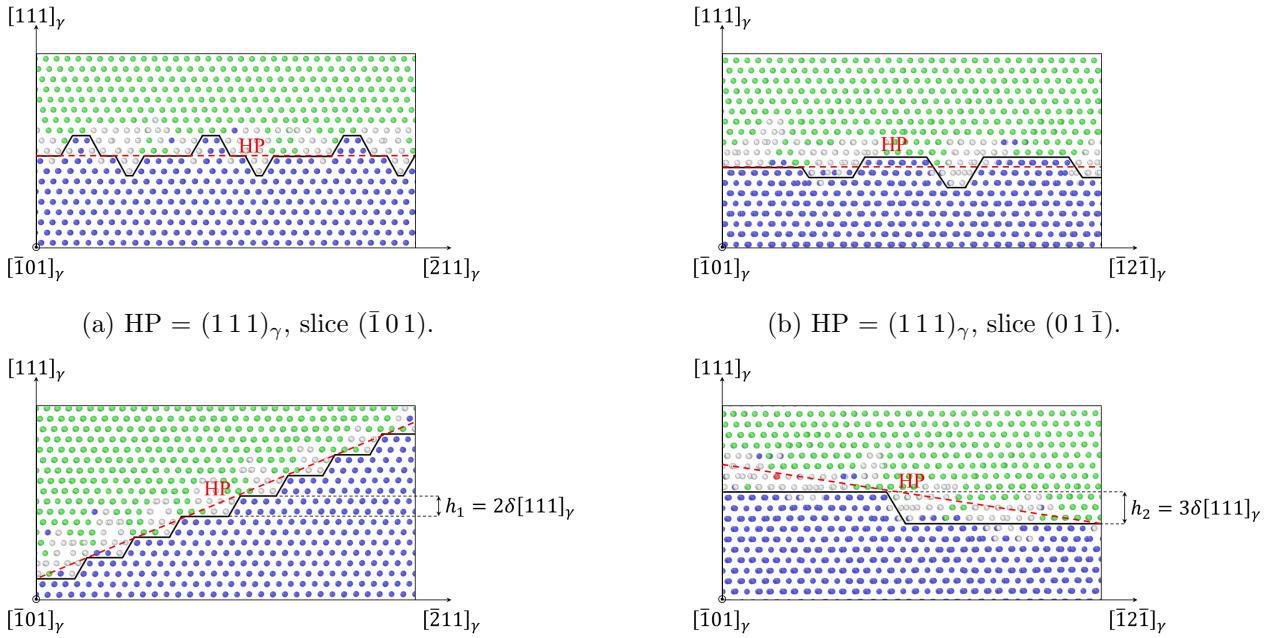

(a) HP = $(1\,1\,1)_\gamma$, slice $(\bar{1}\,0\,1)$.

(b) HP = $(1\,1\,1)_\gamma$, slice $(0\,1\,\bar{1})$.

(c) HP = $(1\,2\,1)_\gamma$, slice $(\bar{1}\,0\,1)$.

(d) HP = $(1\,2\,1)_\gamma$, slice $(0\,1\,\bar{1})$.

Figure 3.13: Two dimensional views of the area around the FCC-BCC interface for GT OR, extracted from the QA simulation at $t^* = 70$. Green: FCC, blue: BCC, white: unknown. The dark lines are qualitative guides, indicating the overall shape of the interface.

It can be concluded that, for GT OR, that a higher angle between the terrace plane $(0\,1\,1)_\alpha||(1\,1\,1)_\gamma$ and the HP favors higher step heights. Moreover, for the $(5\,7\,5)_\gamma$ HP , multiple step heights were observed along the same step direction. This is in agreement with experimental observations and simulations results [4, 5, 14]. For $(1\,1\,1)_\gamma$ HP, terrace still form, however, steps do not participate in the tilt of interface as it is already aligned with the HP.

Although the Topological Model (TM) predicts the step heights between 1 and $2\delta(1\,2\,1)_\gamma$, in the specific case of step (2) for the $(1\,2\,1)_\gamma$ HP shown in Figure 3.13b, a step height of $3\delta(1\,2\,1)_\gamma$ is observed. This phenomenon has also been observed experimentally by Ogawa et al. [5] in HRTEM images of the austenite-martensite interface in an Fe-23.0Ni-3.8Mn alloy, where even larger step heights were noted. Thus, step heights are not strictly limited to 1 or $2\delta(1\,2\,1)_\gamma$ and can be larger to accommodate specific interface geometries.

As discussed previously, the step (1) and (2) directions are expected to align with the directions of the transformation dislocations Burgers vectors. For confirmation, Burgers vector calculated with the SVA are plotted in Figure 3.14a for the GT OR with $(1\,1\,1)_\gamma$ HP. For the $(1\,2\,1)_\gamma$ HP, Burgers vectors are depicted both in the HP, in Figure 3.14b, and in the terrace plane, in Figure 3.14c.

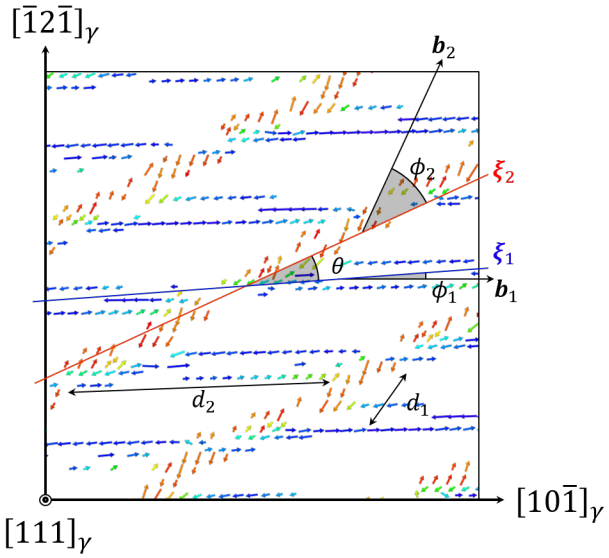

(a) HP = $(1\,1\,1)_\gamma$.

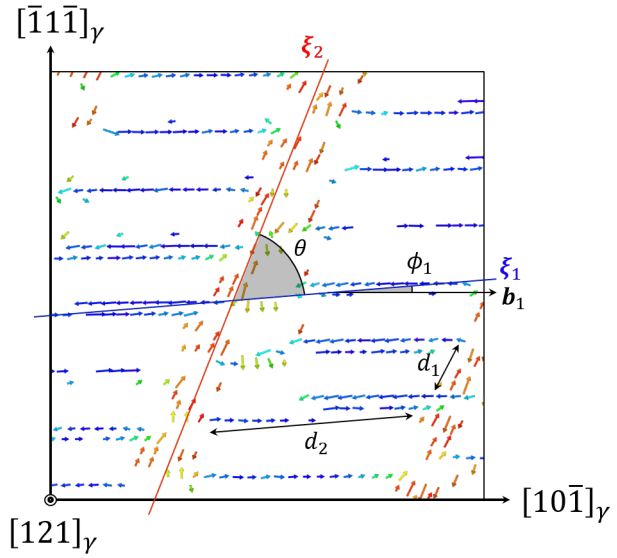

(b) HP = $(1\,2\,1)_\gamma$, shown in $(1\,2\,1)_\gamma$ plane.

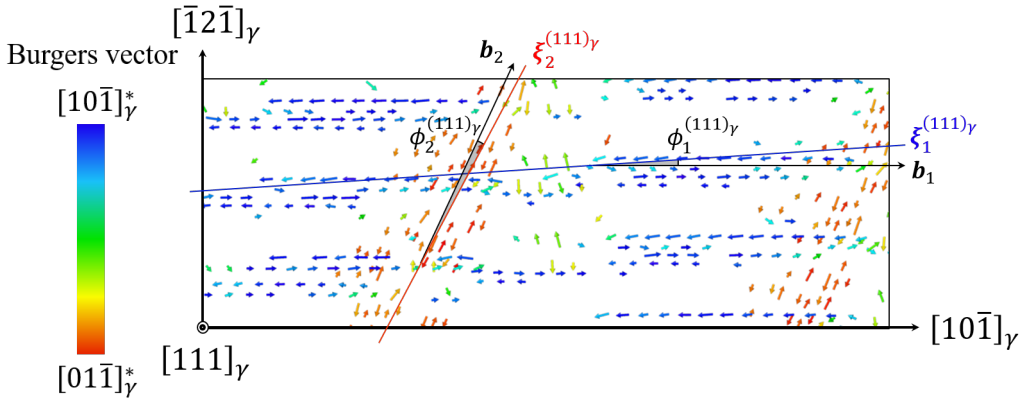

(c) HP = $(1\,2\,1)_\gamma$, shown in $(1\,1\,1)_\gamma$ plane.

Figure 3.14: Slip vector analysis of the dislocation networks at the FCC-BCC interface in the $(1\,1\,1)_\gamma$ plane for GT OR, extracted from the QA simulation at $t^* = 70$. Only slip vectors with an amplitude of $> 0.5\|\boldsymbol{b1, 2}\|$ are displayed. Blue: $[1\,0\,\bar{1}]^*_\gamma$ direction, red: $[0\,1\,\bar{1}]^*_\gamma$ direction. Mean line directions $\boldsymbol{\xi}_1$ and $\boldsymbol{\xi}_2$, steps spacing d_1 and d_2, and Burgers vectors $\boldsymbol{b}_1$, $\boldsymbol{b}_2$ are represented. Vectors are scaled 6 times.

The Burgers vectors obtained by the SVA at the FCC-BCC interface are the same for both HPs, i.e., $\boldsymbol{b}_1 = \frac{a_\gamma}{2}[1\,0\,\bar{1}]^*_\gamma$ and $\boldsymbol{b}_2 = \frac{a_\gamma}{2}[0\,1\,\bar{1}]_\gamma$. For $(1\,1\,1)_\gamma$ HP, the mean line directions are $\boldsymbol{\xi}_1 = [0.69, 0.03, -0.72]_\gamma$ and $\boldsymbol{\xi}_2 = [0.45, 0.37, -0.82]_\gamma$, while for $(1\,2\,1)_\gamma$ HP, the mean line directions are $\boldsymbol{\xi}_1 = [0.67, 0.06, -0.75]_\gamma$ and $\boldsymbol{\xi}_2 = [0.16, 0.50, -0.85]_\gamma$. These dislocations are aligned

along the step directions and mean line directions $\boldsymbol{\xi}_1$ and $\boldsymbol{\xi}_2$ both lie within the HP.

The mean line directions $\boldsymbol{\xi}_1$ and $\boldsymbol{\xi}_2$ deviate from the perfect screw orientations by the angles ϕ_1 and ϕ_2, respectively. For $(1\,2\,1)_\gamma$ HP, the same angle designations, based on the plane of projection, are used as for the NW OR. For GT OR, it appears that $\boldsymbol{\xi}_1$ line directions are less deviated from their Burgers vector than the $\boldsymbol{\xi}_2$ line directions. This is quantitatively supported by the data in Table 3.7, where the angle ϕ_1 is between 2.0° and 4.6° for all simulated HP, indicating only weak deviation from $\boldsymbol{b}_1$. In contrast, the angle ϕ_2 ranges from 17.3° to 33.0° across all HPs, suggesting a higher density of kinks along $\boldsymbol{\xi}_2$ compared to $\boldsymbol{\xi}_1$. The origins of these deviations an be related to cross-slip (CS) and edge character of kinks in the $(1\,1\,1)_\gamma$ plane. This point will be further developed in Section 3.2.2.2.

Although O-lattice calculations were not performed for GT OR, the Moiré pattern can be computed and compared to QA simulation results. The Moiré pattern in the $(1\,1\,1)_\gamma$ plane is depicted in Figure 3.15. This figure indicates that regions of lower coherency between the FCC and BCC phases are located near the mean lines directions of dislocations. Furthermore it indicates a larger misorientation between $\boldsymbol{b}_2$ and $\boldsymbol{\xi}_2$ than between $\boldsymbol{b}_1$ and $\boldsymbol{\xi}_1$, which is observed in QA simulations.

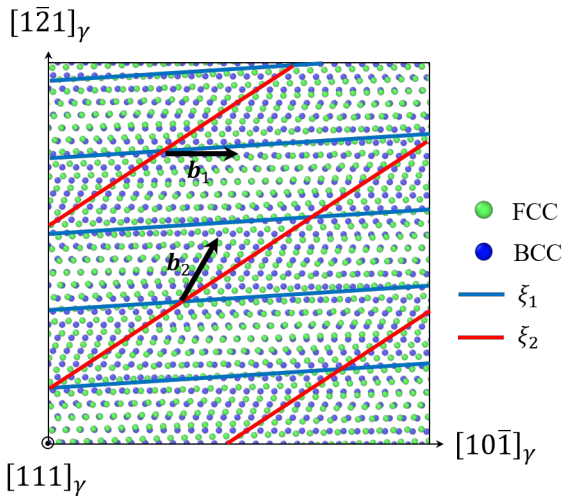

(a) Moiré pattern.

Figure 3.15: Moiré patterns for GT OR in $(1\,1\,1)_\gamma$ with QA simulation misfit of 1.23. Green atoms: FCC, Blue atoms: BCC. Blue and red lines indicates regions of high atomic mismatch and a related to the mean line directions of dislocations $\boldsymbol{b}_1$ and $\boldsymbol{b}_2$, respectively.

The measured steps spacing, provided for all HPs in Table 3.7, are within the experimental range described previously in Section 3.2.1.1. The spacing of step (1) ranges between 1.2 nm and 3.3 nm, while the length of step (2) is between 5.2 nm and 6.2 nm. For every HP, the length of step (2) is significantly greater than that of step (1). This large difference in steps spacing is in

agreement with the Moiré pattern, in Figure 3.15, as the spacing between $\boldsymbol{b}_2$ appears greater than the spacing between $\boldsymbol{b}_1$ dislocations. These results can be compared to those from the TM [43], where at 0.1° from the GT OR, the calculated step (1) spacing is $d_1 = 1.256$ nm and the step (2) spacing is $d_2 = 3.801$ nm. The step (1) spacing d_1 determined by the TM is within the range of the QA simulations and closely matches the values for the $(1\,2\,1)_\gamma$ HP. Nevertheless, the theoretical step (2) spacing computed by the TM is smaller than observed QA simulations, though it remains significantly larger than d_1 in both cases.

The elastic energy $U_e^{\boldsymbol{b_{1,2}}}$ of dislocations, assuming they are straight alongside a terrace step, is computed using Equation 3.2.1. As d_2 is rather consistent across all HPs, the elastic energy of the dislocation with the Burgers vector $\boldsymbol{b}_1$ does not vary too much for different HPs. However, the elastic energy of the second dislocation with the Burgers vector $\boldsymbol{b}_2$ is much smaller for the $(1\,2\,1)_\gamma$ habit plane, due to d_1 decreasing with increasing HP tilt. All dislocation parameters, including $\boldsymbol{\xi}_{1,2}$, $\theta_{1,2}$, $\phi_{1,2}$, $d_{1,2}$ and $U_e^{\boldsymbol{b_{1,2}}}$ for each simulated HP, are provided in Tables 3.6 and 3.7. As shown in these tables, the angle θ between $\boldsymbol{\xi}_1$ and $\boldsymbol{\xi}_2$ increases with the increasing angle between the terrace plane and the HP, while steps spacing decrease. The reduction in steps spacing is more pronounced for step (1), where it goes from 3.3nm for the $(1\,1\,1)_\gamma$ HP tp 1.2 nm for the $(1\,2\,1)_\gamma$ HPs.

OR	HP	$\boldsymbol{\xi}_1$	$\boldsymbol{\xi}_2$	$\theta(^\circ)$
GT v1	$(1\,1\,1)_\gamma$	$[0.69, 0.03, -0.72]_\gamma$	$[0.45, 0.37, -0.82]_\gamma$	24.9
	$(5\,7\,5)_\gamma$	$[0.67, 0.06, -0.75]_\gamma$	$[0.16, 0.50, -0.85]_\gamma$	39.7
	$(1\,2\,1)_\gamma$	$[0.67, 0.03, -0.74]_\gamma$	$[-0.24, 0.53, -0.82]_\gamma$	62.3

Table 3.6: GT OR line directions $\boldsymbol{\xi}_1$, $\boldsymbol{\xi}_2$, and angle θ between the two lines directions.

OR	HP	$\boldsymbol{\phi_1}(^\circ)$	$\boldsymbol{\phi_2}(^\circ)$	d_1 (nm)	d_2 (nm)	$U_e^{\boldsymbol{b_1}}$ (eV)	$U_e^{\boldsymbol{b_2}}$ (eV)
GT v1	$(1\,1\,1)_\gamma$	2.0	33.0	3.3	6.2	95.0	50.6
	$(5\,7\,5)_\gamma$	4.6	17.3	1.8	5.4	82.8	27.6
	$(1\,2\,1)_\gamma$	3.4	18.2	1.2	5.2	79.7	18.4

Table 3.7: GT OR angle $\phi_{1,2}$ between the line directions $\boldsymbol{\xi}_{1,2}$ and Burgers vector $\boldsymbol{b_{1,2}}$ and steps spacing $d_{1,2}$.

3.2.2.2 Interface propagation

To investigate the interface motion, a displacement map was calculated for all GT OR with considered HPs. No meaningful difference was found with NW OR, as high displacements are along mean dislocations lines $\boldsymbol{\xi}_1$ and $\boldsymbol{\xi}_2$, decorating the steps. The propagation and nucleation of the BCC phase are shown in Figure 3.16 at $t^* = 74$, while the nucleation and propagation for a single terrace is shown in Figure 3.17.

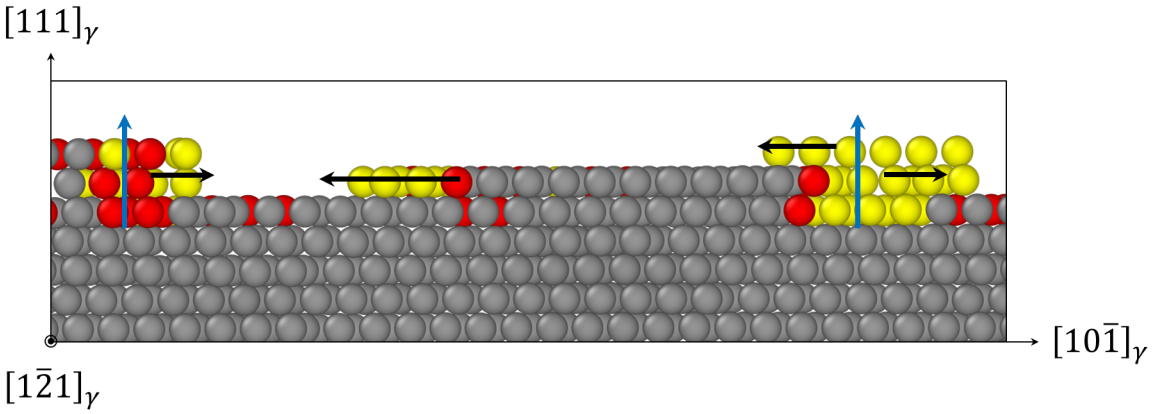

(a) Plane $(1\,\bar{2}\,1)_\gamma$.

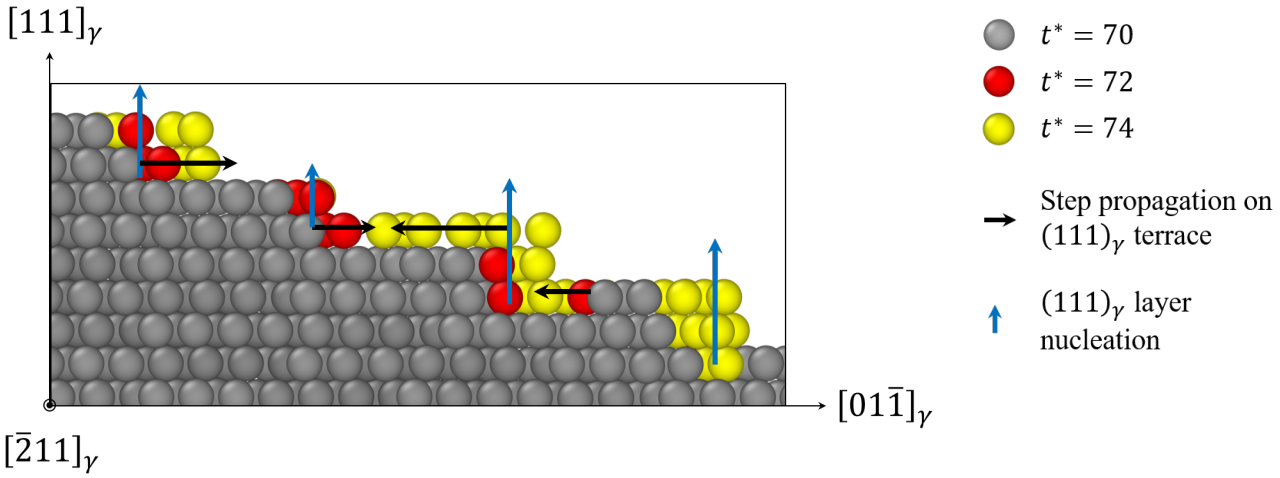

(b) Plane $(\bar{2}\,1\,1)_\gamma$.

Figure 3.16: Step-flow propagation mode of the FCC-BCC interface surface, for GT OR, as extracted from QA simulations between $t^* = 70$ and $t^* = 74$. Only BCC atoms are retained. Grey: atomic configuration at t^*70, red: at $t^* = 72$ and yellow at $t^* = 74$. Blue arrow: $(0\,1\,1)_\alpha$ layer nucleation, black arrow: step propagation in $(0\,1\,1)_\alpha$. **(a)** plane $(1\,\bar{2}\,1)_\gamma$, **(b)** plane $(\bar{2}\,1\,1)_\gamma$.

To conclude, the propagation and nucleation of the BCC phase follow the same step-flow mechanism, as suggested in [143], and involve two processes occurring in parallel: the propagation of existing steps in the $(0\,1\,1)_\alpha$ plane along the step directions and the nucleation of new BCC layers at dislocation intersections.

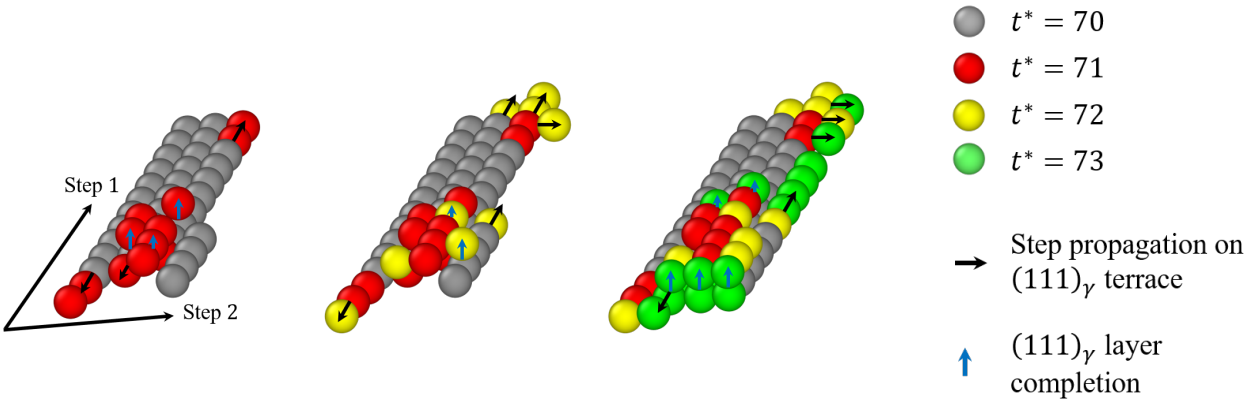

Figure 3.17: Step-flow propagation mode of the FCC-BCC interface for a single terrace, as extracted from QA simulations between $t^* = 70$ and $t^* = 71.5$. Only BCC atoms are retained. Only BCC atoms are retained. Grey: atomic configuration at t^*70, red: at $t^* = 72$ and yellow at $t^* = 74$. Blue arrow: $(0\,1\,1)_\alpha$ layer nucleation, black arrow: step propagation in $(0\,1\,1)_\alpha$.

Furthermore, both dislocations $\boldsymbol{b}_1$ and $\boldsymbol{b}_2$ glide in $(1\,1\,1)_\gamma||(0\,1\,1)_\alpha$ plane, which gives slip systems $(1\,1\,1)_\gamma[1\,0\,\bar{1}]_\gamma$ and $(1\,1\,1)_\gamma[0\,1\,\bar{1}]_\gamma$. The glide of $\boldsymbol{b}_1$ and $\boldsymbol{b}_2$ dislocations is facilitated by the sidewise motion of edge character kinks in the $(1\,1\,1)_\gamma$ plane. These dislocations glide are responsible of the in-plane BCC phase propagation.

3.2.3 Kurdjumov-Sachs orientation relationship

The last OR simulated for the FCC to BCC phase transformation in this chapter is the KS OR. Like the other two ORs, two variants were simulated but only one will be presented. As stated in Table 3.1, KS v1 OR has $(1\,1\,1)_\gamma$ and $(0\,1\,1)_\alpha$ with $[1\,0\,\bar{1}]_\gamma$ and $[1\,1\,\bar{1}]_\alpha$ parallel directions. For consistency, the same denotation $[1\,0\,\bar{1}]^*_\gamma$ will still be used as for the other two ORs. However, the angle between $[0\,1\,\bar{1}]_\gamma$ and $[\bar{1}\,1\,\bar{1}]_\alpha$ directions is 10.52° for KS v1, directions close to $[0\,1\,\bar{1}]_\gamma \sim [\bar{1}\,1\,\bar{1}]_\alpha$ be referred to as $[0\,1\,\bar{1}]^*_\gamma$.

3.2.3.1 Interface structure

For KS OR, only $(5\,7\,5)_\gamma$ and $(1\,2\,1)_\gamma$ HPs will be depicted. Although KS v1 OR with $(1\,1\,1)_\gamma$ HP was simulated, it corresponds to a particular case (flat interface) already treated for NW and GT OR. However, in the case of KS v1 OR, the simulation with $(5\,7\,5)_\gamma$ HP gives an additional insight about the mechanism of FCC to BCC phase transformation. Therefore, the structures of the interface with $(5\,7\,5)_\gamma$ HP and $(1\,2\,1)_\gamma$ HP will be considered. Moreover, a slightly different method of visualization than for the NW and GT OR will be used in the case of KS OR. The same CNA method from Ovito [136] was used to illustrate the interface relief for all FCC-BCC interfaces obtained from QA simulations. However, the stepped structure of the interface can be highlighted easily by keeping, alongside the BCC phase, the atoms that were detected as 'other'. In the KS

OR cases, the CNA was less accurate in distinguishing the BCC phase at the interface, partly due to the small width of step, as it will be observed. The three dimensional views of the interface with $(5\,7\,5)_\gamma$ and $(1\,2\,1)_\gamma$ HP are shown in Figure 3.18. These figures indicate the absence second set of steps (step (2)) for the NW and GT ORs. It appears that each terrace spans the entire interface along the $[1\,0\,\bar{1}]^*_\gamma$ direction. However, the interface is locally perturbed by an interfacial defect. These zones are indicated by the red arrows in Figure 3.18.

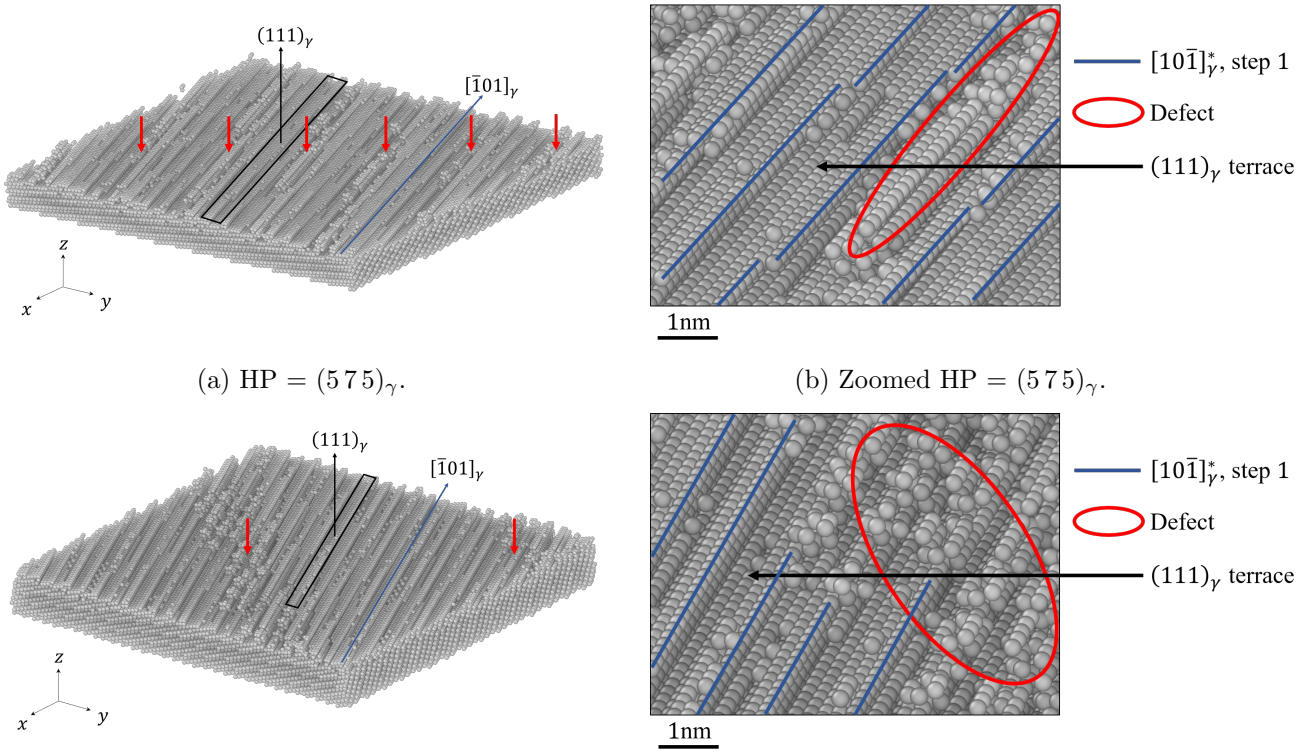

(a) HP = $(5\,7\,5)_\gamma$.

(b) Zoomed HP = $(5\,7\,5)_\gamma$.

(c) HP = $(1\,2\,1)_\gamma$.

(d) Zoomed HP = $(1\,2\,1)_\gamma$.

Figure 3.18: FCC-BCC semi-coherent interface relief for KS OR, extracted from QA simulation at $t^* = 70$. Surface relief obtained using 'ambient occlusion' rendering in Ovito [136], displaying BCC atoms and atoms marked as 'other' by the CNA. Blue arrows indicates $[1\,0\,\bar{1}]^*_\gamma$ direction. Terraces are parallel to $(1\,1\,1)_\gamma$ as indicated by the black rectangle and arrow.

The amplified view of this perturbed area for $(5\,7\,5)_\gamma$ and $(1\,2\,1)_\gamma$ HPs is shown in Figures 3.18b and 3.18d, respectively. It can be seen that the interface consists of a periodic distribution of $(1\,1\,1)_\gamma||(0\,1\,1)_\alpha$ flat terraces. Only one step, whose direction is $[1\,0\,\bar{1}]^*_\gamma$, is visible. It will be referred to as step (1) thereafter to maintain consistency with the terminology used for NW and GT ORs.

The volumetric strain is computed for each atom at the FCC-BCC interface and is shown in Figure 3.19. In this figure, only atoms belonging to the BCC structure are retained. As a result,

no elastic strain is calculated for atoms not identified as part of the BCC phase.

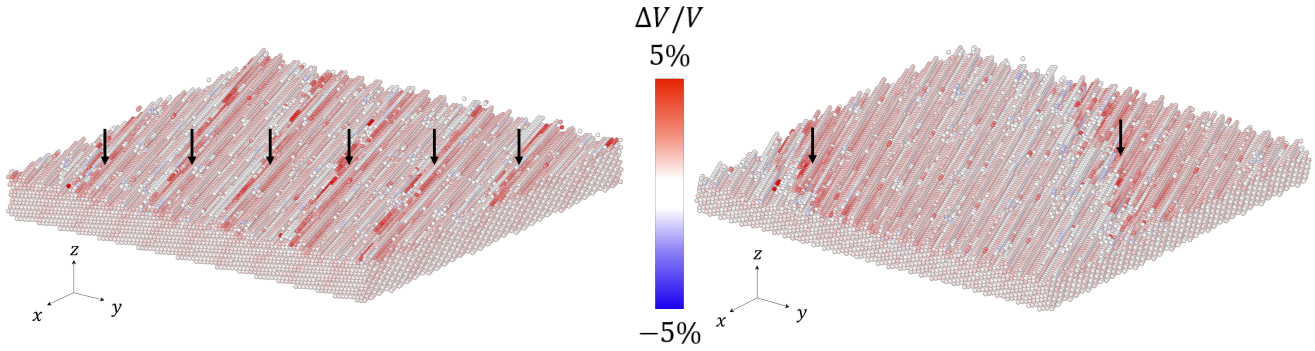

(a) HP = $(5\,7\,5)_\gamma$. (b) HP = $(1\,2\,1)_\gamma$.

Figure 3.19: FCC-BCC semi-coherent interface relief for KS OR, extracted from the QA simulation at $t^* = 70$. Rendering done in Ovito [136], displaying only BCC atoms. Atom coloration is based on elastic strain calculations, displaying volumetric strain $\Delta V/V$. Red indicates the maximum $\Delta V/V$, and blue the minimum.

The regions of high volumetric strain, indicated by black arrows in Figure 3.19, corresponds to the localized interfacial defects in Figure 3.18. Moreover, low volumetric strain was measured in regions were only the step structure was observed without this interfacial defect. The observed volumetric strain can be compared to the potential energy map from molecular dynamics simulations of the FCC to BCC phase transformation with KS OR in the $(1\,1\,1)_\gamma$ plane, conducted by Ou et al. [12], and discussed in Chapter 1 along the Figure 1.16a. In this figure, no diamond-shaped pattern is observed. Instead, only one direction of high potential energy is noted, which has the same direction as regions of low potential energy. This result can be more specifically compared to the QA simulation of KS OR with $(1\,1\,1)_\gamma$ HP or $(5\,7\,5)_\gamma$ HP. The nature of these regions of high volumetric strain will be assessed in more detail in the dislocation analysis.

The stepped nature of the interface is assessed in the same manner as for NW and GT ORs, with slices of the simulation box taken around the interface. These slices are displayed in Figure 3.20 and were obtained outside of the high elastic energy regions detected by the volumetric strain in Figure 3.19. Step (1) along the $[1\,0\,\bar{1}]^*_\gamma$ direction is confirmed for both $(5\,7\,5)_\gamma$ and $(1\,2\,1)_\gamma$ HPs, as indicated by the black lines in Figures 3.20a and 3.20b. For the $(5\,7\,5)_\gamma$ HP, the step height was measured at $1\delta(1\,1\,1)_\gamma$, while for the $(1\,2\,1)_\gamma$ HP, the step height was a mix of $1\delta(1\,1\,1)_\gamma$ and $2\delta(1\,1\,1)_\gamma$. The observation of different step heights for the same HP is again consistent with HRTEM experimental observations [4, 5] and the modified PTMC model by Maresca et al. [14].

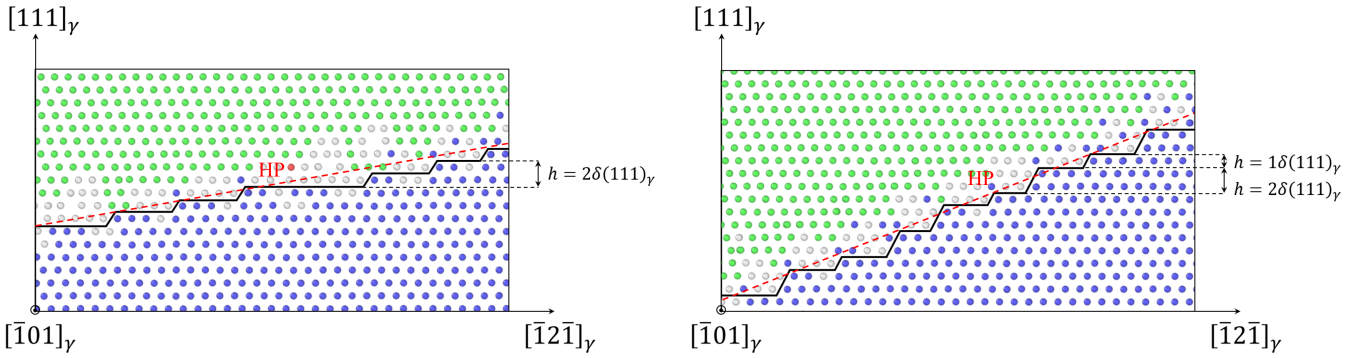

(a) HP = $(5\,7\,5)_\gamma$.

(b) HP = $(1\,2\,1)_\gamma$.

Figure 3.20: Two dimensional views of the area around the FCC-BCC interface for KS OR, extracted from the QA simulation at $t^* = 70$. Green: FCC, blue: BCC, white: unknown. The dark lines are qualitative guides, indicating the overall shape of the interface.

For KS OR, the presence of a single step structure at the interface is consistent with the literature, as most theoretical models consider only one step structure [43, 45]. In QA simulation with KS OR, this steps spacing is between 0.9 nm and 1.1 nm for each HP, as reported in Table 3.8. This is smaller than in Maresca et al. [14] molecular dynamics simulation and than in Sandvick et al. experimental results were the average step spacing was of 1.45 nm and 1.33 nm, respectively. However, it closely matches the TM prediction [43], where this step spacing was of 0.97 nm. The Burgers vectors and line directions of dislocations for the KS OR are plotted using the SVA in Figure 3.21.

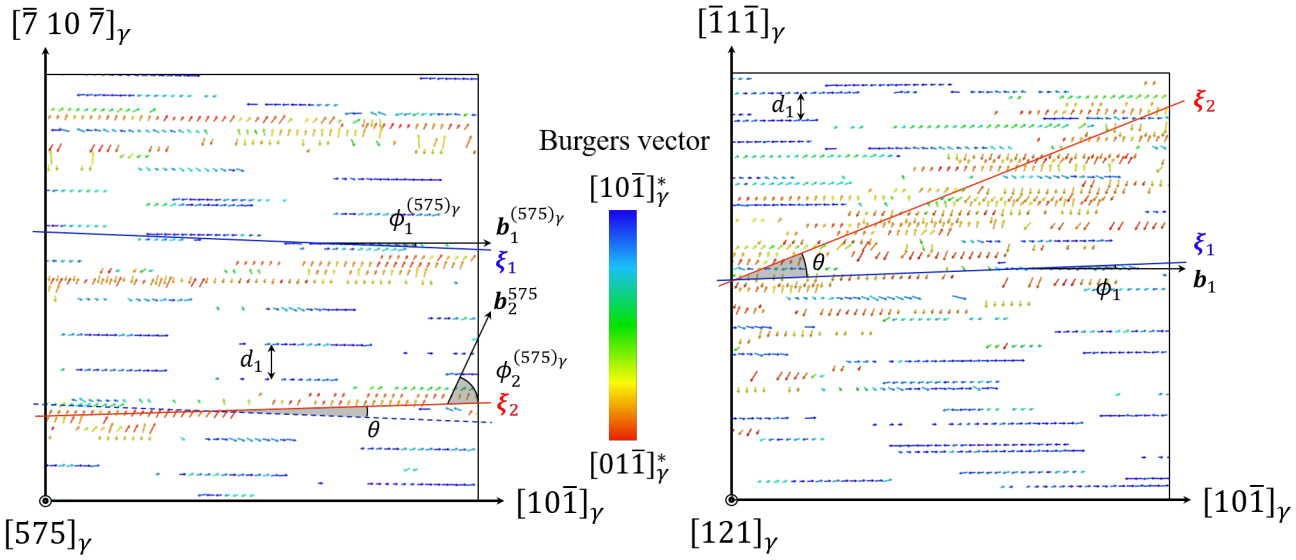

(a) HP = $(5\,7\,5)_\gamma$, shown in $(5\,7\,5)_\gamma$ plane.

(b) HP = $(1\,2\,1)_\gamma$, shown in $(1\,2\,1)_\gamma$ plane.

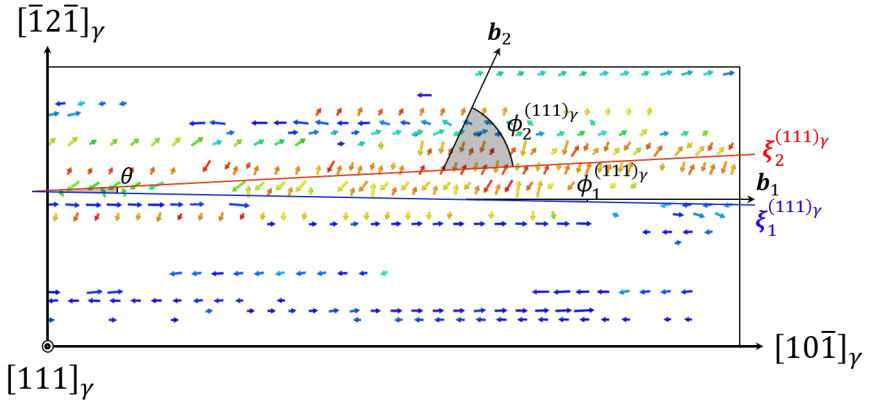

(c) HP = $(5\,7\,5)_\gamma$, shown in $(1\,1\,1)_\gamma$ plane.

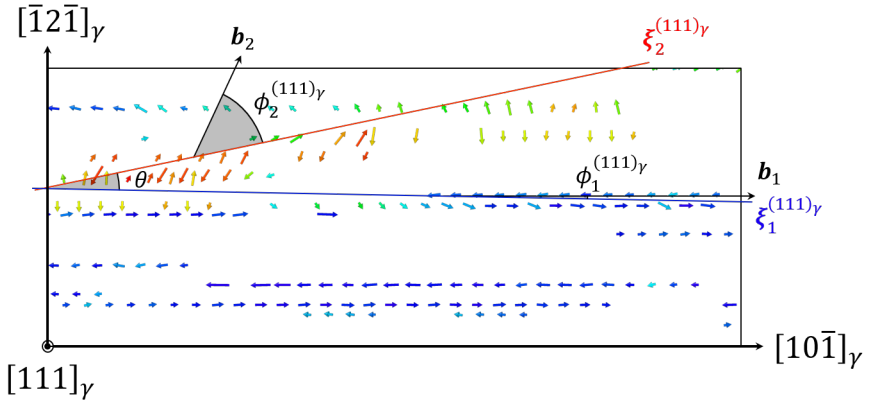

(d) HP = $(1\,2\,1)_\gamma$, shown in $(1\,1\,1)_\gamma$ plane.

Figure 3.21: Slip vector analysis of the dislocation networks at the FCC-BCC interface in the $(1\,1\,1)_\gamma$ plane for NW OR, extracted from the QA simulation at $t^* = 70$. Only slip vectors with an amplitude of $> 0.5\|\boldsymbol{b1, 2}\|$ are displayed. Blue: $[1\,0\,\bar{1}]^*_\gamma$ direction, red: $[0\,1\,\bar{1}]^*_\gamma$ direction. Mean line directions $\boldsymbol{\xi}_1$ and $\boldsymbol{\xi}_2$, steps spacing d_1 and d_2, and Burgers vectors $\boldsymbol{b}_1$, $\boldsymbol{b}_2$ are represented. Vectors are scaled 6 times.

Although, the second step is absent for KS OR, the SVA confirms the presence of the two type of dislocations previously detected: $\boldsymbol{b}_1 = \frac{a_\gamma}{2}[1\,0\,\bar{1}]^*_\gamma$, highlighted by the blue arrows, and $\boldsymbol{b}_2 = \frac{a_\gamma}{2}[0\,1\,\bar{1}]_\gamma$, highlighted by the red arrows. The mean line directions $\boldsymbol{\xi}_1$ and $\boldsymbol{\xi}_2$ deviate from the perfect screw orientations by the angles ϕ_1 and ϕ_2, respectively. Since the line directions and the Burgers vectors of the dislocations do not lie in the same plane, the angles shown in Figure 3.14 represent the angles between the projections of these vectors onto the HP. The mean angle measured between $\boldsymbol{\xi}_1$ and $\boldsymbol{b}_1$ across all HPs ranges from 0.6° to 2.5°. This slight deviation from the perfect screw orientation induces a kinked character of dislocations.

Concerning, $\boldsymbol{b}_2$ dislocations, their mean line direction $\boldsymbol{\xi}_2$ is highly deviated from the pure screw orientation. As indicated in Table 3.9, $\boldsymbol{\xi}_2$ is deviated by an angle between 41.7° and 61.2° from $\boldsymbol{b}_2$, indicating that the dislocation is therefore mixed. Moreover, while $\boldsymbol{\xi}_2$ deviate from $\boldsymbol{b}_2$, it becomes more close to $\boldsymbol{\xi}_1$ with an angle of only 4.9° for $(5\,7\,5)_\gamma$ HP. The presence of these dislocations for KS OR in the FCC-BCC interface does not reach a consensus in the literature. They are described by Maresca et al. [14] as extra half-planes due to edge dislocation cores $\frac{a_\gamma}{2}[1\,\bar{1}\,1]_\alpha$, which is equivalent to $\boldsymbol{b}_2$. However, the results from QA simulations lead to different conclusions. First, the dislocations with Burgers vector $\boldsymbol{b}_2$ can not be considered as pure edge dislocations as the angle between $\boldsymbol{b}_2$ and their mean line direction $\boldsymbol{\xi}_2$ varies between 41.7° and 61.2°. However, the edge component of these dislocations can be detected using a Burgers circuit in the $[1\,0\,\bar{1}]_\gamma$ plane, as shown in Figure 3.22.

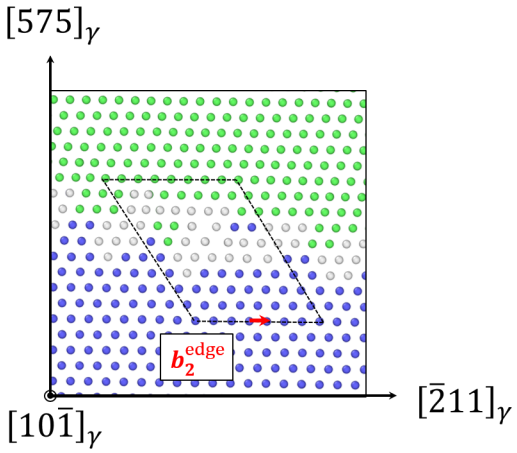

Figure 3.22: Burgers circuit of edge component of dislocation with Burgers vector $b_2 = \frac{a_\gamma}{2}[0\,\bar{1}\,1]^*_\gamma$. Extracted from the QA simulation at $t^* = 7$, for the KS v1 OR with the $(5\,7\,5)_\gamma$ HP. Blue: BCC, green: FCC, grey: undefined crystalline structure.

As indicated by the Moiré pattern, shown in Figure 3.23a, dislocations of type $\boldsymbol{b}_1$ alone do not achieve perfect matching between the BCC and FCC phases in the $(1\,1\,1)_\gamma$ plane. However, adding dislocations of type $\boldsymbol{b}_2$ in a direction close to $\boldsymbol{\xi}_1$ deforms the system to locally match the FCC and BCC structures. Moreover, this type of dislocation was computed by Hall et al. [54] and Moritani et al. [4] using the O-lattice approach. A schematic representation of the direction of dislocations

lines and Burgers vector from the O-lattice is provided in Figure 3.23b.

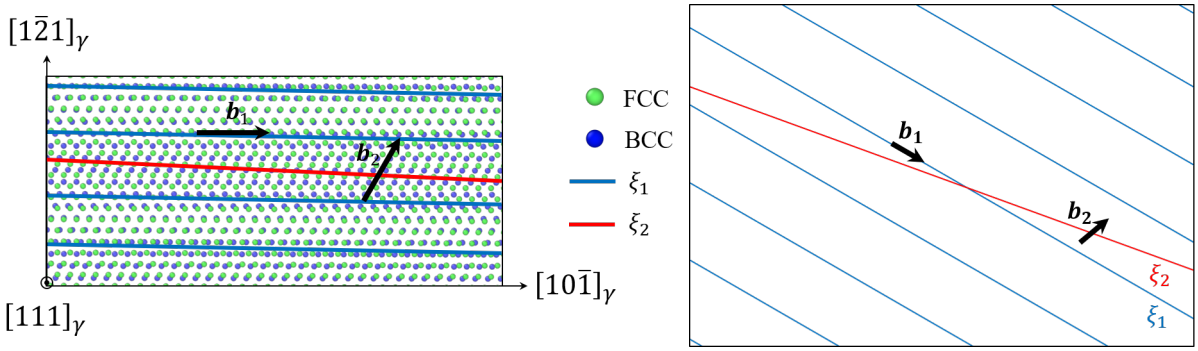

(a) Moiré pattern.

(b) O-lattice theory [4, 54]

Figure 3.23: **(a)** O-lattice calculation for NW OR, schematized from [4, 54]. **(b)** Moiré patterns for NW OR in $(1\,1\,1)_\gamma$ with QA simulation misfit of 1.23. Green atoms: FCC, Blue atoms: BCC. Blue and red lines highlight region of high atomic mismatch between FCC and BCC structure along $\boldsymbol{b}_1$ and $\boldsymbol{b}_2$ respectively.

In Figure 3.24, dislocations lines $\boldsymbol{\xi}_1$ and $\boldsymbol{\xi}_2$ are depicted in a three dimensional view of the interface. Dislocations with Burgers vector $\boldsymbol{b}_1$ are highlighted by the blue colored atoms and dislocations with Burgers vector $\boldsymbol{b}_2$ by the red ones.

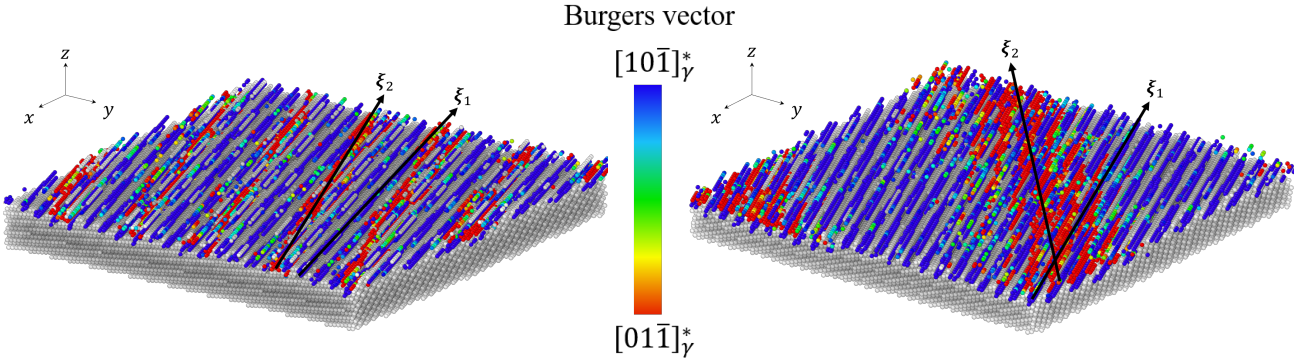

(a) HP = $(5\,7\,5)_\gamma$.

(b) HP = $(1\,2\,1)_\gamma$.

Figure 3.24: Line direction-step connection for KS OR, as determined by slip vector analysis of the FCC-BCC interface, with only BCC atoms remaining, extracted from the QA simulation at $t^* = 70$. Only atoms with slip vectors of amplitude $> 0.5\|\boldsymbol{b_{1,2}}\|$ are colored. Blue atoms have a $\boldsymbol{b}_1$ Burgers vector. Red atoms have a $\boldsymbol{b}_2$ Burgers vector.

As with the NW and KS ORs, the interface structure is composed of two dislocation networks with Burgers vectors $\boldsymbol{b}_1 = \frac{a_\gamma}{2}[1\,0\,\bar{1}]^*_\gamma$ and $\boldsymbol{b}_2 = \frac{a_\gamma}{2}[0\,1\,\bar{1}]^*_\gamma$. For $(5\,7\,5)_\gamma$ HP, the mean line directions are $\boldsymbol{\xi}_1 = [0.73, -0.03, -0.69]_\gamma$ and $\boldsymbol{\xi}_2 = [0.69, -0.03, -0.73]_\gamma$, while for $(1\,2\,1)_\gamma$ HP, the mean line directions are $\boldsymbol{\xi}_1 = [0.71, -0.01, -0.70]_\gamma$ and $\boldsymbol{\xi}_2 = [0.47, 0.20, -0.87]_\gamma$. However, unlike other ORs,

only a single step, which is along the mean dislocation line $\boldsymbol{\xi}_1$ is observed, which can be attributed to specific characteristics of KS OR interfaces.

The mean line directions $\boldsymbol{\xi}_1$ and $\boldsymbol{\xi}_2$ show minimal deviation from each other, with an angle $\theta = 4.9°$ in the case of the $(5\,7\,5)_\gamma$ HP. Although this angle increases to $20.4°$ for the $(1\,2\,1)\gamma$ HP, the mean dislocation line direction does not represent the local morphology of the $\boldsymbol{b}_2$ dislocations. This is shown by the line direction analysis applied to $\boldsymbol{b}_2$ dislocations in Figure 3.25. This algorithm is an extension of the SVA developed for the QA simulations post-treatment and is presented alongside the SVA in Appending B. It is observed that local line directions $\boldsymbol{\xi}_2^{loc}$ of $\boldsymbol{b}_2$ dislocations, indicated by black arrows are aligned with $\boldsymbol{\xi}_1$. Additionally, because $\boldsymbol{\xi}_1$ deviates only slightly from $\boldsymbol{b}_1$, with a maximum deviation of $2.5°$ across all HPs, $\boldsymbol{\xi}_2$ is generally closer to $\boldsymbol{b}_1$ than to $\boldsymbol{b}_2$.

In other ORs, it was observed that the step directions with kinks align with the mean line directions $\boldsymbol{\xi}_{1,2}$, while the step itself follows the direction of its associated Burgers vector: $\boldsymbol{b}_1$ for step (1) and $\boldsymbol{b}_2$ for step (2). Consequently, in the case of KS OR, the theoretical steps (2) and their kinks should align with the mean line direction $\boldsymbol{\xi}_2$, which is closer to $\boldsymbol{b}_1$ than to $\boldsymbol{b}_2$. This results in only small segments of steps oriented along $\boldsymbol{b}_2$, which could be identified as kinks for the step (1) along $\boldsymbol{b}_1$.

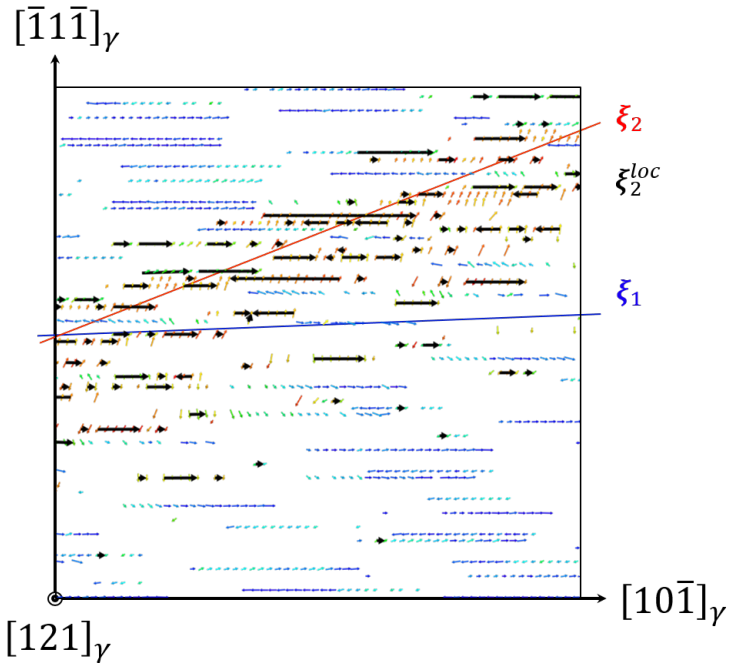

Figure 3.25: Line direction analysis applied to dislocations with Burgers vector $\boldsymbol{b}_2$ computed by the SVA at the FCC-BCC interface in the $(1\,1\,1)_\gamma$ plane for KS OR, extracted from the QA simulation at $t^* = 70$. Only slip vectors with an amplitude of $> 0.5\|\boldsymbol{b_{1,2}}\|$ are displayed. Blue: $[1\,0\,\bar{1}]^*_\gamma$ direction, red: $[0\,1\,\bar{1}]^*_\gamma$ direction. Mean lines directions $\boldsymbol{\xi}_1$ and $\boldsymbol{\xi}_2$, and local dislocation line $\boldsymbol{\xi}_2^{loc}$ are represented in blue, red, and black, respectively. Burgers vectors are scaled 6 times for improved visualization.

The influence of the HP on interface characteristics for KS OR is summarized in Table 3.8 for the line directions $\boldsymbol{\xi}_{1,2}$ and the angle θ between, and in Table 3.9 the deviation angles $\phi_{1,2}$ and steps spacing $d_{1,2}$ are noted. Since no second step was detected, the spacing for step (2) is denoted as ø for each HP. The HP orientation appears to have minimal effect on $\boldsymbol{\xi}_1$, as its deviation angle from $\boldsymbol{b}_1$ remains close to 1 degree across the tested HPs. However, as shown in Figure 3.24b for the $(1\,2\,1)_\gamma$ HP, increasing the angle between the HP and terrace plane reduces the deviation angle ϕ_2 and increases the angle between $\boldsymbol{\xi}_1$ and $\boldsymbol{\xi}_2$. Additionally, this changes the periodicity of the $\boldsymbol{b}_2$ dislocations at the interface, as seen in Figure 3.5. Since dislocation lines along step (1) remain uninterrupted, their total elastic energy cannot be calculated for KS OR. Similarly, the geometry of the interface prevents this calculation for $\boldsymbol{b}_2$.

OR	HP	$\boldsymbol{\xi}_1$	$\boldsymbol{\xi}_2$	$\theta(^\circ)$
KS v1	$(1\,1\,1)_\gamma$	$[0.71, -0.01, -0.70]_\gamma$	$[0.72, -0.02, -0.70]_\gamma$	0.2
	$(5\,7\,5)_\gamma$	$[0.73, -0.03, -0.69]_\gamma$	$[0.69, 0.03, -0.73]_\gamma$	4.9
	$(1\,2\,1)_\gamma$	$[0.71, -0.01, -0.70]_\gamma$	$[0.47, 0.20, -0.87]_\gamma$	20.4

Table 3.8: KS OR line directions $\boldsymbol{\xi}_1$, $\boldsymbol{\xi}_2$, and angle between the two line directions. All x, y and z values of the mean dislocations lines $[x, y, z]_\gamma$ have a maximum error of ± 0.02.

OR	HP	$\boldsymbol{\phi_1}(^\circ)$	$\boldsymbol{\phi_2}(^\circ)$	d_1 (nm)	d_2 (nm)
KS v1	$(1\,1\,1)_\gamma$	0.9	61.2	1.1	ø
	$(5\,7\,5)_\gamma$	2.5	57.6	0.9	ø
	$(1\,2\,1)_\gamma$	0.6	41.7	0.9	ø

Table 3.9: KS OR angle $\phi_{1,2}$ between the mean line directions $\boldsymbol{\xi}_{1,2}$ and Burgers vector $\boldsymbol{b_{1,2}}$ and steps spacing $d_{1,2}$.

3.2.3.2 Interface propagation

The displacement vector analysis is applied to the KS OR simulation results, the displacement maps are displayed in Figure 3.26.

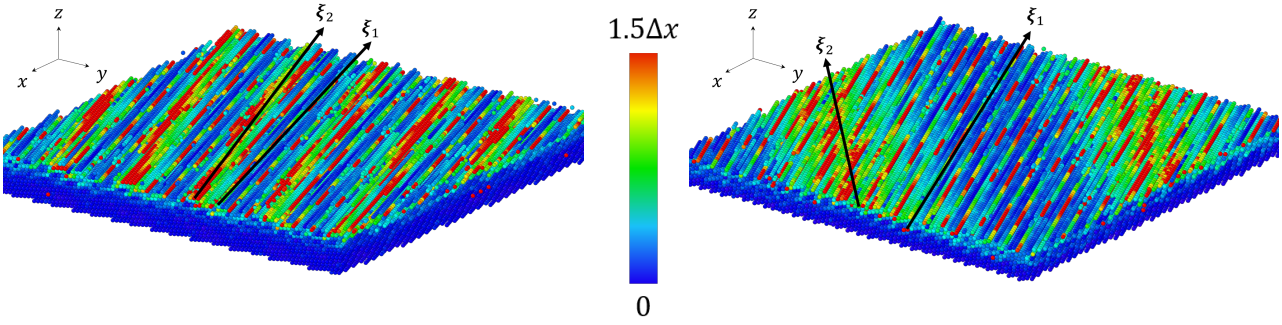

(a) HP = $(5\,7\,5)_\gamma$. (c) HP = $(1\,2\,1)_\gamma$.

Figure 3.26: Atomic displacement map at the FCC-BCC interface, with only BCC atoms remaining and KS OR. Extracted from QA simulation at $t^* = 70$, with atomic displacement vectors calculated between $t^* = 60$ and $t^* = 70$. Color coding based on atomic displacement amplitude.

The regions of highest atomic displacement are located alongside $\boldsymbol{\xi}_2$. The displacement amplitude in these regions is greater than in areas where only the $\boldsymbol{b}_1$ screw dislocations are present, suggesting that the presence of the mixed dislocation $\boldsymbol{b}_2$ plays an important role in the phase transformation for the KS OR.

Moreover, the step structure is particularly visible, with high-displacement regions located at the terrace edges. Moreover, these displacements are not homogeneous, with small portions along step (1) exhibiting notably higher values of displacement. In Figure 3.27, for the $(1\,2\,1)_\gamma$ HP, a zoom into a step (1) terrace ledge indicates that these high displacement zones coincide with the presence of kinks. It can be concluded that $\boldsymbol{b}_1$ dislocation glides in the $(1\,1\,1)_\gamma$ plane via side-wise kink motion.

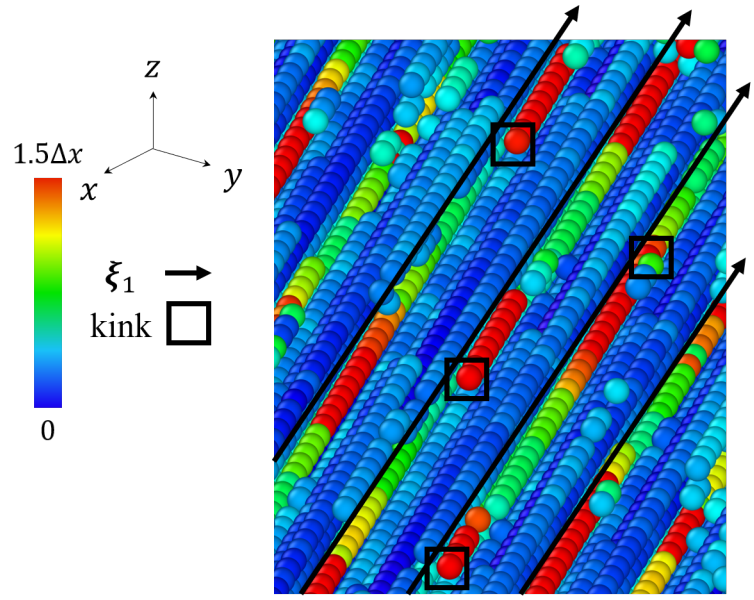

Figure 3.27: Atomic displacement map at the FCC-BCC interface, with only BCC atoms remaining and KS OR and $(5\,7\,5)_\gamma$ HP. Extracted from QA simulation at $t^* = 70$, with atomic displacement vectors calculated between $t^* = 60$ and $t^* = 70$. Color coding based on atomic displacement amplitude. Zoom on the $\boldsymbol{b}_2$ dislocation free region, showcasing the kinks along the line direction $\boldsymbol{\xi}_1$ of dislocations $\boldsymbol{b}_1$.

From the displacement maps, two propagation rates can be distinguished: in $\boldsymbol{b}_2$-rich regions, more BCC phase forms over a given time t^* than in regions where only $\boldsymbol{b}_1$ dislocations are detected. In fact, most of the BCC phase nucleation and propagation occurs in these regions, further indicating their significant role in the FCC to BCC phase transformation for the KS OR.

The nucleation and propagation of the BCC phase are illustrated in Figure 3.28 where the forming BCC phase is marked by red atoms. In this figure, two propagation rates can be distinguished: in $\boldsymbol{b}_2$-rich regions, mode BCC phase forms over a given time t^* than in regions where only $\boldsymbol{b}_1$ dislocations are detected. In fact, most of the BCC phase nucleation and propagation occurs in the regions, further indicating their significant role in the FCC to BCC phase transformation for the KS OR.

To determine the differences in propagation mode between regions where $\boldsymbol{b}_2$ dislocations are detected or not, the nucleation and propagation of the BCC phase in $\boldsymbol{b}_2$-free and $\boldsymbol{b}_2$-rich regions is treated in more details and separately in Figures 3.29a and 3.29b, respectively.

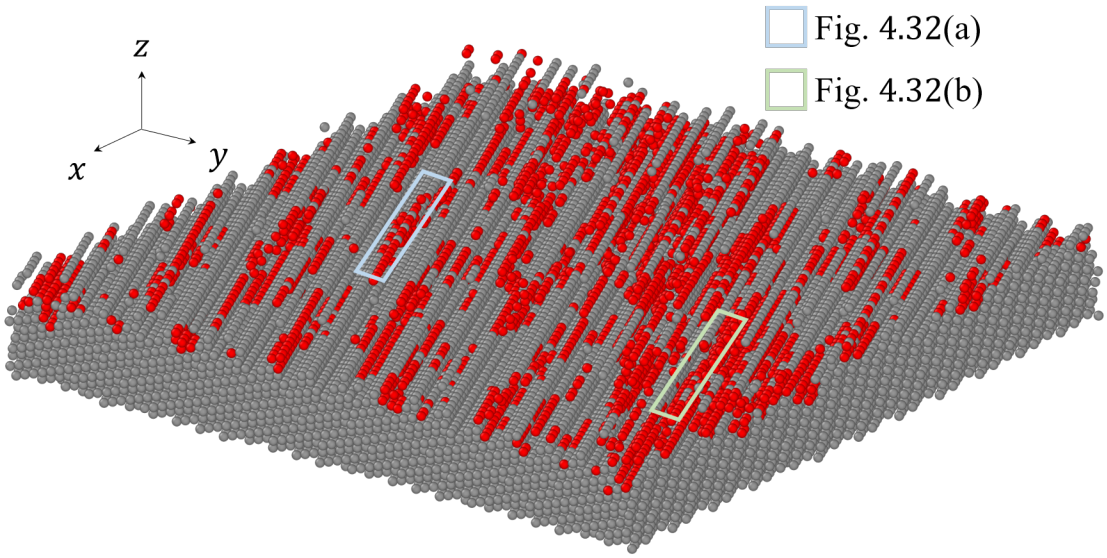

Figure 3.28: BCC phase formation at the FCC-BCC interface, where only the atoms belonging to the BCC structure are shown. Extracted from QA simulation with KS OR and $(1\,2\,1)_\gamma$ HP at $t^* = 72$. Red atoms: BCC phase formation between $t^* = 70$ and $t^* = 72$.

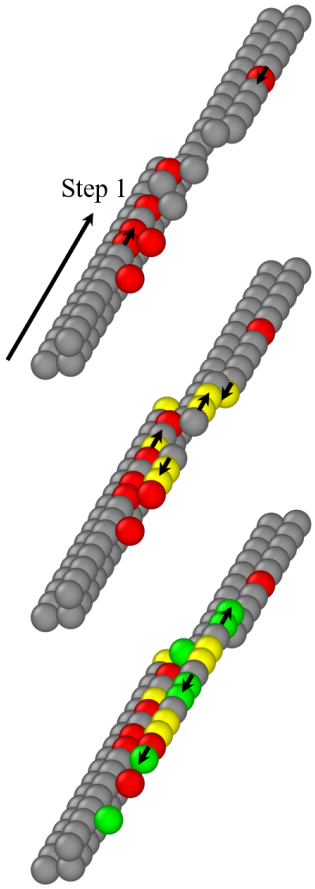

(a) BCC phase propagation and nucleation in $\boldsymbol{b}_2$-free regions.

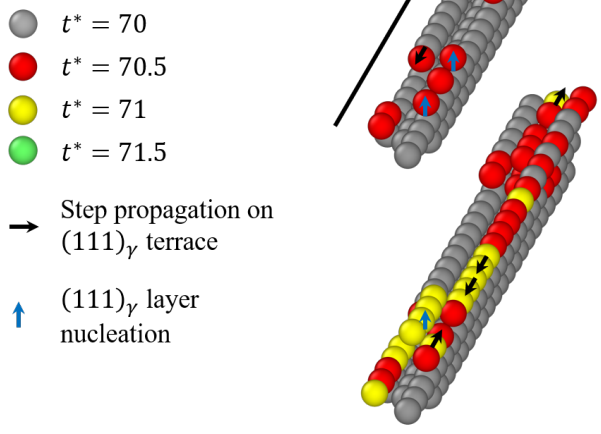

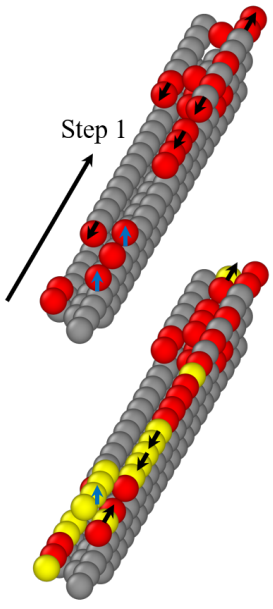

(b) BCC phase propagation and nucleation in $\boldsymbol{b}_2$-rich regions.

In regions where only $\boldsymbol{b}_1$ dislocations were detected, no layer nucleation was observed. However step propagation, showcased by black arrows, is achieved by the glide of $\boldsymbol{b}_1$ dislocations in the $(0\,1\,1)_\alpha||(1\,1\,1)_\gamma$plane, with the assistance of side-wise kink motion. In regions where dislocations $\boldsymbol{b}_2$ are detected, the BCC nucleation and propagation are more complex. Due to the presence of both $\boldsymbol{b}_1$ and $\boldsymbol{b}_2$ dislocations in these areas, several phenomena occur simultaneously. First, as observed in $\boldsymbol{b}_2$-free regions, step propagation is achieved by the glide of $\boldsymbol{b}_1$ dislocations in the $(0\,1\,1)_\alpha||(1\,1\,1)_\gamma$ plane. Second, layer nucleation is observed in $\boldsymbol{b}_2$-rich regions while it was absent in the regions were only $\boldsymbol{b}_1$ dislocations are detected.

From the propagation and nucleation mechanisms of the BCC phase, it can be postulated that both $\boldsymbol{b}_1$ and $\boldsymbol{b}_2$ dislocations glide in the $(0\,1\,1)_\alpha||(1\,1\,1)_\gamma$ plane, which gives the $(1\,1\,1)_\gamma[1\,0\,\bar{1}]_\gamma$ slip system for $\boldsymbol{b}_1$ dislocations and the $(1\,1\,1)_\gamma[0\,1\,\bar{1}]_\gamma$ slip system for $\boldsymbol{b}_2$ dislocations. With these slip systems, and the presence of both $\boldsymbol{b}_1$ and $\boldsymbol{b}_2$ dislocations in the $\boldsymbol{b}_2$-rich region shown in Figure 3.29b, it can be concluded that the BCC phase propagation and nucleation is achieved by the glide of $\boldsymbol{b}_1$ and $\boldsymbol{b}_2$ dislocations.

In summary, for KS OR, the formation of the BCC phase is non-homogeneous across the interface. Its nucleation and propagation occurs primarily in regions where mixed dislocations $\boldsymbol{b}_2$ are located. In region of the interface where there is no $\boldsymbol{b}_2$ dislocation, only the BCC phase propagation in the already nucleated $(0\,1\,1)_\alpha$ terrace happens, due to the glide of $\boldsymbol{b}_1$ dislocations in this plane and the side-wise kink motion. The BCC phase nucleation is achieved only in regions where both $\boldsymbol{b}_1$ and $\boldsymbol{b}_2$ are present, due to the cross-slip mechanism happening at dislocations intersections. Furthermore, $\boldsymbol{b}_2$ dislocations also contribute to the step propagation in the $(0\,1\,1)_\alpha$ terrace. It can be concluded that the high density of displacements in regions where $\boldsymbol{b}_2$ dislocations are detected is due to the glide of both $\boldsymbol{b}_1$ and $\boldsymbol{b}_2$ dislocations in $(0\,1\,1)_\alpha||(1\,1\,1)_\gamma$.

3.2.4 Discussion

The FCC to BCC phase transformation interface structure and motion have been analyzed for NW, GT, and KS ORs. For all ORs, a semi-coherent stepped interface structure was detected, characterized by $(0\,1\,1)_\alpha||(1\,1\,1)_\gamma$ terraces. In the cases of the NW and GT ORs, two step structures were observed. The terrace ledges are accompanied by two kind of screw dislocations $\boldsymbol{b}_1 = \frac{a_\gamma}{2}[1\,0\,\bar{1}]^*_\gamma$ and $\boldsymbol{b}_2 = \frac{a\gamma}{2}[0\,1\,\bar{1}]^*_\gamma$. While this direct observation of a double-stepped interface with two dislocations was not previously discussed, interfaces displaying these two arrays of screw dislocations were observed experimentally by Moritani et al. [4] in the case of lath martensite in Fe-20Ni-5.5Mn. Moreover, in their study, while they did not directly show a second step, they have stated that the step direction was identical to the Burgers vectors of the transformation dislocations, which happen to be the same as $\boldsymbol{b}_1$ and $\boldsymbol{b}_2$ detected in the QA simulation of the austenite-ferrite phase transformation. A schematic representation of the two-stepped interface is shown in Figure 3.30, showcasing the terrace planes $(1\,1\,1)_\gamma||(0\,1\,1)_\alpha$, the line directions $\boldsymbol{\xi}_{1,2}$, their angle θ, the habit plane

normal $\boldsymbol{n}_{\mathrm{HP}}$ and the step heights $h_{1,2}$.

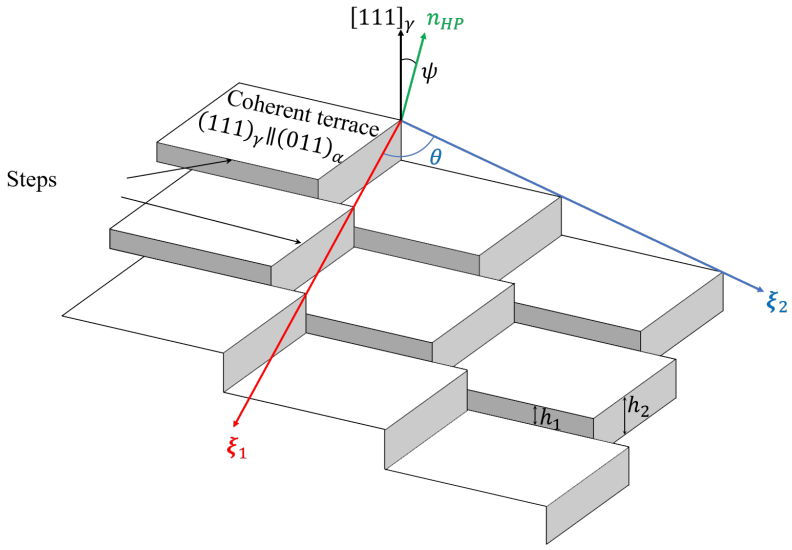

Figure 3.30: Schematic representation of a double stepped interface. Line directions $\boldsymbol{\xi}_1$: blue, $\boldsymbol{\xi}_2$: red, step height $h_{1,2}$: black, habit plane normal n_hp: green.

Moreover, for the NW OR, the volumetric strain analysis shown in Figure 3.4 can be compared to potential energy calculations in molecular dynamics simulations [12, 13]. Both displayed a diamond-shaped pattern with high potential energy/volumetric strain along the QA-detected step directions and their intersections. This diamond shape pattern corresponds to the Moiré pattern in Figure 3.31a. This diamond structure was also discussed in [4], were they schematized the regions of atomic matching, as shown in Figure 3.31b. The regions of atomic mismatch correspond to the formation of dislocations with Burgers vector $\boldsymbol{b}_1$ and $\boldsymbol{b}_2$ along their respective mean line directions $\boldsymbol{\xi}_1$ and $\boldsymbol{\xi}_2$. Moreover, this pattern and the formation of transformation dislocations were observed in recent molecular dynamics simulations by Tripathi et al. [16]. The apparent difference in the diamond angles of the Moiré pattern between the NW OR QA simulation and theoretical predictions is due to the difference in lattice misfit: 1.23 in the QA simulation compared to 1.25 in [4].

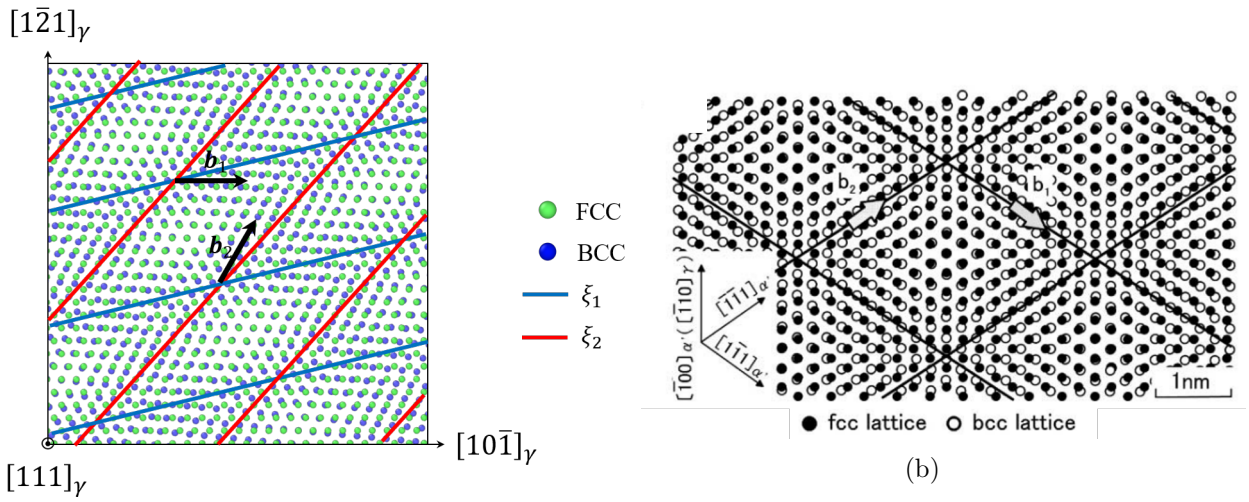

(a) (b)

Figure 3.31: **(a)** NW Moire pattern with QA simulations misfit. **(b)**Atomic matching for NW OR as represented by Moritani et al. [4].

For the KS OR, although both $\boldsymbol{b}_1$ and $\boldsymbol{b}_2$ are still detected at the interface, a step formation occurs only along the $\boldsymbol{b}_1$ dislocations. This type of interface is more commonly found and considered to characterize FCC-BCC interphases [5, 12, 14, 43, 144]. However, the reasons of a second step absence compared to the QA simulations of the NW and GT ORs need to be discussed.

As observed for the NW and GT ORs, $\boldsymbol{b}_1$ and $\boldsymbol{b}_2$ dislocations are aligned with the steps directions. However, as quantified by the misorientation angles ϕ_1 and ϕ_2 between the Burgers vectors $\boldsymbol{b}_1$ and $\boldsymbol{b}_2$ and their respective mean line directions $\boldsymbol{\xi}_1$ and $\boldsymbol{\xi}_2$, in Table 3.10, the orientation of the line direction $\boldsymbol{\xi}_2$ is dependent on the OR. From NW to KS OR, the angle between $[1\,0\,\bar{1}]_\gamma$ and $[1\,1\,\bar{1}]_\alpha$ decreases from 5.26° to 0°, with the GT OR having an intermediary angle of 2.4°. As a consequence, the mean line direction $\boldsymbol{\xi}_2$ becomes increasingly deviated from its Burgers vector $\boldsymbol{b}_2$. Thus, as this angle decreases, $\boldsymbol{\xi}_2$ becomes more kinked. As previously discussed, in the case of KS OR, this results in only small segments of steps oriented along $\boldsymbol{b}_2$, with a local line direction $\boldsymbol{\xi}_2^{loc}$ close to $\boldsymbol{b}_1$. These small segments can therefore be identified as kinks for step (1) along $\boldsymbol{b}_1$, while step (2) becomes invisible.

O-lattice calculations [4, 54], illustrated for QA simulations in Figure 3.32, displayed the theoretical mean line directions $\boldsymbol{\xi}_1$ (blue) and $\boldsymbol{\xi}_2$ (red), for NW, GT, and KS ORs, alongside their respective Burgers vectors.

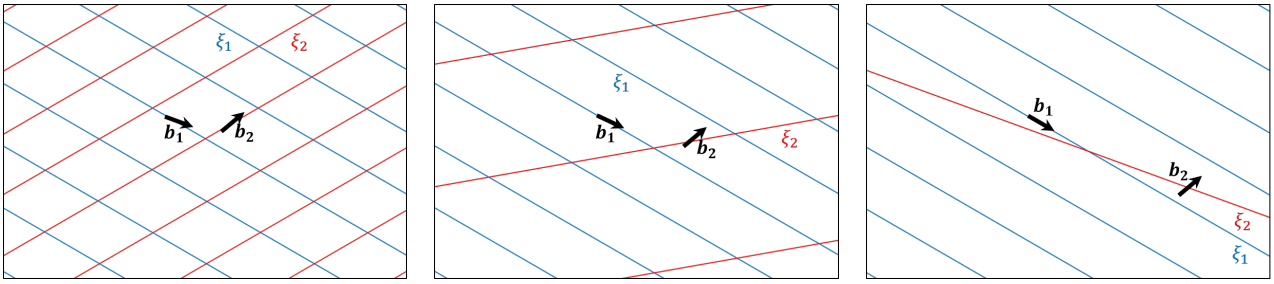

(a) NW OR (b) GT OR (c) KS OR

Figure 3.32: Schematic mean line directions $\boldsymbol{\xi}_1$, in blue and $\boldsymbol{\xi}_2$, in red, with Burgers vectors $\boldsymbol{b}_1 = \frac{a_\gamma}{2}[1\,0\,\bar{1}]^*_\gamma$ and $\boldsymbol{b}_2 = \frac{a_\gamma}{2}[0\,1,\bar{1}]^*_\gamma$ for **(a)** NW OR, **(b)** GT OR and **(c)** KS OR.

Moreover, as shown in Figure 3.32, the spacing between line directions $\boldsymbol{\xi}_2$ increases as the OR shifts from NW to KS. This explains the wider step (2) spacing for GT OR compared to NW OR. Moreover, regarding $\boldsymbol{\xi}_1$, the decreasing disorientation angle ϕ_1 from NW to KS OR, as indicated in Table 3.10, can be attributed to a decreasing number of intersections with the $\boldsymbol{b}_2$ dislocations for a given line direction.

OR	ϕ_1	ϕ_2
NW	8.8 to 13.7	8.2 to 24.6
GT	2.0 to 4.6	17.3 to 33.0
KS	0.7 to 2.5	41.7 to 61.2

Table 3.10: ϕ_1 and ϕ_2 misorientation angle of $\boldsymbol{\xi}_1$ and $\boldsymbol{\xi}_2$ line directions from their respective Burgers vector for each OR.

It was observed for all ORs that the HP also plays an important role in the interface structure. Increasing the angle between the HP and the terrace planes produces larger step heights, while the spacing between terraces becomes smaller. This was particularly noted for NW and GT ORs, where the step (1) length was more affected by the change in HP than step (2). Moreover, the HP has an opposite impact on the deviation of the line direction $\boldsymbol{\xi}_2$ compared to the OR. As the HP angle increases, the angle θ between $\boldsymbol{xi}_1$ and $\boldsymbol{\xi}_2$ also increases, altering the direction of $\boldsymbol{\xi}_2$. This trend was observed for all ORs, and is particularly visible for KS OR in Figure 3.24, where $\boldsymbol{\xi}_1$ and $\boldsymbol{\xi}_2$ have similar directions for smaller HP angles, while $\boldsymbol{\xi}_2$ becomes more deviated from $\boldsymbol{\xi}_1$ for the $(1\,2\,1)_\gamma$ HP.

As shown by the interface motion characterization for different OR, dislocations $\boldsymbol{b}_1$ and $\boldsymbol{b}_2$ glide in the $(0\,1\,1)_\alpha||(1\,1\,1)_\gamma$ plane. The propagation of the BCC phase at the interface is achieved through the glide of both dislocations. This glide, particularly observed for the $\boldsymbol{b}_1$ dislocation in the KS OR, occurs via side wise kink motion. These kinks form alongside the dislocation and are independent of the cross-slip mechanism and/or an interaction with the other dislocations.

The nucleation of new $(0\,1\,1)_\alpha$ terraces takes place at the intersections of $\boldsymbol{b}_1$ and $\boldsymbol{b}_2$, where both dislocations can glide in the $(0\,1\,1)_\alpha||(1\,1\,1)_\gamma$ upper plane due to a cross-slip mechanism. Therefore, it can be concluded that both $\boldsymbol{b}_1$ and $\boldsymbol{b}_2$ dislocations are necessary for the interface to propagate and for the FCC to BCC phase transformation to proceed. The absence of either of these dislocations could impede interface propagation, as the CS mechanism would not be activated. In the literature [4, 5, 14], it was observed that for particular misfits and HPs, $\boldsymbol{b}_2$ could be absent in KS OR, which could hypothetically result in an immobile interface. This conclusion is in contradiction with Maresca et al. [14], that stated that this dislocation was just accommodating the misfit for NW OR without contributing to the interface propagation.

Additionally, the interfacial energies were calculated for each OR and HP. First, the total free energy of the initial FCC and BCC phases was determined. Then, at a specific time step during the FCC to BCC transformation, where approximately half of the system consists of FCC and the other half of BCC, the total free energy of the system was extracted. By using proportionality, the free energies of the FCC and BCC phases were subtracted to determine the free energy of the two interfaces in the system. This energy, for a single interface, is presented in reduced units of $u.\text{nm}^{-2}$ in Table 3.11.

OR	HP	Interfacial free energy ($u.\text{nm}^{-2}$)
NW	$(1\,1\,1)_\gamma$	129
	$(5\,7\,5)_\gamma$	98
	$(2\,3\,2)_\gamma$	83
	$(1\,2\,1)_\gamma$	101
GT	$(1\,1\,1)_\gamma$	136
	$(5\,7\,5)_\gamma$	121
	$(1\,2\,1)_\gamma$	121
KS	$(1\,1\,1)_\gamma$	149
	$(5\,7\,5)_\gamma$	124
	$(1\,2\,1)_\gamma$	111

Table 3.11: Interfacial free energy values for the each OR and HP.

Two conclusions can be drawn from the interfacial free energy results. First, the HP with the lowest interfacial free energy is $(2\,3\,2)_\gamma$ for the NW OR and $(1\,2\,1)_\gamma$ for the KS OR, which correspond to the HP calculated using the PTMC of Maresca et al. [14]. Thus, the most stable interface computed by the QA aligns with the PTMC model. Based on these results, the most stable interface for the GT OR is likely obtained for an HP between $(2\,3\,2)_\gamma$ and $(1\,2\,1)_\gamma$. Furthermore, for a given HP, NW OR interfaces are more stable than those for GT and KS OR.

3.3 Conclusion

In this chapter, the QA method was employed to simulate the FCC to BCC phase transformation in pure iron across three ORs: KS, GT, and NW. The integration of advanced analysis tools, such as Slip Vector Analysis (SVA) and displacement vectors, enabled an understanding of the interface structure and its motion.

It was shown that the FCC-BCC interface is semi-coherent, with a periodic distribution of flat $(1\,1\,1)_\gamma||(0\,1\,1)_\alpha$ terraces , separated by arrays of transformation dislocations. For each OR and HP combination, the primary array of defects consists of screw dislocations with a Burgers vector $\boldsymbol{b}_1 = \frac{a_\gamma}{2}[1\,0\,\bar{1}]^*_\gamma$. The second array, composed of dislocations with a Burgers vector $\boldsymbol{b}_2 = \frac{a_\gamma}{2}[0\,1\,\bar{1}]^*_\gamma$, transitions from screw in the NW OR to a progressively kinked and mixed type for KS OR, with local line directions aligning to $\boldsymbol{b}_1$ dislocation line direction.

For NW and GT ORs, each transformation dislocation aligns along a step direction, forming a double-stepped interface. While these two dislocations and their step-following behavior have been proposed in the literature, this is the first time that a clear double stepped interface is observed in simulations. Moreover, it was demonstrated that the mean line direction of dislocations depends on both the HP and the OR, with the latter having a major influence on the interface shape. Specifically, the spacing between the mean line directions $\boldsymbol{\xi}_2$ of $\boldsymbol{b}_2$ dislocations increases as the OR shifts from NW to KS. Concurrently, $\boldsymbol{\xi}_2$ becomes increasingly misaligned with $\boldsymbol{b}_2$ and tends to align with $\boldsymbol{b}_1$ in the case of KS OR.

Although the overall shape of the interface changes between ORs, a unique transformation mode was identified. The transformation follows a step-flow mode of transformation driven by dislocation glide. The interface propagates along the $\boldsymbol{b}_1$ and $\boldsymbol{b}_2$ directions, with nucleation occurring at their intersections. The presence of $\boldsymbol{b}_1$ and $\boldsymbol{b}_2$ dislocations across all simulated ORs and HPs, coupled with consistent BCC phase nucleation and propagation modes, suggests a shared atomic transformation path for NW, GT, and KS ORs.

Chapter 4

FCC to BCC transformation path

The phase transformation from the FCC to BCC structures is characterized by a significant rearrangement atomic positions, which can profoundly affect the mechanical properties, phase stability and overall performance of materials.

This chapter explores the fundamental aspects of the FCC to BCC phase transformation with different ORs, based on results obtained from QA simulations. In particular, the atomic displacement during the FCC to BCC transformation will be analyzed. Using this data, the mechanism of displacive phase transformation will be discussed.

4.1 Displacement vectors maps

In the previous section, for all ORs, the presence of transformation dislocations $\boldsymbol{b}_1$ and $\boldsymbol{b}_2$ with slip systems $(1\,1\,1)_\gamma[1\,0\,\bar{1}]_\gamma$ and $(1\,1\,1)_\gamma[0\,1\,\bar{1}]_\gamma$ at the interface was attested. The glide of these dislocations is coherent with the KS mechanism [39] involving a shear in the $[1\,0\,\bar{1}]_\gamma$ direction. In the Chapter 1, three major theoretical mechanisms for the FCC to BCC phase transformation were considered: the KS[39], the KSN [46], and the BB/OC [40, 41] mechanisms. Both involve the presence of a shear in the $[1, 1, \bar{2}]_\gamma$ direction, which has not yet been detected.

In order to detect the possible shear in the $[1\,1\,\bar{2}]_\gamma$ direction, displacement maps for NW, GT, and KS ORs, all with a $(1\,1\,1)_\gamma$ HP, are depicted in Figure 4.1. Displacements along the $[1\,0\,\bar{1}]^*_\gamma$ direction are shown in blue, and displacements along the $[0\,1\,\bar{1}]^*_\gamma$ direction are shown in red. Intermediary displacements, between these directions, are shown in green. Displacements in green can corresponds to two different directions: $[1\,\bar{1}\,0]_\gamma \sim [1\,0\,0]_\alpha$ direction, and $[1\,1\,\bar{2}]_\gamma \sim [0\,1\,\bar{1}]_\alpha$ direction. These directions are denoted as $[1\,\bar{1}\,0]^*_\gamma$ and $[1\,1\,\bar{2}]^*_\gamma$ respectively. Burgers vectors of dislocation detected in the previous chapter along their mean line directions are superimposed on the displacement maps, with $\boldsymbol{b}_1 = \frac{a_\gamma}{2}[1\,0\,\bar{1}]^*_\gamma$ and $\boldsymbol{b}_2 = \frac{a_\gamma}{2}[0\,1\,\bar{1}]^*_\gamma$.

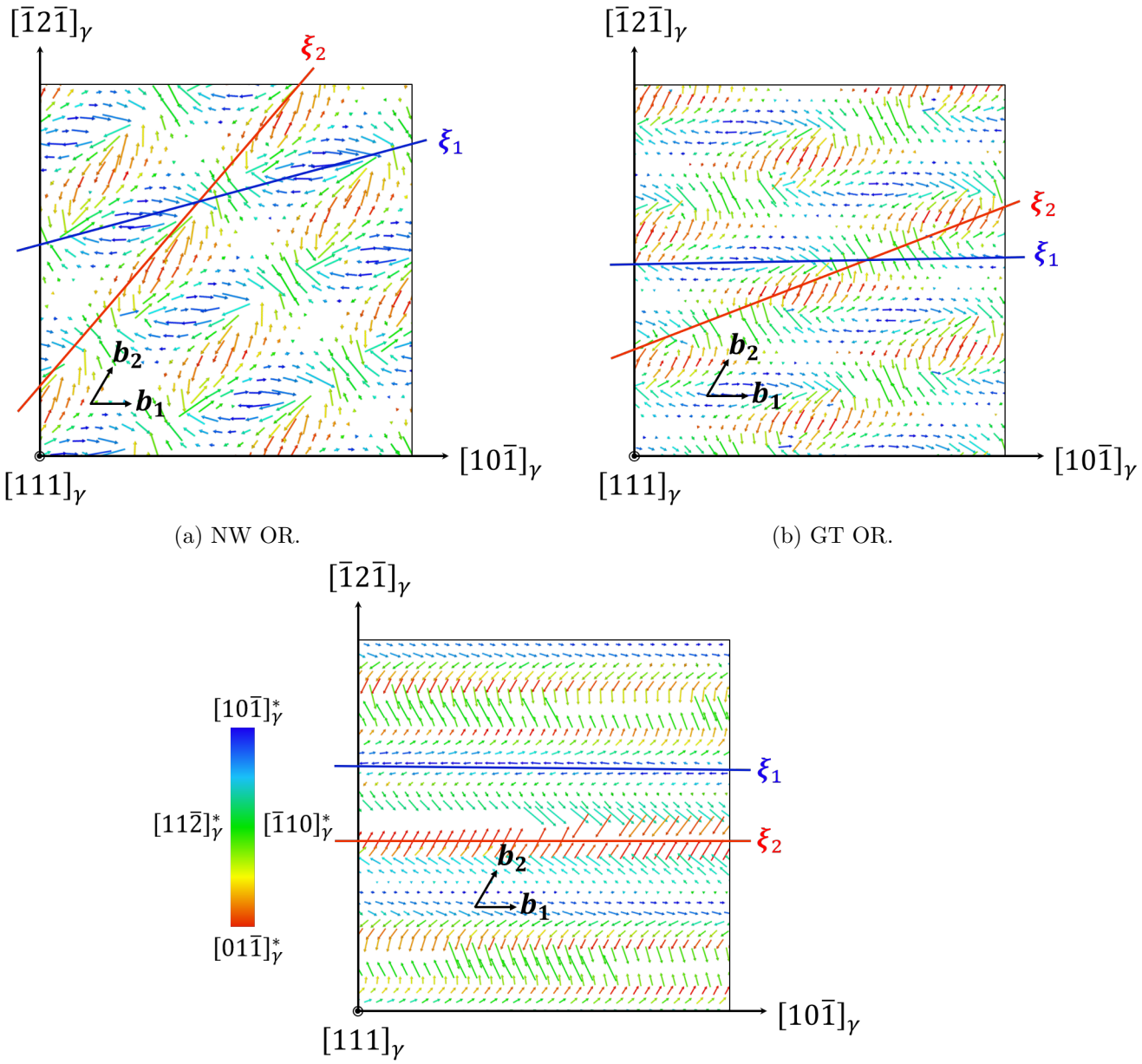

(a) NW OR.

(b) GT OR.

(c) KS OR.

Figure 4.1: Atomic displacement vectors maps at the FCC-BCC interface in the $(1\,1\,1)_\gamma$ plane for ORs with $(1\,1\,1)_\gamma$ HP. Extracted from the QA simulation at $t^* = 70$, with atomic displacement vectors calculated between $t^* = 60$ and $t^* = 70$. Color coding based on atomic displacement direction. Displacement vectors are scaled by a factor of 10 for better visualization. Blue: direction along $[1\,0\,\bar{1}]^*_\gamma$, red: direction along $[0\,\bar{1}\,1]^*_\gamma$. **(a)** NW OR , **(b)** GT OR, **(c)** KS OR.

Displacements along $[1\,0\,\bar{1}]^*_\gamma$ (blue) and $[0\,1\,\bar{1}]^*_\gamma$ (red) correspond to shear displacements associated with the glide of dislocations $\boldsymbol{b}_1$ and $\boldsymbol{b}_2$. However, additional displacements are detected at the intersections of $\boldsymbol{\xi}_1$ and $\boldsymbol{\xi}_2$, occurring along $[\bar{1}\,1\,0]^*_\gamma$ and $[1\,1\,\bar{2}]^*_\gamma$. The observed displacements in the $[1\,\bar{1}\,0]^*_\gamma$ and $[1\,1\,\bar{2}]^*_\gamma$ directions are the sum of the displacements along $[1\,0\,\bar{1}]^*_\gamma$ and $[0\,1\,\bar{1}]^*_\gamma$, both

associated with the glide of dislocations $\boldsymbol{b}_1$ and $\boldsymbol{b}_2$.

Moreover, Moritani et al. [4] suggested that the shear strain in the $\frac{a_\gamma}{2}[1\,1\,\bar{2}]_\gamma$ direction can be accommodated by two perfect dislocations with Burgers vectors $\boldsymbol{b}_1$ and $\boldsymbol{b}_2$. Although only two perfect dislocations were detected by the SVA, an additional perfect dislocation in the FCC, with a Burgers vector direction of $[1\,\bar{1}\,0]^*_\gamma$ and a partial dislocation $\frac{a_\gamma}{6}[1\,1\,\bar{2}]^*_\gamma$, might also be present at the interface for considered ORs. These dislocations results of the local recombination of $\boldsymbol{b}_1$ and $\boldsymbol{b}_2$ Burgers vectors, as indicated by the displacement along $[\bar{1}\,1\,0]^*_\gamma$ and $[1\,1\,\bar{2}]^*_\gamma$ in the displacement maps of all ORs.

4.2 Transformation path determination

Based on the displacement maps and the theoretical models reviewed in Chapter 1, this section will explore the transformation mechanism for the FCC to BCC phase transformation. Observed displacements along the directions $[1\,0\,\bar{1}]^*_\gamma$, $[0\,1\,\bar{1}]^*_\gamma$ and $[1\,1\,\bar{2}]^*_\gamma$ allow to formulate the hypothesis of a KS or KSN mechanism. Indeed, displacement maps in a single structural unit containing all major displacements suggest the presence of KS and KSN transformation mechanism. These displacements maps are shown for each OR in Figure 4.2.

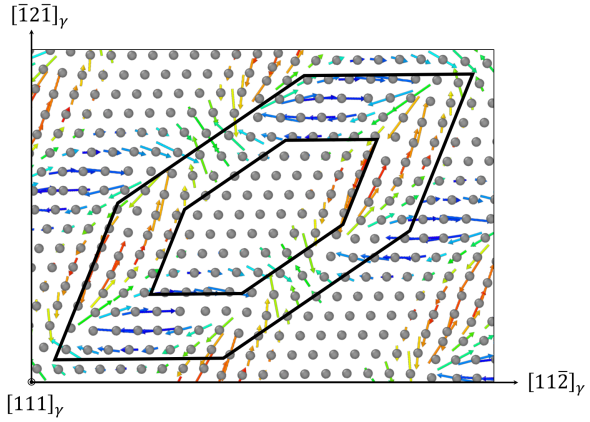

(a) NW OR: QA simulation structural unit

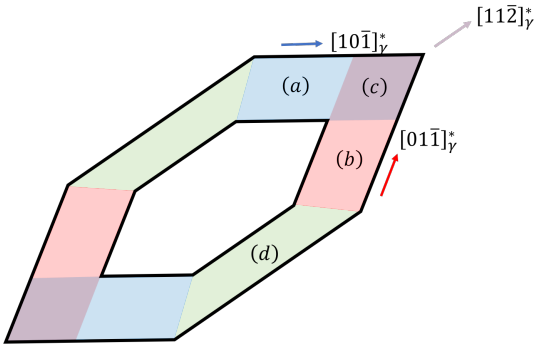

(b) NW OR: Schematic structural unit

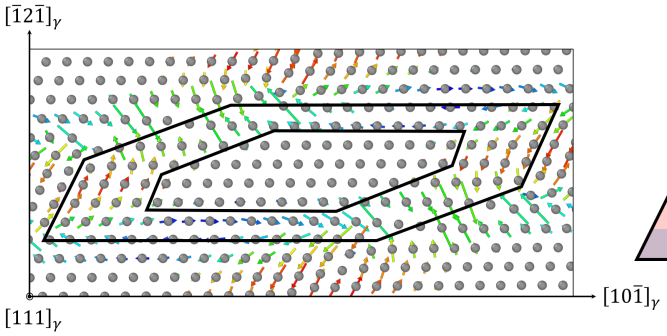

(c) GT OR: QA simulation structural unit

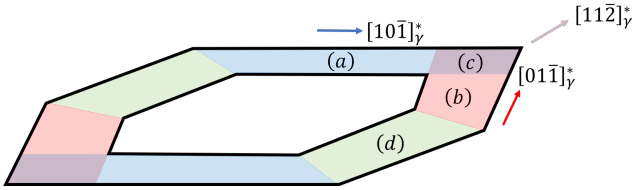

(d) GT OR: Schematic structural unit

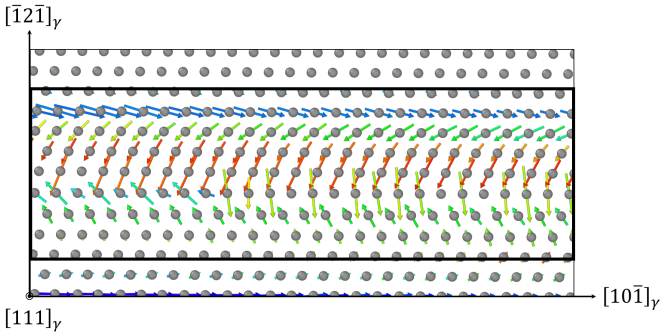

(e) KS OR: QA simulation structural unit

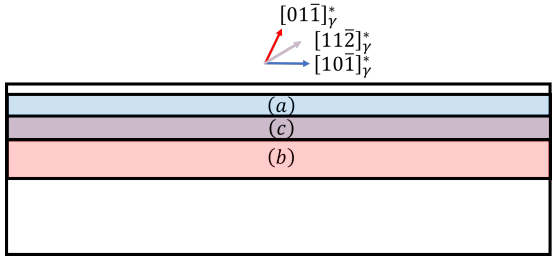

(f) KS OR: Schematic structural unit

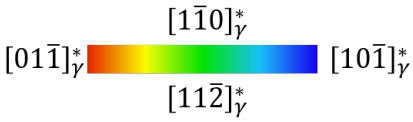

(a) KS v1
(b) KS v6
(c) KSN v2
(d) KSN v2′

Figure 4.2: Displacement maps in structural units in the $(1\,1\,1)_\gamma$ plane at the FCC-BCC interface. Extracted from the QA simulation at $t^* = 70$, for **(a)** NW OR, **(c)** GT OR and **(e)** KS OR. All simulated ORs have $(1\,1\,1)_\gamma$ HP. Displacement vectors are scaled by a factor of 10 for better visualization. Blue: direction along $[1\,0\,\bar{1}]^*_\gamma$, red: direction along $[0\,\bar{1}\,1]^*_\gamma$,green: $[1\,\bar{1}\,0]^*_\gamma$ or $[1\,1\,\bar{2}]^*_\gamma$. Black line delimitate the scheme of structural unit. Schematic representation of structural units, highlighting zones with different types of transformation mechanism indicated in distinct colors: **(b)** NW OR, **(d)** GT OR and **(e)** KS OR.

The FCC to BCC phase transformation can be interpreted as the combined action of two KS mechanism variants. At the edges of the steps, KS v1 and KS v6 variants propagate through the KS mechanism, while at the intersections of KS v1 and KS v6, the KSN mechanism is activated. Both KS and KSN transformation mechanism were previously identified in atomistic simulations of the FCC to BCC phase transformation [16, 64, 84]. Areas where this transformation mechanism takes place are schematically represented for each OR in Figure 4.2, alongside the atomic displacements observed in the QA simulation. In these schemes, the propagation is indicated by fill color: blue for KS v1, red for KS v6, purple for KSN v2, and green for KSN v2'. KS v1 and KS v6 variants are along dislocations $\boldsymbol{b}_1$ and $\boldsymbol{b}_2$, respectively. The observation of the displacement in their respective areas, depicted in Figure 4.2 is coherent with the description of these mechanism given in Chapter 1.

The KS v1 and KS v6 variants each have two possible orientations, corresponding to two opposite orientations for the second shear displacement along $[1\,0\,\bar{1}]^*_\gamma$ and $[0\,1\,\bar{1}]^*_\gamma$ on either side of the dislocation line. KS v1 and KS v6 variants of the KS mechanism overlap in regions (c) and (d) of Figure 4.2. When KS v1 and KS v6 share the same orientation for the first shear, i.e both having $[1, 1, \bar{2}]^*\gamma$ or $[\bar{1}, \bar{1}, 2]^*_\gamma$ as the first shear direction, they produce the KSN v2 mechanism, shown in Figure 4.3c and corresponding to region (c) in Figure 4.2 [46, 69]. This configuration results in a major shear along the $[1\,1\,\bar{2}]^*_\gamma$ direction, with the stretch of the rhombi representing the mean displacements along $[1\,0\,\bar{1}]^*_\gamma$ and $[0\,1\,\bar{1}]^*_\gamma$ between KS v1 and KS v6. However, when KS v1 and KS v6 overlap with opposite first shear directions, there is no net displacement along the $[1\,1\,\bar{2}]^*_\gamma$ direction, and the stretch displacement occurs along the $[\bar{1}\,1\,0]^*_\gamma$ direction. This mechanism is denoted KSN v2' and was previously identified in [64]. It is located in region (d) of Figure 4.2 and depicted in Figure 4.3d.

The KS v1, KS v6, KSN v2 and KSN v2' transformation mechanism observed in the QA simulation are illustrated in Figure 4.3 by following a unit cell throughout its transformation in these regions. These images were extracted from the QA simulation with GT OR and $(1\,1\,1)_\gamma$ HP. The figures of the FCC unit cell were taken at $t^* = 20$, and the figures of the BCC unit cell were taken at $t^* = 100$, in order to show the complete transformation path. Alongside QA observation, the schematic representation of KS v1, KS v6 and KSN v2 mechanism presented in Chapter 1 are depicted. Red vectors correspond to the total atomic displacement, and atoms are color-coded to indicate both the structural lattice (green: FCC, blue: BCC) in the three consecutive $(1\,1\,1)_\gamma$ planes (dark: p_1, neutral: p_0, light: p_{-1} planes).

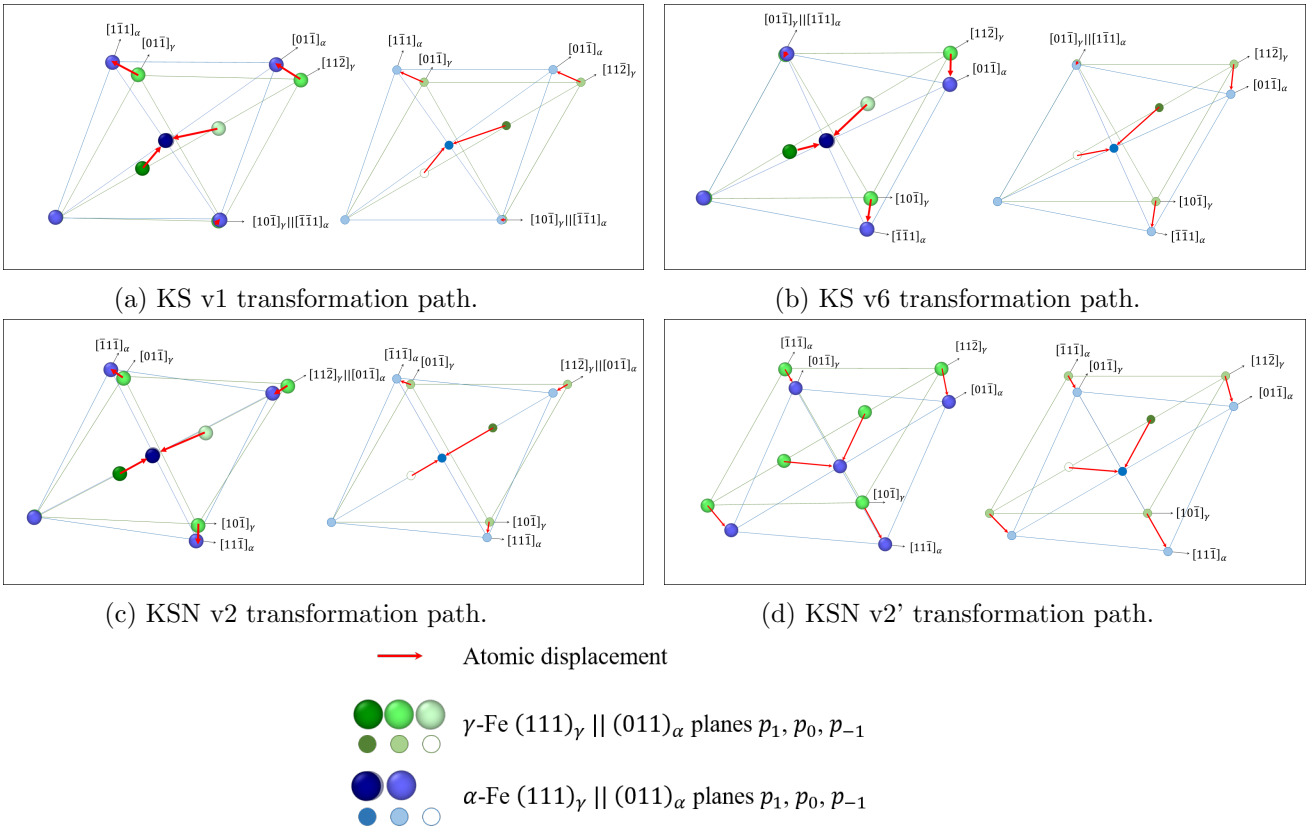

(a) KS v1 transformation path.

(b) KS v6 transformation path.

(c) KSN v2 transformation path.

(d) KSN v2' transformation path.

Figure 4.3: Local transformation mechanism from FCC to BCC lattice. QA simulations alongside their schematic representation discussed in Chapter 1. QA FCC lattice were extracted at $t^* = 20$ while BCC lattice were extracted at $t^* = 100$. Color indicate both the structural lattice (green: FCC, blue: BCC) and the position of atoms in three consecutive $(1\,1\,1)_\gamma$ planes (dark: p_1, neutral: p_0, light: p_{-1} planes). Red arrows represent the total atomic displacement for each atom.

Atomic displacement associated with the KS v1, KS v6, and KSN v2 transformation mechanism in the QA simulation are shown in Figure 4.2 for each OR. The precise role of these transformation paths in the propagation and nucleation of the BCC phase can be clarified using results from the interface motion analysis. Indeed, it was demonstrated in the Chapter 3, that the interface propagation and nucleation follow a step-growth mechanism. This mechanism was characterize by in $(1\,1\,1)_\gamma||(0\,1\,1)_\alpha$ plane propagation of the BCC phase due to dislocation glide and its nucleation on the upper $(1\,1\,1)_\gamma||(0\,1\,1)_\alpha$ planes at dislocations intersections. Moreover, BCC phase nucleation was found to result from the cross-slip of $\boldsymbol{b}_1$ and $\boldsymbol{b}_2$ dislocations. These findings can therefore be applied to regions at the interface where the KS v1 transformation mechanism is present. While the KS v1 transformation mechanism alone does not initiate BCC phase nucleation, it facilitates propagation along a terrace. The same conclusion applies to the KS v6 transformation mechanism. The KSN v2 transformation mechanism is located at the intersections of $\boldsymbol{b}_1$ and $\boldsymbol{b}_2$ dislocations, where BCC phase nucleation was observed in the upper $(1\,1\,1)_\gamma||(0\,1\,1)_\alpha$ planes. This suggests that the KSN mechanism may be responsible for the nucleation of the BCC phase.

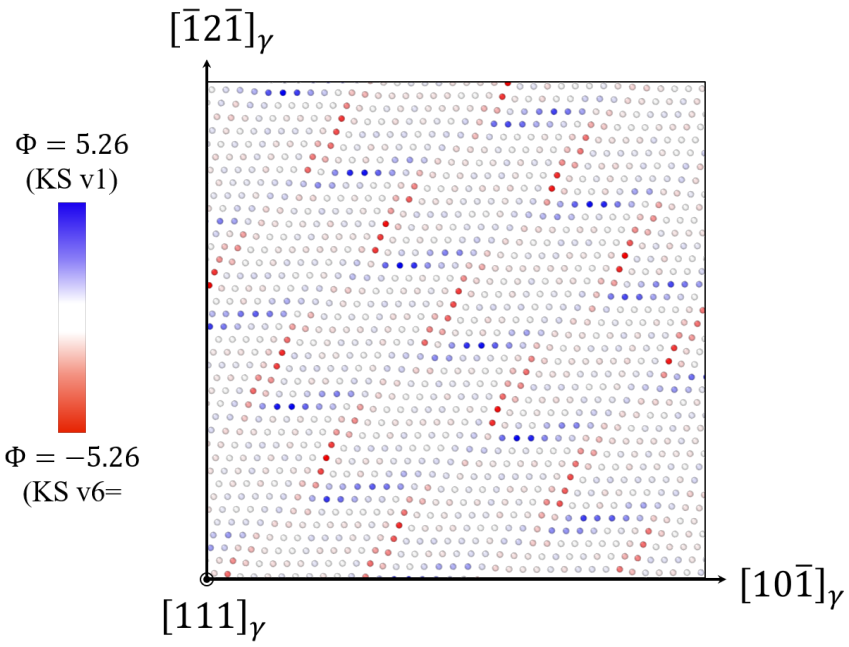

Figure 4.4: NW OR with $(1\,1\,1)_\gamma$ HP local misorientation angle Φ in the $(1\,1\,1)_\gamma$ plane between the lattice direction initially aligned with the $[1\,1\,\bar{2}]_\gamma$ direction ($\phi = 0°$) before the FCC to BCC transformation and the $[0\,1\,\bar{1}]_\alpha$ direction. Extracted from QA simulations at $t^* = 70$.

As introduced by Nishiyama [46], the KSN v2 transformation mechanism should result in the NW v2 OR and in the same manner, KS v1 and KS v6 transformation mechanism should yield KS v1 and KS v6 ORs. The parallel action of KS v1, KS v6, KSN and KSN v2' transformation mechanism, observed in all ORs, results in a BCC structure with transiently heterogeneous OR. It is best observed for NW OR in Figure 4.4, where the local misorientation angle Φ between the lattice direction initially aligned with the $[1\,1\,\bar{2}]_\gamma$ direction ($\Phi = 0°$) before the FCC to BCC transformation, and the transient $[0\,1\,\bar{1}]_\gamma$ direction after the transformation, is displayed at $t^* = 70$. In this figure, blue areas along $\boldsymbol{b}_1$ dislocations correspond to $\Phi = 5.26°$, which indicates the BCC structure with KS v1 variant, while the blue areas along $\boldsymbol{b}_2$ dislocations correspond to $\Phi = -5.26°$ which indicates the BCC structure with KS v6 variant. Also, white areas correspond to $\Phi = 0°$, with indicates the BCC structure with NW v2 OR.

This results in a BCC structure with a transiently heterogeneous OR. The locally misoriented BCC structure then undergoes a slow, symmetric relaxation process until a homogeneous OR is achieved. For the NW OR, the KS v1 and KS v6 transformation mechanisms are present in equal proportions, collectively producing an overall OR equivalent to that of the KSN v2 transformation alone. Consequently, after the relaxation process, the NW v2 OR is microscopically retrieved. In contrast, for the GT OR the KS v1 transformation path slightly outweighs the KS v6 path, resulting in an OR intermediate between NW v2 and KS v1. Thus, similar to NW v2 OR, the GT v1 OR is macroscopically retrieved following the relaxation process.

However, the interpretation for the KS v1 OR is more complex. Since the macroscopic orientation is already KS v1, only the KS v1 transformation mechanism is expected to be present at the interface. As indicated by the Moiré pattern in Figure 3.7a of Chapter 3, local displacements corresponding to the glide of $\boldsymbol{b}_1$ and $\boldsymbol{b}_2$ dislocations are required, and these displacements necessitate both local KS v1 and KS v6 transformations. In Figure 4.5, displacement vectors corresponding to $[0\,1\,\bar{1}]_\gamma$ and $[0\,\bar{1}\,1]_\gamma$ are marked by black rectangles and labeled as $-\boldsymbol{b}_2$ and $+\boldsymbol{b}_2$, respectively. In both regions, the KS v6 transformation mechanism occurs. However, as indicated by the displacement vectors in the intermediary regions between $-\boldsymbol{b}_2$ and $+\boldsymbol{b}_2$, displacements due to these transformation paths cancel each other out.

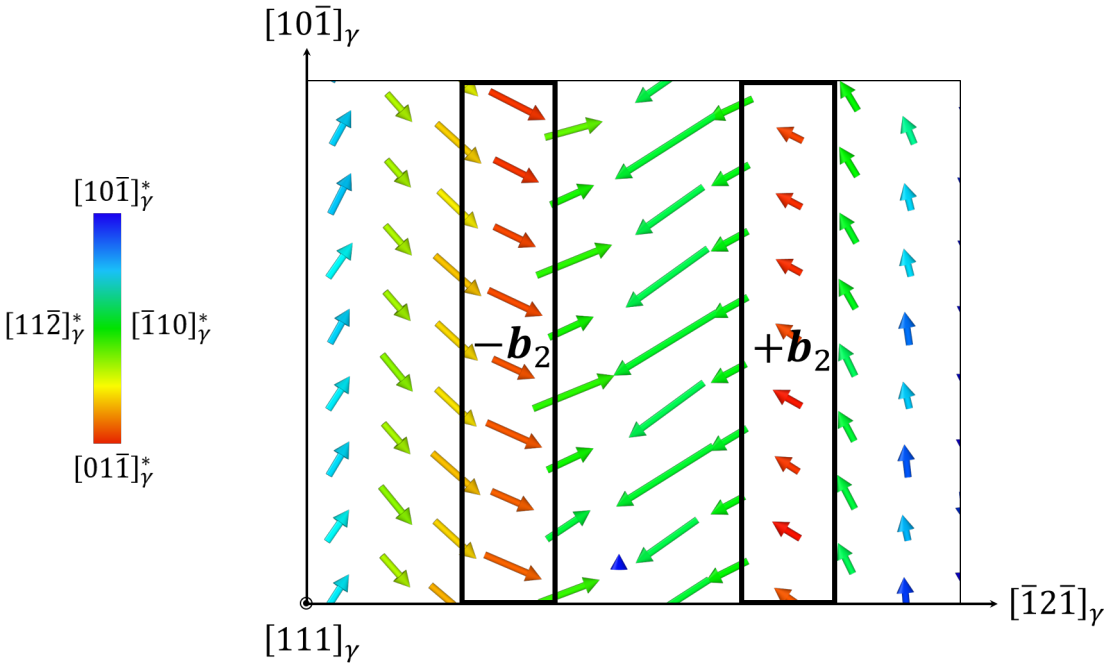

Figure 4.5: Map of atomic displacement vectors at the FCC-BCC interface in the $(1\,1\,1)_\gamma$ plane for KS OR with $(1\,1\,1)_\gamma$ HP. Atomic displacement vectors are calculated between $t^* = 60$ and $t^* = 70$. Extracted from the QA simulation at $t^* = 70$, at the intersection two KS v6 regions. Color coding based on atomic displacement direction. Displacement vectors are scaled by a factor of 10 for better visualization. Blue: direction along $[1\,0\,\bar{1}]_\gamma$, red: direction along $[0\,\bar{1}\,1]_\gamma$.

4.3 Diffraction patterns

According to KS or KSN mechanisms, during the FCC to BCC phase transformation, the ABCABC sequence of $(1\,1\,1)_\gamma$ planes should be transformed to the ABAB sequence of $(1\,1\,1)_\alpha$ planes in the BCC structure. This transformation is operated by the shear of one of the $(1\,1\,1)_\gamma$ plane in $[1\,1\,\bar{2}]_\gamma$ direction. This shear, at intermediate stage, should create the HCP structure. Furthermore, the atomic displacement in the $[1\,1\,\bar{2}]_\gamma$ direction can be interpreted as a partial dislocation glide, with the creation of Shockley partial dislocations associated with the stacking fault and having a

Burgers vector of $\frac{a_\gamma}{6}[1\,1\,\bar{2}]^*_\gamma$.

Furthermore, while the KS/KSN mechanisms have been demonstrated, the absence of a BB/OC transformation path has not been conclusively proven. This transformation path occurs through the intersection of two HCP plates generated by stacking faults due to two distinct Shockley partial dislocations. Diffraction diagrams can potentially reveal the formation of the HCP phase associated with the presence of these partial dislocations. These diffraction patterns were produced directly from the QA simulation without the *fraton2atom*[137] method, therefore accessing more direct information. The diffraction patterns based on the atomic configuration extracted at $t^* = 70$ for NW, GT, KS ORs with $(2\,3\,2)_\gamma$ HP for NW OR and $(1\,2\,1)_\gamma$ for the other two are shown in Figure 4.6. These diffraction pattern were calculated for zone axis $z = [1\,1\,1]_\gamma$. In this figure, diffraction spots corresponding to the FCC, BCC, and HCP phases are indicated, with their spots circled in green, red, and blue, respectively.

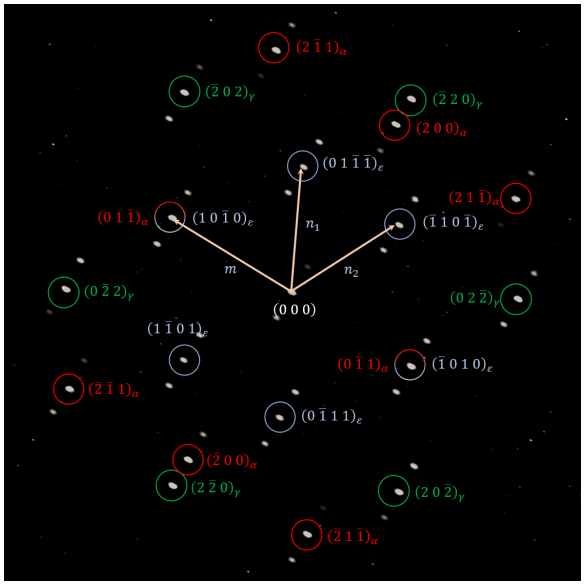

(a) NW OR.

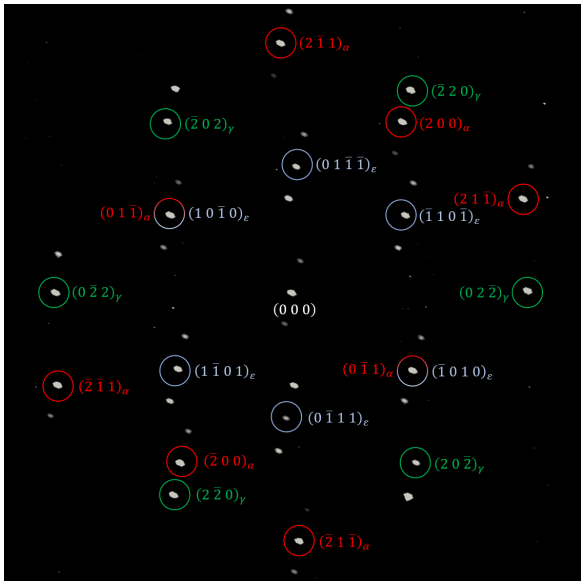

(b) GT OR.

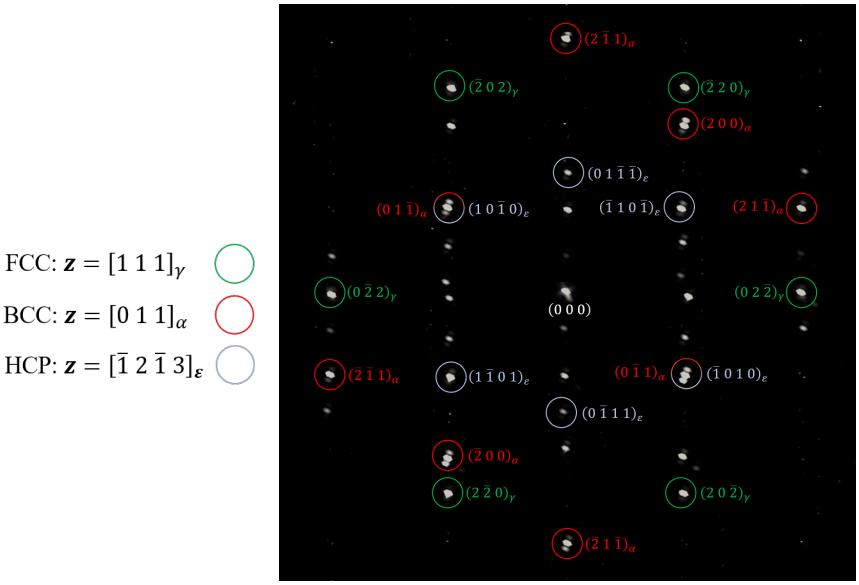

(c) KS OR.

Figure 4.6: FCC-BCC diffraction pattern, with zone axis $z = [1\,1\,1]_\gamma$ extracted from QA simulation at $t^* = 70$. Diffraction spots are indexed, with BCC, FCC and HCP diffraction spots circled in red, green and blue, respectively. **(a)**NW OR with $(2\,3\,2)_\gamma$ HP, **(b)** GT OR with $(1\,2\,1)_\gamma$ HP, **(c)** KS OR with $(1\,2\,1)_\gamma$ HP.

For all ORs, FCC and BCC structures can be identified [145]. In NW OR, the diffraction pattern of the HCP phase expected for the zone axis $z = [\bar{1}\,2\,\bar{1}\,3]_\varepsilon$ is clearly observed. The HCP structures for this zone axis can be defined by the angles and ratios between vectors $\boldsymbol{m}$, $\boldsymbol{n_1}$ and $\boldsymbol{n_2}$ shown in Figure 4.6a [145]. As shown in Table 4.1, theoretical calculations [145] of angles between vectors $\boldsymbol{m}$ and $\boldsymbol{n_1}$, $\boldsymbol{n_1}$ and $\boldsymbol{n_2}$, and the ratio between $\boldsymbol{n}$ and $\boldsymbol{n_1}$ magnitudes, match QA simulation results for NW OR. These vectors are represented for the NW OR in Figure 4.6a.

However, the diffraction pattern of the HCP phase in the case of GT and KS ORs indicate that this phase is deformed. This deformation is greater for KS than for GT OR, indicating that it increases the further from NW OR. The other additional diffraction spots observed for all ORs could be due to the shear taking place at the interface, which can locally shifts all phases.

	$\widehat{\boldsymbol{mn_1}}$	$\widehat{\boldsymbol{n_1n_2}}$	$\frac{n_1}{m}$
Theory [145]	63.97°	52.06°	1.139
QA simulation	63.96°	52.34°	1.12

Table 4.1: HCP phase diffraction spots characteristics in the QA simulation of the FCC-BCC interface for NW OR, compared with theoretical predictions [145]

The HCP structure detected by the diffraction pattern shown in Figure 4.6 can also be interpreted as and indication of the stacking fault structure, generated by a $\frac{a_\gamma}{6}[1\,1\,\bar{2}]^*_\gamma$ dislocation. Moreover, the existence of $[1\,1\,\bar{2}]_\gamma$ partial dislocations at FCC-BCC interfaces is attested in several molecular dynamics simulations [12, 13, 16, 84] and experimental observations [2, 92, 93]. Some Burgers vectors corresponding to these partial dislocations were detected by the SVA. However, as they are small and localized only at dislocation intersections, most of these partials fell below the SVA detection threshold. It can also be concluded that the SVA is less sensitive in detection of partial dislocations compared to perfect dislocations.

As only one HCP phase orientation was detected in the diffraction patterns in Figure 4.6, and only one direction of shear along a $\langle 1\,1\,\bar{2}\rangle_\gamma$ was observed, it can be concluded that only one type of partial dislocation exists at the simulated interfaces, with $\boldsymbol{b} = \frac{a_\gamma}{2}[1\,1\,\bar{2}]_\gamma$. This does not coincide with a BB/OC type of transformation path, where two different partial dislocations are expected. Moreover, additional diffraction patterns conducted along different zone axes did not reveal a second HCP phase and the large displacements in the directions $[1\,0\,\bar{1}]_\gamma$ and $[0\,1\,\bar{1}]_\gamma$ does not align with the transformation path suggested by the BB/OC mechanism. The BB/OC transformation path can thus be excluded in the case of the FCC to BCC phase transformation considered in this work.

Then, it can be concluded that the observed KS and KSN transformations are responsible of the FCC to BCC phase transformation. Moreover, the theoretical shear and stretch displacements produced by the KS and KSN mechanisms perfectly match both the present simulations and MD simulations [12, 16]. While the second shear of the BB/OC mechanism in their work was only speculated and not observed directly in [12, 16]. Finally, HRTEM observations [4, 5] of the interface structure at austenite/martensite interface align with the KS/KSN models and present simulations.

4.4 Conclusion

Based on the QA simulation, it can be concluded that the complete FCC to BCC transformation path for NW, GT, and KS ORs involves the action of the KS mechanism in two variants along $\boldsymbol{b}_1$ and $\boldsymbol{b}_2$ dislocations, with the KSN mechanism emerging as the average of the two KS mechanisms. This transformation was observed for the first time on a stepped interface. Additionally, the periodic repetition of the structural unit transformation path at the FCC-BCC interface corresponds to a collective atomic movement, characteristic of displacive transformations at a larger scale. By comparing with the determined propagation and nucleation mode of the BCC phase from the previous chapter, the role of each transformation path can be clarified. The KS v1 and KS v6 transformation mechanisms occur along the $\boldsymbol{b}_1$ and $\boldsymbol{b}_2$ dislocations, respectively, and it was shown that the interface propagates in the $(0\,1\,1)_\alpha$ plane through the glide of these dislocations. Thus, the KS v1 and KS v6 transformation mechanisms are the main contributors to this propagation. However, BCC phase nucleation was found at dislocation intersections where the KSN transformation mechanism is detected, indicating that the KSN mechanism plays a major role in BCC phase nucleation.

Chapter 5

Carbon interaction with the FCC-BCC interface

This chapter will explore the interactions of carbon with the moving FCC-BCC interface. Consistently with Chapter 3 and 4, the KS and NW ORs between the FCC and BCC structure will be considered. Understanding carbon segregation mechanisms at interfaces during the FCC to BCC phase transformation is essential for optimizing material performance. A prime example can be found in steels, as the Fe-C binary system serves as the basis for all steel grades [7, 146]. Notwithstanding significant achievements from ab initio [95–97, 101–103] and molecular dynamics (MD) simulations [100, 104–106], including the modeling of carbon spatial distribution in a Cottrell atmosphere as a function of carbon concentration in BCC iron [105] and the influence of carbon segregation on the driving force of the FCC to BCC phase transformation [96]. However, the description of carbon segregation at moving FCC-BCC interfaces remains challenging for these methods. On the one hand, ab initio methods are confined to very small space scales (a few nanometers) and 0K calculations. On the other hand, diffusional time scales remain behind reach for MD, which precludes the simulation of carbon diffusion toward the moving FCC-BCC interface on sufficiently long times. The quasi-particles approach (QA) opens a way to overcome this problem, as this approach allows to reproduce the kinetics at diffusion time scale.

This chapter is organized as follows. First, the numerical implementation of the binary Fe-C system in QA simulation for the austenite-to-ferrite phase transformation in pure iron is presented. Then, the carbon interaction with the FCC-BCC interface structure will be examined. Finally, the interface mobility will be discussed.

5.1 Numerical implementation

5.1.1 Numerical parameters

For the Fe-C two-component systems, different spatial and temporal step settings are required compared to those used in Chapter 3 and 4 (for pure iron). In particular, the length scale for Fe-C simulations was set to be twice as fine as that of single-component systems, with $\Delta x = 0.0223$ nm. Accordingly, the lattice parameters were set to $a_\gamma = 16\Delta x = 0.356$ nm for the FCC phase and $a_\alpha = 6.5\Delta x = 0.289$ nm for the BCC phase. Moreover, a smaller time step than that used in the one-component system is necessary to ensure numerical stability for simulations with low carbon concentrations. Therefore a reduced time step of $\Delta t = 5.10^{-5}$ was used in the case of binary system. This change feeds through to the reduced time scale $t^* = N_{it}\Delta t$, where N_{it} is the number of iterations. All parameters used in simulation are listed in Table 5.1.

a_α	a_γ	R_{Fe}	R_C	ΔR	ξ
16.0	13.0	5.65	2.82	0.48	4.0

λ^{lr}_{Fe-Fe}	λ^{sr}_{Fe-Fe}	λ^{lr}_{C-C}	λ^{sr}_{C-C}	λ_{Fe-C}	ϵ	σ^α	$\sigma^\gamma_{1,2}$	k_BT	$\bar{\rho}_{Fe}$
1.0	0.2	32.0	2.0	7.0	0.4	0.03	0.03	0.05	0.17

Table 5.1: Parameters used in two-components QA simulations.

Interaction potentials for binary Fe-C system

For Fe-C system, the potential embodies three different contributions: iron-iron, iron-carbon, and carbon-carbon interactions. The relative amplitudes of these 3 contributions are set by the parameters λ^{lr}_{Fe}, λ^{sr}_{Fe}, λ^{sr}_{C}, λ^{lr}_{C} and λ_{Fe-C}. Regarding the Fe-Fe interaction potential, the same amplitudes λ^{lr}_{Fe} and λ^{sr}_{Fe} as in Chapter 3 and 4 have been used: $\lambda^{sr}_{Fe} = 1.0$ and $\lambda^{lr}_{Fe} = 0.2$. However, the parameter ξ that set the depth of the second well of the FCC phase in the FCC-BCC potential is increased from 0.1 to 0.3. This modification was necessary to ensure the stability of the FCC phase thoughout the simulation with a controlled phase transformation at the interface.

In order to ensure the diffusion of carbon atoms accross the FCC phase to the interface, a small amplitude was chosen for the short range C-C interaction, with $\lambda^{sr}_{C-C} = 2$, while a strong amplitude was chosen for the long range C-C interaction, with $\lambda^{lr}_{C-C} = 32$. In this case, the probability to find a carbon atom at any octahedral sites is a constant equivalent to the carbon concentration. Moreover, the iron-carbon potential amplitude was set at $\lambda_{Fe-C} = 7$. The setting of C-C and Fe-C amplitudes ensures a homogeneous distribution of carbon atoms on the octahedral interstitial sites of the FCC crystal.

5.1.2 Simulation model

In order to accurately describe the carbon interaction with the interface, the box size should be greater than terraces spacings, measured in Chapter 3. Therefore, the simulation box was set to $(256\Delta x)^3$, which is equivalent to $(5.8\,\mathrm{nm})^3$.

In the same manner as in the one-component iron simulations, FCC and BCC phases were rotated so that the habit plane was aligned with the z axis, ensuring the propagation of the FCC-BCC interface perpendicular to this direction.

At the beginning, preliminary simulations of the FCC and BCC structure, already oriented according to the specific HP-OR combinations, were conducted. Additionally, the FCC phase was then relaxed with a carbon concentration of 0.92 wt% (4.32 at%). Then, a slice of pure iron (no carbon atom) with the BCC structure was embedded in the FCC phase, with a thickness of $40\Delta x = 0.9$ nm. This yield a total carbon concentration in the system of 0.74 wt% (3.44 at%). The inital configuration with the NW v2 OR with $(2\,3\,2)_\gamma$ HP is depicted in Figure 5.1a using CNA method from Ovito [136]. In this figure, blue atoms belongs to the BCC phase, green atoms to the FCC phase, while white atoms at the interface indicate a perturbed structure. In Figure 5.1b the distribution of carbon fratons are shown using Paraview visualization [135].

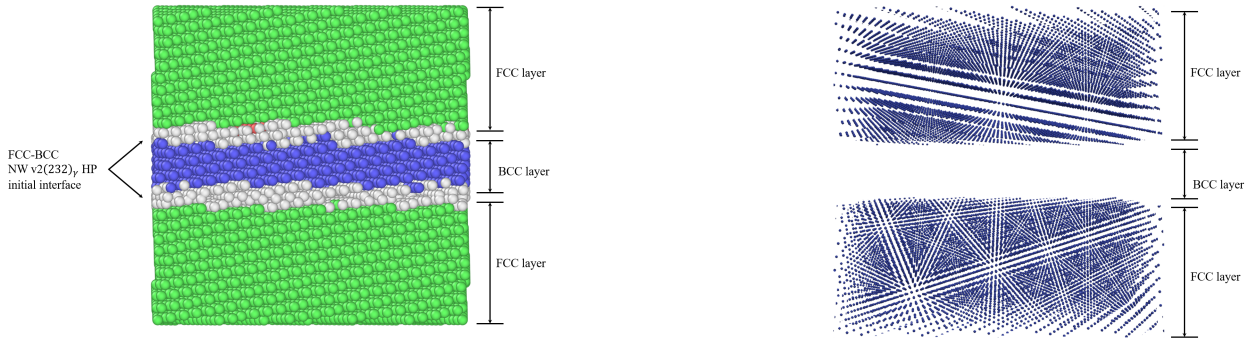

(a) Fe initial configuration

(b) C initial configuration

Figure 5.1: Initial configuration in QA simulation of the FCC to BCC phase transformation for the NW v2 OR with the $(2\,3\,2)_\gamma$ HP. **(a)** Visualization of iron atoms using the CNA method in Ovito [136]: green represents FCC, blue represents BCC, and grey indicates unknown or perturbed structures. **(b)** Visualization of carbon fratons with $\rho_C \geq 0.03$ in Paraview [135] .

The interface relaxation for two-component systems was achieved after 2.10^6 simulation iterations, corresponding to $t^* = 100$. Consequently, all simulation results will be presented for $t^* > 100$.

5.2 Carbon interaction with the interface structure

As it was previously demonstrated in Chapter 3, the QA simulations of the FCC to BCC phase transformation in iron correctly reproduce the interface structure: the interface is semi-coherent, with a periodic distribution of flat terraces $(1\,1\,1)_\gamma||(0\,1\,1)_\alpha$ separated by arrays of transformation dislocations associated with step ledges. In the NW OR configuration, two sets of kinked screw dislocations were identified, with Burgers vectors $\boldsymbol{b}_1 = \frac{a_\gamma}{2}[1\,0\,\bar{1}]^*_\gamma$ and $\boldsymbol{b}_2 = \frac{a_\gamma}{2}[0\,1\,\bar{1}]^*_\gamma$. However, for KS OR, the second set of dislocation was mixed, with its line direction close to Burgers vector $\boldsymbol{b}_1$. Therefore, carbon interactions with the moving interface will be analyzed specifically in terms of interactions with these two sets of dislocations.

In Figure 5.2, the interface shape is shown at $t^* = 300$ for NW OR and at $t^* = 200$ for KS OR. In this figure, terrace ledges along $[1\,0\,\bar{1}]^*_\gamma$ and $[0\,1\,\bar{1}]^*_\gamma$ directions are indicated by blue and red segments, respectively. Unlike the one-component simulations and NW OR, the KS OR top $(1\,1\,1)_\gamma||(0\,1\,1)_\alpha$ and bottom $(\bar{1}\,\bar{1}\,\bar{1})_\gamma||(0\,\bar{1}\,\bar{1})_\alpha$ interfaces exhibit distinct shapes and periodicities. Consequently, the top interface is shown in Figure 5.2b, while the bottom interface is presented in Figure 5.2c. For NW OR, the two terrace steps observed in the one-component simulation are also detected here. Similarly to one-component simulations, the KS OR configuration displays only a single step along the $[1\,0\,\bar{1}]^*_\gamma$ direction.

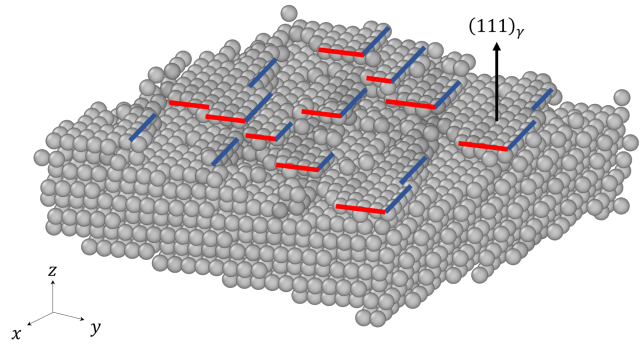

(a) NW v2 with $(2\,3\,2)_\gamma$ HP.

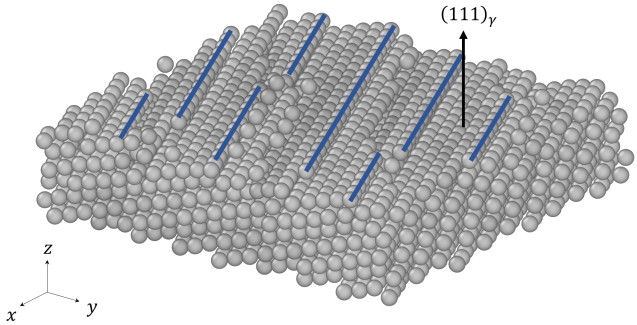

(b) Top interface of KS v1 OR with $(1\,2\,1)_\gamma$ HP.

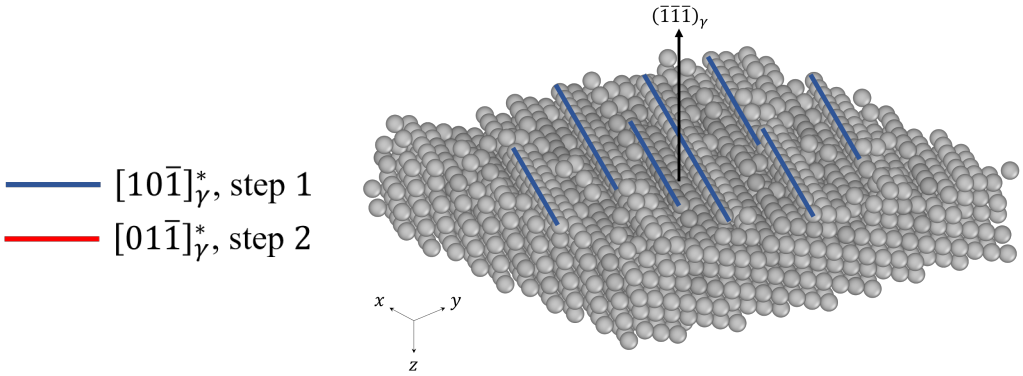

(c) Bottom interface of KS v1 OR with $(1\,2\,1)_\gamma$ HP.

Figure 5.2: FCC-BCC semi-coherent interface relief, extracted from the QA simulation. Surface relief was obtained using 'ambient occlusion' rendering in Ovito [136], displaying BCC atoms and atoms marked as 'other' by the CNA. Blue and red segments the steps along the $[1\,0\,\bar{1}]^*_\gamma$ and $[0\,1\,\bar{1}]^*_\gamma$ directions, respectively. Terraces are parallel to $(1\,1\,1)_\gamma$ as indicated by the black arrow. **(a)** NW v2 OR with $(1\,2\,1)_\gamma$ HP at $t^* = 300$, **(b)** Interface (1) KS v1 OR with $(1\,2\,1)_\gamma$ HP at $t^* = 200$, **(c)** Interface (2) KS v1 OR with $(1\,2\,1)_\gamma$ HP at $t^* = 200$.

The preferential location of C atoms at the interface is prospected in Figure 5.3 for the NW and KS ORs. Therein, a visualization cutoff value ρ_C was used for the carbon probability function. In the present simulations, the cutoff value was set at $\rho_C = 0.06$. It means that the position indicated in figure 5.3, represent the site where the carbon atoms can be find with the probability bigger than ρ_c. Iron atoms are displayed with transparency to emphasize the preferential carbon segregation sites, shown in black.

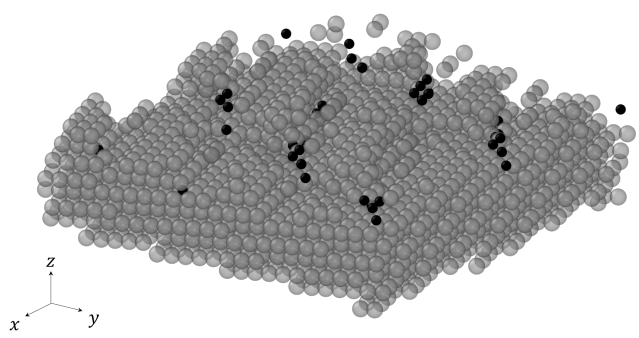

(a) NW v2 with $(2\,3\,2)_\gamma$ HP.

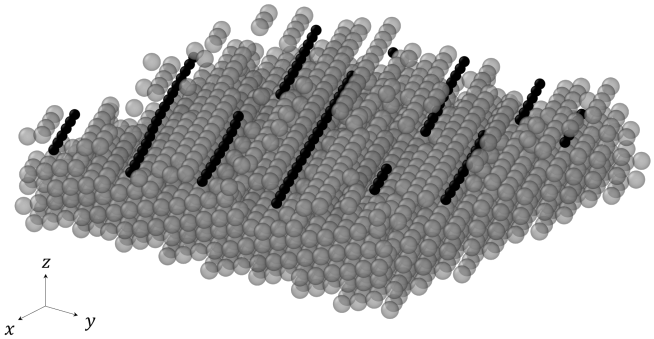

(b) Top interface of KS v1 OR with $(1\,2\,1)_\gamma$ HP.

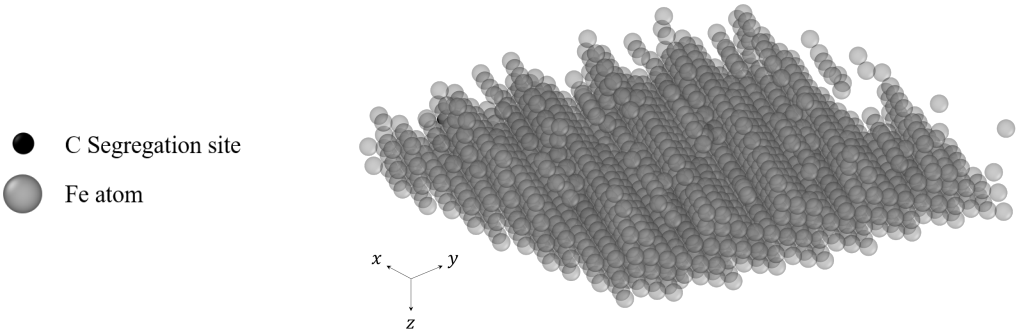

(c) Bottom interface of KS v1 OR with $(1\,2\,1)_\gamma$ HP.

Figure 5.3: FCC-BCC semi-coherent interface relief in transparency, with carbon preferential segregation sites in black. Extracted from the QA simulation, displaying BCC atoms and atoms marked as 'other' by Ovito's CNA [136]. **(a)** NW v2 OR with $(1\,2\,1)_\gamma$ HP at $t^* = 300$, **(b)** Top interface of KS v1 OR with $(1\,2\,1)_\gamma$ HP at $t^* = 200$, **(c)** Bottom interface of KS v1 OR with $(1\,2\,1)_\gamma$ HP at $t^* = 200$.

For both NW OR in Figure 5.3a, and the top interface of KS OR in Figure 5.3c, it appears that carbon atoms have preferential segregation sites at the interface. In the case of the NW OR, the segregation sites seems mostly located at the intersection of the terrace ledges. Whereas for the KS OR top interface, the preferential segregation sites align with the step ledges identified in Figure 5.2. However, distinct differences emerge between the two KS interfaces, at the bottom interface the segregation of carbon was not observed. To accurately determine the carbon segregation sites, the SVA was used to compute the Burgers vector at the interface, following the same methodology as in Chapter 3.

To better understand the link between the dislocations and the sites of carbon segregation, the Burgers vectors distribution in the HP is displayed in Figure 5.4, using the same color coding as in the previous chapters: blue vectors align along $[1\,0\,\bar{1}]^*_\gamma$, red vectors along $[0\,1\,\bar{1}]^*_\gamma$ and green vectors represent intermediary orientations. Additionally, the mean line directions $\boldsymbol{\xi}_{1,2}$ for each dislocation

are indicated for NW OR and the bottom KS OR.

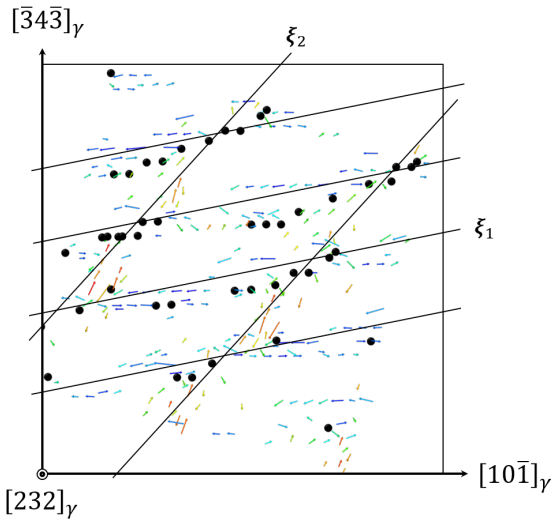

(a) NW v2 with $(2\,3\,2)_\gamma$ HP.

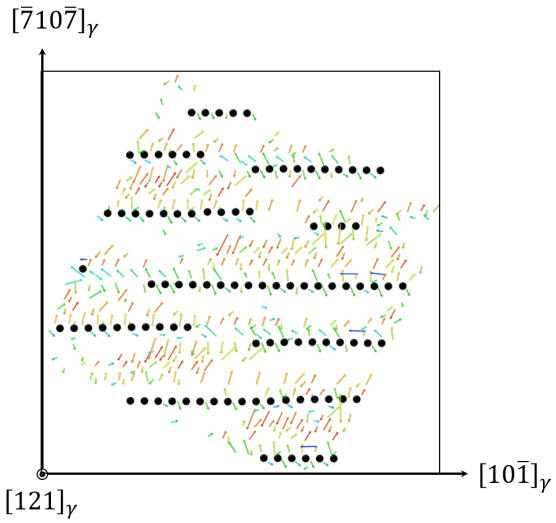

(b) Top interface of KS v1 OR with $(1\,2\,1)_\gamma$ HP.

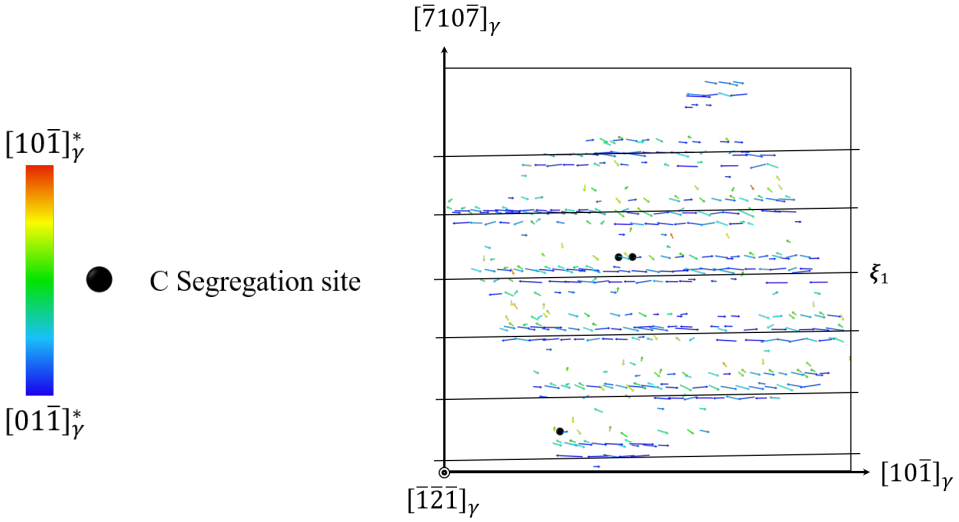

(c) Bottom interface of KS v1 OR with $(1\,2\,1)_\gamma$ HP.

Figure 5.4: Carbon segregation sites (black spheres) overlaid on Burgers vectors from the slip vector analysis at the FCC-BCC interface in the $(1\,1\,1)_\gamma$ plane for NW OR, extracted from the QA simulation. Only slip vectors with an amplitude of $> 0.5\|\boldsymbol{b_{1,2}}\|$ are displayed. Blue: $[1\,0\,\bar{1}]^*_\gamma$ direction, red: $[0\,1\,\bar{1}]^*_\gamma$ direction. **(a)** NW v2 OR with $(1\,2\,1)_\gamma$ HP at $t^* = 300$, **(b)** Top interface of KS v1 OR with $(1\,2\,1)_\gamma$ HP at $t^* = 200$, **(c)** Bottom interface of KS v1 OR with $(1\,2\,1)_\gamma$ HP at $t^* = 200$.

Several observations can be made. For the NW OR interface, preferential segregation sites are along the dislocations $\boldsymbol{b}_1$ and at the intersections of $\boldsymbol{b}_1$ and $\boldsymbol{b}_2$. In the case of the KS OR (Figure 5.4b and 5.4c), carbon segregation exhibited two distinct behaviors depending on the interface. At the top interface, shown in Figure 5.4b, the dislocations are highly perturbed. While most Burgers

vectors align along $[0\,1\,\bar{1}]^*_\gamma$, a clear dislocation line could not be identified. However, segregation sites are aligned with $[1\,0\,\bar{1}]_\gamma$ which was shown to be close to the local dislocation line of $\boldsymbol{b}_2$ dislocations for KS OR with $(1\,2\,1)_\gamma$ HP in Figure 3.25 of Chapter 3. By referring to the SVA results from Chapter 3, it seems that this interface corresponds to the highly perturbed region where both $\boldsymbol{b}_1$ and $\boldsymbol{b}_2$ dislocations were detected. While in contrast, the bottom interface shows only dislocation lines with $\boldsymbol{b}_1$ dislocations, consistent with observations for this OR.

A first piece of interpretation of the preferential location of carbon atoms at the FCC-BCC interface is provided in Figure 5.5a. In this figure, the volumetric strain $\Delta V/V$ is computed, at the NW interface (Figure 5.5a) and the top KS interface (Figure 5.5b). Low volumetric strain in indicated in white and high volumetric strain is indicated in blue (compressive strain) or red (tensile strain). Preferential segregation sites of carbon are indicated by small black spheres. From this figure, and compared to SVA results, it can be observed that segregation sites are located close to the deformed regions due to the presence of dislocations.

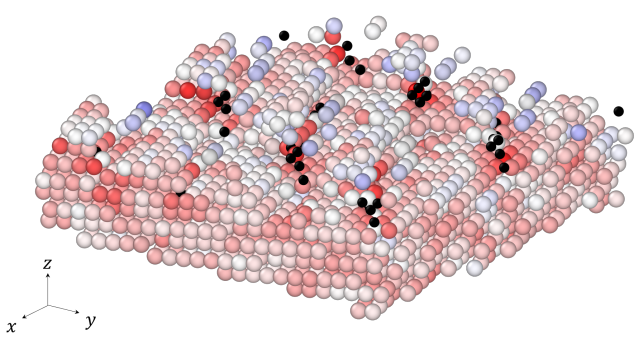

(a) NW v2 with $(2\,3\,2)_\gamma$ HP.

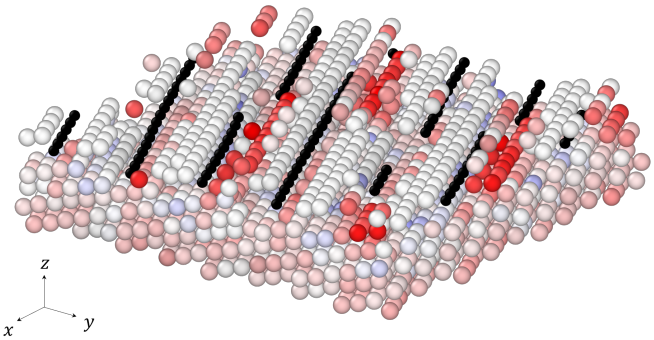

(b) Top interface of KS v1 OR with $(1\,2\,1)_\gamma$ HP.

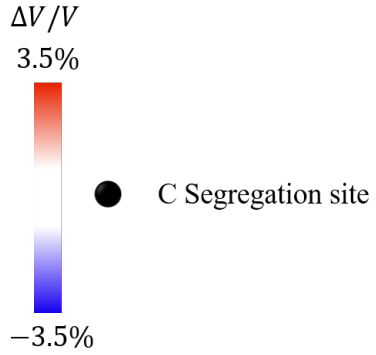

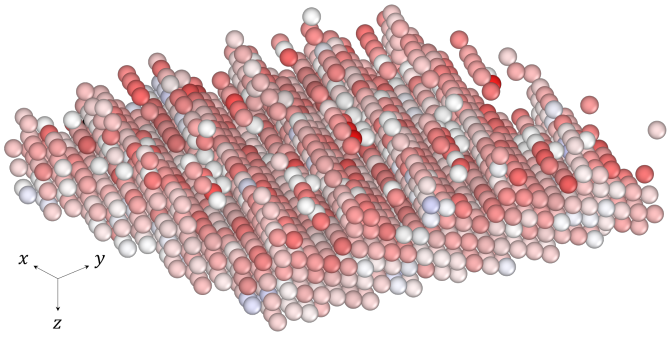

(c) Bottom interface of KS v1 OR with $(1\,2\,1)_\gamma$ HP.

Figure 5.5: Carbon segregation sites (black spheres) overlaid volumetric strain for FCC-BCC semi-coherent interface relief. Extracted from the QA simulation for NW v2 OR with $(1\,2\,1)_\gamma$ HP at $t^* = 300$. Rendering done in Ovito [136], displaying only BCC atoms. Iron atoms coloration is based on elastic strain calculations, showcasing volumetric strain $\Delta V/V$. Red indicates the maximum $\Delta V/V$, and blue the minimum.

For the bottom KS OR interface, in Figure 5.5c, a relatively uniform elastic strain field was observed, with no distinct areas of high or low volumetric strain. Furthermore, as shown in Figure 3.19 of Chapter 3.25 for KS OR, regions of higher volumetric strain were identified in areas where $\boldsymbol{b}_2$ dislocations were present, while regions with only $\boldsymbol{b}_1$ dislocations exhibited significantly lower strain, closer to BCC bulk values. This difference may explain the variation in carbon segregation at KS OR interfaces, as higher elastic strain tends to promote carbon segregation.

5.3 Interface mobility

To assess interface mobility, carbon concentration profiles for each OR are shown in Figure 5.6. Carbon concentrations from QA simulations are obtained by computing the mean occupation probabilities of iron, $\bar{\rho}_{Fe}$, and carbon, $\bar{\rho}_C$, across several box subsets centered along the z-axis.

Each subset has a size of $(256\Delta x)^3 \times (8\Delta x)$. Since iron and carbon atoms have different atomic volumes, V_{Fe} and V_C, this difference is taken into account in the calculation of carbon concentration in each subset. Consequently, the carbon content can be expressed as:

$$C_C = \frac{\bar{\rho}_C(V_{Fe} + V_C)}{V_C(\bar{\rho}_{Fe}V_C + \bar{\rho}_C V_{Fe})}. \tag{5.3.1}$$

In Figure 5.6, the carbon content is displayed for NW OR at times $t^* = 200$ and $t^* = 300$, and for KS OR at time $t^* = 200$. At $t^* = 200$, the NW OR and the top KS OR interface carbon concentration profiles are similar, showing narrow, symmetric segregation peaks with a thickness of approximately 0.5 nm and a maximum concentration around 6.5 at.%. Additionally, carbon-depleted regions close to the interface are observed for both ORs. This depletion is more pronounced for KS OR, where the carbon content reaches 3 at.% in the depleted regions, compared to 3.5 at.% further from the interface. However, the bottom interface of KS OR differs (Figure 5.6b), showing a smaller segregation peak of only 4.5 at.%. Furthermore, this segregation peak is asymmetrical, with a broader distribution in the austenite region compared to the ferrite. This observation aligns with expectations, as no specific segregation sites were detected for this interface.

The time evolution of carbon content can only be assessed for NW OR at $t^* = 300$, as the simulation of KS OR was not prolongated. It shows a smaller amplitude of the segregation peaks compared to $t^* = 200$, with a maximum carbon content of 6 at.%. Moreover, the interface became asymmetrical, with a broader distribution in the austenite region compared to the ferrite.

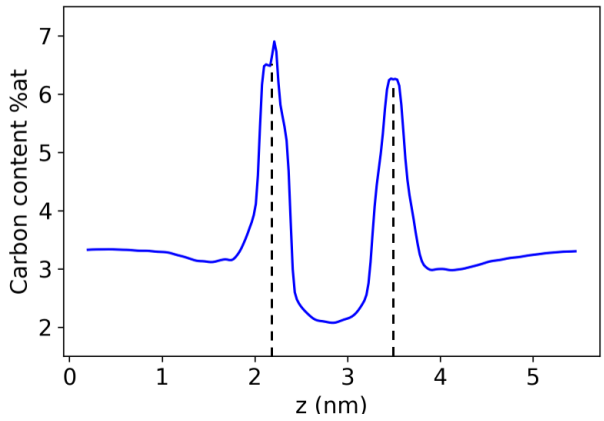

(a) NW v2 with $(2\,3\,2)_\gamma$ HP, $t^* = 200$.

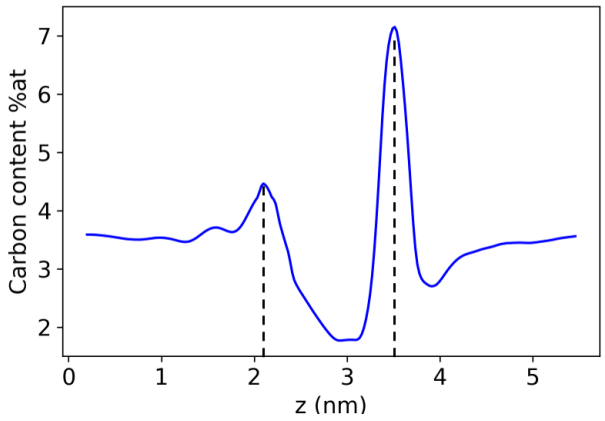

(b) KS v1 OR with $(1\,2\,1)_\gamma$ HP.

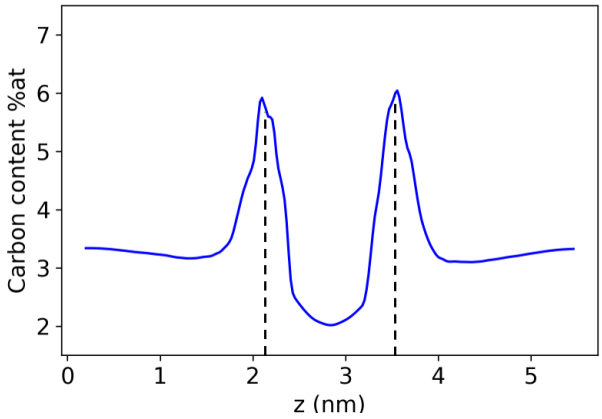

(c) NW v2 with $(2\,3\,2)_\gamma$ HP, $t^* = 300$.

Figure 5.6: Concentration profile of carbon across the FCC-BCC interface, dotted black lines indicate positions of interfaces. **(a)** NW v2 OR with $(1\,2\,1)_\gamma$ HP at $t^* = 200$, **(b)** KS v1 OR with $(1\,2\,1)_\gamma$ HP at $t^* = 200$, **(c)** NW v2 with $(1\,2\,1)_\gamma$ HP at $t^* = 300$.

The asymmetrical peaks of carbon concentration for NW OR at $t^* = 300$ indicate that the carbon diffuse from the interface into the austenite. This type of profile is compatible with local equilibrium (LE) conditions at the interface. Moreover, at $t^* = 200$, the depletion regions in the austenite near the interface are caused by the initial diffusion of carbon at the forming FCC-BCC interface until local equilibrium is reached. For Fe-C binary systems, LE conditions have been successfully used by many authors to describe the concentration profiles of carbon concentration at austenite-ferrite interfaces [147–151].

While LE conditions are typical for a diffusion-controlled transformation rate, the rapid diffusion of carbon indicates that the transformation rate may still be governed by the driving force at the interface. A mixed-mode model, provides a more accurate description of interface propagation than a purely diffusion-controlled model, with the limiting rate determined by either the interface

of diffusion controlled transformation rate. Additionally, solute drag may occur, further slowing the transformation rate.

In the case of the bottom KS OR interface, the asymmetrical segregation peak indicates that carbon continues to diffuse from the newly formed ferrite into the austenite, which is characteristic of a local equilibrium (LE) condition. Furthermore, the asymmetry of this peak is identical to that of NW OR, suggesting a similar diffusion rate of carbon when the maximum solubility at the interface is reached. Therefore, despite the small carbon segregation observed at the interface, the same conclusions can be drawn for the bottom KS OR interface, with LE conditions and a mixed-mode propagation rate.

5.4 Conclusion

In this chapter, the QA method was employed to simulate the FCC to BCC phase transformation in an Fe-C system for NW and KS ORs. Carbon segregation sites were found to be located in regions of high volumetric strain. It was shown in Chapter 3, that this strain is induced by the presence of $\boldsymbol{b}_1$ and $\boldsymbol{b}_2$ dislocations at the interface, with a significantly higher strain at their intersections. This observation is confirmed in this chapter for NW OR, where carbon segregation sites are concentrated at dislocation intersections and along $\boldsymbol{b}_1$.

Furthermore, the influence of interface morphology on carbon segregation was demonstrated. For NW OR and the top KS interface, carbon segregation was observed. However, this was not the case for the bottom KS OR interface. Unlike the other two, this interface contained only perfect $\boldsymbol{b}_1$ screw dislocations, with close to no kinks. This particular geometry can be attributed to the size of the simulation box. Indeed, in Chapter 3, regions larger than the two-component simulation box with only $\boldsymbol{b}_1$ dislocations were detected. Therefore, the real KS OR interaction with carbon solutes likely represents a combination of behaviors observed at the top and bottom interfaces.

Local equilibrium (LE) conditions may correspond to the results observed for all simulated interfaces. However, the propagation of the interface may not be purely diffusion-controlled: the rapid diffusion of carbon into the austenite could shift the regime to interface-controlled, with the interface driving force as the limiting factor. Additionally, solute drag may occur, further limiting the transformation rate. To determine the limiting factor for interface propagation rates, additional simulations of Fe-C binary systems over an extended timeframe are necessary. These simulations could then be compared with the propagation rates in pure iron phases to discern whether the limiting factor is carbon content or the interface driving force.

QA simulations of the FCC to BCC phase transformation in an Fe-C system have shown promis-

ing results. Extending the temporal and spatial scales of these simulations could provide deeper insights into the interaction of the interface with carbon solutes and its propagation mode.

Conclusions and future prospects

The main purpose of this work was to improve our understanding of the FCC-BCC structural transformation from the austenite (γ) to the ferrite (α) phases of iron, as it is a pivotal process in the production of contemporary steels such as Dual Phase steels for the automotive industry. This phase transformation gives rise to different microstructures, depending on the crystallography (lattice misfit and OR between FCC and BCC structures), the interface properties (HP, coherency, thickness, etc.), and the chemical composition of the alloy. In this work, we thus aimed at connecting the different parameters of the FCC-BCC transformation, including the OR and HP, to the structure and propagation mode of the FCC-BCC interface, the underlying FCC-BCC transformation paths at atomic scale, and the interaction of the alloying elements with the moving interface. To address this problematic, a recent numerical model called the Quasiparticle Approach (QA) was used in this work to investigate the mechanisms driving the FCC-BCC transformation, for different ORs and HPs. For that purpose, the QA was first applied to the fundamental study case of pure iron, as a mean to identify the structure and propagation mode of the FCC-BCC interface, as well as its connection with the transformation path at atomic scale. Then, the present model was extended to the binary Fe-C system, in order to model the complex interaction of interstitial carbon atoms with the migrating interface.

The QA enables to model atomic movements at sub-interatomic distances while operating on the timescale of the FCC to BCC phase transformation. It was successfully used to analyze the interface characteristics of various geometries, including different orientation relationships (ORs) and habit planes (HPs). In particular, the QA was applied to model the displacive FCC to BCC phase transformation with the Nishiyama-Wasserman (NW), Greninger-Troiano (GT), and Kurdjumov-Sachs (KS) ORs. The crystallography of the FCC-BCC interface has already been studied extensively in the literature and these different crystallographic ORs have been reported. Moreover, in order to extract valuable information from the QA simulations, several analyses tools were adapted to the QA framework, such as the Slip Vector Analysis (SVA) which allow an accurate characterization of interface dislocations.

It was shown that, for all NW, GT and KS ORs, a semi-coherent stepped interface structure was detected, characterized by $(1\,1\,1)_\gamma||(0\,1\,1)_\alpha$ terraces. The step height, which corresponds to several interplanar spacings of the $(1\,1\,1)_\gamma$ planes, depends on the habit plane (HP) angle with the terrace

plane. It was concluded that as this angle increase, the step heights also increase. In the NW and GT ORs, two stepped structures were observed, while only one was detected for the KS OR. These steps are accompanied by sets of kink screw dislocations with Burgers vectors $\boldsymbol{b}_1 = \frac{a_\gamma}{2}[1\,0\,\bar{1}]^*_\gamma$ and $\boldsymbol{b}_2 = \frac{a_\gamma}{2}[0\,1\,\bar{1}]^*_\gamma$. Although the second step is absent in KS OR, the $\boldsymbol{b}_2$ dislocations associated with it are still present at the interface.

This difference in the interface structure between the various ORs can be connected to the orientation of the mean dislocation line of the transformation dislocations at the FCC-BCC interface. In the present work, only NW, KS and GT ORs were prospected. While they share the same $\{1\,1\,1\}_\gamma||(0\,1\,1)_\alpha$ parallel dense planes between the FCC and BCC structures, they differentiate regarding the deviation angle between the $\langle 1\,0\,\bar{1}\rangle_\gamma$ and $\langle 1\,1\,\bar{1}\rangle_\alpha$ dense directions. Considering that a key factor governing the position and orientation of the mean dislocation lines is the location and direction of maximum lattice mismatch between the FCC and BCC phases in the Moiré pattern at the FCC-BCC interface, the different misorientations between the $\langle 1\,0\,\bar{1}\rangle_\gamma$ and $\langle 1\,1\,\bar{1}\rangle_\alpha$ depending on the OR, lead to the different dislocation line orientations observed in this work. This, in turn, affects dislocation mobility through the frequency of kinks along their length.

Moreover, the HP also influences the angle between the line directions, with a higher HP angle relative to the terrace plane resulting in a greater angle between $\boldsymbol{\xi}_1$ and $\boldsymbol{\xi}_2$. This produces slight variations in interface morphology within the same OR for different HPs. These changes in dislocation line directions result in different step spacings for the ORs. For the step associated with the $\boldsymbol{b}_1$ dislocations, spacings are measured between 1.0 and 3.3 nm, with higher HP angles relative to the terrace plane producing smaller spacings across all ORs. It should be noted that even if the HP influences the spacing between the second set of steps for the NW and GT ORs, the OR remain the leading factor for the spacing between terrace steps.

Overall, this work provides a detailed description of the FCC-BCC interface using QA simulations. The interface morphology, including dislocation characteristics, step heights, and spacings, shows encouraging agreement with various theoretical models, experimental observations, and atomic simulations. However, a unique feature of the QA-simulated interface, namely the presence of a double step for the NW and GT ORs, has not been previously described in the literature. While $\boldsymbol{b}_2$ dislocations were known to appear at the FCC-BCC interface for the KS OR, this is the first time they have been directly observed.

Moreover, although the interface characteristics depend on the OR and HP, a single transformation mechanism was identified, characterized by a step-flow mode of transformation driven by dislocation glide. The FCC-BCC interface propagates along the $\boldsymbol{b}_1$ and $\boldsymbol{b}_2$ dislocations in the $(0\,1\,1)_\alpha||(1\,1\,1)_\gamma$ plane, with nucleation of the BCC phase occurring at dislocation intersections. It was determined that they are due to similar transformation path taking place for all ORs. Specifi-

cally, it was concluded that the complete FCC to BCC transformation path for the NW, GT, and KS ORs involves the concurrent action of two twinning variants of the KS transformation path along $\boldsymbol{b}_1$ and $\boldsymbol{b}_2$ dislocations. Moreover, the overlaying of these two variants of the KS transformation path at the intersection of $\boldsymbol{b}_1$ and $\boldsymbol{b}_2$ dislocations mimics the shear displacement of KSN transformation path, which was often mistaken for the BB/OC transformation mechanism in previous MD studies of the FCC to BCC phase transformation. Displacement vector analysis and diffraction patterns revealed that this mechanism involves the formation of Shockley partial dislocations with a Burgers vector of $\boldsymbol{b} = \frac{a_\gamma}{6}[1\,1\,\bar{2}]^*_\gamma$ and the creation of an HCP interphase.

The detailed description provided for one-component iron systems then served as a basis for studying carbon segregation at the FCC-BCC interface. Although this remains a work in progress, it was shown that carbon segregation is influenced by the interface structure, with preferential segregation sites located near regions of higher elastic strain. Moreover, the carbon concentration profiles were consistent with local equilibrium conditions at the interface, with carbon diffusing from the ferrite into the austenite.

A first blind spot of this work concerns the influence of the misfit on the FCC-BCC transformation. Indeed, only one misfit ratio between the FCC and BCC structures was considered in this work (1.23). The PTMC suggest that the lattice misfit sets the HP, which in turn influences the geometry of the FCC-BCC interface, including the spacing between terrace steps, step height etc. Moreover, different lattice misfits result in different Moiré patterns at the interface, which in turn lead to different deviation angles for the two dislocation sets at the interface and potentially different mobility of the interface linked with different kink numbers along dislocations. An important development of the QA, would be to extend the model to different lattice misfits, in order to assess the connection between lattice misfit and FCC-BCC interface structure and mobility.

While the detailed analysis of the FCC-BCC interface structure and transformation mechanism in pure iron provided valuable insights, the FCC to BCC phase transformation under constraint was not prospected in this work. In particular, it was suggested in the literature that external constraints applied to the system could change the FCC to BCC transformation path from the KS and KSN paths, to the BB/OC path. A perspective of this work would be to account for different strains in the long range interaction potential, as it was done in previous QA studies, and prospect strain induced FCC to BCC transformation paths and interface structure and mobility.

More generally, the QA can be applied to describe displacive phase transformations in systems with different crystal structures, including the HCP or monoclinic structures. For instance, the FCC to HCP displacive transformation is observed in high entropy alloys where it contributes to high work hardening behavior during tensile deformation. The QA has previously demonstrated its capacity to reproduce different crystal structures, such as the diamond and the HCP structures.

Therefore, an interesting perspective would be to prospect displacive transformations in systems with different crystal structure, based on the capacity of the QA to model diverse crystal structures.

However, it is in multi-component systems that the most promising developments lie. While carbon segregation at the interface was observed, the time and spatial resolution were limited compared to the one-component system. Further work using higher resolutions and extended time frames, that could be accessed by improving the numerical scheme, could enable a more accurate representation of carbon interactions with interface dislocations. This approach may also clarify whether the FCC to BCC phase transformation is driven primarily by carbon diffusion or the interface driving force, and whether solute drag occurs. Additionally, refining the interaction potentials used in this work could yield more accurate results. Once the Fe-C two-component system has been more thoroughly explored, the next step could be QA simulations of ternary alloys, such as Fe-C-Mn systems.

In parallel, including substitutional solute atoms in the QA simulations of FCC-BCC transformations would allow to open up the field of mutli-component systems accessible to the approach. This two developments would bring a twofold insight on the FCC-BCC transformation in steels. First, it would improve our understanding on fundamental segregation processes on a moving FCC-BCC interface in multi-component systems, such as co-segregation and desegregation processes. It might allow to correlate the concentration profile at the interface with the different modes of segregation (LE, NPLE, PE), thereby addressing the gaps in the literature regarding the segregation mode at the FCC-BCC interface. Second, it would enable more quantitative comparisons of QA simulations with experimental observations on industrial prototype alloys, paving the way for using QA to guide and even substitute certain experiments.

From a methodological standpoint, new numerical tools have recently emerged in material science, with Machine Learning (ML) as an emblematic figure. This class of approaches propose a paradigm shift in the modeling and simulation of materials evolution and characterization at various scales. In particular, ML was applied to develop new interaction potentials for MD, classify experimental observation of microstructures, detect and analyze atomic defects, predict and upscale mesoscale simulations such as phase field methods, and assist new materials design. A very promising perspective would be to develop ML tools for QA at three levels. First, ML could be implemented to develop a new class of parametric interaction potentials, in order to improve the reproduction of materials properties, such as the elastic constants, and the tetragonality of cubic cells in steel. Second, ML methods for defects analysis could be added to the current post-treatment tools used in this work (SVA, CNA etc.), in order to spot and characterize more accurately interface dislocations. Finally, advanced deep neural networks such as X-LSTM could be used to predict and upscale three-dimensional QA simulations, thus overcoming current computational limitations in simulating FCC-BCC phase transitions across large spatial domains in multi-component systems.

Appendix A

List of KS, NW and GT variants

OR	FCC plane	BCC plane	FCC direction	BCC direction	Bain variant
KS1	$(1\,1\,1)_\gamma$	$(0\,1\,1)_\alpha$	$[1\,0\,\bar{1}]_\gamma$	$[1\,1\,\bar{1}]_\alpha$	B_3
KS2	$(1\,1\,1)_\gamma$	$(0\,1\,1)_\alpha$	$[1\,0\,\bar{1}]_\gamma$	$[\bar{1}\,1\,\bar{1}]_\alpha$	B_1
KS3	$(1\,1\,1)_\gamma$	$(0\,1\,1)_\alpha$	$[\bar{1}\,1\,0]_\gamma$	$[1\,1\,\bar{1}]_\alpha$	B_1
KS4	$(1\,1\,1)_\gamma$	$(0\,1\,1)_\alpha$	$[\bar{1}\,1\,0]_\gamma$	$[\bar{1}\,1\,\bar{1}]_\alpha$	B_2
KS5	$(1\,1\,1)_\gamma$	$(0\,1\,1)_\alpha$	$[0\,\bar{1}\,1]_\gamma$	$[1\,1\,\bar{1}]_\alpha$	B_2
KS6	$(1\,1\,1)_\gamma$	$(0\,1\,1)_\alpha$	$[0\,\bar{1}\,1]_\gamma$	$[\bar{1}\,1\,\bar{1}]_\alpha$	B_3
KS7	$(\bar{1}\,1\,1)_\gamma$	$(0\,1\,1)_\alpha$	$[1\,0\,1]_\gamma$	$[1\,1\,\bar{1}]_\alpha$	B_1
KS8	$(\bar{1}\,1\,1)_\gamma$	$(0\,1\,1)_\alpha$	$[1\,0\,1]_\gamma$	$[\bar{1}\,1\,\bar{1}]_\alpha$	B_3
KS9	$(\bar{1}\,1\,1)_\gamma$	$(0\,1\,1)_\alpha$	$[\bar{1}\,\bar{1}\,0]_\gamma$	$[1\,1\,\bar{1}]_\alpha$	B_2
KS10	$(\bar{1}\,1\,1)_\gamma$	$(0\,1\,1)_\alpha$	$[\bar{1}\,\bar{1}\,0]_\gamma$	$[\bar{1}\,1\,\bar{1}]_\alpha$	B_1
KS11	$(\bar{1}\,1\,1)_\gamma$	$(0\,1\,1)_\alpha$	$[0\,1\,\bar{1}]_\gamma$	$[1\,1\,\bar{1}]_\alpha$	B_3
KS12	$(\bar{1}\,1\,1)_\gamma$	$(0\,1\,1)_\alpha$	$[0\,1\,\bar{1}]_\gamma$	$[\bar{1}\,1\,\bar{1}]_\alpha$	B_2
KS13	$(1\,\bar{1}\,1)_\gamma$	$(0\,1\,1)_\alpha$	$[\bar{1}\,0\,1]_\gamma$	$[1\,1\,\bar{1}]_\alpha$	B_1
KS14	$(1\,\bar{1}\,1)_\gamma$	$(0\,1\,1)_\alpha$	$[\bar{1}\,0\,1]_\gamma$	$[\bar{1}\,1\,\bar{1}]_\alpha$	B_3
KS15	$(1\,\bar{1}\,1)_\gamma$	$(0\,1\,1)_\alpha$	$[1\,1\,0]_\gamma$	$[1\,1\,\bar{1}]_\alpha$	B_2
KS16	$(1\,\bar{1}\,1)_\gamma$	$(0\,1\,1)_\alpha$	$[1\,1\,0]_\gamma$	$[\bar{1}\,1\,\bar{1}]_\alpha$	B_1
KS17	$(1\,\bar{1}\,1)_\gamma$	$(0\,1\,1)_\alpha$	$[0\,\bar{1}\,\bar{1}]_\gamma$	$[1\,1\,\bar{1}]_\alpha$	B_3
KS18	$(1\,\bar{1}\,1)_\gamma$	$(0\,1\,1)_\alpha$	$[0\,\bar{1}\,\bar{1}]_\gamma$	$[\bar{1}\,1\,\bar{1}]_\alpha$	B_2
KS19	$(1\,1\,\bar{1})_\gamma$	$(0\,1\,1)_\alpha$	$[\bar{1}\,0\,\bar{1}]_\gamma$	$[1\,1\,\bar{1}\,]_\alpha$	B_1
KS20	$(1\,1\,\bar{1})_\gamma$	$(0\,1\,1)_\alpha$	$[\bar{1}\,0\,\bar{1}]_\gamma$	$[\bar{1}\,1\,\bar{1}]_\alpha$	B_3
KS21	$(1\,1\,\bar{1})_\gamma$	$(0\,1\,1)_\alpha$	$[1\,\bar{1}\,0]_\gamma$	$[1\,1\,\bar{1}]_\alpha$	B_2
KS22	$(1\,1\,\bar{1})_\gamma$	$(0\,1\,1)_\alpha$	$[1\,\bar{1}\,0]_\gamma$	$[\bar{1}\,1\,\bar{1}]_\alpha$	B_1
KS23	$(1\,1\,\bar{1})_\gamma$	$(0\,1\,1)_\alpha$	$[0\,1\,1]_\gamma$	$[1\,1\,\bar{1}]_\alpha$	B_3
KS24	$(1\,1\,\bar{1})_\gamma$	$(0\,1\,1)_\alpha$	$[0\,1\,1]_\gamma$	$[\bar{1}\,1\,\bar{1}]_\alpha$	B_2

Table A.1: KS variants

OR	FCC plane	BCC plane	FCC direction	BCC direction	Bain variant
NW1	$(1\,1\,1)_\gamma$	$(0\,1\,1)_\alpha$	$[1\,0\,\bar{1}]_\gamma$	$[1\,0\,0]_\alpha$	B_2
NW2	$(1\,1\,1)_\gamma$	$(0\,1\,1)_\alpha$	$[\bar{1}\,1\,0]_\gamma$	$[1\,0\,0]_\alpha$	B_3
NW3	$(1\,1\,1)_\gamma$	$(0\,1\,1)_\alpha$	$[0\,\bar{1}\,1]_\gamma$	$[1\,0\,0]_\alpha$	B_1
NW4	$(\bar{1}\,1\,1)_\gamma$	$(0\,1\,1)_\alpha$	$[1\,0\,1]_\gamma$	$[1\,0\,0]_\alpha$	B_2
NW5	$(\bar{1}\,1\,1)_\gamma$	$(0\,1\,1)_\alpha$	$[\bar{1}\,\bar{1}\,0]_\gamma$	$[1\,0\,0]_\alpha$	B_3
NW6	$(\bar{1}\,1\,1)_\gamma$	$(0\,1\,1)_\alpha$	$[0\,1\,\bar{1}]_\gamma$	$[1\,0\,0]_\alpha$	B_1
NW7	$(1\,\bar{1}\,1)_\gamma$	$(0\,1\,1)_\alpha$	$[\bar{1}\,0\,1]_\gamma$	$[1\,0\,0]_\alpha$	B_2
NW8	$(1\,\bar{1}\,1)_\gamma$	$(0\,1\,1)_\alpha$	$[1\,1\,0]_\gamma$	$[1\,0\,0]_\alpha$	B_3
NW9	$(1\,\bar{1}\,1)_\gamma$	$(0\,1\,1)_\alpha$	$[0\,\bar{1}\,\bar{1}]_\gamma$	$[1\,0\,0]_\alpha$	B_1
NW10	$(1\,1\,\bar{1})_\gamma$	$(0\,1\,1)_\alpha$	$[\bar{1}\,0\,\bar{1}]_\gamma$	$[1\,0\,0]_\alpha$	B_2
NW11	$(1\,1\,\bar{1})_\gamma$	$(0\,1\,1)_\alpha$	$[1\,\bar{1}\,0]_\gamma$	$[1\,0\,0]_\alpha$	B_3
NW12	$(1\,1\,\bar{1})_\gamma$	$(0\,1\,1)_\alpha$	$[0\,1\,1]_\gamma$	$[1\,0\,0]_\alpha$	B_1

Table A.2: NW variants

OR	FCC plane	BCC plane	FCC direction	BCC direction	Bain variant
GT1	$(1\,1\,1)_\gamma$	$(0\,1\,1)_\alpha$	$[12\,5\,\bar{17}]_\gamma$	$[7\,17\,\bar{17}]_\alpha$	B_3
GT2	$(1\,1\,1)_\gamma$	$(0\,1\,1)_\alpha$	$[\bar{17}\,5\,12]_\gamma$	$[7\,\bar{17}\,17]_\alpha$	B_1
GT3	$(1\,1\,1)_\gamma$	$(0\,1\,1)_\alpha$	$[\bar{17}\,12\,5]_\gamma$	$[7\,17\,\bar{17}]_\alpha$	B_1
GT4	$(1\,1\,1)_\gamma$	$(0\,1\,1)_\alpha$	$[12\,\bar{17}\,5]_\gamma$	$[7\,\bar{17}\,17]_\alpha$	B_2
GT5	$(1\,1\,1)_\gamma$	$(0\,1\,1)_\alpha$	$[5\,\bar{17}\,12]_\gamma$	$[7\,17\,\bar{17}]_\alpha$	B_2
GT6	$(1\,1\,1)_\gamma$	$(0\,1\,1)_\alpha$	$[5\,12\,\bar{17}]_\gamma$	$[7\,\bar{17}\,17]_\alpha$	B_3
GT7	$(\bar{1}\,1\,1)_\gamma$	$(0\,1\,1)_\alpha$	$[17\,5\,12]_\gamma$	$[7\,17\,\bar{17}]_\alpha$	B_1
GT8	$(\bar{1}\,1\,1)_\gamma$	$(0\,1\,1)_\alpha$	$[12\,\bar{5}\,17]_\gamma$	$[\bar{7}\,17\,\bar{17}]_\alpha$	B_3
GT9	$(\bar{1}\,1\,1)_\gamma$	$(0\,1\,1)_\alpha$	$[12\,17\,\bar{5}]_\gamma$	$[\bar{7}\,\bar{17}\,17]_\alpha$	B_2
GT10	$(\bar{1}\,1\,1)_\gamma$	$(0\,1\,1)_\alpha$	$[17\,12\,5]_\gamma$	$[7\,\bar{17}\,17]_\alpha$	B_1
GT11	$(\bar{1}\,1\,1)_\gamma$	$(0\,1\,1)_\alpha$	$[5\,\bar{12}\,17]_\gamma$	$[\bar{7}\,\bar{17}\,17]_\alpha$	B_3
GT12	$(\bar{1}\,1\,1)_\gamma$	$(0\,1\,1)_\alpha$	$[5\,17\,\bar{12}]_\gamma$	$[\bar{7}\,17\,\bar{17}]_\alpha$	B_2
GT13	$(1\,\bar{1}\,1)_\gamma$	$(0\,1\,1)_\alpha$	$[17\,5\,\bar{12}]_\gamma$	$[\bar{7}\,\bar{17}\,17]_\alpha$	B_1
GT14	$(1\,\bar{1}\,1)_\gamma$	$(0\,1\,1)_\alpha$	$[\bar{12}\,5\,17]_\gamma$	$[\bar{7}\,17\,\bar{17}]_\alpha$	B_3
GT15	$(1\,\bar{1}\,1)_\gamma$	$(0\,1\,1)_\alpha$	$[12\,17\,5]_\gamma$	$[7\,17\,\bar{17}]_\alpha$	B_2
GT16	$(1\,\bar{1}\,1)_\gamma$	$(0\,1\,1)_\alpha$	$[17\,12\,\bar{5}]_\gamma$	$[\bar{7}\,17\,\bar{17}]_\alpha$	B_1
GT17	$(1\,\bar{1}\,1)_\gamma$	$(0\,1\,1)_\alpha$	$[\bar{5}\,12\,17]_\gamma$	$[\bar{7}\,\bar{17}\,17]_\alpha$	B_3
GT18	$(1\,\bar{1}\,1)_\gamma$	$(0\,1\,1)_\alpha$	$[5\,17\,12]_\gamma$	$[7\,\bar{17}\,17]_\alpha$	B_2
GT19	$(1\,1\,\bar{1})_\gamma$	$(0\,1\,1)_\alpha$	$[17\,\bar{5}\,12]_\gamma$	$[\bar{7}\,\bar{17}\,17]_\alpha$	B_1
GT20	$(1\,1\,\bar{1})_\gamma$	$(0\,1\,1)_\alpha$	$[12\,5\,17]_\gamma$	$[7\,\bar{17}\,17]_\alpha$	B_3
GT21	$(1\,1\,\bar{1})_\gamma$	$(0\,1\,1)_\alpha$	$[\bar{12}\,17\,5]_\gamma$	$[\bar{7}\,\bar{17}\,17]_\alpha$	B_2
GT22	$(1\,1\,\bar{1})_\gamma$	$(0\,1\,1)_\alpha$	$[17\,\bar{12}\,5]_\gamma$	$[\bar{7}\,17\,\bar{17}]_\alpha$	B_1
GT23	$(1\,1\,\bar{1})_\gamma$	$(0\,1\,1)_\alpha$	$[5\,12\,17]_\gamma$	$[7\,17\,\bar{17}]_\alpha$	B_3
GT24	$(1\,1\,\bar{1})_\gamma$	$(0\,1\,1)_\alpha$	$[\bar{5}\,17\,12]_\gamma$	$[\bar{7}\,17\,\bar{17}]_\alpha$	B_2

Table A.3: GT variants

Appendix B

Slip vector analysis

The SVA is a obtained from the differential displacement analysis (DDA) proposed by V. Vitek [152]. The DDA quantifies and characterizes the atomic displacement of each atom's nearest neighbors to reveal the strain fields around a dislocation [142]. This method requires a well-defined, defect-free reference structure to compare with the structure being analyzed. Here, the ideal FCC and BCC structures serve as reference configurations. During DDA, an atomic pair is formed between an atom i and one of its first neighbors j is formed in the reference configuration. The distance between the two atoms of these atomic pair is denoted as $\boldsymbol{R}_{ij}^{ref}$ and expressed as:

$$\boldsymbol{R}_{ij}^{ref} = \boldsymbol{r}_{i}^{ref} - \boldsymbol{r}_{j}^{ref}. \tag{B.0.1}$$

The corresponding pair is also defined at a given step of simulation during the FCC-BCC phase transformation simulation:

$$\boldsymbol{R}_{ij}^{tra} = \boldsymbol{r}_{i}^{sim} - \boldsymbol{r}_{j}^{sim}. \tag{B.0.2}$$

The displacement vector for an atomic pair ij is then calculated:

$$\Delta\boldsymbol{R}_{ij} = \boldsymbol{R}_{ij}^{ref} - \boldsymbol{R}_{ij}^{sim}. \tag{B.0.3}$$

While the DDA stops at this step and a 2D vector plot is used to display the result, the SVA has the advantage of representing a slip vector in a three-dimensional vector plot. This slip vector is defined by [134, 142]:

$$S^{i} = \frac{-1}{N_S} \sum_{i \neq j}^{N} \Delta\boldsymbol{R}_{ij}. \tag{B.0.4}$$

Here, N represents the number of nearest neighbors of the atom i, and N_S represents the number of those neighbors that have slipped. The literature [134] does not provide clear guidance on how to determine which atoms have slipped. Furthermore, due to the discrete approximation of the QA method, loss of information at dislocation cores and small displacements hinder the accurate

determination of the number of slipped neighbors. Therefore, Equation B.0.4 is simplified as follows:

$$S^i = \frac{-1}{N} \sum_{i \neq j}^{N} \Delta \boldsymbol{R}_{ij}. \tag{B.0.5}$$

As detailed in [134, 142], the slip vector for atoms near the slip plane is expected to reflect the gradient distribution of the Burgers vectors. All atoms near a dislocation will exhibit slip vectors, with magnitudes that decrease with distance from the dislocation. Furthermore, slip vectors on opposite sides of a dislocation core will tend to point in opposite directions, as illustrated in Figure B.1.

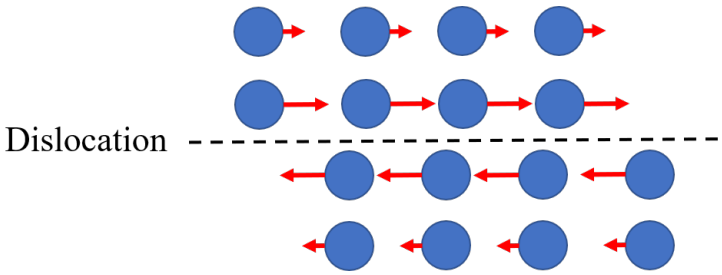

Figure B.1: Schematic gradient distribution of slips vectors, represented by red arrows, around a dislocation core.

Due to the approximation in Equation B.0.5, the magnitude of the Burgers vector cannot be determined with a good precision but it can be estimated. The direction and the line direction of the dislocation can then be determined with good precision.

However, adapting the SVA for use in QA is necessary due to information loss at dislocation cores, which arises from the application of the F2A method that converts the continuous distribution of fratons into discrete atoms. This information loss can be attributed to two specific causes. Firstly, the density of fratons at dislocation cores may be too low to convert them into individual atoms, potentially resulting in atom disappearance while conserving the total fraton density within the simulation box. Secondly, when two high-density fraton regions are in close proximity, they may form a 'peanut' structure (see Figure B.2), which the F2A algorithm then converts into a single atom.

Consequently, the reference structure may not have matching indexing with the corresponding phase during the FCC-BCC phase transformation. Therefore, it was necessary to adapt the SVA to establish a correspondence between atomic sites. To achieve this, Common Neighbor Analysis (CNA) is performed using the adaptive algorithm proposed in Ovito [153]. This analysis distinguishes between three types of structures: FCC, BCC, and 'others', which encompass all atomic sites not identified as FCC or BCC. By employing this approach, the appropriate reference structure can be used to calculate slip vectors. Atoms classified as 'others' are often near or within

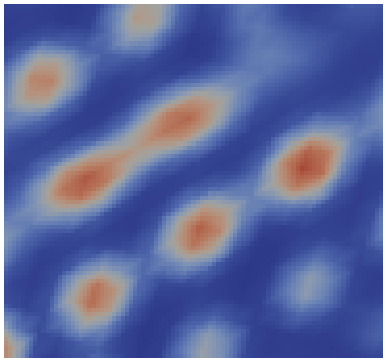

Figure B.2: 2-Dimensions visualization in Paraview of 'peanut' structure in an FCC-BCC interface simulated by the Quasi-particles approach. Red areas denotes a high fraton density and blue areas a low fraton density.

dislocation cores, so the comparison is made between a reference phase (FCC or BCC) and the corresponding phase, including atoms categorized as 'others' (i.e., FCC and 'others' or BCC and 'others').

To ensure accurate matching of atomic sites, the following procedure is carried out. First, data sets containing atomic positions of the reference structures and atomic positions of the analyzed phase are merged into a single data set. The cKDTree algorithm from SciPy [154] is then employed to calculate and detect the nearest neighbors for each atomic position in the merged data set. As atomic positions from the reference structure and from the selected FCC or BCC phase align in defect-free regions, this allows the reindexation of corresponding atoms. Outside dislocation cores, where information loss due to *fraton2atom* can introduce artifacts, the atomic displacement is smaller than the distance between nearest neighbors in FCC or BCC structures. Therefore, it does not impede correct indexing. Furthermore, this reindexing method has the advantage of detecting atoms that disappear in the FCC-BCC simulation, along with other numerical artifacts arising from the F2A post-processing step. These atoms and artifacts are removed from the subsequent SVA calculations.

In order to accurately determine the line directions of dislocations and improve the identification of Burgers vectors, an enhancement of the SVA technique has been made. The principle is that the Burgers vector of a dislocation remains constant along the dislocation line. Therefore, the LDA first scans for neighboring atoms within a specified cutoff distance, dependent on the lattice parameter, that exhibit the same slip vector direction as the central atom. If an atom has no neighbors with the same slip vector direction or has more than two neighbors with the same slip vectors, it is removed from the list to eliminate isolated atoms and dislocation intersections. Consequently, each remaining atom has one or two neighbors with the same slip vector direction. Based on this list, the line directions of the dislocations can be determined, as schematized in Figure B.3

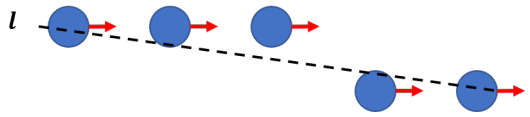

Figure B.3: Schematic dislocation lines $\boldsymbol{l}$ detected by the LDA. Slip vectors are represented by red arrows

An additional verification step is performed to ensure that the calculated lines accurately follow the atomic sites. For a given atom at position p_i in a line direction, the angle θ formed by the line from the atom indexed $i-1$ to the atom i and the line from the atom i to the atom $i+1$ is evaluated. If θ exceeds a predetermined cutoff threshold, the line direction is split into two segments. This process, depicted in Figure.(B.4), is repeated for the new line segment starting at atom $i+1$ in the previous dislocation line, ensuring that the new dislocation line also follows the atomic sites. By implementing this approach, the line directions of dislocations can be accurately determined, and the plot of the directions of Burgers vectors is significantly improved.

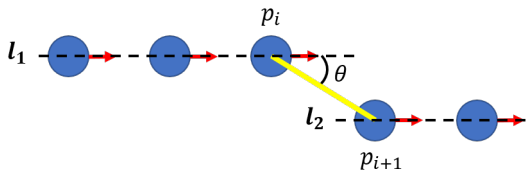

Figure B.4: Schematic dislocation lines splitting.

Bibliography

[1] R. E. Smallman and R. J. Bishop. *Modern physical metallurgy and materials engineering.* Butterworth-Heinemann, 1999.

[2] G. J. Mahon, J. M. Howe, and S. Mahajan. "HRTEM study of the $\{252\}_{\gamma}$ austenite–martensite interface in an Fe—8Cr–1C alloy". en. In: *Philosophical Magazine Letters* 59.6 (June 1989), pp. 273–279.

[3] S. Kajiwara, K. Ogawa, and T. Kikuchi. "High-resolution electron microscopy observations of transient lattices from fcc to bcc at the austenite martensite interface". en. In: *Philosophical Magazine Letters* 74.6 (Dec. 1996), pp. 405–414.

[4] T. Moritani et al. "Comparison of interphase boundary structure between bainite and martensite in steel". en. In: *Scripta Materialia* 47.3 (Aug. 2002), pp. 193–199.

[5] K. Ogawa and S. Kajiwara. "High-resolution electron microscopy study of ledge structures and transition lattices at the austenite–martensite interface in Fe-based alloys". en. In: *Philosophical Magazine* 84.27 (Sept. 2004), pp. 2919–2947.

[6] K. Ogawa and S. Kajiwara. "High-Resolution Electron Microscopic Study on Atomic Arrangements at Growing Tips of Martensite Plates and a Nucleating Martensite in Fe-Ni-Mn and Fe-Cr-C Alloys". en. In: *MATERIALS TRANSACTIONS* 48.4 (2007), pp. 860–868.

[7] O. Nakonechna. "Etude à l'échelle nanométrique des interfaces de transformations austénite/ferrite dans Fe-Mn-C à différentes températures intercritiques". fr. In: ().

[8] Y. Toji et al. "Atomic-scale analysis of carbon partitioning between martensite and austenite by atom probe tomography and correlative transmission electron microscopy". In: *Acta Materialia* 65 (2014), pp. 215–228.

[9] H. Koohdar et al. "On the stability of reversely formed austenite and related mechanism of transformation in an Fe-Ni-Mn martensitic steel aided by electron backscattering diffraction and atom probe tomography". In: *Metallurgical and Materials Transactions A* 48 (2017), pp. 5244–5257.

[10] S. Tateyama, Y. Shibuta, and T. Suzuki. "A molecular dynamics study of the fcc–bcc phase transformation kinetics of iron". en. In: *Scripta Materialia* 59.9 (Nov. 2008), pp. 971–974.

[11] H. Song and J. Hoyt. “An atomistic simulation study of the migration of an austenite–ferrite interface in pure Fe”. en. In: *Acta Materialia* 61.4 (Feb. 2013), pp. 1189–1196.

[12] X. Ou, J. Sietsma, and M. J. Santofimia. “Molecular dynamics simulations of the mechanisms controlling the propagation of bcc/fcc semi-coherent interfaces in iron”. en. In: *Modelling and Simulation in Materials Science and Engineering* 24.5 (June 2016), p. 055019.

[13] X. Ou. “Molecular dynamics simulations of fcc-to-bcc transformation in pure iron: a review”. en. In: *Materials Science and Technology* 33.7 (May 2017), pp. 822–835.

[14] F. Maresca and W. Curtin. “The austenite/lath martensite interface in steels: Structure, athermal motion, and in-situ transformation strain revealed by simulation and theory”. en. In: *Acta Materialia* 134 (Aug. 2017), pp. 302–323.

[15] P. K. Tripathi, S. K. Maurya, and S. Bhowmick. “Role of disconnections in mobility of the austenite-ferrite inter-phase boundary in Fe”. en. In: *Physical Review Materials* 2.11 (Nov. 2018). arXiv: 1808.03432, p. 113403.

[16] P. K. Tripathi et al. “Role of interface morphology on the martensitic transformation in pure Fe”. en. In: *Materialia* 16 (May 2021). arXiv:2101.07468 [cond-mat], p. 101085.

[17] T. Castán and P.-A. Lindgård. “Kinetics of domain growth, theory, and Monte Carlo simulations: A two-dimensional martensitic phase transition model system”. In: *Physical Review B* 40.7 (1989), p. 5069.

[18] Y. Chen and C. A. Schuh. “A coupled kinetic Monte Carlo–finite element mesoscale model for thermoelastic martensitic phase transformations in shape memory alloys”. In: *Acta Materialia* 83 (2015), pp. 431–447.

[19] R. Veiga et al. “Monte Carlo and molecular dynamics simulations of screw dislocation locking by Cottrell atmospheres in low carbon Fe–C alloys”. en. In: *Scripta Materialia* 108 (Nov. 2015), pp. 19–22.

[20] L. Huang and P. Maugis. “Atomistic simulation of the collective carbon motion in body-centered tetragonal iron: A new insight into the martensite ageing”. en. In: *Acta Materialia* 249 (May 2023), p. 118846.

[21] K. R. Elder et al. “Modeling Elasticity in Crystal Growth”. en. In: *Physical Review Letters* 88.24 (June 2002), p. 245701.

[22] M. Militzer et al. “Multiscale Modeling of Phase Transformations in Steels”. en. In: *JOM* 66.5 (May 2014), pp. 740–746.

[23] M. Militzer et al. “Modelling of the diffusional austenite-ferrite transformation”. In: *International Materials Reviews* 68.7 (2023), pp. 725–754.

[24] M. Lavrskyi. *Modélisation en fonctionelle de la densité atomique des transformations de phases dans le système Fe-C à basse température*. anglais. Jan. 2017.

[25] G. Demange et al. “Atomistic study of the fcc → bcc transformation in a binary system: Insights from the Quasi-particle Approach”. en. In: *Acta Materialia* 226 (Mar. 2022), p. 117599.

[26] L. Casillas-Trujillo et al. “Dynamics of interaction between dislocations and point defects in bcc iron”. en. In: *Physical Review Materials* 2.10 (Oct. 2018), p. 103604.

[27] A. Adland et al. “Phase-field-crystal study of grain boundary premelting and shearing in bcc iron”. In: *Physical Review B—Condensed Matter and Materials Physics* 87.2 (2013), p. 024110.

[28] J. Li et al. “Phase field crystal modeling of grain boundary structures and growth in polycrystalline graphene”. In: *Journal of the Mechanics and Physics of Solids* 120 (2018), pp. 36–48.

[29] P. Y. Chan et al. “Plasticity and dislocation dynamics in a phase field crystal model”. In: *Physical review letters* 105.1 (2010), p. 015502.

[30] P. Stefanovic, M. Haataja, and N. Provatas. “Phase field crystal study of deformation and plasticity in nanocrystalline materials”. In: *Physical Review E—Statistical, Nonlinear, and Soft Matter Physics* 80.4 (2009), p. 046107.

[31] J. Berry et al. “Atomistic study of diffusion-mediated plasticity and creep using phase field crystal methods”. In: *Physical Review B* 92.13 (2015), p. 134103.

[32] J. Berry et al. “Phase field crystal modeling as a unified atomistic approach to defect dynamics”. In: *Physical Review B* 89.21 (2014), p. 214117.

[33] S. Tang et al. “Three-dimensional phase-field crystal modeling of fcc and bcc dendritic crystal growth”. In: *Journal of crystal growth* 334.1 (2011), pp. 146–152.

[34] A. Yamanaka, K. McReynolds, and P. W. Voorhees. “Phase field crystal simulation of grain boundary motion, grain rotation and dislocation reactions in a BCC bicrystal”. In: *Acta Materialia* 133 (2017), pp. 160–171.

[35] M. Greenwood, C. Sinclair, and M. Militzer. “Phase field crystal model of solute drag”. In: *Acta materialia* 60.16 (2012), pp. 5752–5761.

[36] Y. M. Jin and A. G. Khachaturyan. “Atomic density function theory and modeling of microstructure evolution at the atomic scale”. en. In: *Journal of Applied Physics* 100.1 (July 2006), p. 013519.

[37] F.-Z. Dai, Z.-P. Sun, and W.-Z. Zhang. “From coherent to semicoherent—evolution of precipitation crystallography in an fcc/bcc system”. In: *Acta Materialia* 186 (2020), pp. 124–132.

[38] E. C. Bain and N. Dunkirk. “The nature of martensite”. In: *trans. AIME* 70.1 (1924), pp. 25–47.

[39] V. G. Kurdjumow. “Uber den Mechanismus tier Stahlhartung”. de. In: (1930).

[40] A. Bogers and W. Burgers. “Partial dislocations on the {110} planes in the B.C.C. lattice and the transition of the F.C.C. into the B.C.C. lattice”. en. In: *Acta Metallurgica* 12.2 (Feb. 1964), pp. 255–261.

[41] G. Olson and M. Cohen. “A mechanism for the strain-induced nucleation of martensitic transformations”. en. In: *Journal of the Less Common Metals* 28.1 (July 1972), pp. 107–118.

[42] M. Wechsler, D. Lieberman, and T. Read. “On the theory of the formation of Martensite”. In: *JOURNAL OF METALS* (Nov. 1953).

[43] X. Ma and R. Pond. “Parent–martensite interface structure in ferrous systems”. en. In: *Journal of Nuclear Materials* 361.2-3 (Apr. 2007), pp. 313–321.

[44] H. K. Bhadeshia. *Worked examples in the geometry of crystals*. en. London: Institute of Metals, 1987.

[45] A. Khachaturyan. *Theory of Structural Transformations in Solids*. en. Dover Books on Engineering. OCLC: 900346426. Newburyport: Dover Publications, 2013.

[46] Z. Nishiyama et al. *Martensitic transformation*. en. Materials science and technology. New York: Academic Press, 1978.

[47] M. Sun et al. “The critical impact of intercritical deformation on variant pairing of bainite/martensite in dual-phase steels”. en. In: *Materials Science and Engineering: A* 771 (Jan. 2020), p. 138668.

[48] D. Fukui, N. Nakada, and S. Onaka. “Internal residual stress originated from Bain strain and its effect on hardness in Fe–Ni martensite”. en. In: *Acta Materialia* 196 (Sept. 2020), pp. 660–668.

[49] B. R. Cuenya, M. Doi, and S. Lo. “Observation of the fcc-to-bcc Bain transformation in epitaxial Fe ultrathin ®lms on Cu3Au(0 0 1)”. en. In: *Surface Science* (2001).

[50] J. S. Bowles and C. M. Wayman. “The bain strain, lattice correspondences, and deformations related to martensitic transformations”. en. In: *Metallurgical Transactions* 3.5 (May 1972), pp. 1113–1121.

[51] K. Koumatos and A. Muehlemann. “A theoretical investigation of orientation relationships and transformation strains in steels”. en. In: *Acta Crystallographica Section A Foundations and Advances* 73.2 (Mar. 2017), pp. 115–123.

[52] A. B. Greninger and A. R. Troiano. “The Mechanism of Martensite Formation”. en. In: (1949), p. 9.

[53] J. Bowles and J. Mackenzie. “The crystallography of martensite transformations I”. en. In: *Acta Metallurgica* 2.1 (Jan. 1954), pp. 129–137.

[54] M. Hall, J. Rigsbee, and H. Aaronson. “Application of the “0” lattice calculation to f.c.c./b.c.c. interfaces”. en. In: *Acta Metallurgica* 34.7 (July 1986), pp. 1419–1431.

[55] B. Sandvik and C. Wayman. “Crystallography and substructure of lath martensite formed in carbon steels”. en. In: *Metallography* 16.2 (May 1983), pp. 199–227.

[56] B. P. J. Sandvik and C. M. Wayman. “Characteristics of lath martensite: Part III. Some theoretical considerations”. en. In: *Metallurgical Transactions A* 14.4 (Apr. 1983), pp. 835–844.

[57] Y. He, S. Godet, and J. J. Jonas. “Observations of the Gibeon meteorite and the inverse Greninger–Troiano orientation relationship”. In: *Journal of Applied Crystallography* 39.1 (Feb. 2006), pp. 72–81.

[58] R. Smallman and R. Bishop. *Metals and Materials*. Anglais. Butterworth Heinemann.

[59] U. Messerschmidt. *Dislocation Dynamics During Plastic Deformation*. en. Ed. by R. Hull et al. Vol. 129. Springer Series in Materials Science. Berlin, Heidelberg: Springer Berlin Heidelberg, 2010.

[60] J. Hirth and R. C. Pond. “Steps, dislocations and disconnections as interface defects relating to structure and phase transformations”. anglais. In: *Acta Metallurgica Inc* (Mar. 1996).

[61] R. Pond, S. Celotto, and J. Hirth. “A comparison of the phenomenological theory of martensitic transformations with a model based on interfacial defects”. en. In: *Acta Materialia* 51.18 (Oct. 2003), pp. 5385–5398.

[62] J. Howe, R. Pond, and J. Hirth. “The role of disconnections in phase transformations”. en. In: *Progress in Materials Science* 54.6 (Aug. 2009), pp. 792–838.

[63] R. Pond and J. Hirth. “Elastic and plastic aspects of martensitic transformations”. en. In: *Philosophical Magazine* 90.7-8 (Mar. 2010), pp. 805–819.

[64] G. J. Shiflet and J. H. Merwe. “The role of structural ledges as misfit- compensating defects: fcc-bcc interphase boundaries”. en. In: *Metallurgical and Materials Transactions A* 25.9 (Sept. 1994), pp. 1895–1903.

[65] S. Morito et al. “The morphology and crystallography of lath martensite in Fe-C alloys”. en. In: *Acta Materialia* 51.6 (Apr. 2003), pp. 1789–1799.

[66] F. Nabarro and M. Duesbery. *Dislocations in Solids*. Dislocations in Solids vol. 11. Elsevier Science, 2002.

[67] “Continuous distributions of dislocations: a new application of the methods of non-Riemannian geometry”. en. In: *Proceedings of the Royal Society of London. Series A. Mathematical and Physical Sciences* 231.1185 (Aug. 1955), pp. 263–273.

[68] P. McDougall and C. Wayman. “The crystallography and morphology of ferrous martensites”. In: *ASM International, Martensite(USA), 1992,* (1992), pp. 59–95.

[69] Z. Nishiyama. “X-ray investigation of the mechanism of the transformation from face centered cubic lattice to body centered cubic”. In: *Sci. Rep. Tohoku Univ.* 23 (1934), p. 637.

[70] C. Cayron. "One-step model of the face-centred-cubic to body-centred-cubic martensitic transformation". en. In: *Acta Crystallographica Section A Foundations of Crystallography* 69.5 (Sept. 2013), pp. 498–509.

[71] L. Bracke, L. Kestens, and J. Penning. "Transformation mechanism of α'-martensite in an austenitic Fe–Mn–C–N alloy". en. In: *Scripta Materialia* 57.5 (Sept. 2007), pp. 385–388.

[72] J. Rigsbee and H. Aaronson. "A computer modeling study of partially coherent f.c.c.:b.c.c. boundaries". en. In: *Acta Metallurgica* 27.3 (Mar. 1979), pp. 351–363.

[73] W. Bollmann. "O-Lattice calculation of an FCC–BCC interface". In: *Physica status solidi (a)* 21.2 (1974), pp. 543–550.

[74] L.-Q. Chen. "Phase-field models for microstructure evolution". In: *Annual review of materials research* 32.1 (2002), pp. 113–140.

[75] W. Zhang, Y. Jin, and A. Khachaturyan. "Phase field microelasticity modeling of heterogeneous nucleation and growth in martensitic alloys". In: *Acta Materialia* 55.2 (2007), pp. 565–574.

[76] M. Mamivand, M. A. Zaeem, and H. El Kadiri. "A review on phase field modeling of martensitic phase transformation". In: *Computational Materials Science* 77 (2013), pp. 304–311.

[77] J. Fischer and M. Wendland. "On the history of key empirical intermolecular potentials". In: *Fluid Phase Equilibria* 573 (2023), p. 113876.

[78] M. S. Daw and M. I. Baskes. "Embedded-atom method: Derivation and application to impurities, surfaces, and other defects in metals". In: *Physical Review B* 29.12 (1984), p. 6443.

[79] M. I. Baskes. "Modified embedded-atom potentials for cubic materials and impurities". In: *Physical review B* 46.5 (1992), p. 2727.

[80] R. A. Johnson and D. J. Oh. "Analytic embedded atom method model for bcc metals". en. In: *Journal of Materials Research* 4.5 (Oct. 1989), pp. 1195–1201.

[81] G. J. Ackland et al. "Computer simulation of point defect properties in dilute Fe—Cu alloy using a many-body interatomic potential". en. In: *Philosophical Magazine A* 75.3 (Mar. 1997), pp. 713–732.

[82] R. Meyer and P. Entel. "Martensite-austenite transition and phonon dispersion curves of Fe 1 - x Ni x studied by molecular-dynamics simulations". en. In: *Physical Review B* 57.9 (Mar. 1998), pp. 5140–5147.

[83] T. Lee et al. "Atomistic modeling of thermodynamic equilibrium and polymorphism of iron". In: *Journal of Physics: Condensed Matter* 24.22 (May 2012), p. 225404.

[84] S. Karewar et al. "An atomistic perspective of martensite twinning in Iron". en. In: (Jan. 2020). arXiv:2001.11053 [cond-mat].

[85] C. Bos, J. Sietsma, and B. J. Thijsse. “Molecular dynamics simulation of interface dynamics during the fcc-bcc transformation of a martensitic nature”. en. In: *Physical Review B* 73.10 (Mar. 2006), p. 104117.

[86] B. P. J. Sandvik and C. M. Wayman. “Characteristics of lath martensite: Part I. crystallographic and substructural features”. en. In: *Metallurgical Transactions A* 14.4 (Apr. 1983), pp. 809–822.

[87] B. P. J. Sandvik and C. M. Wayman. “Characteristics of lath martensite: Part II. The martensite-austenite interface”. en. In: *Metallurgical Transactions A* 14.4 (Apr. 1983), pp. 823–834.

[88] A. D. King and T. Bell. “Crystallography of grain boundary proeutectoid ferrite”. en. In: *Metallurgical Transactions A* 6.7 (July 1975), pp. 1419–1429.

[89] P. Kelly, A. Jostsons, and R. Blake. “The orientation relationship between lath martensite and austenite in low carbon, low alloy steels”. en. In: *Acta Metallurgica et Materialia* 38.6 (June 1990), pp. 1075–1081.

[90] G. Miyamoto, N. Takayama, and T. Furuhara. “Accurate measurement of the orientation relationship of lath martensite and bainite by electron backscatter diffraction analysis”. en. In: *Scripta Materialia* 60.12 (June 2009), pp. 1113–1116.

[91] G. Purdy. “The dynamics of transformation interfaces in steels—I. The ferrite-austenite interface in Fe-C-Mo alloys”. en. In: *Acta Metallurgica* 26.3 (Mar. 1978), pp. 477–486.

[92] Y. He et al. “The mechanisms of γ (fcc) $\rightarrow$ ϵ (hcp) $\rightarrow$ α' (bcc) and direct γ (fcc) $\rightarrow$ α' (bcc) martensitic transformation in a gradient austenitic stainless steel”. en. In: *Journal of Materials Science* 57.8 (Feb. 2022), pp. 5230–5240.

[93] Z. Weina et al. “The crystallographic mechanism for deformation induced martensitic transformation observed by high resolution transmission electron microscope”. en. In: *Materials Letters* 91 (Jan. 2013), pp. 158–160.

[94] X.-S. Yang et al. “Dissecting the Mechanism of Martensitic Transformation via Atomic-Scale Observations”. en. In: *Scientific Reports* 4.1 (Aug. 2014), p. 6141.

[95] H. Jin. “Atomistic Simulations of Solute-Interface Interactions in Iron”. en. In: ().

[96] T. Q. Nguyen, K. Sato, and Y. Shibutani. “First-Principles Study of BCC/FCC Phase Transition Promoted by Interstitial Carbon in Iron”. en. In: *MATERIALS TRANSACTIONS* 59.6 (June 2018), pp. 870–875.

[97] H. Wang et al. “Segregation mechanism of alloying elements at the fcc-Fe/bcc-Fe interface and its effects on carbon diffusion across the boundary”. en. In: *Journal of Physics and Chemistry of Solids* 183 (Dec. 2023), p. 111657.

[98] A. H. Cottrell and M. Jaswon. “Distribution of solute atoms round a slow dislocation”. In: *Proceedings of the Royal Society of London. Series A. Mathematical and Physical Sciences* 199.1056 (1949), pp. 104–114.

[99] A. Cottrell. "LXXXVI. A note on the Portevin-Le Chatelier effect". In: *The London, Edinburgh, and Dublin Philosophical Magazine and Journal of Science* 44.355 (1953), pp. 829–832.

[100] E. Clouet et al. "Dislocation interaction with C in α-Fe: A comparison between atomic simulations and elasticity theory". en. In: *Acta Materialia* 56.14 (Aug. 2008), pp. 3450–3460.

[101] H. Jin, I. Elfimov, and M. Militzer. "First-principles simulations of binding energies of alloying elements to the ferrite-austenite interface in iron". en. In: *Journal of Applied Physics* 123.8 (Feb. 2018), p. 085303.

[102] X. Zhu et al. "First-Principles Study on the Effect of H, C, and N at the Interface on Austenite/Ferrite Homojunction". en. In: *Metals* 13.2 (Feb. 2023), p. 317.

[103] G. Hachet et al. "Screw dislocation-carbon interaction in BCC tungsten: an ab initio study". en. In: *Acta Materialia* 200 (Nov. 2020), pp. 481–489.

[104] C. Becquart et al. "Atomistic modeling of an Fe system with a small concentration of C". en. In: *Computational Materials Science* 40.1 (July 2007), pp. 119–129.

[105] R. G. A. Veiga et al. "Atomistic modeling of carbon Cottrell atmospheres in bcc iron". en. In: *Journal of Physics: Condensed Matter* 25.2 (Jan. 2013), p. 025401.

[106] R. Isozaki and Y. Shibuta. "Molecular Dynamic Simulation of Kinetics of fcc–bcc Heterointerface in Phase Transformation of Iron and Carbon Steel". en. In: *ISIJ International* 64.2 (Jan. 2024), pp. 184–191.

[107] L. Ventelon et al. "Dislocation core reconstruction induced by carbon segregation in bcc iron". en. In: *Physical Review B* 91.22 (June 2015), p. 220102.

[108] J. Wilde, A. Cerezo, and G. Smith. "Three-dimensional atomic-scale mapping of a cottrell atmosphere around a dislocation in iron". en. In: *Scripta Materialia* 43.1 (June 2000), pp. 39–48.

[109] C. Zener. "Kinetics of the decomposition of austenite". In: *Trans. Aime* 167 (1946), pp. 550–595.

[110] C. Zener. "Theory of growth of spherical precipitates from solid solution". In: *Journal of applied physics* 20.10 (1949), pp. 950–953.

[111] M. Gouné et al. "Overview of the current issues in austenite to ferrite transformation and the role of migrating interfaces therein for low alloyed steels". en. In: *Materials Science and Engineering: R: Reports* 92 (June 2015), pp. 1–38.

[112] A. Saha, G. Ghosh, and G. Olson. "An assessment of interfacial dissipation effects at reconstructive ferrite–austenite interfaces". en. In: *Acta Materialia* 53.1 (Jan. 2005), pp. 141–149.

[113] Y. van LEEUWEN and J. Sietsma. “The Influence of Carbon Diffusion on the Character of the g–a Phase Transformation in Steel”. en. In: *ISIJ International* 43.5 (2003).

[114] J. Sietsma and S. van der Zwaag. “A concise model for mixed-mode phase transformations in the solid state”. en. In: *Acta Materialia* 52.14 (Aug. 2004), pp. 4143–4152.

[115] E. Gamsjäger et al. “Interface mobility in case of the austenite-to-ferrite phase transformation”. en. In: *Computational Materials Science* 37.1-2 (Aug. 2006), pp. 94–100.

[116] C. Bos and J. Sietsma. “A mixed-mode model for partitioning phase transformations”. en. In: *Scripta Materialia* 57.12 (Dec. 2007), pp. 1085–1088.

[117] K. R. Kinsman and H. I. Aaronson. “Influence of al, co, and si upon the kinetics of the proeutectoid ferrite reaction”. en. In: *Metallurgical Transactions* 4.4 (Apr. 1973), pp. 959–967.

[118] C. Atkinson et al. “On the growth kinetics of grain boundary ferrite allotriomorphs”. en. In: *Metallurgical Transactions* 4.3 (Mar. 1973), pp. 783–792.

[119] J. R. Bradley et al. “Effects of austenitizing temperature on the kinetics of the proeutectoid ferrite reaction at constant austenite grain size in an Fe-C alloy”. en. In: *Metallurgical Transactions A* 8.12 (Dec. 1977), pp. 1955–1961.

[120] G. P. Krielaart, J. Sietsma, and S. van der Zwaag. “Ferrite formation in Fe-C alloys during austenite decomposition under non-equilibrium interface conditions”. en. In: *Materials Science and Engineering: A* 237.2 (Sept. 1997), pp. 216–223.

[121] J. Svoboda, F. Fischer, and E. Gamsjäger. “Influence of solute segregation and drag on properties of migrating interfaces”. en. In: *Acta Materialia* 50.5 (Mar. 2002), pp. 967–977.

[122] A. Khachaturian. *Ordering in Substitutional and Interstitial Solid Solutions*. Ordering in Substitutional and Interstitial Solid Solutions vol. 22,n° 1 -vol. 23,n° 4. Pergamon Press, 1978.

[123] K. R. Elder and M. Grant. “Modeling elastic and plastic deformations in nonequilibrium processing using phase field crystals”. en. In: *Physical Review E* 70.5 (Nov. 2004), p. 051605.

[124] M. Lavrskyi, H. Zapolsky, and A. G. Khachaturyan. “Quasiparticle approach to diffusional atomic scale self-assembly of complex structures: from disorder to complex crystals and double-helix polymers”. en. In: *npj Computational Materials* 2.1 (Nov. 2016), p. 15013.

[125] M. Certain. “Développement de la méthode du champ de phase cristallin et modélisation des transitions de phase displacives”. fr. In: (2013).

[126] H. Zapolsky et al. “Size-Dependent Solute Segregation at Symmetric Tilt Grain Boundaries in alpha-Fe: A Quasiparticle Approach Study”. en. In: *Materials* 14.15 (July 2021), p. 4197.

[127] R. Poduri and L.-Q. Chen. “Computer simulation of atomic ordering and compositional clustering in the pseudobinary Ni3Al–Ni3V system”. en. In: *Acta Materialia* 46.5 (Mar. 1998), pp. 1719–1729.

[128] A. V. Ruban. “Self-trapping of carbon atoms in $_{a}lpha'$-Fe during the martensitic transformation: A qualitative picture from *ab initio* calculations”. en. In: *Physical Review B* 90.14 (Oct. 2014), p. 144106.

[129] A. Udyansky et al. “Orientational ordering of interstitial atoms and martensite formation in dilute Fe-based solid solutions”. en. In: *Physical Review B* 83.18 (May 2011), p. 184112.

[130] A. Khachaturyan and B. Pokrovskii. “Concentration wave approach in structural and thermodynamic characterization of ceramic crystals”. en. In: *Progress in Materials Science* 29.1-2 (Jan. 1985), pp. 1–138.

[131] D. J. Eyre. “An Unconditionally Stable One-Step Scheme for Gradient Systems”. en. In: *Unpublished article* (1998).

[132] G. Demange et al. “Generalization of the Fourier-spectral Eyre scheme for the phase-field equations: Application to self-assembly dynamics in materials”. en. In: *Computational Materials Science* 144 (Mar. 2018), pp. 11–22.

[133] L. Chen and J. Shen. “Applications of semi-implicit Fourier-spectral method to phase field equations”. en. In: *Computer Physics Communications* 108.2-3 (Feb. 1998), pp. 147–158.

[134] J. A. Zimmerman et al. “Surface Step Effects on Nanoindentation”. en. In: *Physical Review Letters* 87.16 (Oct. 2001), p. 165507.

[135] C. D. Hansen and C. R. Johnson, eds. *The visualization handbook*. en. Amsterdam ; Boston: Elsevier-Butterworth Heinemann, 2005.

[136] A. Stukowski. “Visualization and analysis of atomistic simulation data with OVITO–the Open Visualization Tool”. en. In: *Modelling and Simulation in Materials Science and Engineering* 18.1 (Jan. 2010), p. 015012.

[137] A. Goryaeva. *fratons2atoms.* `https://github.com/agoryaeva/fratons2atoms`. 2021.

[138] T. Maki. “Morphology and substructure of martensite in steels”. en. In: *Phase Transformations in Steels*. Elsevier, 2012, pp. 34–58.

[139] S. Tateyama, Y. Shibuta, and T. Suzuki. “Orientation Relationship in Fcc–Bcc Phase Transformation Kinetics of Iron: a Molecular Dynamics Study”. en. In: *ISIJ International* 50.8 (2010), pp. 1211–1216.

[140] C. Stassis. “Inelastic neutron scattering of γ-iron and the determination of the elastic constants by lattice dynamics”. In: *AIP Conference Proceedings* 309.1 (July 1994), pp. 955–958.

[141] D. R. Lide. *CRC handbook of chemistry and physics*. Vol. 85. CRC press, 2004.

[142] B. Yao and R. Zhang. “AADIS: An atomistic analyzer for dislocation character and distribution”. en. In: *Computer Physics Communications* 247 (Feb. 2020), p. 106857.

[143] H. Brune. “Growth modes”. In: *Encyclopedia of Materials: Science and Technology, Sect. 1.9, Physical Properties of Thin Films and Artificial Multilayers* (2001), pp. 3683–3693.

[144] H. Song and J. Hoyt. “A molecular dynamics simulation study of the velocities, mobility and activation energy of an austenite–ferrite interface in pure Fe”. en. In: *Acta Materialia* 60.10 (June 2012), pp. 4328–4335.

[145] D. B. Williams and C. B. Carter. *Transmission Electron Microscopy*. en. Boston, MA: Springer US, 1996.

[146] M. Mazinani and W. Poole. “Effect of Martensite Plasticity on the Deformation Behavior of a Low-Carbon Dual-Phase Steel”. en. In: *Metallurgical and Materials Transactions A* 38.2 (Feb. 2007), pp. 328–339.

[147] S. Crusius et al. “On the Growth of Ferrite Allotriomorphs in Fe-C Alloys/Das Wachstum von allotriomorphem Ferrit in Fe—C-Legierungen: Dedicated to Professor Dr. rer. nat. Wolfgang Pitsch on the occasion of his 65th birthday”. In: *International Journal of Materials Research* 83.10 (1992), pp. 729–738.

[148] C. Atkinson et al. “On the growth kinetics of grain boundary ferrite allotriomorphs”. In: *Metallurgical Transactions* 4 (1973), pp. 783–792.

[149] K. Kinsman and H. Aaronson. “Influence of Al, Co, and Si upon the kinetics of the proeutectoid ferrite reaction”. In: *Metallurgical transactions* 4 (1973), pp. 959–967.

[150] J. Bradley, J. Rigsbee, and H. Aaronson. “Growth kinetics of grain boundary ferrite allotriomorphs in Fe- C alloys”. In: *Metallurgical Transactions A* 8 (1977), pp. 323–333.

[151] G. R. Purdy. “Kinetics of the proeutectoid ferrite reaction at an incoherent interface, as determined by a diffusion couple”. In: *Trans TMS-AIME* 227 (1963), p. 1255.

[152] V. Vítek, R. C. Perrin, and D. K. Bowen. “The core structure of $\frac{1}{2}(111)$ screw dislocations in b.c.c. crystals”. en. In: *Philosophical Magazine* 21.173 (May 1970), pp. 1049–1073.

[153] A. Stukowski. “Structure identification methods for atomistic simulations of crystalline materials”. en. In: *Modelling and Simulation in Materials Science and Engineering* 20.4 (June 2012), p. 045021.

[154] P. Virtanen et al. “SciPy 1.0: fundamental algorithms for scientific computing in Python”. en. In: *Nature Methods* 17.3 (Mar. 2020), pp. 261–272.

Modélisation atomistique de la transition de phase austénite-ferrite dans les aciers.

Résumé

Cette thèse applique l'approche des Quasiparticles (QA) pour étudier les mécanismes à l'échelle atomique qui conduisent à la transformation de phase CFC à CC dans le fer. Dans un premier temps, cette étude se concentre sur le fer pur, fournissant des résulats détaillés sur la nature et le rôle des dislocations à l'interface CFC-CC. Il a été montré que l'interface CFC-CC est semi-cohérente, avec des marches, et contient deux réseaux de dislocations de transformations. L'approche des Quasiparticles a permis de révéler l'influence de la relation d'orientation sur les caractéristiques de l'interface. Bien que les relations d'orientation étudiées ont montré diférentes structures d'interface, il a été démontré que toutes suivent le même chemin de transformation atomique, dû au glissement des dislocations de transformation à l'interface. Il a été conclu que la transformation complète de CFC à CC implique le mécanisme de transformation de Kurdjumov-Sachs (KS) en deux variantes le long des lignes de dislocations, avec le mécanisme de transformation de Kurdjumov-Sachs-Nishiyama (KSN) qui émerge comme la moyenne de l'action des deux mécanismes KS. Cette description détaillée a servi de base pour l'étude des systèmes Fe-C, où la ségrégation du carbone à l'interface a été observée. De plus, il a été montré que les profils de concentration de carbone sont cohérents avec des conditions d'équilibre local à l'interface.

Abstract

This thesis applies the Quasiparticle Approach (QA) to investigate the atomic scale mechanisms driving the phase transformation from FCC to BCC structures in iron. Initially, the study focuses on pure iron, providing detailed results into the nature and role of dislocations, at the FCC-BCC interface. It was shown that the FCC-BCC interface is semi-coherent and stepped, with two sets of transformations dislocations at the interface. The QA framework reveals how each orientation relationship (OR) influences the interface characteristics. Although the ORs displayed different interface structures, all were ultimately found to follow the same atomic transformation path, driven by the glide of transformation dislocations at the interface. It was concluded that the complete FCC to BCC phase transformation involves the action of the Kurdjumov-Sachs (KS) transformation mechanism in two variants along the two sets of dislocations, with the Kurdjumov-Sachs-Nishiyama (KSN) mechanism emerging as the average of the two KS mechanisms. This detailed description served as a basis for the study of Fe-C systems, where carbon segregation at the interface was observed. Moreover, it was shown that the carbon concentration profiles were consistent with local equilibrium conditions at the interface.

Mots clés : Transformation de phase austénite-ferrite, interfaces de transformation de phase, mécanisme de transformation, dislocations, ségrégation du carbone, simulation atomistique, champ de phase cristallin, quasiparticules, modélisation, fer, fer-carbone, acier.